

Measurements of Dynamics in an Orientationally Anisotropic System

by
Matthew A. Borthwick


Bachelor of Science in Applied & Engineering Physics
Cornell University, 1995

Master of Science in Physics
McGill University, 1997


Submitted to the Department of Physics
in partial fulfillment of the requirements for the degree of
Doctor of Philosophy
at the

MASSACHUSETTS INSTITUTE OF TECHNOLOGY
September 2004

© Massachusetts Institute of Technology 2004. All rights reserved.

Author 
Department of Physics

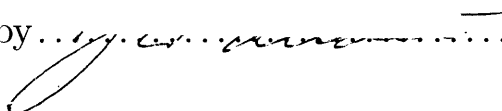
August 6, 2004

Certified by 

Simon G. J. Mochrie

Professor of Physics and Applied Physics, Yale University

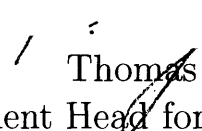
Thesis Supervisor

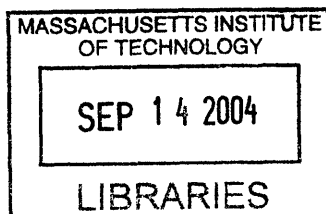
Certified by 

J. David Litster

Professor of Physics

Thesis Supervisor

Accepted by 
Thomas J. Greytak
Associate Department Head for Education



ARCHIVES

Measurements of Dynamics in an Orientationally Anisotropic System

by

Matthew A. Borthwick

Submitted to the Department of Physics
on August 6, 2004 in partial fulfillment
requirements for the degree of Doctor of Philosophy in
Physics

Abstract

We present X-ray photon correlation spectroscopy and small-angle X-ray scattering studies of charge-stabilized, rodlike boehmite (AlOOH) particles in semidilute and concentrated suspensions in glycerol, both in an isotropic phase and an orientationally ordered, lyotropic liquid crystalline phase. Using an array detector, simultaneous measurements were made along both the radial and azimuthal directions of the scattering vector.

The measured scattering was compared to the isotropic, polydisperse rod form factor, and an electrical double-layer was included in the model. Two distinct sets of nematic ordering were seen in each sample: one, we believe, aligned by flow and the other by interactions with the sample cell surface. Two independent indications of weak, direction-dependent positional ordering in the nematic phase were observed. The first involved nematic order parameters obtained by fitting the scattering's azimuthal dependence at each radial coordinate. Those order parameters displayed an apparent increase near the interparticle structure factor peak. The second indication came from measurements of the radial interparticle structure factor peak position itself. In a small range of concentration just above the nematic transition, the peak position was independent of concentration, deviating from the otherwise-observed dependence on the square root of concentration.

Equilibrium dynamics in the isotropic phase were studied on length scales well below the rod lengths. Time autocorrelation functions were fitted using the common double-exponential form as well as Maeda's matrix implementation of the Doi-Shimada-Okano self-consistent mean field form for the dynamic structure factor. The latter produced direct estimates of the self-diffusion coefficients, and these were compared to the "effective" coefficients yielded by the former.

Because scattering from a nematic domain is limited to a narrow azimuthal range, while an isotropic domain scatters uniformly to all azimuthal angles, separate but simultaneous measurements of dynamics in coexisting isotropic and orientationally ordered domains were possible. The observed correlation functions indicated that the flow-aligned, equilibrium nematic phase predominant just above the ordering transition was supplanted by a surface-aligned, nonequilibrium, "jammed" phase as the concentration of rods was further increased.

Thesis Supervisor: Simon G. J. Mochrie
Title: Professor of Physics and Applied Physics, Yale University

Thesis Supervisor: J. David Litster
Title: Professor of Physics

Acknowledgements

I received an enormous amount of support during the course of this work, and would like to express my gratitude to all those who helped me—in large ways or small—to complete this thesis. There are a number of people I wish to expressly thank.

My thesis advisor was Prof. Simon Mochrie. Simon has a talent for immediately boiling down complex problems to their roots. I learned a great deal from him on how to approach problems and think critically about them. Above and beyond the usual research guidance an advisor provides, Simon also gave me the rare and valuable opportunity to take part in the development of the 8-ID beamline.

Simon was first and foremost among those whose assistance and generosity permitted me to remain at MIT throughout my entire Ph.D. program. Prof. Dave Litster served as my MIT-based co-supervisor for the last several years and I am truly grateful to him for volunteering to serve in that capacity as well as for donating office and lab space for my use. In addition to Simon, I am indebted to several others for direct financial support: Prof. Mark Sutton of McGill University, Prof. Marc Kastner and the MIT Physics Department, and Drs. Alec Sandy and Jin Wang of XOR at the Advanced Photon Source. The road was significantly smoothed by Karen Foshier, Ron Haseltine, Heather Williams, and Jonathan Bartels, and I received initial guidance from Profs. Ophelia Tsui and Mirang Yoon.

This thesis benefited from the insightful comments of my committee: Profs. Mochrie, Litster, Alexander van Oudenaarden, Young Lee, and Takashi Imai. I was lucky enough to work as a recitation instructor alongside Profs. Litster and van Oudenaarden, and also “lucky” enough to occasionally split late-night hours at the beamline with Prof. Lee. Their encouragement regarding those efforts as well as my thesis was greatly appreciated.

I enjoyed collaborating with Prof. Bob Leheny and Dennis Liang of Johns Hopkins University. They helped clarify my picture of what was going on inside the capillaries and also introduced me to a wider scope of intriguing liquid crystalline systems.

The success of my runs at Argonne was due largely to several talented individuals:

- Prof. Sutton, from whom I could still learn a great deal about programming despite nearly a decade under his wing.
- Dr. Adrian Rühm, who helped get the ball rolling on the first böhmite measurements and somehow never lost his enthusiasm for tweaking the motors even after the beam had been lost for days.
- Harold Gibson, whose dedication to and talent for making controls more convenient for users made me eager to revisit the beamline every few months to see how my life was going to be easier.
- Dr. Sandy, who welcomed my questions and then patiently expanded his explanations until I understood the answers. Alec showed me that one can usually say more by

using fewer words.

- Prof. Laurence Lurio of Northern Illinois University. Scientists are prone to describing their work—or occasionally someone else’s—as “exciting.” Their delivery, though, is typically so deadpan as to seem ripe with irony. Or fatigue, bordering on catatonia. But when Larry says something is exciting, he means *exciting!* Larry contributed enormously to ‘coherent’, from the lowest-level syntax to the most abstract concepts of what XPCS really measures. He was even glad to take time to help troubleshoot the hardware as well. Larry further sparked my own interest in my thesis topic and in the field as a whole.
- Dr. Dirk Lumma. Dirk is always an idealist dreamer except for most of the time when he’s a skeptical pragmatist. If Simon, Larry, and Alec taught me the overarching tenets of XPCS, it Dirk who showed me what would actually get the experiments to work. I also received from him a vision that what we were trying to achieve was important and relevant, and it helped me set more ambitious goals for myself.
- Dr. Péter Falus. Péter has been my comrade-in-arms, lo these many years. I learned one-and-a-half things from him. The one was that when you’re making something, designing in all the elegance in the world is fine—but only if you bothered to check first whether the thing will ever work at all. The half was that, as far as I can tell, Hungarian culture (which Péter graciously invited me in many different ways to experience) senses no paradox whatsoever in finding an experience to be both abysmal and delightful at the same time. I regret never fully understanding that concept, although in hindsight writing a thesis does seem a perfect example. Péter assisted and often guided me through almost all of the work presented here. I frequently turned to him for sanity checks, relied on his mathematical prowess for uncannily precise estimates, asked him for reminders of why I had decided to do something in the first place, and imposed on him far too many times to customize or repair parts that weren’t behaving the way I wanted. It was reassuring to know he was watching over my shoulder to catch any mistakes before they became disasters. In addition, the high-speed camera Péter designed produced most of the XPCS data in this thesis.

When I needed intermittent respites from X-ray scattering, a large and devoted group of friends was there to share their diverse, fascinating, and amusing perspectives on life. The list of such people is long, so I will not reproduce it here. Instead, I will single out one nuclear individual, Sajan Saini. (No, by “nuclear” I mean “central.”) Anyone who knows me and has ever met Sajan shall consider themselves on this list and hence eligible for equivalent levels of gratitude. Sajan is a particularly good example because he has been a fellow MIT grad student but our common interests generally lie away from science. He has routinely reminded me that there is a marvelous world outside the laboratory. He has also reflected

my own dismay at how much slower than we ever anticipated does research progress, but in the end we have looked back in amazement at how much we each accomplished.

I also gained much-needed balance from my participation in Isshinryu Karate-do at MIT. My sincere thanks go to all who took the time and effort to study with the club. It is the greatest gift I could imagine to know that the MIT *dojo* will continue.

This thesis echoes the voices of my sister, Jane Borthwick, my parents, William and Arlene Borthwick, my grandparents, Irene Grambo and Ernest and Lois Borthwick, and my extended family. They shaped the way I talk, write, and think about the world. If there is a common thread among members of the Borthwick and Grambo families, it is that we all enjoy solving puzzles of one sort or another. Their unwavering support of my esoteric studies has been a constant source of strength.

If one combines the last three paragraphs, it begins to scratch the surface of the roles my wife, Lisa McGill, has played in my graduate life. I thank her for her patience and her impatience, for her trust and her doubts, all impeccably timed. I doubt our lives will proceed along quite so parallel professional tracks in the future, but it certainly was fun to work in the same building for a few years. Lisa's presence throughout this process has turned what otherwise would have been a difficult but rewarding endeavor into a rich and profoundly meaningful experience.

Contents

1	Introduction	15
1.1	Böhmite, a mineral liquid crystal	15
1.2	The isotropic-nematic phase transition	17
1.2.1	Self-consistent mean field approximation	17
1.2.2	Evaluating the Mayer function	18
1.2.2.1	Noninteracting particles and hard spherocylinders	18
1.2.2.2	Charged spherocylinders	19
1.2.3	Free energy of isotropic and nematic phases	20
1.2.3.1	Hard spherocylinders	20
1.2.3.2	Charged spherocylinders	20
1.2.4	Two-phase coexistence of hard rods	21
1.2.5	Effects of polydispersity	22
1.3	Phase transition observed with polarized light microscopy	22
1.4	X-ray Photon Correlation Spectroscopy	23
1.5	Overview	26
1.6	Outline	27
2	Azimuthal variations in static scattering due to nematic alignment	29
2.1	Determining the distribution of rod orientations	29
2.1.1	Scattering from a rigid rod	29
2.1.2	Scattering from a dilute, oriented suspension of rigid rods	30
2.1.2.1	The Maier-Saupe orientational distribution function	31
2.1.2.2	Davidson's generalized orientational distribution function	32
2.1.3	Scattering from a concentrated, oriented suspension of rigid rods	34
2.2	Limitations on information about isotropic-nematic coexistence from scattering measurements	34
2.2.1	Two-phase ($I - N$) coexistence	35
2.2.1.1	Equivalence of scattering from isotropic and a_0 terms	35
2.2.1.2	Experimental uncertainties and fitted proportions	36
2.2.2	Three-phase ($I - N_I - N_{II}$) coexistence	37
2.2.2.1	Interchangability of scattering from nematic domains	37
2.2.2.2	Experimental uncertainties and fitted order parameters	40
2.3	Characterization of orientational ordering in suspensions of böhmite in glycerol	40
2.3.1	Azimuthal dependence of scattering	40
2.3.2	Nematic director orientations	44
2.3.3	Nematic order parameters	47
2.3.4	Proportions of I , N_I , and N_{II} phases	49

3	The static interparticle structure factor across the isotropic-to-nematic transition	53
3.1	Determining the form factor	53
3.1.1	Scattering from a dilute, isotropic suspension of polydisperse rodlike particles	53
3.1.2	Absolute cross-section normalization	54
3.1.3	Form factor of a rigid rod with a surface layer	56
3.1.4	Numerical evaluation of polydisperse form factors	56
3.1.5	Direct evaluation of the form factor for böhmite in glycerol	57
3.1.6	Results of least-squares fits to the measured cross-section	59
3.2	Structure factor in the isotropic phase	61
3.2.1	Identifying the interparticle structure factor in X-ray scattering	61
3.2.1.1	Removing the effects of intraparticle scattering	61
3.2.1.2	Relation between the structure factor and pair correlation function	61
3.2.1.3	Accounting for polydispersity	63
3.2.2	Structure factors of isotropic suspensions of böhmite in glycerol	63
3.3	Structure factors in the orientationally ordered phase of böhmite in glycerol	67
3.3.1	Relating the nematic form factor to the isotropic form factor	67
3.3.2	Peak position and width versus azimuthal angle	69
3.3.3	Peak position and width versus volume fraction	71
3.3.4	Separating the structure factors of three domains	72
4	X-ray photon correlation spectroscopy study of semidilute, isotropic suspensions of rigid rods	77
4.1	Theoretical formulation of the dynamic structure factor	77
4.1.1	The Smoluchowski equation	77
4.1.2	Dynamic structure factor and the fluctuation dissipation theorem	78
4.1.3	The Smoluchowski equation in reciprocal space	79
4.1.4	Solving for the rod distribution function and the dynamic structure factor	80
4.2	Dynamic structure factor in matrix form	81
4.2.1	Useful identities	82
4.2.1.1	x^2	82
4.2.1.2	$e^{i\mathbf{q}\cdot\mathbf{r}\mathbf{u}}$	82
4.2.1.3	$j_0(\mathbf{q}\frac{L}{2}\cdot\mathbf{u})$	83
4.2.1.4	$ \mathbf{u}\times\mathbf{u}' $	83
4.2.2	Matrix representations of operators	84
4.2.3	Matrix representation of $S(\mathbf{q}, t)$	85
4.2.3.1	Full solution	85
4.2.3.2	Special case of no interactions and isotropic diffusion	86
4.2.4	Summary	86
4.3	Measured dynamics of isotropic suspensions of böhmite in glycerol	87
5	X-ray photon correlation spectroscopy study of concentrated, nematic suspensions of rigid rods	93
5.1	Models of dynamics in nematic liquid crystals	93
5.1.1	Director fluctuations	93

5.1.2	Self-diffusion	94
5.2	Measured dynamics of orientationally ordered suspensions of böhmite in glycerol	95
5.2.1	Near the orientational transition point	95
5.2.2	High concentration	98
6	Conclusion	107
A	Data analysis for anisotropic correlation functions	109
A.1	Data structure	110
A.2	Image partitioning and masking	110
A.3	Averaging analysis results over partitions	112
A.4	Image correction	113
A.4.1	Before time-averaging	113
A.4.2	After time-averaging	114
A.5	Multiple tau correlation	114
A.6	Normalizing correlation functions	116
A.6.1	Accounting for long-term intensity variations	116
A.6.1.1	Standard normalization	117
A.6.1.2	Symmetric normalization	117
A.6.2	Precisely accounting for long-range intensity variations	118
A.6.3	Image segments and normalization	120
B	Lower-level discrimination: Noise reduction for CCD measurements at low intensities	121
B.1	CCD response	121
B.1.1	Photon detection	121
B.1.2	Dark background	122
B.1.3	Variable response	123
B.1.4	Charge spreading	125
B.1.5	Experimentally characterizing the single-photon response	125
B.1.6	Determining photon rate from measured intensities	129
B.2	Lower-level discrimination	129
B.2.1	Ideal lower-level discrimination	130
B.2.2	Real lower-level discrimination, ignoring dark background	130
B.2.3	Real lower-level discrimination, including dark background	132
B.2.4	Determining Photon Rate from Discriminated Intensities	134
	Bibliography	137

List of Figures

1-1	0.7-mm diameter borosilicate glass capillaries containing 0.2% (<i>upper</i>) and 7.5% (<i>lower</i>) volume-fraction suspensions of böhmite in glycerol. Material can be seen at the left end of each capillary.	16
1-2	Schematic of lyotropic transition from isotropic (<i>left</i>) to nematic (<i>center</i>) phase. As the concentration of the nematic increases, the degree of alignment correspondingly increases (<i>right</i>).	17
1-3	Polarized light microscopy images from several böhmite in glycerol specimens.	24
1-4	Small-angle X-ray scattering and X-ray photon correlation spectroscopy apparatus: beamline 8-ID-I at the Advanced Photon Source.	25
2-1	Two different theoretical $I - N_I - N_{II}$ configurations that give rise to mathematically identical azimuthal scattering profiles. Thin lines represent individual domains' contributions. Thick lines represent the total scattering. The specific parameter values used are listed in Table 2.1.	39
2-2	Transmission geometry for scattering experiments. Azimuthal angles $\varphi = 0^\circ, 180^\circ$ represented directions perpendicular to the capillary; $\varphi = 90^\circ, 270^\circ$ were parallel to the capillary.	41
2-3	Azimuthal dependence of the scattered intensity at $q \frac{\langle L \rangle}{2} \simeq 48$. The samples' nominal volume fractions are indicated at the right. For clarity, offsets of 0, 1, 2, 3, 4, 5, 6, and 7 have been added to each curve, respectively.	42
2-4	High-resolution azimuthal profiling of 7.5% sample. Four sets of points are shown. The sample was moved horizontally by 0.1 mm (four times the beam size) and vertically by 0.2 mm between each set. The two angular ranges correspond to two different detector positions.	43
2-5	Azimuthal dependence of (a) 3.5% and (b) 6.5% samples' scattering at the three q values indicated. Thick lines are fits to Eqn. 2.57 using the Maier-Saupe form from Eqn. 2.13 (<i>solid</i>) or Davidson's form from Eqn. 2.28 (<i>dashed</i> , behind solid lines). Thin lines show the isotropic and nematic contributions in the fit for $q = 0.012 \text{ \AA}^{-1}$	44
2-6	Fitted directions perpendicular to the two nematic directors for each anisotropic sample. Points indicate the median value across q from 0.0097 to 0.063 \AA^{-1} . Error bars span the full range of φ_0 found. Capillaries holding the samples were oriented along $\varphi \simeq 90^\circ$	45

2-7	Schematic of possible configuration of nematic directors in samples studied. Shown is a cross-section through the cylindrical capillary tube holding the sample. Bars represent the projections into the page of local nematic directors, with dots indicating directors oriented along the capillary length. The “empty” region midway between the capillary walls and center is effectively isotropic.	46
2-8	Best-fit values of nematic order parameter for each of two domains in four böhmite-in-glycerol samples.	48
2-9	Fitted order parameters for each anisotropic sample. Points indicate the median value across q from 0.0097 to 0.063 Å ⁻¹ . Error bars span the full range of $\langle P_2 \rangle$ found.	49
2-10	Fitted proportions of one isotropic (I) and two nematic phases (I, II), for each anisotropic sample. Dashed lines are linear least-squares fits for each phase, intended as a guide to the eye.	50
3-1	Scattering cross section for dilute ($\phi = 0.002$) suspension of böhmite in glycerol. Circles are measured results, lines are predicted or fitted form factors using parameters in Table 3.1. Curves (C) and (D) fall atop one another. . .	58
3-2	Scattering vector times cross section for data and functions in Fig. 3-1. . . .	59
3-3	Measured scattering cross-section of isotropic suspensions of böhmite in glycerol. The 0.2% results were used in Sec. 3.1.6 to determine the form factor. .	64
3-4	Measured interparticle structure factor of isotropic suspensions of böhmite in glycerol.	65
3-5	Interparticle structure factor peak position vs. volume fraction for isotropic samples. Lines are best-fits to $q_{\text{peak}} \propto \phi^{\frac{1}{2}}$ (<i>solid</i>) and, for comparison, $q_{\text{peak}} \propto \phi^{\frac{1}{3}}$ (<i>dashed</i>). Rod size parameters were taken from Table 3.1(C).	66
3-6	Measured effective interparticle structure factor as defined in Eqn. 3.41, plotted at several azimuthal angles for each of four böhmite-in-glycerol samples. .	68
3-7	Azimuthal dependence of radial peak position for the effective structure factors plotted in Fig. 3-6.	69
3-8	Azimuthal dependence of radial peak half-width for the effective structure factors plotted in Fig. 3-6.	70
3-9	Azimuthal average of effective structure factor peak position vs. volume fraction for nematic samples. Isotropic data from Fig. 3-5 are included as well. Sloped lines represent $q_{\text{peak}} \propto \phi^{\frac{1}{2}}$. Dashed lines are guides to the eye. Error bars cover the full azimuthal variation of q_{peak}	72
3-10	Azimuthal average of main peak width for structure factors in Figs. 3-4 and 3-6. Dashed lines are guides to the eye, one a constant value and the other displaying a $\phi^{\frac{1}{2}}$ dependence. Error bars cover the full azimuthal variation of σ_{peak}	73
3-11	Best-fit values of nematic order parameter for each of three domains— I , N_I , and N_{II} —in four böhmite-in-glycerol samples.	74
3-12	Effective structure factor radial peak positions for three phases as determined by fitting a three-phase model of the azimuthal scattering profile separately at each q	75

3-13	Effective structure factor radial peak half-widths for three phases as determined by fitting a three-phase model of the azimuthal scattering profile separately at each q . Dashed lines are guides to the eye, either constant in value or displaying a $\phi^{\frac{1}{2}}$ dependence.	76
4-1	Intensity-intensity autocorrelation functions for 1.5% volume fraction sample of böhmite in glycerol at -12.0°C as measured by XPCS. Lines are fits to double-exponential decay (<i>solid</i>) and Maeda's matrix expression (<i>dashed</i>). . .	88
4-2	Fitted characteristic times of double-exponential decays as in Eqn. 4.72 for 1.0% and 1.5% böhmite volume fractions. Lines indicate $\tau \propto q^{-2}$	89
4-3	Decay coefficients $1/\tau_{\text{fast,slow}}(q)$ for the double-exponential fits (<i>points</i>) and $\Gamma_l(q)$ for fits to Maeda's form (<i>curves</i>). Curves are labeled at right.	90
4-4	Relative mode amplitudes $S_{\text{fast,slow}}/(S_{\text{fast}} + S_{\text{slow}})$ and $S_l(q)/\sum_l S_l(q)$ for correlation functions fitted to the double-exponential form (<i>points</i>) and the Maeda form (<i>curves</i>), respectively. Curve labels are shown in Fig. 4-3. Generally speaking, $S_l(q)$ peaks at higher q as l is increased.	92
5-1	Intensity-intensity autocorrelation functions at azimuthal angle $\varphi = 144^\circ$ for 2.0% volume fraction sample of böhmite in glycerol at -12.3°C as measured by XPCS. Lines are fits to double-exponential decay.	96
5-2	Intensity-intensity autocorrelation functions at $q = 0.00519 \text{ \AA}^{-1}$ for 2.0% volume fraction sample of böhmite in glycerol at -12.3°C as measured by XPCS. Lines are fits to double-exponential decay.	97
5-3	Fitted characteristic times of double-exponential decays as in Eqn. 4.72 for 2.0% volume fraction sample of böhmite in glycerol at -12.3°C . Several φ values are shown for both $\tau_{\text{fast}}(q, \varphi)$ (a) and $\tau_{\text{slow}}(q, \varphi)$ (b). Lines indicate $\tau \propto q^{-2}$	98
5-4	Relative amplitude of fast decay mode for the 2.0% sample at several azimuthal angles. Lines are guides to the eye.	99
5-5	Azimuthal dependences of (a) the static scattering as in Sec. 2.3.1, (b) the apparent fast-mode diffusion coefficient, and (c) the fast-mode amplitude for the 2.0% sample. The four sets of points in (c) correspond to $q = 0.00235 \text{ \AA}^{-1}$ (<i>circles</i>), 0.00519 \AA^{-1} (<i>squares</i>), 0.00882 \AA^{-1} (<i>X's</i>), and 0.01151 \AA^{-1} (<i>triangles</i>). Lines are guides to the eye.	100
5-6	Intensity-intensity autocorrelation functions at azimuthal angle $\varphi = 144^\circ$ for 7.5% volume fraction sample of böhmite in glycerol at 25.5°C as measured by XPCS. Lines are fits to stretched- (or compressed-) exponential decay. . .	101
5-7	Intensity-intensity autocorrelation functions at $q = 0.00519 \text{ \AA}^{-1}$ for 7.5% volume fraction sample of böhmite in glycerol at 25.5°C as measured by XPCS. Lines are fits to stretched- (or compressed-) exponential decay. . . .	102
5-8	Fitted characteristic times of stretched-exponential decays as in Eqn. 5.10 for 7.5% volume fraction sample of böhmite in glycerol at 25.5°C . Several φ values are shown. Lines indicate $\tau \propto q^{-1}$	103
5-9	Fitted characteristic exponents of stretched-exponential decays as in Eqn. 5.10 for 7.5% volume fraction sample of böhmite in glycerol at 25.5°C . Several φ values are shown. Lines are a guide to the eye.	104

5-10	Azimuthal dependences of (a) the static scattering, (b) the time constant proportionality coefficient, and (c) the stretching (compressing) exponent. The four sets of points in (c) correspond to $q = 0.00235 \text{ \AA}^{-1}$ (<i>circles</i>), 0.00519 \AA^{-1} (<i>squares</i>), 0.00882 \AA^{-1} (<i>X's</i>), and 0.01151 \AA^{-1} (<i>triangles</i>) . Lines are guides to the eye.	105
A-1	Three examples of image partitioning: radial only in transmission geometry (<i>top</i>), radial and azimuthal in transmission (<i>middle</i>), and radial and axial in reflection geometry (<i>bottom</i>). Colors represent measured scattering intensity, white being greatest. Lines represent partition boundaries. Black regions at the lower ends of each image represent areas blocked by a beamstop, and have been masked out. The top and middle data sets correspond, respectively, to 1.5% and 7.5% volume fraction suspensions of böhmite in glycerol.	111
A-2	Flatfield correction. Points represent intensity histograms from two separate 8000-pixel regions of a CCD array, each over a sequence of 850 exposures. Lines are a guide to the eye.	113
A-3	Schematic of multiple tau averaging scheme. Rectangles represent frames (or kinetics mode slices), and all times are given as multiples of the time per frame (slice). Correlations for delays listed at left are calculated at the corresponding multiple tau level; this example utilizes four delays per level and averages pairs of frames between each level.	115
A-4	Comparison between smoothing and simple averaging normalization methods in correlation function calculation.	119
B-1	Extracting the single-photon response, $P_1(A)$, from a measured single-photon intensity distribution, $P(I)$, for 200 msec exposures with the SMD1M60 CCD described in Refs. [55, 168]. The eight pixels closest each photon event were used to generate $P(I)$. Details of the deconvolution process are given in the text.	127
B-2	Expected and measured values of the intensity distribution function, Eqn. B.18, at various photon rates.	128
B-3	Effect of LLD and LLD distortion correction on measured, high-speed data. Points represent the same data set of 850 frames of 20 msec exposures analyzed three different ways. Line represents 200 msec exposures on the same sample. "No LLD" points (<i>triangles</i>) at $q > 0.006 \text{ \AA}^{-1}$ were negative and $ I(q) $ is plotted instead.	134

List of Tables

2.1	Parameters used to generate three-phase scattering intensities as seen in Fig. 2-1(a) and (b). For simplicity, $I_I = \langle I_{N_I} \rangle_\varphi = \langle I_{N_{II}} \rangle_\varphi = 1$ and $a_{i \geq 3}^{(I)} = a_{i \geq 3}^{(II)} = 0$.	39
3.1	Parameters used in calculating form factors shown in Figs 3-1 and 3-2. Based on Ref. [26], fixed values of $\phi = 0.002$, $\langle L \rangle = 1935 \text{ \AA}$, and $\sigma_L = 0.27$ were used, except for $\sigma_L = 0$ in the monodisperse curve, (A).	58
4.1	Fitted diffusion coefficients from two fitting methods. Units of D_{slow} , D_{fast} , D_{\parallel} , and D_{\perp} are $\text{\AA}^2/\text{s}$. Units of D_r are $1/\text{s}$.	89

Chapter 1

Introduction

1.1 Böhmite, a mineral liquid crystal

Liquid crystals comprise a vast assortment of materials, all of which, by virtue of anisotropic constituent particles, exhibit an intriguing suite of phases that possess varying degrees of orientational and positional order [1]. The simplest anisotropic shapes—rods and disks—possess cylindrical symmetry, and it is under the assumption of such symmetry that the majority of theoretical efforts toward understanding and predicting each phase’s properties operate. Not coincidentally, much of the experimental and technological work on liquid crystals to date has focused on approximately rodlike particles.

Although the most common liquid crystals encountered in modern devices (*e.g.* displays) consist of small, organic molecules, substantially larger macromolecules such as DNA [2], tobacco mosaic virus, and fd virus [3] in colloidal suspensions also undergo liquid crystalline ordering, as do rodlike polymer micelles [4, 5]. These larger particles fall into the category of lyotropic liquid crystals, which exhibit liquid crystalline phase transitions in response to changes in concentration rather than temperature.

Inorganic, lyotropic liquid crystals have proven to be of increasing interest of late. Anisotropic colloidal particles composed of inorganic materials include the following: rodlike imoglite, akaganeite, and Chevrel-Sergent phases $\text{Li}_2\text{Mo}_3\text{Se}_3$ and $\text{Li}_2\text{Mo}_6\text{Se}_6$; ribbonlike vanadium pentoxide; and disklike gibbsite, bentonite, and laponite [6, 7]. In addition, the liquid crystalline properties of rodlike colloidal particles of göthite [8] and gold [9, 10] have recently been demonstrated. Although it is difficult to produce large quantities of monodisperse mineral particles (unlike, *e.g.*, viruses), mineral liquid crystals offer the advantages of high rigidity and tunable aspect ratios. And from an X-ray scattering perspective, they possess high electron densities relative to most solvents, providing for large scattering cross-sections.

One mineral liquid crystal whose phase behavior has been closely studied is γ -AlO(OH), also known as böhmite [11, 12]. In aqueous solutions, böhmite rods have been found to be charge-stabilized and to form birefringent gels at high rod volume fractions and high salt

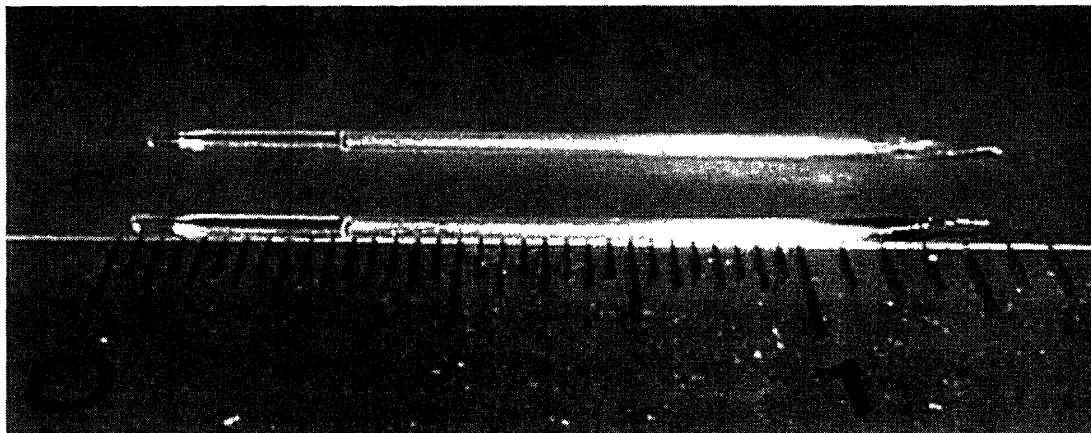


Figure 1-1: 0.7-mm diameter borosilicate glass capillaries containing 0.2% (*upper*) and 7.5% (*lower*) volume-fraction suspensions of böhmite in glycerol. Material can be seen at the left end of each capillary.

concentrations [13–15]. Böhmite rods with a grafted poly(isobutadine) coating were seen in cyclohexane solutions to form sterically stabilized clusters which would undergo nematic ordering at high volume fractions and low excess poly(isobutadine) concentrations [16–23]. Silica coatings were also successfully applied to böhmite, making it possible to disperse these rigid rods in a variety of solvents such as propanol and ethanol, and to graft a variety of polymers for steric stabilization in cyclohexane or alcohols. No orientational ordering was seen with “bare” silica-coated rods in suspension, but ordering was again found to occur among clusters of rods with grafted polymers [24, 25].

For this thesis, dilute aqueous suspensions of uncoated boehmite rods were obtained courtesy of the Debye Institute at Utrecht University. The rods’ average length and diameter were reported as 193.54 nm and 9.11 nm, with standard deviations of 52.19 nm and 1.83 nm, respectively [26]. We opted to replace water with glycerol as a suspending medium for our studies, in order that the dynamics would proceed on timescales of 0.1–10 sec and could be tuned by raising or lowering the sample temperature *in situ*. Known amounts of glycerol were added and the water evaporated to produce a series of suspensions with nominal böhmite volume fractions ranging from 0.2% to 7.5%. For mounting in the X-ray apparatus, small quantities of these viscous suspensions were placed at the open ends of 0.7-mm-diameter borosilicate glass capillary tubes of wall thickness 0.01 mm, as shown in Fig. 1-1. Samples were then centrifuged at 6000 rcf for five minutes to load the material into the tubes. The open tube ends were later sealed via heating. This capillary diameter was chosen as it is on the order of the absorption length of 7 keV X-rays for glycerol.

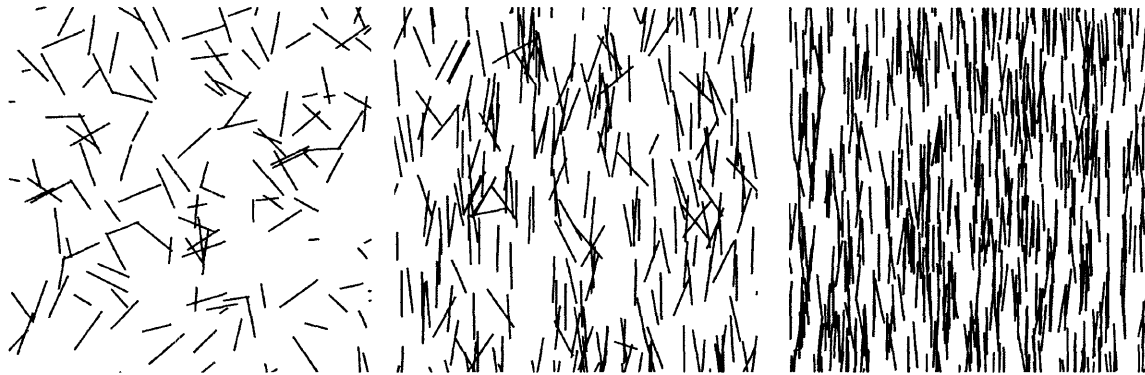


Figure 1-2: Schematic of lyotropic transition from isotropic (*left*) to nematic (*center*) phase. As the concentration of the nematic increases, the degree of alignment correspondingly increases (*right*).

1.2 The isotropic-nematic phase transition

When the concentration of anisotropic particles in suspension is great enough, the orientational entropy accrued by allowing the particles to adopt any orientation is outweighed by the packing entropy gained by allowing the particles to access positions close to their neighbors. This is the mechanism behind the lyotropic transition to the nematic phase, in which a preferred direction—or “director”—for the particles arises spontaneously [27]. The process is sketched in Fig. 1-2. The concentration at which the transition occurs depends on the interaction energy between particles.

1.2.1 Self-consistent mean field approximation

In principle, any exact calculation of the potential felt by a given particle in suspension depends on the locations and orientations of all other particles in the sample. For more than a few particles, this situation quickly becomes mathematically intractable. Several approximations can be used to simplify the treatment.

First, any quantity tied to the particular configuration of rods is approximately the same as the ensemble average of that quantity. If we take the configuration of the i^{th} individual rigid, cylindrical particle to be completely specified by its center-of-mass location $\mathbf{R}_i(t)$ and long axis direction unit vector $\mathbf{u}_i(t)$, then this approximation amounts to replacing $\sum_i \delta(\mathbf{R} - \mathbf{R}_i(t)) \delta(\mathbf{u} - \mathbf{u}_i(t))$ by an integral over a probability distribution of the form $N \int d\mathbf{R} \int d\mathbf{u} f(\mathbf{R}, \mathbf{u}, t)$.

A second approximation is that the interaction potential arises only from pairs of particles. That is, third- and higher-order virial coefficients [28, 29] are ignored, and the pair potential can be written as $U_{\text{pair}}(\mathbf{R} - \mathbf{R}', \mathbf{u}, \mathbf{u}')$.

Using both of these approximations, the virial expansion of the free energy is, to second

order [27, 28, 30–33],

$$F = ck_B T (\ln c - 1) + ck_B T \int d\mathbf{R} \int d\mathbf{u} f(\mathbf{R}, \mathbf{u}, t) \ln [4\pi f(\mathbf{R}, \mathbf{u}, t)] \\ + \frac{1}{2} c^2 k_B T \int d\mathbf{R} \int d\mathbf{u} \int d\mathbf{R}' \int d\mathbf{u}' f(\mathbf{R}, \mathbf{u}, t) f(\mathbf{R}', \mathbf{u}', t) w(\mathbf{R} - \mathbf{R}', \mathbf{u}, \mathbf{u}') \quad (1.1)$$

where $c \equiv N/V$ is the concentration of particles, and w is the Mayer function,

$$w(\mathbf{R} - \mathbf{R}', \mathbf{u}, \mathbf{u}') \equiv 1 - \exp \left[-\frac{1}{k_B T} U_{\text{pair}}(\mathbf{R} - \mathbf{R}', \mathbf{u}, \mathbf{u}') \right]. \quad (1.2)$$

We can find the equilibrium configuration of rods by minimizing the free energy in Eqn. 1.1 with respect to the distribution function $f(\mathbf{R}, \mathbf{u}, t)$. Doing so yields the nonlinear equation [30, 32, 33],

$$f(\mathbf{R}, \mathbf{u}, t) \propto \exp \left[-c \int d\mathbf{R}' \int d\mathbf{u}' w(\mathbf{R} - \mathbf{R}', \mathbf{u}, \mathbf{u}') f(\mathbf{R}', \mathbf{u}', t) \right], \quad (1.3)$$

in which the proportionality constant is determined by the normalization condition,

$$\int d\mathbf{R} \int d\mathbf{u} f(\mathbf{R}, \mathbf{u}, t) = 1. \quad (1.4)$$

We can consider this an equilibrium distribution if the time dependence of any external field is slow compared to the relaxation of the distribution function in response to the interparticle potential. Provided it is an equilibrium distribution, then, one should be able to recast f in the Boltzmann form, $f \propto \exp(-U/k_B T)$. In this form the potential is an effective “mean field” potential, obtained by substituting the ensemble-averaged potential in place of that arising from the specific configuration of particles in the sample. Eqn. 1.3 indicates that in the second virial expansion [30],

$$U_{\text{mean}}(\mathbf{R}, \mathbf{u}, t) = ck_B T \int d\mathbf{R}' \int d\mathbf{u}' w(\mathbf{R} - \mathbf{R}', \mathbf{u}, \mathbf{u}') f(\mathbf{R}', \mathbf{u}', t). \quad (1.5)$$

This is often referred to as a “self-consistent” mean field potential since the expression for U contains U itself: $U_{\text{mean}} \propto \int d\mathbf{R}' \int d\mathbf{u}' w \exp(-U_{\text{mean}}/k_B T)$.

1.2.2 Evaluating the Mayer function

1.2.2.1 Noninteracting particles and hard spherocylinders

Left unstated thusfar has been the specific form of the interaction potential $U_{\text{pair}}(\mathbf{R} - \mathbf{R}', \mathbf{u}, \mathbf{u}')$ and hence the Mayer function as defined in Eqn. 1.2. For noninteracting particles, $U_{\text{pair}} = 0$ and thus $w = 0$. The next-simplest form for the potential is the one for hard particles, given

by [33]

$$\begin{aligned} U_{\text{pair}}(\mathbf{R} - \mathbf{R}', \mathbf{u}, \mathbf{u}') &= \infty \quad , \quad w(\mathbf{R} - \mathbf{R}', \mathbf{u}, \mathbf{u}') = 1 \quad ; \quad \text{particles overlap} \\ U_{\text{pair}}(\mathbf{R} - \mathbf{R}', \mathbf{u}, \mathbf{u}') &= 0 \quad , \quad w(\mathbf{R} - \mathbf{R}', \mathbf{u}, \mathbf{u}') = 0 \quad ; \quad \text{particles do not overlap.} \end{aligned} \quad (1.6)$$

The volume integral of the hard-particle Mayer function yields the “excluded volume” for two particles, *i.e.* the amount of space forbidden to one particle’s center of mass by virtue of the other’s presence. The excluded volume is not simply the two particles’ total volume, but will typically depend on their mutual orientations, and can be calculated via geometric arguments. For two perpendicular cylinders, the excluded volume is $4RL^2 + (8 + 2\pi)R^2L + (8/3)\pi R^3$, while for parallel cylinders, it is $8\pi R^2L$. Terms of order R^2 and higher arise from end effects and can be neglected when $L \gg R$. The excluded volume of two spherocylinders is particularly simple at all angles [33],

$$\frac{1}{V} \int d\mathbf{R}' w(\mathbf{R} - \mathbf{R}', \mathbf{u}, \mathbf{u}') = 4RL^2 |\mathbf{u} \times \mathbf{u}'| + 8\pi R^2L + (32/3)\pi R^3 \quad (1.7)$$

$$\approx 4RL^2 |\mathbf{u} \times \mathbf{u}'|. \quad (1.8)$$

1.2.2.2 Charged spherocylinders

Pairs of cylinders with uniform charge density σ , placed in a medium of dielectric constant ϵ along with additional electrolyte of concentration c_{salt} , experience a screened, repulsive electrostatic potential of the Debye-Hückel form [28, 33–36],

$$U_{\text{pair}}(\mathbf{R} - \mathbf{R}', \mathbf{u}, \mathbf{u}') = \int_{-L/2}^{L/2} dr \int_{-L/2}^{L/2} dr' \frac{\sigma^2 e^{-\kappa|\mathbf{R} + r\mathbf{u} - \mathbf{R}' - r'\mathbf{u}'|}}{\epsilon |\mathbf{R} + r\mathbf{u} - \mathbf{R}' - r'\mathbf{u}'|} \quad (1.9)$$

$$\approx \frac{2\pi\sigma^2 e^{-\kappa x}}{\kappa\epsilon |\mathbf{u} \times \mathbf{u}'|}, \quad (1.10)$$

where x is the distance of closest approach of the two rods and the inverse Debye screening length, $\kappa \equiv \sqrt{8\pi e^2 c_{\text{salt}} / (\epsilon k_B T)}$. Notice that the cross product in the denominator causes the rods to tend to avoid the parallel configuration.

If we define

$$Y \equiv \frac{2\pi\sigma^2}{\kappa\epsilon k_B T} e^{-2\kappa R}, \quad (1.11)$$

then the total excluded volume, including both electrostatic (for $x \geq 2R$) and hard-core contributions, is [33, 35, 37]

$$\begin{aligned} \frac{1}{V} \int d\mathbf{R}' w(\mathbf{R} - \mathbf{R}', \mathbf{u}, \mathbf{u}') &= 4RL^2 |\mathbf{u} \times \mathbf{u}'| + 2\frac{L^2}{\kappa} |\mathbf{u} \times \mathbf{u}'| \left[\gamma + \ln \frac{Y}{|\mathbf{u} \times \mathbf{u}'|} \right. \\ &\quad \left. + \int_1^\infty dz \frac{1}{z} \exp\left(-\frac{zY}{|\mathbf{u} \times \mathbf{u}'|}\right) \right] \end{aligned} \quad (1.12)$$

$$\simeq 4L^2 |\mathbf{u} \times \mathbf{u}'| \left[R + \frac{1}{2\kappa} (\gamma + \ln Y - \ln |\mathbf{u} \times \mathbf{u}'|) \right]. \quad (1.13)$$

Here $\gamma \equiv 0.5772156649\dots$ is Euler's constant, and the approximation [28, 33, 36] is accurate for $Y \gtrsim 2$, since then the exponential integral is negligible. Eqn. 1.13 resembles Eqn. 1.8 except for the additional term in the square brackets. We will examine this more closely.

1.2.3 Free energy of isotropic and nematic phases

1.2.3.1 Hard spherocylinders

In the isotropic phase, the distribution function $f(\mathbf{R}, \mathbf{u}, t) = 1/(4\pi V)$ and, referring back to Eqn. 1.8, the free energy, Eqn. 1.1, reduces to [33, 35]

$$F_{\text{iso}} = c_{\text{iso}} k_B T (\ln c_{\text{iso}} - 1) + \frac{L^2 R}{8\pi^2} c_{\text{iso}}^2 k_B T \int d\mathbf{u} \int d\mathbf{u}' |\mathbf{u} \times \mathbf{u}'| \quad (1.14)$$

$$= c_{\text{iso}} k_B T \left(\ln c_{\text{iso}} - 1 + c_{\text{iso}} \frac{\pi}{2} L^2 R \right). \quad (1.15)$$

In the nematic phase, the rod distribution function is $f(\mathbf{R}, \mathbf{u}, t) = (1/V) f(\mathbf{u})$, making the free energy

$$F_{\text{nem}} = c_{\text{nem}} k_B T \left[(\ln c_{\text{nem}} - 1) + \int d\mathbf{u} f(\mathbf{u}) \ln [4\pi f(\mathbf{u})] \right. \\ \left. + 2c_{\text{nem}} L^2 R \int d\mathbf{u} \int d\mathbf{u}' f(\mathbf{u}) f(\mathbf{u}') |\mathbf{u} \times \mathbf{u}'| \right]. \quad (1.16)$$

1.2.3.2 Charged spherocylinders

Along the same lines as for hard particles, we find that for charged rods in the isotropic phase [33, 35, 36],

$$F_{\text{iso}} = c_{\text{iso}} k_B T (\ln c_{\text{iso}} - 1) \\ + \frac{L^2}{8\pi^2} c_{\text{iso}}^2 k_B T \int d\mathbf{u} \int d\mathbf{u}' |\mathbf{u} \times \mathbf{u}'| \left[R + \frac{1}{2\kappa} (\gamma + \ln Y - \ln |\mathbf{u} \times \mathbf{u}'|) \right] \quad (1.17)$$

$$= c_{\text{iso}} k_B T (\ln c_{\text{iso}} - 1) + \frac{\pi}{2} L^2 c_{\text{iso}}^2 k_B T \left[R + \frac{1}{2\kappa} \left(\gamma + \ln Y + \ln 2 - \frac{1}{2} \right) \right] \quad (1.18)$$

$$= c_{\text{iso}} k_B T \left(\ln c_{\text{iso}} - 1 + c_{\text{iso}} \frac{\pi}{2} L^2 R_{\text{eff}} \right). \quad (1.19)$$

This has been cast into the same form as Eqn. 1.15. Evidently, when isotropically distributed, interactions among charged rods will resemble those of hard rods of radius R_{eff} ,

$$R_{\text{eff}} \equiv R + \frac{1}{2\kappa} \left(\gamma + \ln Y + \ln 2 - \frac{1}{2} \right). \quad (1.20)$$

Treating the nematic phase proceeds similarly, although it is slightly more complicated.

$$\begin{aligned}
F_{\text{nem}} &= c_{\text{nem}}k_B T (\ln c - 1) + c_{\text{nem}}k_B T \int d\mathbf{u} f(\mathbf{u}) \ln [4\pi f(\mathbf{u})] + 2L^2 c_{\text{nem}}^2 k_B T \\
&\times \int d\mathbf{u} \int d\mathbf{u}' f(\mathbf{u}) f(\mathbf{u}') |\mathbf{u} \times \mathbf{u}'| \left[R + \frac{1}{2\kappa} (\gamma + \ln Y - \ln |\mathbf{u} \times \mathbf{u}'|) \right]. \quad (1.21)
\end{aligned}$$

Keeping the same definition of R_{eff} from Eqn. 1.20,

$$\begin{aligned}
F_{\text{nem}} &= c_{\text{nem}}k_B T (\ln c - 1) + c_{\text{nem}}k_B T \int d\mathbf{u} f(\mathbf{u}) \ln [4\pi f(\mathbf{u})] + 2L^2 c_{\text{nem}}^2 k_B T \\
&\times \int d\mathbf{u} \int d\mathbf{u}' f(\mathbf{u}) f(\mathbf{u}') |\mathbf{u} \times \mathbf{u}'| \left[R_{\text{eff}} - \frac{1}{2\kappa} \left(\ln 2 - \frac{1}{2} + \ln |\mathbf{u} \times \mathbf{u}'| \right) \right]. \quad (1.22)
\end{aligned}$$

The second term inside the square brackets has no counterpart for hard particles in Eqn. 1.16. It is a ‘‘twist’’ effect that represents the tendency of charged rods to avoid aligning with one another [33, 35].

1.2.4 Two-phase coexistence of hard rods

We now have a means to characterize the isotropic-nematic transition as a competition between the free energies of the two phases at a given concentration. However, there may be some concentrations at which the free energy can be further minimized by separating part of the system into an isotropic component of concentration c_{iso} and a nematic component of concentration c_{nem} [30]. Were this to occur, both the osmotic pressure and the chemical potential of one component would be equivalent to the other’s [33, 35, 37].

$$\left(\frac{\partial F_{\text{nem}}}{\partial V} \right)_{T,N} = \left(\frac{\partial F_{\text{iso}}}{\partial V} \right)_{T,N} \quad (1.23)$$

and

$$\left(\frac{\partial F_{\text{nem}}}{\partial N} \right)_{V,T} = \left(\frac{\partial F_{\text{iso}}}{\partial N} \right)_{V,T}. \quad (1.24)$$

To solve for the concentrations c_{iso} and c_{nem} , one selects a functional form for the nematic $f(\mathbf{u})$ that possesses some adjustable parameter characterizing the width of the angular distribution of rods. The value of that parameter as a function of concentration can be determined with the free energy minimization condition, Eqn. 1.3. One then substitutes into the above the corresponding solutions of Eqns. 1.15 and 1.16. The resulting values of c_{iso} and c_{nem} represent, respectively, the highest stable isotropic concentration and the lowest stable nematic concentration. When the total system concentration sits between these two values, the suspension separates into coexisting isotropic and nematic phases of concentrations c_{iso} and c_{nem} .

The model of isotropic-nematic phase separation that has been outlined here was originally developed by Onsager in the 1940s [38]. Onsager chose the following nematic distri-

bution function

$$f(\mathbf{u}) = \frac{\alpha \cosh(\alpha \cos \beta)}{4\pi \sinh \alpha}, \quad (1.25)$$

with adjustable parameter α and with β representing the angle away from the director. Onsager found for the transitional volume fractions $\phi \equiv \pi R^2 L c$ of hard, rigid rods,

$$\begin{aligned} \phi_{\text{iso}} &= 3.340 \frac{2R}{L} \\ \phi_{\text{nem}} &= 4.486 \frac{2R}{L}. \end{aligned} \quad (1.26)$$

Incorporating charge effects proceeds along much the same lines [35].

1.2.5 Effects of polydispersity

In general, accounting for polydisperse rods entails treating each rod length as a separate species and then setting the chemical potentials and osmotic pressures of all species equal. The complexity of this approach clearly limits theoretical treatments to simple systems such as bidisperse [39–42] and tridisperse [43] length distributions. Very recently, however, intriguing new numerical work has appeared in regard to systems possessing a continuous distribution of particle sizes [44–46]. Two separate nematic phases (N_{I} and N_{II}) are indicated, and at certain concentrations and polydispersity levels, both coexist in equilibrium with the isotropic (I) phase. As volume fraction increases, the system moves from I to $I - N_{\text{II}}$ to $I - N_{\text{I}} - N_{\text{II}}$ to $I - N_{\text{I}}$ to N . The N_{II} phase is composed primarily of the longest rods in the sample, while the N_{I} phase comprises more typical rods. Putative three-phase coexistence has been reported in binary solutions of rodlike molecules [47], as well as in sterically stabilized suspensions of continuously polydisperse böhmite rods [17, 23].

Wensink and Vroege’s [46] work indicates that three-phase coexistence may occur for polydispersities between 24% and 38%. Our samples’ length polydispersity was approximately 27% [26], well within the expected range. Unfortunately the current state of these studies does not yet lend itself to quantitative comparisons of the three-phase coexistence concentrations or the critical volume fractions. Regarding the latter quantity, Wensink and Vroege found that the exact volume fraction of the $I - N_{\text{II}}$ initial transition depended strongly on the length of the longest rods present in the sample, and we were unable to determine that value for our samples.

1.3 Phase transition observed with polarized light microscopy

Although one generally expects the nematic transition to be self-evident in X-ray scattering insofar as it produces an asymmetric scattering pattern, we nevertheless utilized the well-known technique of polarized light microscopy to characterize the phase transition. An aligned sample will exhibit an index of refraction different along the nematic director than in the perpendicular direction. When such a sample is placed between crossed polarizers,

its birefringence causes light to pass through both polarizers to the viewer. The results are shown in Fig. 1-3. The birefringent textures seen were qualitatively stable over timescales of several months, and qualitatively uniform under rotation of the capillary about its long axis.

For our samples, the orientational transition appeared to occur around $\phi = 2.0\%$. The Onsager model would predict the transition to occur at 15.7% based on the dimensions of our böhmite particles. This was a surprising result, and it is not clear that polydispersity effects could account entirely for the substantial discrepancy. Subsequent chapters of this thesis discuss other alternatives.

1.4 X-ray Photon Correlation Spectroscopy

In addition to conventional small-angle X-ray scattering [48–50] to study the structure of colloidal suspensions of böhmite in glycerol, we utilized the emerging technique of X-ray Photon Correlation Spectroscopy (XPCS) [51] to characterize the equilibrium dynamics of those suspensions.

At its most basic level, XPCS is simply the extension to X-ray wavelengths of common Dynamic Light Scattering (DLS) techniques. In DLS [34], coherent illumination of a fluctuating system gives rise to a time-varying, “speckled” scattering pattern. The time dependence of the intensity $I(\mathbf{q}, t)$ at a scattering vector \mathbf{q} provides a measure of the system’s dynamic structure factor, which, for a system of N identical, pointlike scattering elements on trajectories $\mathbf{R}_n(t)$, is given by

$$S(\mathbf{q}, \Delta t) \propto \left\langle \sum_{n \leq m}^N e^{-i\mathbf{q} \cdot [\mathbf{R}_m(t) - \mathbf{R}_n(t + \Delta t)]} \right\rangle_t. \quad (1.27)$$

Finite-sized particles can be treated analytically as continua of infinitesimal points. The Siegert relation connects the measured intensity to the dynamic structure factor:

$$g_2(\mathbf{q}, \Delta t) = \frac{\langle I(\mathbf{q}, t) I(\mathbf{q}, t + \Delta t) \rangle_t}{\langle I(\mathbf{q}, t) \rangle_t^2} = 1 + \beta(\mathbf{q}) \left[\frac{S(\mathbf{q}, \Delta t)}{S(\mathbf{q}, 0)} \right]^2, \quad (1.28)$$

where $\beta(\mathbf{q})$ is an apparatus-dependent contrast [52]. Since $\lim_{\Delta t \rightarrow \infty} S(\mathbf{q}, \Delta t) = 0$, the value of $g_2(\mathbf{q}, \Delta t)$ decays from $1 + \beta(\mathbf{q})$ to 1. The term $S(\mathbf{q}, 0) = S(\mathbf{q})$ is the static structure factor.

XPCS allows several types of measurements that would be inaccessible to DLS. Obviously with smaller wavelengths XPCS can probe further out in $|\mathbf{q}|$ than DLS, reaching length scales comparable to colloidal particle dimensions. In addition, multiple scattering effects tend to be negligible at X-ray wavelengths, making it possible to study samples for which multiple scattering is significant at optical wavelengths, or even completely opaque samples.

Full details of the experimental apparatus are presented elsewhere [52–55]. A schematic

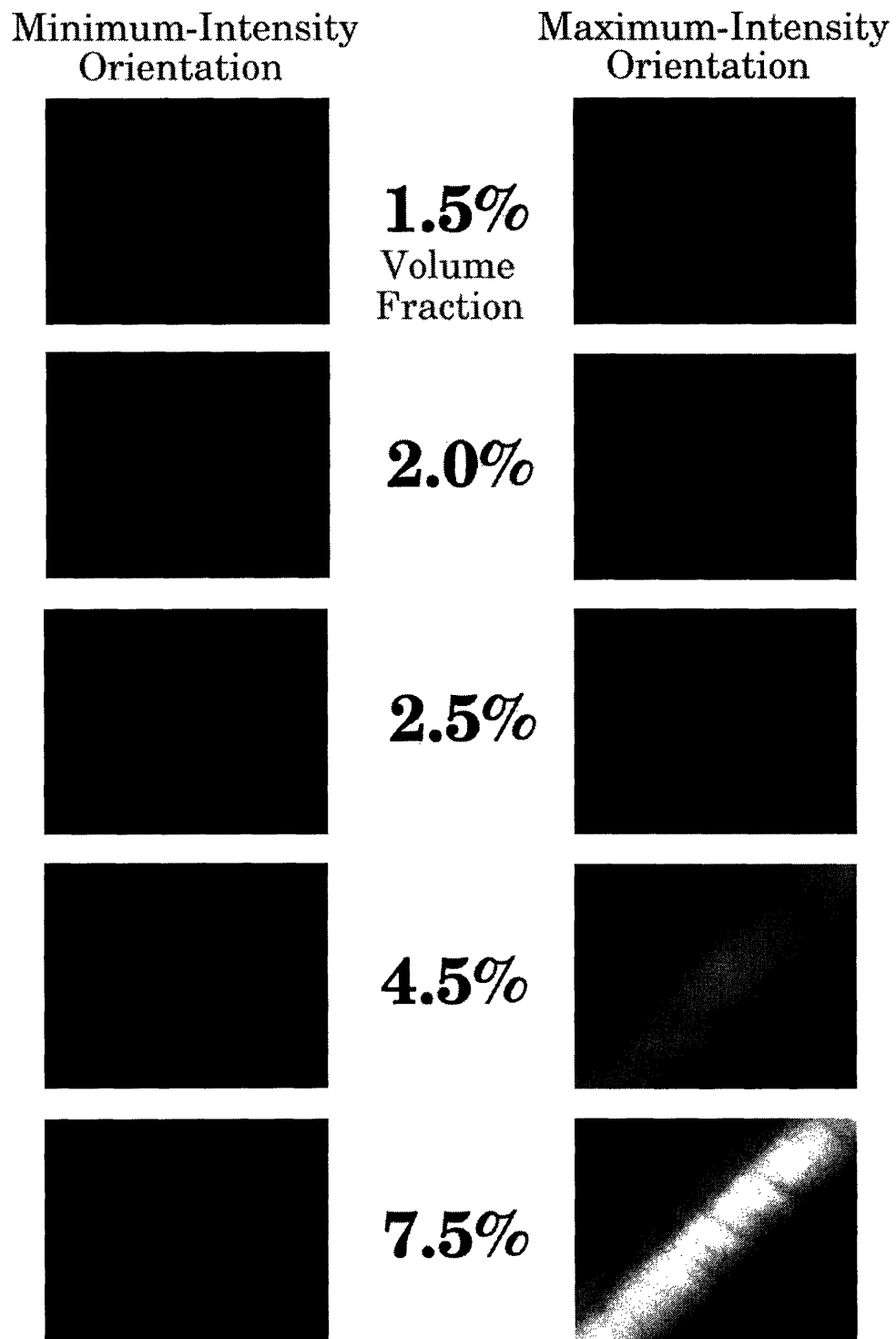


Figure 1-3: Polarized light microscopy images from several böhmite in glycerol specimens.

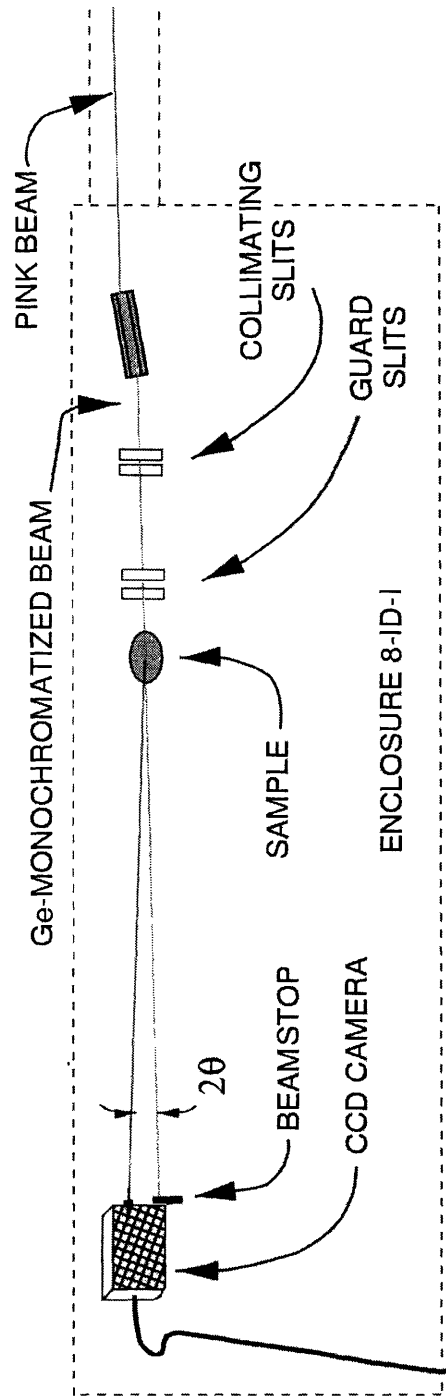


Figure 1-4: Small-angle X-ray scattering and X-ray photon correlation spectroscopy apparatus: beamline 8-ID-I at the Advanced Photon Source.

can be seen in Fig. 1-4. In short, a 6.6 keV, Ge-monochromatized beam 60 meters from an undulator source was incident on a pair of precision-crossed tantalum slit blades that cut the beam size to $20 \times 20 \mu\text{m}^2$, passing $\sim 10^{10}$ partially coherent photons per second. The partially coherent beam entered a temperature-controlled chamber containing a sample mounted in a borosilicate glass capillary. The sample scattered the beam in a transmission geometry. Approximately 3 meters downstream of the sample, an area detector recorded scattered intensity. Detectors used in this thesis included a Princeton Instruments EEV model 37 CCD array and a SMD 1M60 CCD array.

1.5 Overview

This thesis, to our knowledge, marks the first experiments probing colloidal böhmite on sub-optical length scales. Although a number of XPCS measurements have been performed on various liquid crystalline materials [56–61], we believe this work represents the first use of XPCS to study a rodlike, lyotropic system.

In azimuthally anisotropic samples, both static scattering and intensity autocorrelation functions display azimuthal variations in addition to the usual radial variations. To allow simultaneous measurement of both, we have implemented a quantitative, fully two-dimensional method for analyzing area detector data. Such a system had not previously existed for correlation function measurements. In the process, it became necessary to address several data analysis issues that arise under low-intensity conditions in scattering and correlation spectroscopy experiments.

We seek with these measurements to investigate colloidal suspensions of anisotropic particles in a regime where strong interparticle interactions profoundly influence collective behavior, and to study these interactions on single-particle length scales. Bulk equilibrium dynamics at this combination of relatively high concentration and high q have historically been difficult to access quantitatively, both from theoretical and experimental standpoints—even for particles as conceptually simple as cylinders.

In this thesis we examine the differences in statics and dynamics between samples with concentrations just below and just above the orientational ordering transition. We test the premise that the onset of alignment has no effect on the liquidlike positional structure of a suspension. We investigate what role affecting dynamics is played by the strong confinement of rods by their neighbors in aligned suspensions at concentrations well above the transition. Also, with regard to aligned samples, we explore in depth how to take advantage of the azimuthal anisotropy inherent in scattering from aligned systems to simultaneously probe multiple nematic domains in a sample and extract information specific to each domain.

1.6 Outline

In Chapter 2 we characterize the phase behavior further by studying quantitatively the orientational ordering via azimuthally dependent static structure factor measurements. Chapter 3 discusses the isotropic, polydisperse rod form factor as well as the behavior of the radial dependence of the static structure factor in both the isotropic and aligned phases. Chapter 4 concerns the dynamics of two isotropic suspensions. In Chapter 5 we examine the full radial and azimuthal dependence of the dynamic structure factor in the orientationally ordered phase. Appendix A covers several issues central to XPCS/DLS data analysis for azimuthally anisotropic materials. In Appendix B we introduce a method for enhancing signal-to-noise in high-speed and/or anisotropic scattering data.

Chapter 2

Azimuthal variations in static scattering due to nematic alignment

2.1 Determining the distribution of rod orientations

2.1.1 Scattering from a rigid rod

The intensity of X rays scattered by an object arises from the coherent superposition of scattered fields from all scattering centers (atoms) in the object [62]. When the object is a single particle of roughly uniform electron density and the scattering angle is small, the sum over atoms can be approximated by an integral over the particle's volume, and the angular dependence of the scattered intensity is given by

$$F(\mathbf{q}) \propto \left| \int_{\text{particle}} d\mathbf{r} e^{-i\mathbf{q}\cdot\mathbf{r}} \right|^2. \quad (2.1)$$

This is known as the particle's form factor. The vector \mathbf{q} is the difference between the incident and scattered wavevectors. When X rays of wavelength λ are elastically scattered to an angle 2θ away from the incident beam direction, the scattering vector magnitude is $q = \frac{4\pi}{\lambda} \sin \theta$.

For a rigid, cylindrical particle of length L and diameter $2R$, the form factor is [48]

$$F_{\text{rod}}(\mathbf{q}) \propto \left(\pi R^2 L \frac{\sin(q\frac{L}{2} \cos \gamma)}{q\frac{L}{2} \cos \gamma} \frac{2J_1(qR \sin \gamma)}{qR \sin \gamma} \right)^2, \quad (2.2)$$

where $J_1(x)$ is the first-order Bessel function of the first kind and γ is the angle between \mathbf{q} and the rod's long axis. At $q\frac{L}{2} \gg 1$ —provided $\frac{L}{2} \gg R$ —the $\sin(q\frac{L}{2} \cos \gamma)/(q\frac{L}{2} \cos \gamma)$ term will make F_{rod} all but vanish except where $\cos \gamma = 0$. In other words, at high q the scattering is confined to directions perpendicular to the rod's length.

When the scattering is projected onto a screen (or other area detector) oriented perpen-

dicular to the incident beam direction, a coordinate system naturally arises in which the unit vectors $\hat{\mathbf{x}}$ and $\hat{\mathbf{z}}$ are aligned with the screen's horizontal and vertical directions, respectively. As long as $q\lambda \ll 1$, the scattering vector is for all intents and purposes completely parallel to the screen, and thus

$$\mathbf{q} = q \cos \varphi \hat{\mathbf{x}} + q \sin \varphi \hat{\mathbf{z}}. \quad (2.3)$$

This defines φ as the azimuthal angle around the screen. If the rod is oriented at an angle β to and an angle α around the the \mathbf{z} -axis, then

$$\cos \gamma = \sin \beta \cos \alpha \cos \varphi + \cos \beta \sin \varphi \quad (2.4)$$

and the scattering will be seen on the screen at [63] whichever φ satisfy $\cos \gamma = 0$:

$$\tan \varphi = -\tan \beta \cos \alpha. \quad (2.5)$$

Note that this limits $-\beta \leq \varphi \leq \beta$ for any α .

2.1.2 Scattering from a dilute, oriented suspension of rigid rods

If a group of several rods are orientationally limited to small β , the prior result, $|\varphi| < \beta$, implies that the rods will scatter only into a narrow range of azimuthal angles. In this section we will see how this concept leads to a determination of rod orientations from scattering data.

X rays scattered from multiple rods will *incoherently* sum, provided that the rods are all at a distance $\gg 2\pi/q$ from one another. If identical rods are distributed among orientations with probability $f(\beta, \alpha)$, subject to the normalization condition,

$$\int_0^1 d(\cos \beta) \int_0^{2\pi} d\alpha f(\beta, \alpha) = 1, \quad (2.6)$$

then in the limit of infinite dilution the scattered intensity will be [64]:

$$I(\mathbf{q}) = \int_0^1 d(\cos \beta) \int_0^{2\pi} d\alpha f(\beta, \alpha) F_{\text{rod}}(\mathbf{q}). \quad (2.7)$$

In the special case of nematic order with a director parallel to $\hat{\mathbf{z}}$, the orientational distribution function reduces to $f(\beta, \alpha) = f(\beta)/2\pi$ and $I(\mathbf{q}) = \int d(\cos \beta) f(\beta) F_{\text{rod}}(\mathbf{q})$. Eqn. 2.5 then leads to [63]

$$I(q, \varphi) = F_{\text{rod}}(q) I(\varphi) \propto \int_{\varphi}^{\pi/2} d\beta \sin \beta \frac{f(\beta)}{\cos^2 \varphi \sqrt{\tan^2 \beta - \tan^2 \varphi}}. \quad (2.8)$$

Although an analytic inversion of Eqn. 2.8 exists [65], it involves derivatives of the measured intensity and as a result is not commonly used on experimental data [66,67]. It is also possible

to numerically invert Eqn. 2.8 [67–69]. Another alternative [70–72] is to choose an analytic trial form for $f(\beta)$ with some finite number of adjustable parameters and then perform a least-squares fit to the measured $I(q, \varphi)$.

2.1.2.1 The Maier-Saupe orientational distribution function

A simple example of such a trial function is the Maier-Saupe distribution [73, 74],

$$f(\beta) \propto e^{\frac{1}{k_B T} \varepsilon \langle P_2 \rangle P_2(\cos \beta)}, \quad (2.9)$$

which comes from the first term in an expansion of the mean field, rod-rod interaction energy into spherical harmonic components. Here $P_2(\cos \beta)$ refers to the Legendre polynomial of order 2 and ε represents the (unknown) mean radial contribution to the rod-rod potential. $\langle P_2 \rangle = \int d(\cos \beta) f(\beta) P_2(\cos \beta)$ is the ensemble average of $P_2(\cos \beta)$ and is an important indicator of the degree of orientational order. In general, $\langle P_l \rangle$, with l even, will be order parameters for a nematic system. They will range from zero in the isotropic phase to one when all rods are perfectly aligned. The use of $\langle P_l \rangle$ in lieu of the full set of generalized spherical harmonics, $\langle D_{m,n}^l \rangle$, is allowed due to the cylindrical symmetry of the particles and the subsequent symmetry in their interactions.

For the purpose of fitting experimental results, we replace the factor $\frac{3}{2k_B T} \varepsilon \langle P_2 \rangle$ with a single parameter, m , such that the distribution function becomes [66, 75, 76]

$$f(\beta) = \frac{1}{Z(m)} e^{m \cos^2 \beta}. \quad (2.10)$$

Here Z is the normalization coefficient,

$$Z(m) = \frac{1}{\sqrt{m}} \int_0^{\sqrt{m}} dx e^{x^2}, \quad (2.11)$$

necessary to satisfy Eqn. 2.6. (The form $f(\beta) \propto \exp(-\sin^2(\beta)/2\alpha^2)$ used by Oldenbourg et al. in Ref. [70] is equivalent to Eqn. 2.10 with $\alpha = 1/\sqrt{2m}$.)

With m as an adjustable parameter, one can then fit the experimentally measured intensity to the form

$$I(\varphi) \propto \frac{1}{Z(m)} J(m \cos^2 \varphi), \quad (2.12)$$

where [66, 75, 76]

$$J(x) \equiv \frac{e^x}{\sqrt{x}} \frac{\sqrt{\pi}}{2} \operatorname{erf}(\sqrt{x}) \quad (2.13)$$

$$= \sum_{i=0}^{\infty} \frac{2^i}{(2i+1)!!} x^i. \quad (2.14)$$

Eqn. 2.12 arises from substituting Eqn. 2.9 into Eqn. 2.8. It follows [66] that

$$I(\varphi) \propto \frac{1}{Z(m)} \left(1 + \frac{2m}{3} \cos^2 \varphi + \frac{4m^2}{15} \cos^4 \varphi + \dots \right) \quad (2.15)$$

and

$$\langle \cos^2 \beta \rangle = \frac{1}{Z(m)} \int_0^1 d(\cos \beta) \cos^2 \beta e^{m \cos^2 \beta} \quad (2.16)$$

$$= \frac{1}{2m} \left(\frac{e^m}{Z(m)} - 1 \right), \quad (2.17)$$

$$\langle P_2 \rangle = \frac{1}{2} \left[\frac{3}{2m} \left(\frac{e^m}{Z(m)} - 1 \right) - 1 \right]. \quad (2.18)$$

Hence, using the Maier-Saupe distribution facilitates a straightforward evaluation of the lowest-order nematic order parameter, depending solely on the parameter m .

2.1.2.2 Davidson's generalized orientational distribution function

A natural generalization of Eqn. 2.9 to higher orders gives [67, 74]

$$f(\beta) = \frac{1}{Z(m)} e^{\frac{1}{k_B T} \sum_{\ell \text{ even}} \langle u_{\ell} \rangle \langle P_{\ell} \rangle P_{\ell}(\cos \beta)}, \quad (2.19)$$

but as yet no direct inversion has been found for extracting $\langle P_{\ell} \rangle$ from Eqn. 2.8 when this form is used. Recently, Davidson *et al.* [66] proposed a similar alternative that *can* be inverted. It involves expanding the orientational distribution function not in Legendre polynomials but instead in circular functions,

$$f(\beta) = \sum_{i=0}^{\infty} f_{2i} \cos^{2i} \beta. \quad (2.20)$$

Here $\{f_{2i}\}$ is a set of adjustable parameters; it is practical to set f_{2i} to zero above some cutoff i . Note that the Boltzmann form is not used in this particular expansion.

Substituting this form into Eqn. 2.8, the intensity is given by

$$I(\varphi) \propto \sum_{i=0}^{\infty} I_{2i} \cos^{2i} \varphi, \quad (2.21)$$

with

$$I_{2i} \equiv f_{2i} \frac{1}{2} B \left(\frac{1}{2}, i+1 \right) = f_{2i} \frac{2^i i!}{(2i+1)!!}, \quad (2.22)$$

$B(\frac{1}{2}, i+1)$ being the beta function [77]. A comparison of Eqns. 2.10 and 2.20 (or Eqns.

2.14 and 2.22) shows that the Maier-Saupe treatment corresponds to the special case of [66]

$$f_{2i} = \frac{m^i}{i!Z(m)}. \quad (2.23)$$

For convenience, we adopt a slightly different notation for Davidson's orientational distribution function,

$$f(\beta) = \sum_{i=0}^{\infty} a_i (2i+1) \cos^{2i} \beta. \quad (2.24)$$

In this form, the normalization condition, Eqn. 2.6, becomes

$$\int_0^1 d(\cos \beta) f(\beta) = \sum_{i=0}^{\infty} a_i = 1. \quad (2.25)$$

The adjustable parameters, a_i , are constrained to the range $0 \leq a_i \leq 1$. One of them, which we choose to be a_0 , is determined by the normalization condition. This makes

$$a_0 = 1 - \sum_{i=1}^{\infty} a_i, \quad (2.26)$$

$$f(\beta) = 1 + \sum_{i=1}^{\infty} a_i [(2i+1) \cos^{2i} \beta - 1], \quad (2.27)$$

$$I(\varphi) \propto 1 + \sum_{i=1}^{\infty} a_i (c_i \cos^{2i} \varphi - 1) \quad (2.28)$$

$$\propto 1 + a_1 (2 \cos^2 \varphi - 1) + a_2 \left(\frac{8}{3} \cos^4 \varphi - 1 \right) + \dots, \quad (2.29)$$

with

$$c_i \equiv \left(i + \frac{1}{2} \right) B \left(\frac{1}{2}, i + 1 \right) \quad (2.30)$$

$$= \frac{(2i)!!}{(2i-1)!!} \quad (2.31)$$

$$= \frac{1}{\langle \cos^{2i} \varphi \rangle_{\varphi}}. \quad (2.32)$$

One advantage of this particular notation is that Eqn. 2.32 clearly demonstrates that the azimuthal average of the right side of Eqn. 2.28 is unity. Another is that it yields relatively

simple forms for the “full” set (*i.e.* for all even l up to the cutoff) of $\langle P_l \rangle$,

$$\langle P_2 \rangle = \frac{3}{2} \int_0^1 d(\cos \beta) f(\beta) \cos^2 \beta - \frac{1}{2} = \sum_{i=1}^{\infty} a_i \frac{2i}{(2i+3)}, \quad (2.33)$$

$$\langle P_4 \rangle = \sum_{i=2}^{\infty} a_i \frac{2(i-1)}{(2i+5)} \frac{2i}{(2i+3)}, \quad \textit{etc.} \quad (2.34)$$

The presence of multiple adjustable parameters in Eqns. 2.28 and 2.33 has led to their being infrequently used to analyze measured scattering, unlike other forms such as Eqns. 2.12 and 2.18 [63, 66, 70, 71, 75] or a even simple Gaussian $f(\beta)$ [72].

2.1.3 Scattering from a concentrated, oriented suspension of rigid rods

When rods in suspension are packed densely enough, multi-rod interference effects may arise in the scattering. This will be discussed thoroughly in the next chapter. Although the formalism above made no reference to positional interactions among rods, orientational distribution functions (ODF) for nematics are typically measured [63–68, 71, 75] at a q value corresponding to a maximum in interparticle interference, where these interactions are by definition significant. Measurements at higher q values [70, 72] can in principle yield an ODF independent of interparticle effects, although the overall reduction in scattering cross-section may result in signal-to-noise disadvantages.

ODF data collected at the interparticle peak is taken to be representative of the distribution of “clusters” in the sample [63]. These clusters are assumed to exhibit a very high degree of short-range alignment, meaning that the spread in scattering to a range of φ angles is solely the result of long-range variations of the nematic director. A recent study by Purdy et al. [72] compared data from both small and large q and found good agreement in both cases. In this thesis we attempt to test the “cluster” model further by measuring the order parameter continuously throughout a range of q that extends well above and below the interparticle interference maximum. This will serve to verify the implicit assumption above that the intensity may be separated into two independent terms: $I(\mathbf{q}) = I_{\text{radial}}(q) I_{\text{azimuthal}}(\varphi)$.

2.2 Limitations on information about isotropic-nematic coexistence from scattering measurements

When both isotropic and nematic domains coexist in a sample, one would ideally hope to extract from scattering data three different characteristics of each nematic domain: proportion relative to other domains, order parameter, and director orientation. Additionally, the relative proportion of isotropic material would be of interest. Generally speaking, however, when the illuminated portion of a sample contains two or more components of differing structure, small-angle X-ray scattering cannot be used to distinguish whether macroscopi-

cally separated domains exist or the sample is instead a macroscopically uniform mixture of the various components. We will demonstrate here that unless specific constraints on the orientational distribution function (such as the Maier-Saupe form) are assumed *a priori*, neither the nematic order parameter(s) nor the relative proportions of isotropic and nematic domains in a multidomain sample can be uniquely identified by measuring the azimuthal dependence of scattered intensity. Furthermore, we will also show that noise in real experimental data can obscure the determination of the relative proportions even after a particular ODF is chosen.

2.2.1 Two-phase ($I - N$) coexistence

2.2.1.1 Equivalence of scattering from isotropic and a_0 terms

If a portion, ν_I , of the sample exists in an isotropic phase along with a nematic domain comprising ν_N of the sample, the azimuthal X-ray scattering profile can be expected to be the weighted superposition of the respective azimuthally constant and varying profiles,

$$I(\varphi) = \nu_I I_I + \nu_N I_N(\varphi). \quad (2.35)$$

Substituting Eqn. 2.28,

$$I(\varphi) = \nu_I I_I + \nu_N \langle I_N \rangle_\varphi \left[1 + \sum_{i=1}^{\infty} a_i (c_i \cos^{2i} \varphi - 1) \right]. \quad (2.36)$$

The coefficient $\langle I_N \rangle_\varphi$ represents the azimuthally averaged scattering strength. It can be thought of as the scattering from a domain with all rod centers positioned as in the nematic domain, but possessing instead a completely uniform distribution of rod orientations. Both of the coefficients I_I and $\langle I_N \rangle_\varphi$ implicitly contain the full dependence on the radial coordinate, q , of the scattering vector. We will ignore this q -dependence until the next chapter, and will treat them for now as known quantities.

It is straightforward to rewrite Eqn. 2.36 as,

$$I(\varphi) = \left(\nu_I I_I + \nu_N \langle I_N \rangle_\varphi \right) \left[1 + \sum_{i=1}^{\infty} a_i \frac{\nu_N \langle I_N \rangle_\varphi}{\nu_I I_I + \nu_N \langle I_N \rangle_\varphi} (c_i \cos^{2i} \varphi - 1) \right] \quad (2.37)$$

$$= \langle I'_N \rangle_\varphi \left[1 + \sum_{i=1}^{\infty} a'_i (c_i \cos^{2i} \varphi - 1) \right], \quad (2.38)$$

with

$$\langle I'_N \rangle_\varphi \equiv \nu_I I_I + \nu_N \langle I_N \rangle_\varphi, \quad (2.39)$$

$$a'_i \equiv a_i \frac{\nu_N \langle I_N \rangle_\varphi}{\nu_I I_I + \nu_N \langle I_N \rangle_\varphi}. \quad (2.40)$$

Eqn. 2.38 shows the composite scattering from two phases rearranged into a form consistent with scattering exclusively from a nematic domain. Since the inequality $0 \leq a'_i \leq 1$ is satisfied for all i , the single-domain configuration is a physically realizable system that would produce a scattering profile identical to that of the original $I - N$ combination. These are two of a multitude of $I - N$ mixtures of various ratios that would be consistent with the measured scattering.

Such ambiguity is eliminated if specific relations between the distribution function components are imposed. For example, when the Maier-Saupe orientational distribution function is assumed (see Eqns. 2.20, 2.23, and 2.24),

$$a_i = \frac{m(2i-1)}{i(2i+1)} a_{i-1}. \quad (2.41)$$

In Eqn. 2.38,

$$a'_0 = 1 - \sum_{i=1}^{\infty} a'_i \neq \frac{3}{m} a'_1, \quad (2.42)$$

which means that a single nematic domain possessing a Maier-Saupe ODF would not give rise to the scattering in Eqn. 2.36, nor in fact could any combination of isotropic and Maier-Saupe nematic domains except the original.

2.2.1.2 Experimental uncertainties and fitted proportions

Despite the mathematical uniqueness of scattering from any Maier-Saupe $I - N$ pair, experimental evaluations of the relative proportions of the two phases based on fits to scattering data can be highly uncertain, especially when the orientational order parameter is significantly less than unity. To see how, suppose that the extrema, $I(\varphi = 0)$ and $I(\varphi = \pi/2)$, are well-known values. Eqns. 2.12 and 2.35 then combine to give

$$I(\varphi) = \nu_I I_I + \nu_N \langle I_N \rangle_{\varphi} \frac{J(m \cos^2 \varphi)}{Z(m)}, \quad (2.43)$$

$$\nu_I I_I = \frac{J(m) I(\varphi = \frac{\pi}{2}) - I(\varphi = 0)}{J(m) - 1}. \quad (2.44)$$

(Incidentally, this reveals a convenient calculation for a lower bound on physically reasonable values of m ,

$$\nu_I I_I \geq 0 \quad (2.45)$$

$$J(m) \geq \frac{I(\varphi = 0)}{I(\varphi = \frac{\pi}{2})}, \quad (2.46)$$

and $J(m)$ monotonically increases with m , starting at $J(m = 0) = 1$.)

Making use of the identities,

$$\frac{dJ}{dm} = \frac{(2m-1)J(m)+1}{2m}, \quad (2.47)$$

$$\lim_{m \rightarrow 0} \frac{dJ}{dm} = \frac{2}{3} \quad (2.48)$$

we find that

$$\frac{d\nu_I}{dm} \propto \frac{(2m-1)J(m)+1}{2m(J(m)-1)^2} \quad (2.49)$$

which decreases monotonically with m . For $m \ll 1$, $d\nu_I/dm \propto 3/2m^2$. At high orientational order parameters, $m \gg 1$ and $d\nu_I/dm \propto 1/J(m)$; in this case the isotropic domain's contribution is easily distinguishable since the nematic domain presents negligible scattering at $\varphi = \pi/2$. For lower order parameters ($m \lesssim 5$, say), $d\nu_I/dm$ will be large, meaning that significant uncertainties in the fitted proportions, $\nu_{I,N}$, may accompany even small uncertainties encountered in the fitting of m .

2.2.2 Three-phase ($I - N_I - N_{II}$) coexistence

2.2.2.1 Interchangability of scattering from nematic domains

When a second nematic domain is present in the sample, none of the three interesting characteristics of the nematics—orientation, order parameter, and proportion—nor the isotropic proportion can be uniquely discerned from scattering without constraining the orientational distribution function. This impossibility can be demonstrated by extending Eqn. 2.36 to apply to a system with two distinct nematic domains,

$$I(\varphi) = \nu_I I_I + \nu_{N_I} I_{N_I}(\varphi) + \nu_{N_{II}} I_{N_{II}}(\varphi) \quad (2.50)$$

$$= \nu_I I_I + \nu_{N_I} \langle I_{N_I} \rangle_\varphi \left[1 + \sum_{i=1}^{\infty} a_i^{(I)} \left(c_i \cos^{2i}(\varphi - \varphi_0^{(I)}) - 1 \right) \right] \\ + \nu_{N_{II}} \langle I_{N_{II}} \rangle_\varphi \left[1 + \sum_{i=1}^{\infty} a_i^{(II)} \left(c_i \cos^{2i}(\varphi - \varphi_0^{(II)}) - 1 \right) \right], \quad (2.51)$$

and then reorganizing it as

$$I(\varphi) = \alpha_0 + \sum_{p=1}^{\infty} \alpha_p^{(c)} \cos(2p\varphi) + \sum_{p=1}^{\infty} \alpha_p^{(s)} \sin(2p\varphi), \quad (2.52)$$

where

$$\alpha_0 \equiv \nu_I I_I + \nu_{N_I} \langle I_{N_I} \rangle_\varphi + \nu_{N_{II}} \langle I_{N_{II}} \rangle_\varphi, \quad (2.53)$$

$$\alpha_p^{(c)} \equiv \sum_{i=p}^{\infty} \frac{2(i!)^2}{(i-p)!(i+p)!} \left[\nu_{N_I} \langle I_{N_I} \rangle_{\varphi} a_i^{(I)} \cos\left(2p\varphi_0^{(I)}\right) + \nu_{N_{II}} \langle I_{N_{II}} \rangle_{\varphi} a_i^{(II)} \cos\left(2p\varphi_0^{(II)}\right) \right], \quad (2.54)$$

$$\alpha_p^{(s)} \equiv \sum_{i=p}^{\infty} \frac{2(i!)^2}{(i-p)!(i+p)!} \left[\nu_{N_I} \langle I_{N_I} \rangle_{\varphi} a_i^{(I)} \sin\left(2p\varphi_0^{(I)}\right) + \nu_{N_{II}} \langle I_{N_{II}} \rangle_{\varphi} a_i^{(II)} \sin\left(2p\varphi_0^{(II)}\right) \right]. \quad (2.55)$$

Notice the introduction in Eqn. 2.51 of the parameters, $\varphi_0^{(I,II)}$, reflecting the separate orientations of the two nematic domains.

Eqn. 2.52 shows the connection between a Fourier series expansion of the measured intensity and the Davidson expansion coefficients a_i of the orientational distribution function(s). Suppose we terminate the expansions after some arbitrarily large number of terms, i_{\max} ; that is to say, $a_{i>i_{\max}}^{(I)} = a_{i>i_{\max}}^{(II)} = 0$. The quantities we wish to solve for are $\left\{ a_{i \leq i_{\max}}^{(I)} \right\}$, $\left\{ a_{i \leq i_{\max}}^{(II)} \right\}$, $\varphi_0^{(I)}$, $\varphi_0^{(II)}$, ν_I , ν_{N_I} , and $\nu_{N_{II}}$, for a total of $2i_{\max} + 5$ unknowns. The cutoff also ensures that $\alpha_{p>i_{\max}}^{(c)} = \alpha_{p>i_{\max}}^{(s)} = 0$. Eqn. 2.52 then implicitly contains $2i_{\max} + 1$ independent equations. The requirement that the proportions must sum to the whole provides the equation: $\nu_I + \nu_{N_I} + \nu_{N_{II}} = 1$, which is independent of the others unless, for example, $I_I = \langle I_{N_I} \rangle_{\varphi} = \langle I_{N_{II}} \rangle_{\varphi}$. This leaves three more unknowns than equations, meaning a unique solution is impossible. Two of these degrees of freedom arise from the interchangeability of the scattering from isotropic and nematic domains as discussed in Sec. 2.2.1.1. The third comes from a similar relationship between the two nematic domains. One particular graphical example of this inherent ambiguity is displayed in Fig. 2-1.

A few exceptions arise under special circumstances. For example, if the domains both possess order parameters large enough that their scattering does not significantly overlap in φ , then it will be empirically evident that $a_{i < i_{\min}}^{(I)} = a_{i < i_{\min}}^{(II)} \simeq 0$ up to some i_{\min} . This effectively yields $2i_{\min}$ new constraining equations and will permit determinations of at least the director orientations, if not a full solution. Similarly, the orientations will be evident if the two directors are orthogonal to one another; in this case $I(\varphi)$ will display a reflection symmetry every $\frac{\pi}{2}$ radians, and in addition, $\varphi_0^{(II)} = \varphi_0^{(I)} + \frac{\pi}{2}$, thereby making

$$\alpha_p^{(c)} \equiv \sum_{i=p}^{\infty} \frac{2(i!)^2}{(i-p)!(i+p)!} \left[\nu_{N_I} \langle I_{N_I} \rangle_{\varphi} a_i^{(I)} + (-1)^p \nu_{N_{II}} \langle I_{N_{II}} \rangle_{\varphi} a_i^{(II)} \right] \cos\left(2p\varphi_0^{(I)}\right), \quad (2.56)$$

and similarly for $\alpha_p^{(s)}$.

As mentioned earlier, another way to add sufficient constraints is to adopt *a priori* a specific class of orientational distribution functions. The Maier-Saupe form provides constraints that can be treated as $2i_{\max} - 2$ additional equations, as seen in Eqn. 2.41 (allowing $i_{\max} \rightarrow \infty$). Maier-Saupe distributions effectively overconstrain the unknowns, providing a unique relationship between scattering and domain structure. In principle, one then need only obtain three components of the Fourier series expansion, for example α_0 , $\alpha_1^{(c)}$, and

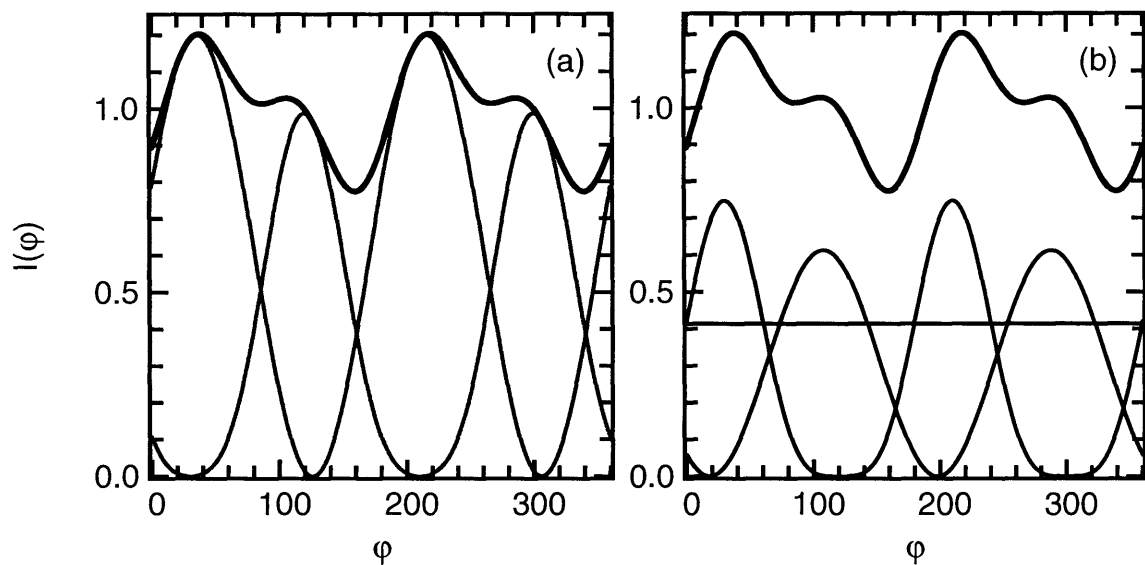


Figure 2-1: Two different theoretical $I - N_I - N_{II}$ configurations that give rise to mathematically identical azimuthal scattering profiles. Thin lines represent individual domains' contributions. Thick lines represent the total scattering. The specific parameter values used are listed in Table 2.1.

	ν_I	ν_{N_I}	$\varphi_0^{(I)}$	$\langle P_2^{(I)} \rangle$	$\langle P_4^{(I)} \rangle$	$a_0^{(I)}$	$a_1^{(I)}$	$a_2^{(I)}$
(a)	0	$\frac{3}{5}$	36°	0.40	0	0	1	0
(b)	0.41367	$\frac{7}{25}$	30°	0.57	0.13	0	0	1

	$\nu_{N_{II}}$	$\varphi_0^{(II)}$	$\langle P_2^{(II)} \rangle$	$\langle P_4^{(II)} \rangle$	$a_0^{(II)}$	$a_1^{(II)}$	$a_2^{(II)}$
(a)	$\frac{2}{5}$	120°	0.52	0.089	0	$\frac{3}{10}$	$\frac{7}{10}$
(b)	0.30633	107.98°	0.40	0	0	1	0

Table 2.1: Parameters used to generate three-phase scattering intensities as seen in Fig. 2-1(a) and (b). For simplicity, $I_I = \langle I_{N_I} \rangle_\varphi = \langle I_{N_{II}} \rangle_\varphi = 1$ and $a_{i \geq 3}^{(I)} = a_{i \geq 3}^{(II)} = 0$.

$\alpha_1^{(s)}$, in order to completely specify the properties of all three domains. Nevertheless, the discussion in Sec. 2.2.1.2 regarding experimental uncertainties is still entirely relevant.

2.2.2.2 Experimental uncertainties and fitted order parameters

Order parameters of experimental three-phase data may be more difficult to extract than in the analogous two-phase ($I-N$) case. The isotropic component of the scattering serves only to add an offset, as a constant background would, and does not change the overall shape of the nematic's azimuthal scattering profile. By comparison, a second nematic phase does distort that shape.

This has two significant effects: first, the tails ($\varphi - \varphi_0 \approx \pi/2$) of scattering from one domain can easily become washed out by the central portion of the other domain's scattering. A similar situation is encountered when an azimuthal angular range less than $\pi/2$ is experimentally accessible. While information from the full range is not strictly necessary to determine an order parameter once the Maier-Saupe ODF is adopted, it does significantly improve the quality of fitted results.

The second effect is that even though two local maxima may be evident in the raw data, the constituent peaks may be substantially offset in angle and may be significantly narrower than a visual inspection of their sum might seem to indicate. An example of this can be found in Fig. 2-1(a), where the lesser domain's scattering profile is rather distinct from the composite peak. Once again, the Maier-Saupe ODF constrains the lineshapes sufficiently to resolve the ambiguity in principle, but with the presence of measurement noise and the allowance of a constant (isotropic) background of unknown magnitude, even small changes to the director orientations during the fitting process can cause significant swings in the best-fit order parameters.

2.3 Characterization of orientational ordering in suspensions of böhmite in glycerol

2.3.1 Azimuthal dependence of scattering

We have measured the X-ray scattering cross section of the böhmite in glycerol samples described in Sec. 1.1. Intensities were recorded over continuous ranges of q and φ simultaneously. We chose $\varphi = 0$ to be perpendicular to the capillary, as shown in Fig. 2-2. The azimuthal dependence at a relatively high q value is plotted in Fig. 2-3 for several different concentrations. (Strictly speaking, the quantity plotted is the effective structure factor, $S_{\text{eff}}(q, \varphi)$ —its azimuthal dependence is identical to that of the raw intensity; see Sec. 3.3.1 for details.) Orientational ordering, indicated by azimuthal intensity variations, was apparent at 2% volume fraction and above, in agreement with the optical birefringence studies discussed in the previous chapter. Azimuthal dependences were qualitatively similar

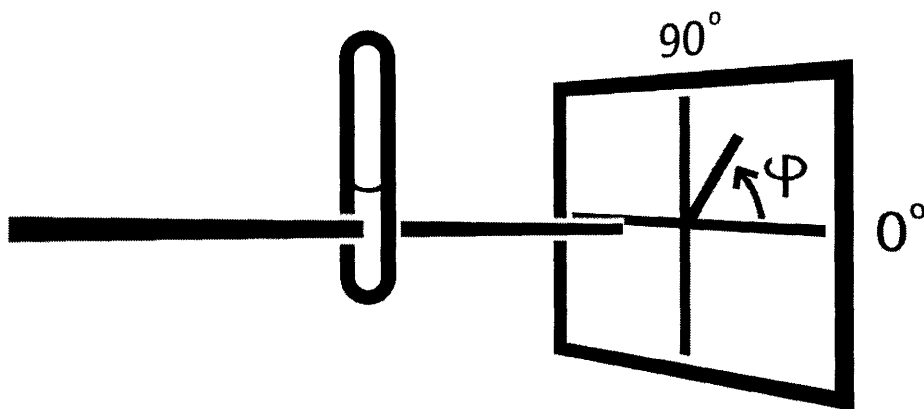


Figure 2-2: Transmission geometry for scattering experiments. Azimuthal angles $\varphi = 0^\circ, 180^\circ$ represented directions perpendicular to the capillary; $\varphi = 90^\circ, 270^\circ$ were parallel to the capillary.

at all q for a given sample, and, as shown in Fig. 2-4, did not significantly vary as the beam position on the sample was changed.

The ordering process was not a simple one, however. While periodic every π radians in accordance with Friedel's law [78], none of the curves in Fig. 2-3 demonstrated the usual indicator of a single nematic domain: inversion symmetry about a maximum along φ . Typically they displayed a main peak together with a secondary peak or shoulder. Even curves with a single dominant peak, such as those of the 6.5% and 7.5% samples, displayed slight asymmetries near the minima, betraying the presence of a relatively weaker, additional source of scattering. The simplest scenario consistent with these double-peaked profiles is that of isotropic-nematic-nematic coexistence. Azimuthal variations were of sufficient magnitude relative to the azimuthal average to indicate that each nematic domain occupied a significant portion of the entire sample, and were not confined, for example, to a thin layer on the wall of the capillary tube in which the sample was loaded.

Attempts to merge and reorient the domains using magnetic and AC electric fields were unsuccessful. Annealing at 80°C over several months also yielded no changes in the domain structure.

We extracted from the azimuthal profiles quantitative information about the relative proportions of the sample in each phase, along with the director orientations and order parameters of the nematic domains. Having ruled out in Sec. 2.2 the use of Davidson's general function, we fit the data to the form,

$$I(\varphi) = \nu_I I_I + \nu_{N_I} \langle I_{N_I} \rangle_\varphi \frac{J\left(m^{(I)} \cos^2\left(\varphi - \varphi_0^{(I)}\right)\right)}{Z\left(m^{(I)}\right)} + \nu_{N_{II}} \langle I_{N_{II}} \rangle_\varphi \frac{J\left(m^{(II)} \cos^2\left(\varphi - \varphi_0^{(II)}\right)\right)}{Z\left(m^{(II)}\right)}, \quad (2.57)$$

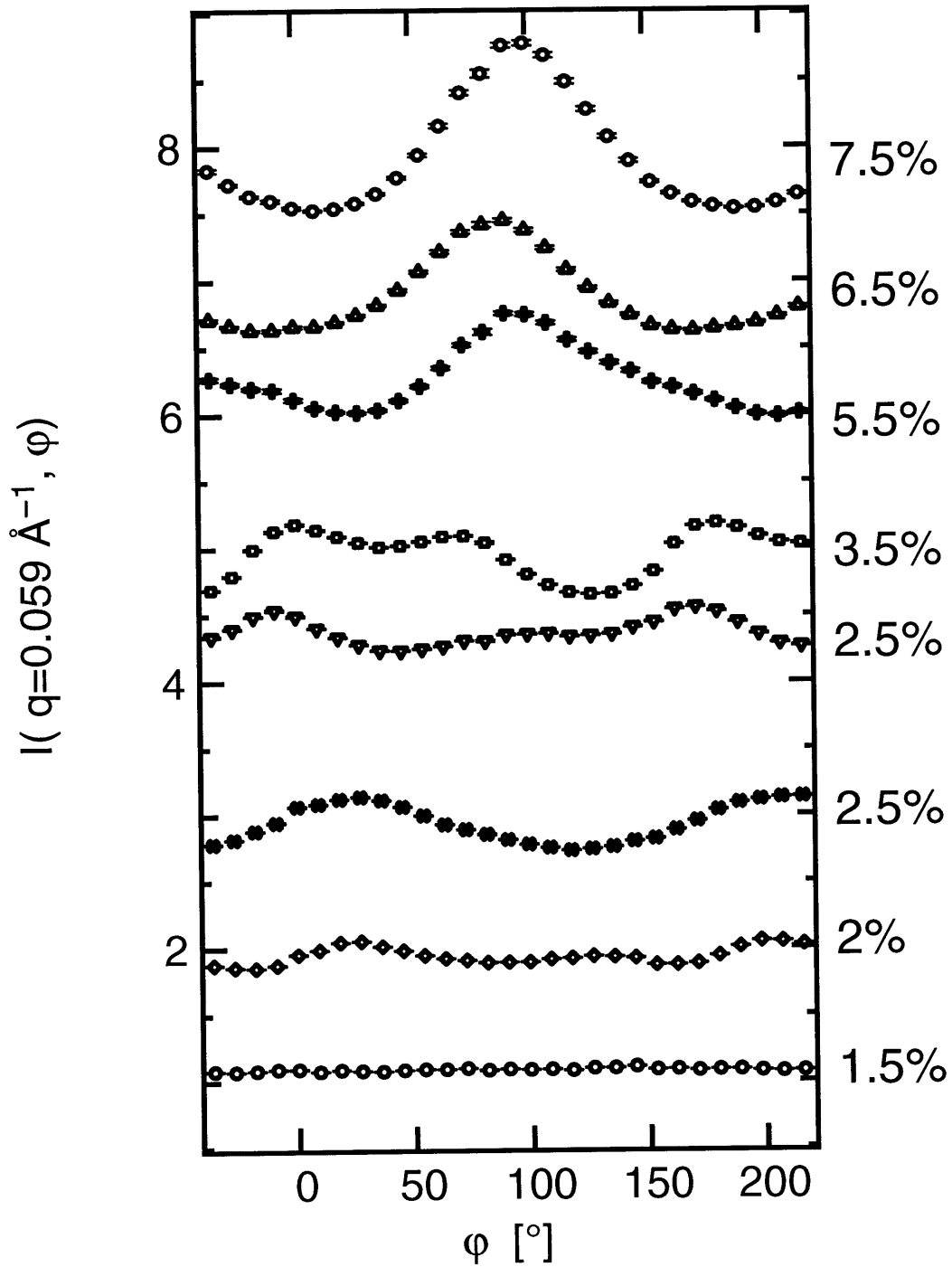


Figure 2-3: Azimuthal dependence of the scattered intensity at $q \frac{\langle L \rangle}{2} \simeq 48$. The samples' nominal volume fractions are indicated at the right. For clarity, offsets of 0, 1, 2, 3, 4, 5, 6, and 7 have been added to each curve, respectively.

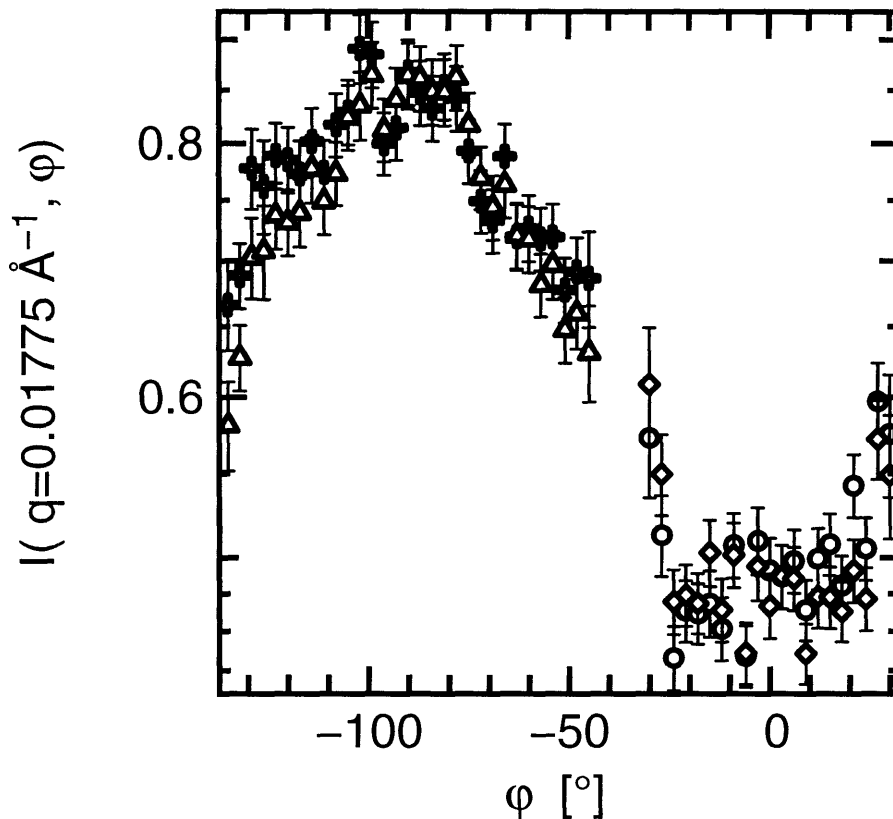


Figure 2-4: High-resolution azimuthal profiling of 7.5% sample. Four sets of points are shown. The sample was moved horizontally by 0.1 mm (four times the beam size) and vertically by 0.2 mm between each set. The two angular ranges correspond to two different detector positions.

which is the natural extension of Eqn. 2.43 to a three-component system. Representative examples of the fits are shown in Fig. 2-5. The seven adjustable parameters were $\nu_I I_I$, $\nu_{N_I} \langle I_{N_I} \rangle_\varphi$, $\nu_{N_{II}} \langle I_{N_{II}} \rangle_\varphi$, $m^{(I)}$, $m^{(II)}$, $\varphi_0^{(I)}$, and $\varphi_0^{(II)}$. With this large number of parameters, fits did not always immediately converge to sensible values. For each sample, fits were first made separately at each q . The medians of the parameter values across q were then used as the starting point for a second round of fitting, once again independently at every q . This produced reasonable agreement without precise predeterminations of the parameters. Successful fitting required constraining m and $\nu \langle I \rangle$ values to be nonnegative, as well as holding $\nu \langle I \rangle$ values below the maximum measured intensity.

We made little effort to compare the data to models accounting for four-phase or greater coexistence, for two reasons. First, doing so involves at least ten adjustable parameters, making reasonable convergence even more difficult to achieve. Second, no obvious discrepancies from the three-phase model occurred in the data—for example, no sample displayed more than two azimuthal peaks.

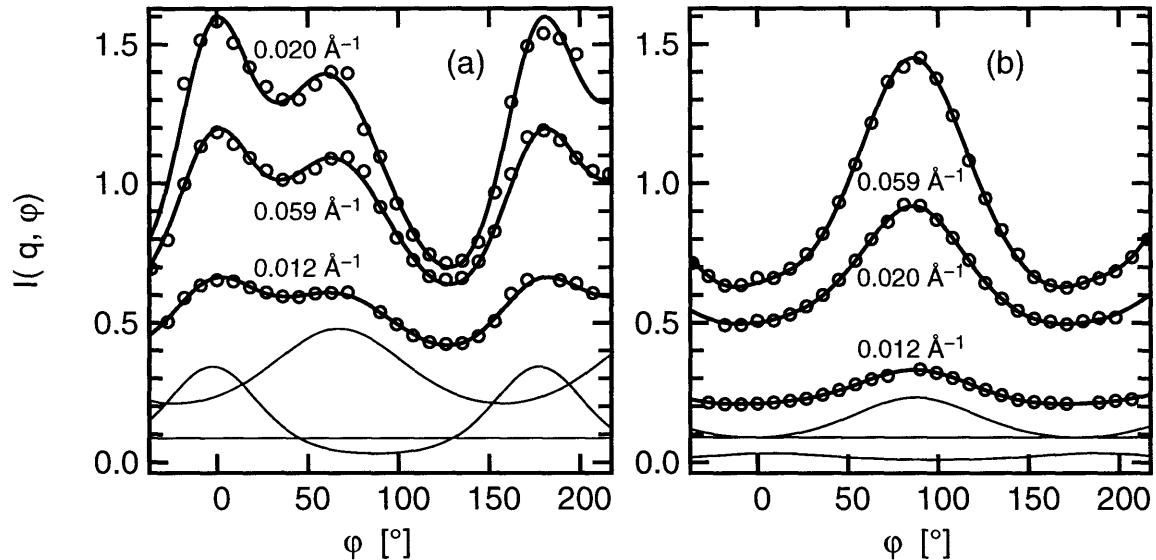


Figure 2-5: Azimuthal dependence of (a) 3.5% and (b) 6.5% samples' scattering at the three q values indicated. Thick lines are fits to Eqn. 2.57 using the Maier-Saupe form from Eqn. 2.13 (*solid*) or Davidson's form from Eqn. 2.28 (*dashed*, behind solid lines). Thin lines show the isotropic and nematic contributions in the fit for $q = 0.012 \text{ \AA}^{-1}$.

Similarly, our analysis did not include any parameters to account for either nematic director possessing a component along the incident beam. A director partially parallel to the beam would alter the azimuthal intensity profile considerably. A simple example illustrates how: imagine a near-perfectly aligned sample with a director at (β, α) . From Eqn. 2.5,

$$\frac{\partial \varphi}{\partial \beta} = -\frac{\cos \alpha}{\cos^2 \beta + \sin^2 \beta \cos^2 \alpha} = \frac{\sin(2\varphi)}{\sin(2\beta)}. \quad (2.58)$$

As $\alpha \rightarrow \pi/2$ and $\beta \rightarrow \pi/2$, the derivative becomes arbitrarily large. Thus for some (β, α) scattering will be directed to a wide range of φ despite the order parameter being arbitrarily close to 1. Had such a "tilt" in the director(s) been significant, the scattering profile would have been "stretched" near the azimuthal maximum [63], and the simple three-phase model based on Eqn. 2.12 would have displayed far less agreement with the data.

2.3.2 Nematic director orientations

The directions, $\varphi_0^{(I)}$ and $\varphi_0^{(II)}$, into which the nematic domains most strongly scattered did not vary substantially along q , as can be seen in Fig. 2-6. The greatest variation was observed in high-volume-fraction samples, where the scattering from one domain was so weak as to be difficult to distinguish from the isotropic contribution. Consequently, we further refined the fitting of other parameters by fixing $\varphi_0^{(I)}$ and $\varphi_0^{(II)}$ to their median values for all q . All results presented hereafter utilized this constraint.

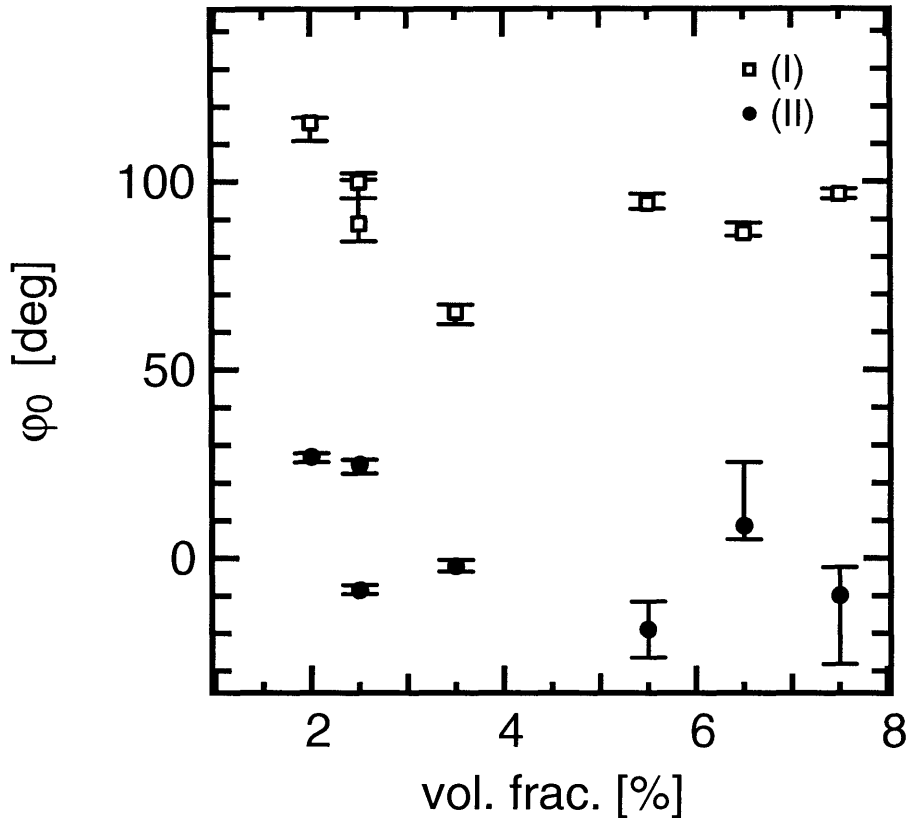


Figure 2-6: Fitted directions perpendicular to the two nematic directors for each anisotropic sample. Points indicate the median value across q from 0.0097 to 0.063 \AA^{-1} . Error bars span the full range of φ_0 found. Capillaries holding the samples were oriented along $\varphi \simeq 90^\circ$.

Overall the two directors (pointed perpendicular to φ_0) were approximately orthogonal to one another in each sample. The first director lay more or less perpendicular to the capillary, while the second was roughly parallel. Despite this general consistency, there was substantial variation of the director orientations among samples. One potential source of such variation was the orientation of the capillary itself, which was not precisely controllable in our apparatus. If this were the only cause, one would expect the difference between the two directors to remain constant across all samples, which was not the case.

This raises the question of what caused the domains to align as they did. Flow and interactions with surfaces are both well known to influence director orientation [1, 79]. Perhaps one domain sat at the capillary walls, while another was primarily influenced by flow down the center of the capillary as the sample was loaded. This situation is diagrammed in Fig. 2-7, and it is consistent with the microscopy studies discussed in the previous chapter, which revealed little variation in birefringence as one rotated the capillary around its long axis. Neither the interior surface of the capillary nor the rate at which material flowed into the tube were directly under our control; if they indeed opposed one another with regard to affecting director orientation, it was purely fortuitous.



Figure 2-7: Schematic of possible configuration of nematic directors in samples studied. Shown is a cross-section through the cylindrical capillary tube holding the sample. Bars represent the projections into the page of local nematic directors, with dots indicating directors oriented along the capillary length. The “empty” region midway between the capillary walls and center is effectively isotropic.

An alternate possibility, also consistent with the microscopy results, is that the phase separation was microscopic rather than macroscopic. In this situation, rods would either tend to align perpendicular to their neighbors, or small pockets of essentially parallel rods, as discussed in Sec. 2.1.3, would arrange in a crosshatched pattern throughout the sample. The bare electrostatic potential of widely separated, similarly charged rods is indeed expected to energetically favor this sort of perpendicular alignment [80]. However, the “bare” repulsive interaction is generally thought of as a tendency toward random, isotropic configurations rather than the highly ordered arrangement necessary to generate the observed, markedly double-peaked scattering. Moreover, in typical solutions the effects of screening, multibody, and excluded volume interactions dominate, inducing parallel alignment of neighbors [80–82] and hence conventional nematic ordering. We therefore were skeptical of the micro-phase separation scenario with regard to our samples, despite the appeal of its simplicity.

Underlying this discussion is the noteworthy fact that in order for X-ray scattering measurements to detect separate, coexisting nematic domains, the directors cannot be collinear. Thus, the common practice of applying an external field to orient the sample [63, 66, 68, 70–72, 76] may effectively erase any detectable contrast between two nematic phases, even if the domains remain otherwise distinct: for example, containing different-

length rods on average [44–46].

2.3.3 Nematic order parameters

Fitted values of $m^{(I)}$ and $m^{(II)}$ were entered into Eqn. 2.18 to extract the order parameters $\langle P_2^{(I)} \rangle$ and $\langle P_2^{(II)} \rangle$ of the two nematic domains. Holding fixed the directors as discussed in the previous section, fits were performed independently at each q to test the proposition of Sec. 2.1.3 that rods are grouped into local clusters of near-complete order. Representative results are shown in Fig. 2-8.

The general q -dependence of the order parameters appeared to be related to the (radial) effective interparticle structure factor, which will be discussed more thoroughly in Secs. 2.3.4 and 3.3.1. The first nematic domain—the one with a director roughly perpendicular to the capillary axis—displayed a peak in the order parameter at q values near the peak in the structure factor for samples of volume fraction $\geq 5.5\%$. The second nematic domain—with a director parallel to the capillary axis—did not display such a clear peak, but instead showed a slight, gradual increase in order parameter as q approached the structure factor peak value for all volume fractions where this domain scattered distinctly enough to allow reliable measurements of the order parameter.

The behavior of $\langle P_2^{(II)} \rangle$ may be understood with the local cluster model: nearest neighbors exhibit a greater degree of alignment than more distantly separated pairs. This would lead to a gradual reduction in the order parameter as the probed length scale increases (q decreases) from the nearest-neighbor length scale. A different mechanism may underlie the peak in $\langle P_2^{(I)} \rangle$, which does not appear consistent with local clustering. An anomalously large order parameter within a limited range of q near q_0 indicates that excess intensity around $(q_0, \varphi_0^{(I)})$ enhanced the ordinary azimuthal maximum. Interparticle interference effects, detailed in Eqn. 3.43, could give rise to just such a localized feature. When \mathbf{q} points along \mathbf{R}_{mn} , the vector connecting two rods' centers, the factor $\exp(-i\mathbf{q} \cdot \mathbf{R}_{mn})$ goes to unity at $q = 2\pi/R_{mn}$. As mentioned in Sec. 3.3.1, rods involved in interparticle interference must be oriented almost perfectly parallel to one another. Thus, an interference peak will emerge at $(q_0, \varphi_0^{(I)})$ only if there is a correlation between nearest neighbors' mutual orientation and the *direction* of \mathbf{R}_{mn} . When separated along the nematic director, the rods would be less likely to be parallel than were they separated perpendicular to the nematic director. The anisotropy of simple hard spherocylinder excluded volumes, discussed in Sec. 1.2.2, could easily explain this tendency—much the same way as in smectic liquid crystalline phases [1].

The qualitative difference between the two order parameters' respective variations with q tends to support the idea that two separate mechanisms brought about the orientation of the two nematic directors. So too does the substantial discrepancy between the two order parameters' magnitudes, as shown for all samples in Fig 2-9.

To summarize, the domain with director parallel to the capillary axis appeared to display local clustering and had an order parameter of, on average, 0.46. We surmise that this

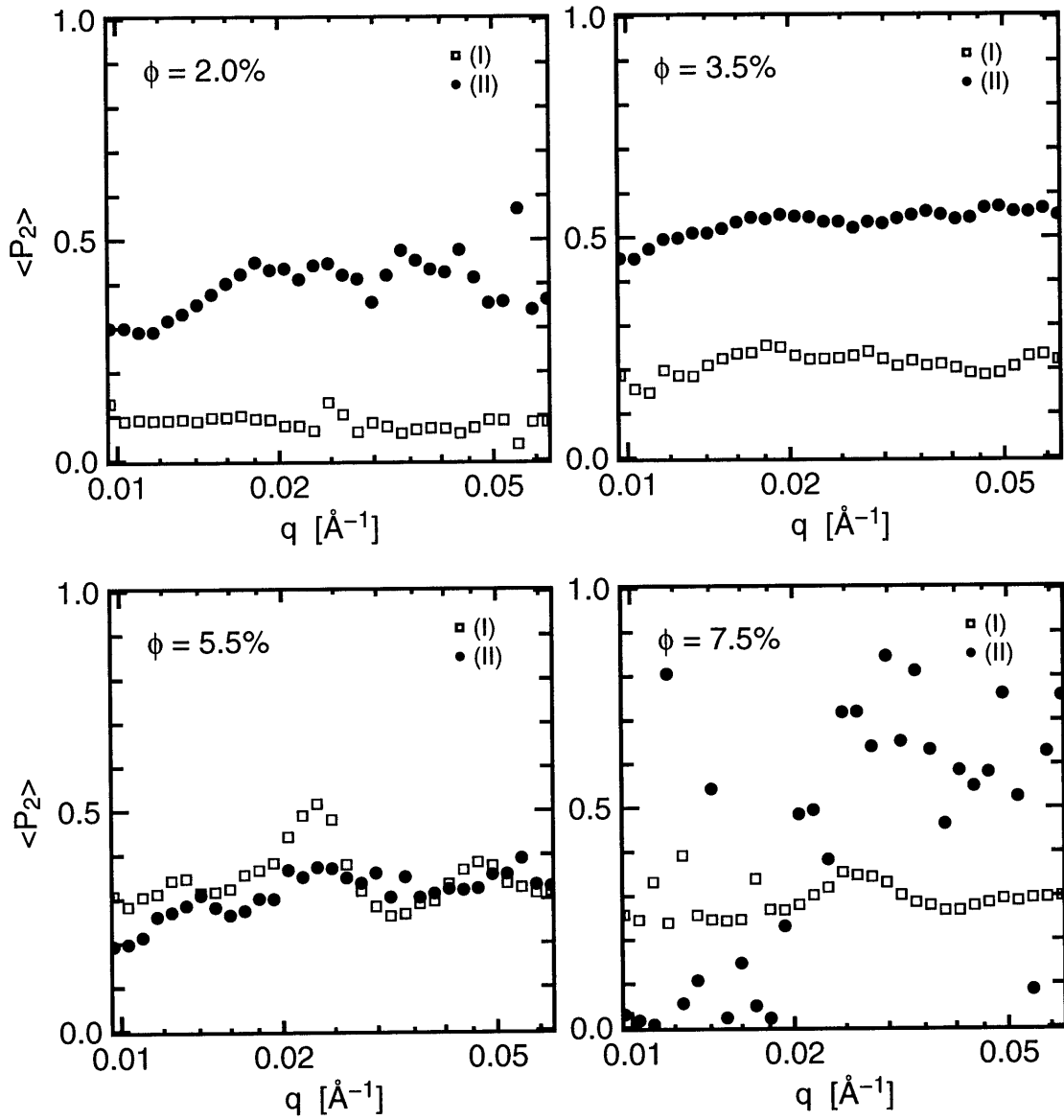


Figure 2-8: Best-fit values of nematic order parameter for each of two domains in four böhmite-in-glycerol samples.

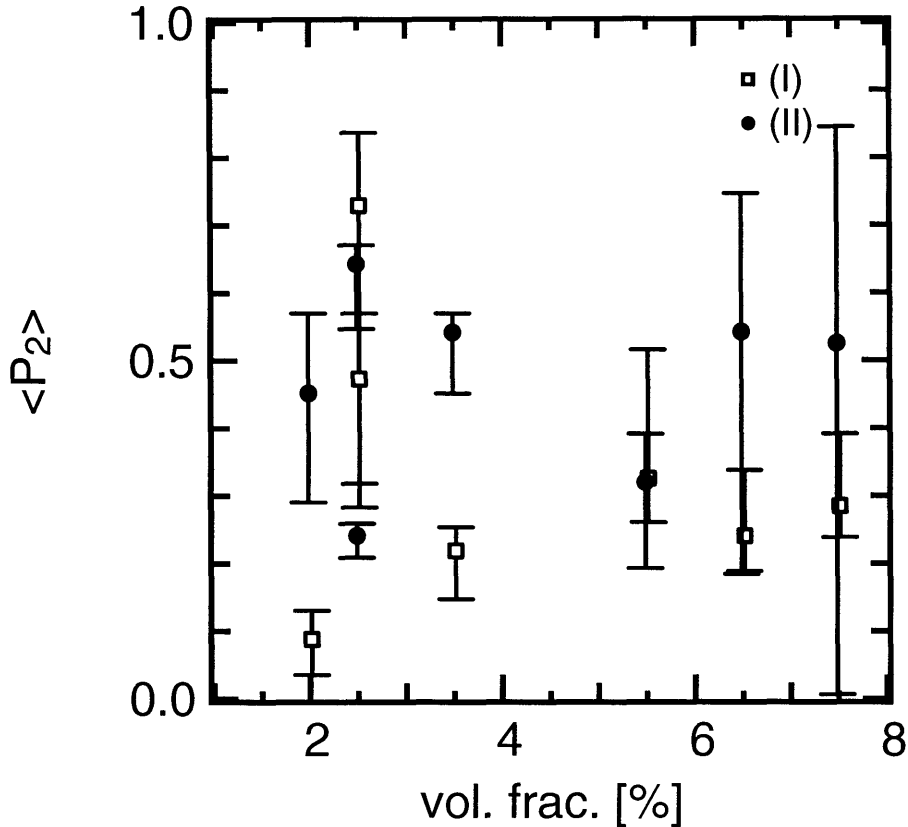


Figure 2-9: Fitted order parameters for each anisotropic sample. Points indicate the median value across q from 0.0097 to 0.063 \AA^{-1} . Error bars span the full range of $\langle P_2 \rangle$ found.

domain was oriented by flow down the center of the capillary tube. The domain with director perpendicular to the capillary axis seemed to indicate that neighboring rods' relative orientations were coupled to the direction of their center-of-mass separation. This domain showed a low order parameter of, on average, 0.27 . It may have been aligned by surface anchoring effects at the capillary walls. Neither order parameter displayed any systematic increase or decrease with volume fraction, but the uncertainty inherent in fitting the three-phase model may have washed out gradual trends.

2.3.4 Proportions of I , N_I , and N_{II} phases

Our results for the q -dependence of the three remaining fit parameters, $\nu_I I_I$, $\nu_{N_I} \langle I_{N_I} \rangle_\varphi$, $\nu_{N_{II}} \langle I_{N_{II}} \rangle_\varphi$, are discussed fully in Sec. 3.3.4. Since both the director orientations and order parameters of the two nematic domains showed little variation at high q , we attempted to extract a rough estimate of the proportions from this region of the measured area. Past its main peak, the effective structure factor is expected to approach $I(\varphi)$ (Sec. 3.3.1). This implies that the proportionality coefficient in Eqn. 2.12 is unity, and we therefore assumed $\nu \langle I \rangle \simeq \nu$ at large q .

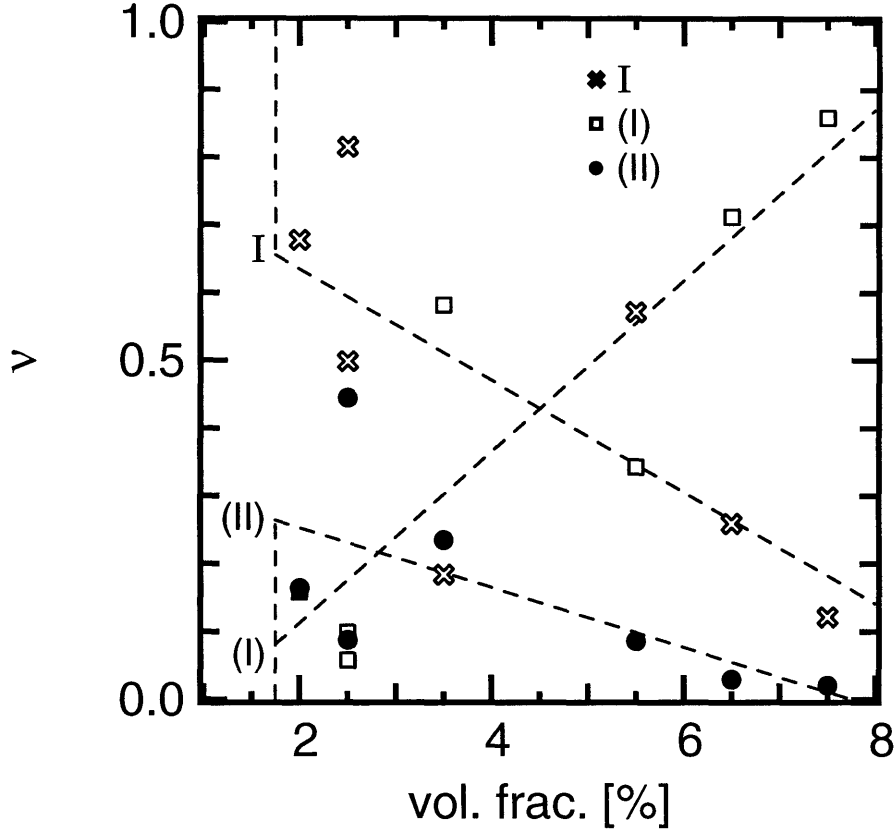


Figure 2-10: Fitted proportions of one isotropic (I) and two nematic phases (I, II), for each anisotropic sample. Dashed lines are linear least-squares fits for each phase, intended as a guide to the eye.

The results in Fig. 2-10 show the average normalized ν for $0.050 \leq q \leq 0.063 \text{ \AA}^{-1}$. To allow for possible inaccuracies in absolute cross-section normalization, such as those discussed later in Sec. 3.1.6, we allowed all three proportions to vary freely, and after fitting scaled them collectively in order to recover the condition $\nu_I + \nu_{N_I} + \nu_{N_{II}} = 1$. Although there was a great deal of scatter, due primarily to the issues raised in Secs. 2.2.1.2 and 2.2.2.2, the trends clearly visible to the eye in Fig. 2-3 are highlighted in Fig. 2-10; the “perpendicular” (to the capillary axis) nematic represented a greater and greater portion of the sample as the volume fraction was increased, displacing the “parallel” nematic and isotropic material.

At first glance, this appears consistent with the picture of microscopic phase separation driven heavily by polydispersity effects as outlined in Sec. 1.2.5. The very longest rods begin to align with one another in a state (N_{II}) of relatively high order even at relatively low volume fractions. With increasing volume fraction, another nematic phase (N_I), this one of lower order parameter and comprising the majority of “normal-length” rods, gradually arises in the material until it completely replaces the first, and then ultimately the isotropic phase as well. Across the range of coexistence concentrations, the order parameters remain

more or less constant, the proportions changing instead. Our measured order parameters and proportions bore this out, but we are left without a mechanism for the disparity in director orientation. This model offers no hint that the longest rods would align one way while the rest were driven toward a distinctly different direction, and for that reason we doubt our samples exhibited such microscopic phase separation.

We introduced in Sec. 2.3.2 a macroscopic phase separation scheme that addressed the unique director orientations. Here the observed trend toward a preponderance of the N_I phase with increasing volume fraction would arise from the enhancement of the range of the anchoring effect as the rods packed closer together. It would be reasonable, then, to expect the order parameters of both the N_I and N_{II} domains to increase significantly with volume fraction. It remains unclear whether this macroscopic picture can be understood to be consistent with our observation of roughly constant order parameters. One possibility comes from the recent work of Potemkin *et al.* [82]. Accounting fully for (unscreened) many-body electrostatic interaction effects, their model indicates that a weakly aligned nematic phase can be stable at very low volume fractions, with an order parameter that varies little until the conventional transition point is reached.

Chapter 3

The static interparticle structure factor across the isotropic-to-nematic transition

3.1 Determining the form factor

3.1.1 Scattering from a dilute, isotropic suspension of polydisperse rod-like particles

Recalling Eqn. 2.2 for a single rod's form factor,

$$F_{\text{rod}}(\mathbf{q}) \propto \left(\pi R^2 L \frac{\sin\left(q\frac{L}{2}\cos\gamma\right)}{q\frac{L}{2}\cos\gamma} \frac{2J_1(qR\sin\gamma)}{qR\sin\gamma} \right)^2. \quad (3.1)$$

In a dilute, isotropic suspension, all orientations are equally likely and thus $f(\gamma) = 1/(4\pi)$. If all N rods are identical, then

$$F_{\text{rods}}(q) = N \int_0^1 d(\cos\gamma) F_{\text{rod}}(\mathbf{q}). \quad (3.2)$$

Notice that this expression is independent of the direction in which \mathbf{q} points. In a polydisperse collection, $Nf(L, R)$ rods will exhibit a length L and radius R . Assuming the length and radius are uncorrelated, the size probabilities separate, *i.e.* $f(L, R) = f(L)f(R)$, and the form factor becomes [49, 83]

$$F_{\text{rods}}(q) = N \int_0^\infty dL f(L) \int_0^\infty dR f(R) \int_0^1 d(\cos\gamma) F_{\text{rod}}(\mathbf{q}). \quad (3.3)$$

X-ray scattering is for the most part insensitive to the precise shape of a polydisperse distribution, so it is convenient to select the lognormal distribution for comparison with data.

The lognormal distribution is consistent with TEM observations of böhmite rods [11, 12], and is also commonly used in theoretical treatments of polydisperse rods [44, 46]. Its form is [44, 84]

$$f(L) = \frac{1}{\sqrt{2\pi w_L L}} e^{-\frac{(\ln L - \mu_L)^2}{2w_L^2}}, \quad (3.4)$$

with mean

$$\langle L \rangle \equiv \int_0^\infty dL f(L) L = e^{\mu_L + \frac{1}{2}w_L^2} \quad (3.5)$$

and polydispersity

$$\sigma_L = \sqrt{\frac{\langle L^2 \rangle}{\langle L \rangle^2} - 1} \quad (3.6)$$

$$= \sqrt{e^{w_L^2} - 1} \quad (3.7)$$

$$\approx w_L \quad \text{for } w_L \ll 1, \quad (3.8)$$

and similarly for R . Possessing only two adjustable parameters, it is well suited for use in nonlinear least-squares fitting algorithms. An advantage of using the lognormal instead of a typical Gaussian distribution is that the lognormal $f(L)$ approaches zero as $L \rightarrow 0$, inherently removing from the model all unphysical particles of zero or negative size.

3.1.2 Absolute cross-section normalization

For any dilute solution of monodisperse particles, q -dependent terms in the form factor approach unity as $q \rightarrow 0$ (for example, Eqn. 3.1 goes to $(\pi R^2 L)^2$). The measured intensity at very low scattering angles is given by [49]

$$I\left(q \ll \frac{2}{L}\right) = I_0 \alpha \Omega d c r_e^2 (V \Delta\rho)^2, \quad (3.9)$$

where I_0 is the incident intensity (corrected for sample absorption), α the detector's quantum efficiency, Ω its solid angle of acceptance, d the sample thickness, c the concentration (number per unit volume) of particles in the sample, r_e the Thomson classical electron radius, V the volume of a particle, and $\Delta\rho$ the electron density difference between the particles and the medium in which they sit. Moving the apparatus-specific terms to the left side of the equation, we recover the form factor,

$$\frac{I(q \ll \frac{2}{L})}{I_0 \alpha \Omega d} = \lim_{\mathbf{q} \rightarrow 0} F(\mathbf{q}) = r_e^2 (\Delta\rho)^2 c V^2, \quad (3.10)$$

meaning that the proportionality coefficient for Eqns. 3.1 and 2.1 is simply $r_e^2 (\Delta\rho)^2$.

Generalizing to polydisperse populations, V^2 should be replaced by $\langle V^2 \rangle$ while $c \propto N$ remains the overall number of particles per unit volume. For polydisperse, cylindrically

shaped particles in a dilute, isotropic solution, then,

$$F_{\text{rods}} \left(q \ll \frac{2}{L} \right) = r_e^2 (\Delta\rho)^2 c \pi^2 \langle R^4 L^2 \rangle. \quad (3.11)$$

When the length and radius distributions are independent and of the lognormal variety, as in Eqns. 3.3 and 3.4,

$$F_{\text{rods}} \left(q \ll \frac{2}{L} \right) = r_e^2 (\Delta\rho)^2 c \pi^2 e^{4\mu_R + 8w_R^2} e^{2\mu_L + 2w_L^2} \quad (3.12)$$

$$\propto \pi^2 e^{4(\mu_R + \frac{1}{2}w_R^2) + 6w_R^2} e^{2(\mu_L + \frac{1}{2}w_L^2) + w_L^2} \quad (3.13)$$

$$\propto \pi^2 \langle R \rangle^4 (\sigma_R^2 + 1)^6 \langle L \rangle^2 (\sigma_L^2 + 1). \quad (3.14)$$

The polydispersity enters directly into this expression because the form factor depends on $\langle (R^2 L)^2 \rangle$ rather than $(\langle R \rangle^2 \langle L \rangle)^2$.

Another q -regime where the form factor simplifies considerably is where $1/q$ is between the rods' long and short dimensions. Specifically, Eqn. 3.2 reduces to [50]

$$F_{\text{rods}} \left(q \gg \frac{2}{L} \right) \approx r_e^2 (\Delta\rho)^2 c \left(\pi R^2 L \frac{2J_1(qR)}{qR} \right)^2 \int_0^\infty d(\cos \gamma) \left(\frac{\sin(q\frac{L}{2} \cos \gamma)}{q\frac{L}{2} \cos \gamma} \right)^2 \quad (3.15)$$

$$\approx r_e^2 (\Delta\rho)^2 c \left(\pi R^2 L \frac{2J_1(qR)}{qR} \right)^2 \frac{\pi}{qL} \quad (3.16)$$

because $[\sin(q(L/2) \cos \gamma) / (q(L/2) \cos \gamma)]^2$ will be negligible except where $\cos \gamma \ll 2/qL$ and $\sin \gamma \simeq 1$. If the monodisperse rods' aspect ratio is large enough, there will then be a range of q in which

$$F_{\text{rods}} \left(\frac{2}{L} \ll q \ll \frac{1}{R} \right) \approx \frac{r_e^2 (\Delta\rho)^2 c \pi^3 R^4 L}{q}. \quad (3.17)$$

In the case of rods with lognormal polydispersity,

$$F_{\text{rods}} \left(\frac{2}{L} \ll q \ll \frac{1}{R} \right) \approx \frac{r_e^2 (\Delta\rho)^2 c \pi^3 e^{4\mu_R + 8w_R^2} e^{\mu_L + \frac{1}{2}w_L^2}}{q} \quad (3.18)$$

$$= \frac{r_e^2 (\Delta\rho)^2 c \pi^3 \langle R \rangle^4 (\sigma_R^2 + 1)^6 \langle L \rangle}{q}. \quad (3.19)$$

This formula must be used with caution, especially with polydisperse samples. Unless all rods possess a very large (~ 10000) aspect ratio, Eqn. 3.17 is accurate only to within 10% or 20%.

Eqns. 3.13 and 3.19, when compared to data, may be useful as checks or constraints on any of the size or concentration parameters or on the accuracy by which the measured scattering has been normalized.

3.1.3 Form factor of a rigid rod with a surface layer

A common model of *charged* rods in solution is a solid cylindrical core covered by a thin electrical double layer [13, 85, 86]. In the case of böhmite [13], ionized hydroxyl groups on the rod surface trap oppositely charged counterions that drift closer to the rod than some critical distance at which the electrostatic interaction is strong enough to overcome thermal diffusion. The counterions “condense” onto the rod, forming the double layer. The double layer’s electron density may thus differ both from the core’s and the solvent’s, and the form factor may show evidence of this double layer.

It is straightforward to extend Eqn. 3.1 to treat a cylindrical particle of radius R and relative electron density $\Delta\rho_1$, surrounded by an adsorbed layer of thickness ΔR and density $\Delta\rho_2$.

$$F_{\text{rod}}(\mathbf{q}) \propto \left(L \frac{\sin\left(\frac{qL}{2} \cos \gamma\right)}{\frac{qL}{2} \cos \gamma} \right)^2 \pi^2 \left[(\Delta\rho_1 - \Delta\rho_2) \left(R^2 \frac{2J_1(qR \sin \gamma)}{qR \sin \gamma} \right) + \Delta\rho_2 \left((R + \Delta R)^2 \frac{2J_1(q(R + \Delta R) \sin \gamma)}{q(R + \Delta R) \sin \gamma} \right) \right]^2. \quad (3.20)$$

Polydispersity may once again be taken into account via Eqn. 3.3 provided ΔR has only weak dependence on R .

This simplistic model ignores variations in the electron density within the surface layer [87] as well as the morphology of the layer at the rods’ ends. Effects of the latter are presumed negligible, while those of the former may be accounted for to some extent by the polydispersity integrals. Qualitatively, as $\Delta\rho_2$ increases, the form factor increases at low q and decreases at high q .

3.1.4 Numerical evaluation of polydisperse form factors

The presence of several integrals means that some care must be taken when constructing an algorithm to calculate the full form factor for polydisperse systems, Eqn. 3.3. Clearly, Eqn. 3.3 must be evaluated separately for each q -value of interest. Let us denote these as q_i . An additional integral of $F_{\text{rods}}(q)$ over a narrow range of q (*e.g.* from $(q_{i-1} + q_i)/2$ to $(q_i + q_{i+1})/2$) may aid direct comparisons with experimental data, *i.e.* correcting for the detector’s acceptance. For CCD arrays this acceptance range corresponds to the scattering vectors covered by any group of pixels whose signals are averaged together.

From an arithmetical standpoint, the integrals may be performed in any order. Computationally, however, integration of smooth functions evaluated at evenly spaced points is straightforward with the family of closed Newton-Cotes forms [77, 88]. We chose to calculate the integrals over q first, then R , followed by L , because our q -ranges were small and F_{rod} tends to vary far more gradually with R than with L . The nine-point Newton-Cotes function (Eqn. 25.4.18 of Ref. [77]) was used over nine points along q , and over 33 values

each of R and L , for a total of 9801 points. Evaluating at more points did not appreciably alter results but did slow calculations considerably.

For accurate results, however, it was crucial that R and L spanned all sizes of non-negligible likelihood. Appropriate limits of integration were automatically selected by inverting the assumed lognormal distribution, Eqn. 3.4, to yield

$$L(f) = \exp \left[\mu_L - w_L^2 \pm w_L \sqrt{w_L^2 - 2\mu_L - \ln(2\pi w_L^2 f^2)} \right], \quad (3.21)$$

and solving for $L(f = 10^{-7})$. The same process was applied for R .

The final remaining integral, over $\cos \gamma$, thus required many evaluations of F_{rod} at each γ . In order to minimize the number of γ values used without sacrificing accuracy, we utilized an iterative, Romberg integration routine along with Richardson extrapolation [88] for this last calculation. Predictably, the number of Romberg iterations necessary was substantial only at $q \geq \frac{1}{R}$.

3.1.5 Direct evaluation of the form factor for böhmite in glycerol

With estimates of the average rod sizes and polydispersity as measured by TEM [14, 26] we used Eqns. 3.1, 3.3, and 3.10 to directly calculate the expected form factor for a dilute solution of böhmite rods in glycerol. Also necessary were the electron density difference, the Thomson radius (2.818×10^{-13} cm), and the concentration. Böhmite's four AlO(OH) groups in a unit cell of dimensions $2.868 \times 12.227 \times 3.700 \text{ \AA}^3$ yield 9.25×10^{23} electrons per cm^3 , making $\Delta\rho = 5.13 \times 10^{23} \text{ cm}^{-3}$ in glycerol [89]. Assuming two independent lognormal distributions for the particle sizes, the concentration corresponding to a given volume fraction, ϕ , is

$$\phi = c \langle V \rangle \quad (3.22)$$

$$= c\pi \langle R^2 \rangle \langle L \rangle \quad (3.23)$$

$$c = \frac{\phi}{\pi \langle R \rangle^2 (\sigma_R^2 + 1) \langle L \rangle}. \quad (3.24)$$

The results are shown as curve (B) in Figs. 3-1 and 3-2. While the predicted form factor agreed with measurements at intermediate q , it surprisingly underestimated the scattering at low q and overestimated it at high q , even when polydispersity was accounted for. The general agreement suggests that both the volume fraction and intensity normalization used were of the correct order of magnitude. However, the profound difference in the curves' shapes, clearly visible in Fig. 3-2, suggests that perhaps very thin rods were present in greater numbers than was evident in the TEM studies. Alternatively, a surface layer with electron density less than glycerol would make $\Delta\rho_2$ in Eqn. 3.20 negative. One possibility for the composition of such a layer would be water, which is known to adsorb strongly to

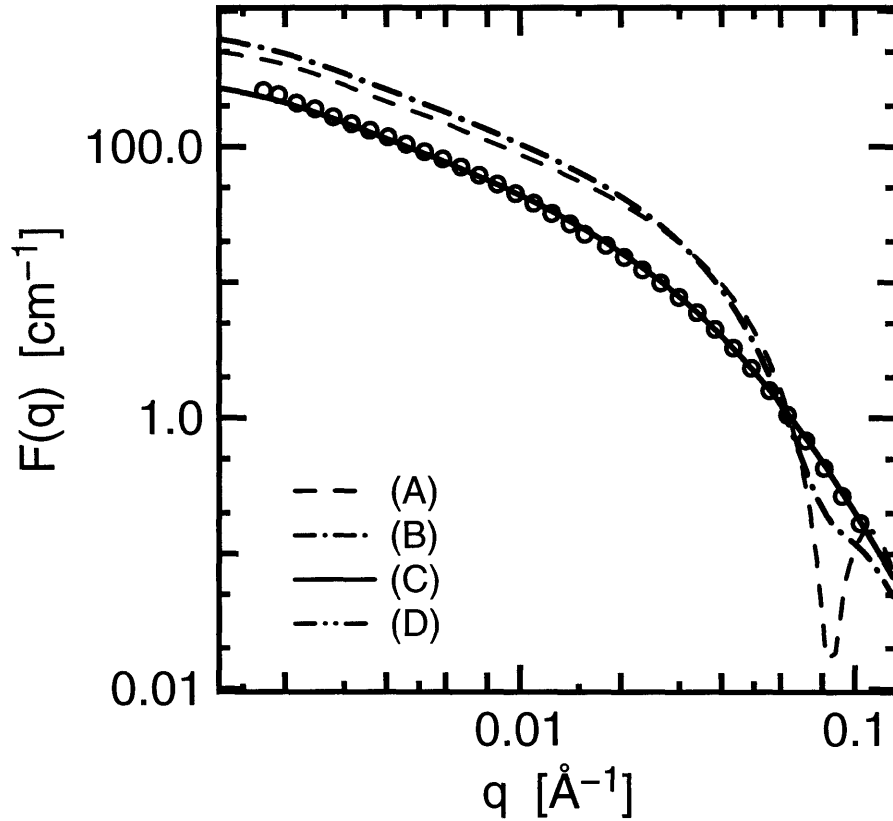


Figure 3-1: Scattering cross section for dilute ($\phi = 0.002$) suspension of böhmite in glycerol. Circles are measured results, lines are predicted or fitted form factors using parameters in Table 3.1. Curves (C) and (D) fall atop one another.

		$\langle R \rangle$ [Å]	σ_R	ΔR [Å]	$\Delta\rho_2$ [cm ⁻³]	normalization
(A)	from TEM [26]	45.6	0	—	—	1
(B)	from TEM [26]	45.6	0.20	—	—	1
(C)	fit results	18.4	0.61	—	—	0.69
(D)	fit with double layer	32.1	0.41	5.7	$-4.12 \times 10^{23*}$	0.72

*Fit did not converge to this value, but was limited by imposed constraints.

Table 3.1: Parameters used in calculating form factors shown in Figs 3-1 and 3-2. Based on Ref. [26], fixed values of $\phi = 0.002$, $\langle L \rangle = 1935$ Å, and $\sigma_L = 0.27$ were used, except for $\sigma_L = 0$ in the monodisperse curve, (A).

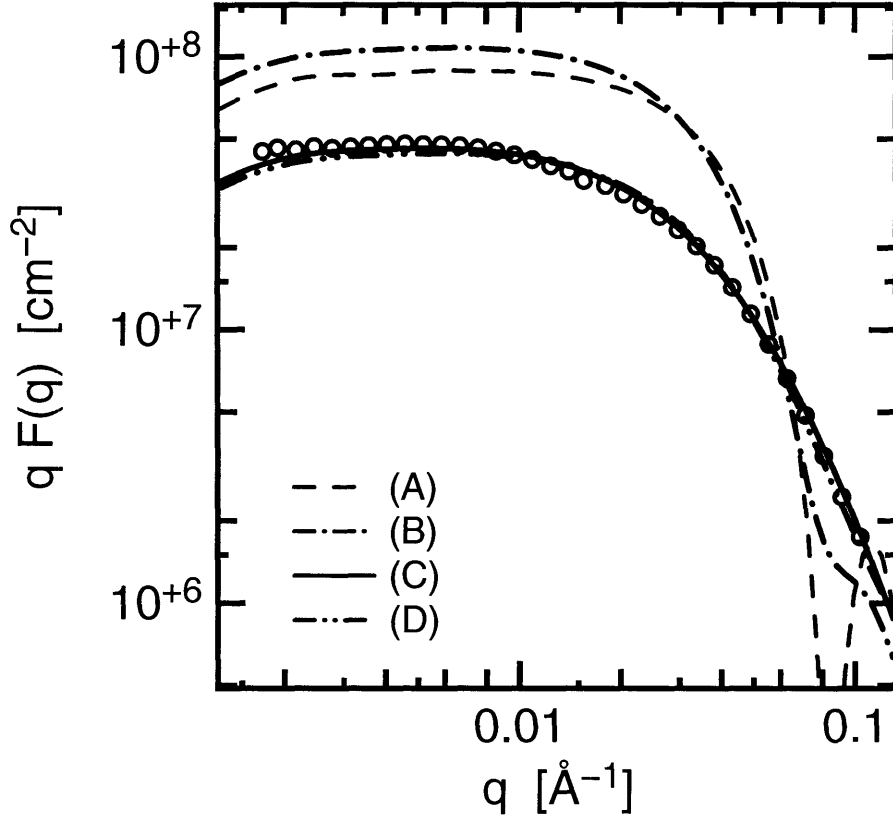


Figure 3-2: Scattering vector times cross section for data and functions in Fig. 3-1.

boehmite surfaces [12] and may not entirely have evaporated or dissolved.

3.1.6 Results of least-squares fits to the measured cross-section

Because the evaluation of $F_{\text{rods}}(q)$ for several dozen q values required only a few minutes in total, and because the choice of lognormal distributions afforded only four adjustable parameters— μ_L , w_L , μ_R , w_R , or equivalently, $\langle L \rangle$, σ_L , $\langle R \rangle$, σ_R —it was possible to perform nonlinear least-squares fits to the measured scattering cross-section of a dilute (0.2% volume fraction) böhmite-in-glycerol suspension. Most fits required one to two hours to evaluate.

To match the curve shape without constraining the overall normalization, fitted results were rescaled at each iteration by a simple average of the ratio of data points to calculated points. Since the curve shapes generally agreed well with the data, remaining deviations from unity of normalizations may be attributable to uncertainties in sample volume fractions, in absolute intensity, and especially in sample thickness, as seen in Eqns. 3.10, 3.13, and 3.19. The final normalization factors, along with the fitted parameters, are listed in Table 3.1.

Unfortunately, our measurements were not able to reach low enough q to witness the form factor “turn over,” *i.e.* displaying no dependence on q , which would enable direct measurement of F_0 as in Eqn. 3.13 and would also place strict upper bounds on the fit

parameters $\langle L \rangle$ and σ_L . Consequently, when those two parameters were allowed to freely vary, they perpetually increased and fitting did not converge. One way to understand this is by substituting Eqn. 3.23 into Eqn. 3.13,

$$F_{\text{rods}} \left(q \ll \frac{2}{\langle L \rangle} \right) = r_e^2 (\Delta\rho)^2 \phi \pi \langle R \rangle^2 (\sigma_R^2 + 1)^5 \langle L \rangle (\sigma_L^2 + 1). \quad (3.25)$$

This shows a linear dependence on rod length at low scattering vectors. Conversely, when substituting Eqn. 3.23 into Eqn. 3.19, we see that

$$F_{\text{rods}} \left(\frac{2}{\langle L \rangle} \ll q \ll \frac{1}{\langle R \rangle} \right) = \frac{\pi}{q} r_e^2 (\Delta\rho)^2 \phi \pi \langle R \rangle^2 (\sigma_R^2 + 1)^5 \quad (3.26)$$

is independent of the rod length. Fig. 3-2 clearly shows our measurements were in this second regime and above. We verified that for $q \gtrsim 0.004 \text{ \AA}^{-1}$ the form factor was insensitive to the specific values of $\langle L \rangle$ and σ_L and we subsequently used the TEM-measured values. The slight slope seen at the lowest q values in curves in Fig. 3-2, as contrasted to the constancy of the measured qF , suggests that perhaps a population of rods longer than the TEM-measured values was present in the sample. However, background noise issues in that range make this impossible to establish with certainty.

Fitting yielded unexpected results for the average radius and radial polydispersity as well. The fitted average radius was clearly less than the TEM-measured value, and accounting for a possible surface layer was not sufficient to restore agreement between the two. The relatively large fitted polydispersity indicates that a significant fraction of the rods ($\gtrsim 15\%$) had radii within the range of 30–70 \AA seen in TEM studies [26], but that the majority of the population was in fact narrower, between 10–30 \AA . One possibility, that the rods had a non-circular cross-section is not readily testable by small-angle X-ray scattering under conditions of significant polydispersity. However, one indication of such a shape would be the divergence of the fits to zero radius and infinite polydispersity, since that would yield a near-constant size distribution over a wide range of sizes. This was not seen in our studies.

If a surface layer was present, it was clearly of a lower electron density than glycerol's $4.12 \times 10^{23} \text{ cm}^{-3}$. Fixing the relative density to a rough estimate for water in glycerol, $\Delta\rho_2 = -7.8 \times 10^{22} \text{ cm}^{-3}$ (not listed in Table 3.1), resulted in the fit diverging to $\Delta R = 0$. When the relative density was allowed to vary, it diverged toward unphysical values of $\Delta\rho_2 < -4.12 \times 10^{23}$, corresponding to a negative absolute electron density. A more detailed model of the electron density might very well converge on a single solution for the layer size and density, but such a function would entail the use of one additional integral, over ΔR , and one or more additional adjustable parameters, thereby requiring substantially more computing time than the present model.

The main conclusion to be reached from this small-angle scattering study of dilute suspensions is that the average rod diameter was likely overestimated by TEM studies by

as much as a factor of 3. It follows from Eqn. 1.26 that our estimate in Sec. 1.3 of the transition concentration was too high by the same factor. This, in addition to charge effects and polydispersity, may underlie the relatively low volume fractions at which ordering transitions were seen to occur. Consequently, we will adopt an undetermined R_{eff} in the rest of this thesis.

3.2 Structure factor in the isotropic phase

3.2.1 Identifying the interparticle structure factor in X-ray scattering

3.2.1.1 Removing the effects of intraparticle scattering

When particles are packed closely enough that scattering from two separate particles may exhibit interference effects, interparticle scattering may be isolated if the intraparticle scattering factor of each particle is known *a priori*. The measured intensity of uniform-density particles [48, 63, 90] will be the generalization of Eqn. 2.1,

$$I(\mathbf{q}) \propto \sum_{m,n} \int_{\text{particle } n} d\mathbf{r}_n \int_{\text{particle } m} d\mathbf{r}_m e^{-i\mathbf{q}\cdot[(\mathbf{R}_m+\mathbf{r}_m)-(\mathbf{R}_n+\mathbf{r}_n)]} \quad (3.27)$$

$$\propto \sum_{m=n} \left| \int d\mathbf{r}_m e^{-i\mathbf{q}\cdot\mathbf{r}_m} \right|^2 + \sum_{m \neq n} e^{-i\mathbf{q}\cdot(\mathbf{R}_m-\mathbf{R}_n)} \int d\mathbf{r}_n e^{i\mathbf{q}\cdot\mathbf{r}_n} \int d\mathbf{r}_m e^{-i\mathbf{q}\cdot\mathbf{r}_m}. \quad (3.28)$$

\mathbf{R}_m denotes the center-of-mass location of particle m . The first term above is identifiable as the form factor of the system, meaning that Eqn. 3.28 may be rewritten as

$$I(\mathbf{q}) = F(\mathbf{q}) S(\mathbf{q}). \quad (3.29)$$

It is important to recall that in this notation, $F(\mathbf{q})$ represents the superposition of all single-particle form factors. It contains the normalization constant as in Eqn. 3.10 and thus is proportional to concentration. $S(\mathbf{q})$ is the interparticle structure factor,

$$S(\mathbf{q}) \equiv 1 + \frac{r_e^2 (\Delta\rho)^2}{F(\mathbf{q})} \sum_{m \neq n} e^{-i\mathbf{q}\cdot\mathbf{R}_{mn}} \int d\mathbf{r}_n e^{i\mathbf{q}\cdot\mathbf{r}_n} \int d\mathbf{r}_m e^{-i\mathbf{q}\cdot\mathbf{r}_m}, \quad (3.30)$$

and $\mathbf{R}_{mn} \equiv \mathbf{R}_m - \mathbf{R}_n$. Eqn. 3.29 shows that the structure factor can be extracted from the measured scattering by simply dividing out the form factor.

3.2.1.2 Relation between the structure factor and pair correlation function

In the special case where all particles possess identical form factors—for example, suspensions of spherical particles, or suspensions of perfectly aligned nonspherical particles—the pair of integrals above reduces to the form factor, and an integral involving the two-particle

correlation function,

$$g_{12}(\mathbf{R}_{12}) \equiv \frac{f(\mathbf{R}_{12})}{f(\mathbf{R}_1)f(\mathbf{R}_2)}, \quad (3.31)$$

may be substituted for the sum over particles. Here \mathbf{R}_{12} is the interparticle separation and $f(\mathbf{R}_1)$ is the probability of a rod's center of mass being located at \mathbf{R}_1 . We assume a lack of any external potential, and hence no explicit dependence on the value of \mathbf{R}_1 . In this case, then, Eqn. 3.30 reduces to [48, 91]

$$S(\mathbf{q}) = 1 + \frac{1}{V} \int d\mathbf{R}_{12} [g_{12}(\mathbf{R}_{12}) - 1] e^{-i\mathbf{q}\cdot\mathbf{R}_{12}}, \quad (3.32)$$

which does not depend on the form factor. Here V is the entire illuminated sample volume. This expression connects a measurable quantity, the structure factor, to a quantity accessible by theory, the correlation function. Incidentally, if a positional isotropy exists, *i.e.* if $g_{12}(\mathbf{R}_{12})$ is independent of the direction of \mathbf{R}_{12} , then $S(\mathbf{q})$ is independent of the direction of \mathbf{q} .

A similar argument may be made regarding the structure factor's independence from the form factor in orientationally isotropic suspensions of rigid, cylindrical particles. Specifically, we refer to instances where the rods' relative orientations are completely independent of their center-to-center separation. As discussed in Sec. 2.1.1, the term

$$\int d\mathbf{r}_m e^{-i\mathbf{q}\cdot\mathbf{r}_m} = \pi R^2 L \frac{\sin(q\frac{L}{2} \cos \gamma_m)}{q\frac{L}{2} \cos \gamma_m} \frac{2J_1(qR \sin \gamma_m)}{qR \sin \gamma_m} \quad (3.33)$$

will be nonzero at $q\frac{L}{2} \gg 1$ only when γ_m , the angle between particle m and \mathbf{q} , is very near $\pi/2$. Eqn. 3.30 thus implies that deviations of the interparticle structure factor from unity arise exclusively from pairs of rods with $\gamma_m \approx \gamma_n \approx \pi/2$, even if the suspension contains rods of all possible orientations. This is not a strict requirement that the rods be parallel but only that both are oriented perpendicular to \mathbf{q} . At the other extreme, when $q\frac{L}{2} \ll 1$, Eqn. 3.33 becomes independent of γ_m . In both limits, then, $\int d\mathbf{r}_n \exp(i\mathbf{q}\cdot\mathbf{r}_n) \int d\mathbf{r}_m \exp(-i\mathbf{q}\cdot\mathbf{r}_m) = F(\mathbf{q})$ and Eqn. 3.32 is again applicable.

A main assumption underlying the previous paragraph is that all rod orientations are completely uncorrelated with the center-to-center separations between neighbors, in other words that the integral over \mathbf{r}_m has no dependence on \mathbf{R}_{12} [91]. This assumption clearly breaks down as concentration increases; indeed, such correlations are the very mechanism by which the transition to the nematic phase in lyotropic liquid crystals is understood. A commonly used model that overcomes this limitation is one where any subregion of the suspension below a certain correlation length exhibits complete orientational ordering [63]. In this "clustering" picture, structure factor peaks that correspond to length scales comparable to the nearest-neighbor separation arise naturally from Eqn. 3.32, while the scattering's azimuthal dependence (or lack thereof) results from macroscopic averaging over many of

these tiny domains of perfect alignment.

3.2.1.3 Accounting for polydispersity

Polydispersity complicates the expression for the structure factor, but not overly so. Provided the interparticle separations are in no way coupled to particle sizes, for rigid rods Eqn. 3.32 becomes

$$S(\mathbf{q}) = 1 + A_S(\mathbf{q}) \frac{1}{V} \int d\mathbf{R}_{12} [g_{12}(\mathbf{R}_{12}) - 1] e^{-i\mathbf{q}\cdot\mathbf{R}_{12}}, \quad (3.34)$$

where

$$A_S(\mathbf{q}) \equiv \frac{\left(\int_0^\infty dL f(L) \int_0^\infty dR f(R) \int_0^1 d(\cos \gamma) \pi R^2 L \frac{\sin\left(\frac{qL}{2} \cos \gamma\right)}{\frac{qL}{2} \cos \gamma} \frac{2J_1(qR \sin \gamma)}{qR \sin \gamma} \right)^2}{\int_0^\infty dL f(L) \int_0^\infty dR f(R) \int_0^1 d(\cos \gamma) \left(\pi R^2 L \frac{\sin\left(\frac{qL}{2} \cos \gamma\right)}{\frac{qL}{2} \cos \gamma} \frac{2J_1(qR \sin \gamma)}{qR \sin \gamma} \right)^2}. \quad (3.35)$$

As one might intuitively expect, this has the effect of “smearing out” the structure factor, drawing it closer to unity than in the monodisperse case. For example, the low- \mathbf{q} limit is

$$A_S\left(q \ll \frac{2}{L}\right) = \frac{\langle R^2 L \rangle^2}{\langle R^4 L^2 \rangle} \quad (3.36)$$

Given independent lognormal distributions in length and radius (Eqns. 3.4–3.7) the “contrast” in S is thus reduced at low \mathbf{q} by an amount,

$$\frac{\langle R^2 L \rangle^2}{\langle R^4 L^2 \rangle} = \frac{1}{(\sigma_R^2 + 1)^4 (\sigma_L^2 + 1)}. \quad (3.37)$$

It should be noted that Eqn. 3.34 is approximate at best when dealing with any non-dilute system. As with the inescapable dependence of the separation of two rods on their relative orientation, in any real suspension the range of rods’ hard-core repulsions will depend explicitly on the particle dimensions. This may hold true for electrostatic interactions as well. Therefore Eqn. 3.34’s requirement that interparticle separation is completely independent of size is never exactly met. Nonetheless, we may argue that since $A_S(\mathbf{q})$ will not depend strongly on \mathbf{q} for $qR \lesssim 1$, polydispersity would not be expected to significantly modify the structure factor in our experiments.

3.2.2 Structure factors of isotropic suspensions of böhmite in glycerol

Measured scattering intensities at several isotropic volume fractions are shown in Fig. 3-3. A clear peak developed at 0.5% volume fraction and above. The intensities were divided by the form factor determined in Sec. 3.1.6 (specifically, the parameters in Table 3.1, row (C)), to produce the interparticle structure factors shown in Fig. 3-4. For each sample, the

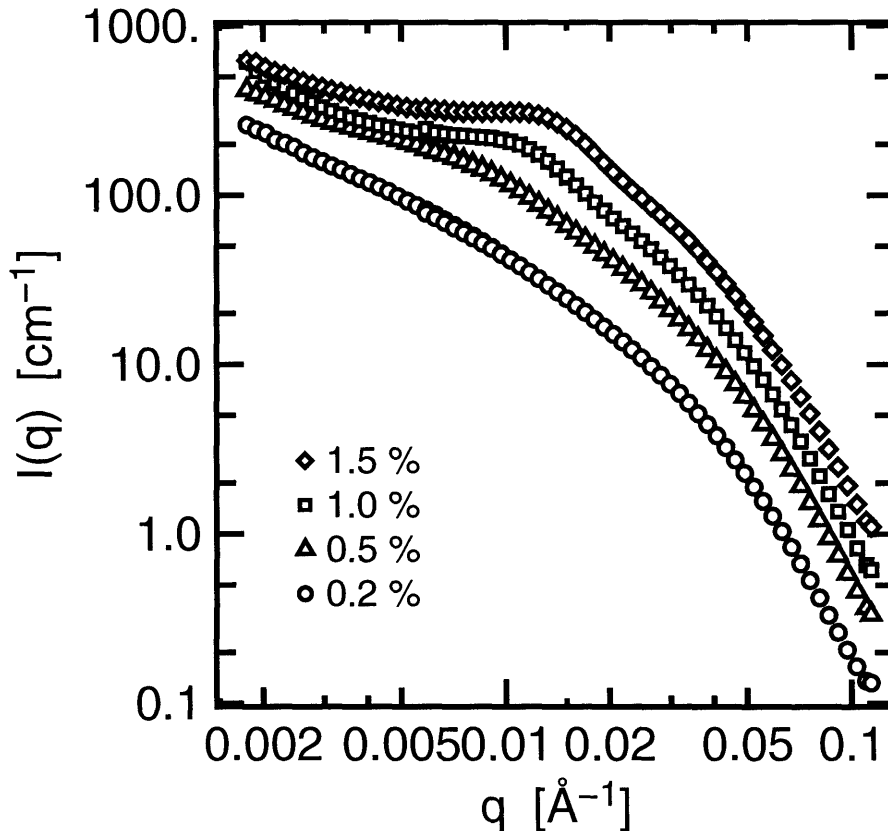


Figure 3-3: Measured scattering cross-section of isotropic suspensions of bohmite in glycerol. The 0.2% results were used in Sec. 3.1.6 to determine the form factor.

form factor was scaled by the appropriate volume fraction. As expected for isotropic suspensions, and as displayed in the lowest curve in Fig. 2-3, there was no significant azimuthal dependence to the scattering, implying complete positional and orientational isotropy. The displayed structure factors have therefore been averaged over all azimuthal angles. The apparent minimum in $S(q)$ around $q = 0.003 \text{ \AA}^{-1}$ may indicate an underestimation of the form factor at $q < 0.003 \text{ \AA}^{-1}$, as discussed in Sec. 3.1.6, or may result from background scattering at $q < 0.003 \text{ \AA}^{-1}$ due to the apparatus.

The structure factor of rodlike particles in isotropic suspensions has been extensively studied theoretically [92–97], numerically [36,98], by Monte Carlo simulations [93,96,99,100], and experimentally [100–104], although we are aware of no prior X-ray or neutron structure factor measurements specifically on böhmite rods. In spite of this body of work, no existing theoretical function satisfactorily reproduces, on length scales comparable to the nearest-neighbor distance, the structure factors measured and simulated for semidilute, isotropic suspensions of long rods with nonzero radius. Recent theoretical work treating many-body [82] and polydispersity effects [32,44–46] has thusfar detailed either general phase behavior or the structure factor only at $qR \ll 1$.

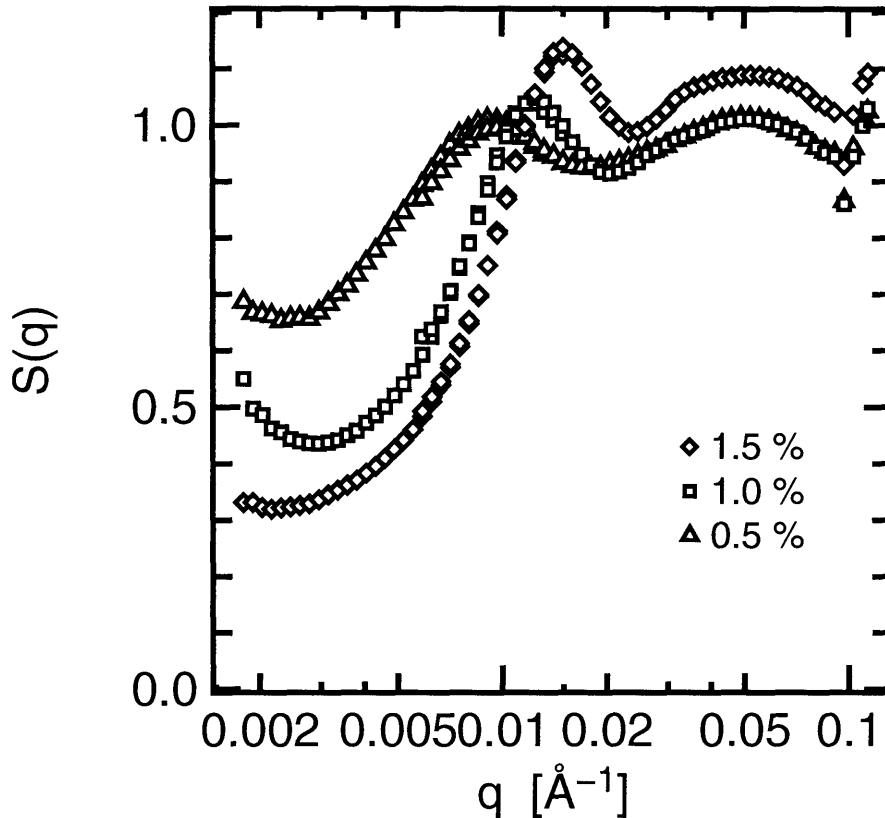


Figure 3-4: Measured interparticle structure factor of isotropic suspensions of böhmite in glycerol.

The positional ordering in these suspensions is expected to be liquidlike, so in lieu of a specific functional form for the structure factor, it is common in the literature to simply chart the concentration dependence of q_{peak} , the scattering vector of the main peak in the isotropic structure factor (see [101] and references therein). Below the overlap concentration, $c^* = L^{-3}$, the particles' cylindrical shape has little effect on interparticle interactions, and q_{peak} is expected to mimic that for charged spheres, $q_{\text{peak}} \propto \left(\frac{c}{c^*}\right)^{\frac{1}{3}} \propto \phi^{\frac{1}{3}}$. In the semidilute regime, where $c > c^*$, the peak is known to vary as $q_{\text{peak}} \propto \left(\frac{c}{c^*}\right)^{\frac{1}{2}} \propto \phi^{\frac{1}{2}}$ as packing entropy outweighs interparticle interactions. For both TMV and fd-virus, the semidilute proportionality coefficient has been found to be approximately 7.0. the coefficient is easily raised by even low concentrations of impurity ions (salts), as demonstrated in Ref. [101]. This effect arises from the excess charge's tendency to screen long-range rod-rod interactions and allow the rodlike particles to sit closer to one another than in a salt-free solution.

In Fig. 3-5 we display the measured structure factor peak locations for isotropic böhmite in glycerol. Precise determinations of q_{peak} were carried out by fitting the ten data points nearest the peak to a fourth-order polynomial and then solving the cubic equation for the fitted curve's analytic derivative to find the position of the maximum.

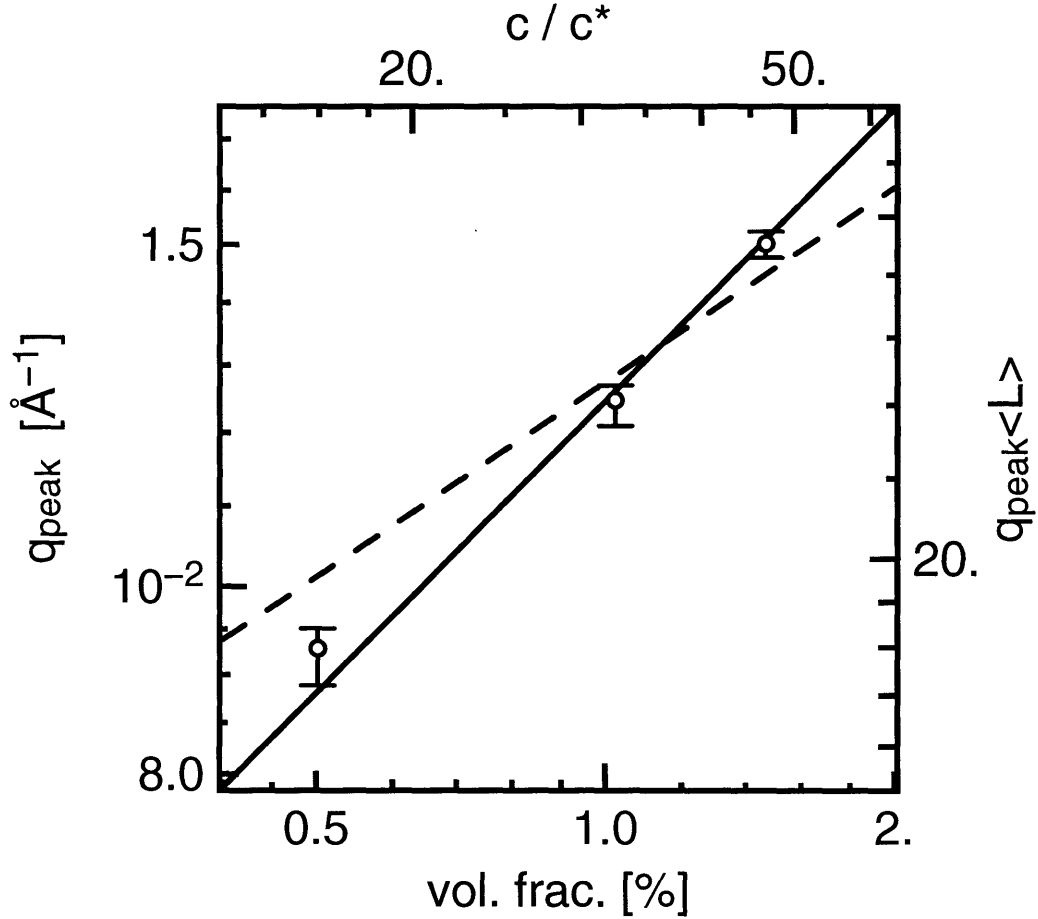


Figure 3-5: Interparticle structure factor peak position vs. volume fraction for isotropic samples. Lines are best-fits to $q_{\text{peak}} \propto \phi^{\frac{1}{2}}$ (solid) and, for comparison, $q_{\text{peak}} \propto \phi^{\frac{1}{3}}$ (dashed). Rod size parameters were taken from Table 3.1(C).

All of our samples were well into the semidilute regime, and, as expected, the peak position was well described by volume fraction to the one-half power. Taking into account lognormal polydispersity, the relation between c/c^* and ϕ is

$$\frac{c}{c^*} = \phi \frac{\langle L^3 \rangle}{\pi \langle R^2 \rangle \langle L \rangle} = \phi \frac{\langle L \rangle^2 (\sigma_L^2 + 1)^3}{\pi \langle R \rangle^2 (\sigma_R^2 + 1)}. \quad (3.38)$$

Therefore the proportionality coefficient,

$$q_{\text{peak}} \langle L \rangle \left(\frac{c}{c^*} \right)^{-\frac{1}{2}} = \frac{q_{\text{peak}} \langle R \rangle}{\sqrt{\phi}} \sqrt{\frac{\pi (\sigma_R^2 + 1)}{(\sigma_L^2 + 1)^3}}, \quad (3.39)$$

does not depend on length for a given volume fraction. For the parameters in Table 3.1 (B), (C), and (D), our best-fit coefficients were 9.24, 4.28, and 6.88, respectively. These are all

close to the value of 7.0 found for other charged, rodlike molecules, with the best agreement afforded by our model (D) of a cylinder with a thin surface layer of low electron density.

3.3 Structure factors in the orientationally ordered phase of böhmite in glycerol

3.3.1 Relating the nematic form factor to the isotropic form factor

The radial dependence of the scattering at $q\frac{L}{2} \gg 1$ is expected to be insensitive to the orientational distribution function. To see this, we recall from Sec. 3.2.1.2 that the interparticle structure factor is determined entirely by those pairs of rods whose orientation vectors both lie in the plane perpendicular to \mathbf{q} . Similarly, the form factor arises from individual rods that are perpendicular to \mathbf{q} . So as the scattering vector magnitude, q , is varied along a fixed azimuthal direction, only a particular subset of rods in the sample contributes at all to the scattering. Neither Eqn. 3.1 nor Eqn. 3.33 contains any term involving in-plane directions. Therefore, the relevant rods may be perfectly aligned with one another, or evenly distributed among all orientations within the plane, or in any other configuration that happens to be perpendicular to the azimuthal direction in question, with no effect whatsoever on the q -dependence of the scattering.

As a result, we expect the radial and azimuthal dependences of the form factor to be separable.

$$F_{\text{nematic}}(\mathbf{q}) = F_{\text{isotropic}}(q) F_{\text{nematic}}(\varphi), \quad (3.40)$$

where $F_{\text{nematic}}(\varphi)$ is given as $I(\varphi)$ in Eqn. 2.8. With experimental data, it is convenient to look at an “effective structure factor” given by

$$S_{\text{eff}}(\mathbf{q}) = \frac{I(\mathbf{q})}{F_{\text{isotropic}}(q)} \quad (3.41)$$

$$= F_{\text{nematic}}(\varphi) S(\mathbf{q}) \quad (3.42)$$

$$= F_{\text{nematic}}(\varphi) + \frac{r_e^2 (\Delta\rho)^2}{F_{\text{isotropic}}(q)} \sum_{m \neq n} e^{-i\mathbf{q} \cdot \mathbf{R}_{mn}} \int d\mathbf{r}_n e^{i\mathbf{q} \cdot \mathbf{r}_n} \int d\mathbf{r}_m e^{-i\mathbf{q} \cdot \mathbf{r}_m}, \quad (3.43)$$

in the vein of Eqn. 3.30. $S_{\text{eff}}(\mathbf{q})$ has the same radial dependence as $S(\mathbf{q})$, but approaches $F_{\text{nematic}}(\varphi)$ rather than unity at $qR \gg 1$.

Representative results of $S_{\text{eff}}(q, \varphi)$ measurements for orientationally ordered suspensions of böhmite in glycerol are plotted against q in Fig. 3-6 and against φ in Figs. 2-3 and 2-5. In all samples, the radial shape of the effective structure factor bore a strong qualitative resemblance to the structure factor seen in isotropic samples (Fig. 3-4), indicating that liquidlike ordering of the particle positions persisted even as the orientational distribution function underwent significant changes.

Our studies of $F_{\text{nematic}}(\varphi)$ in the previous chapter indicated that three phases coexisted

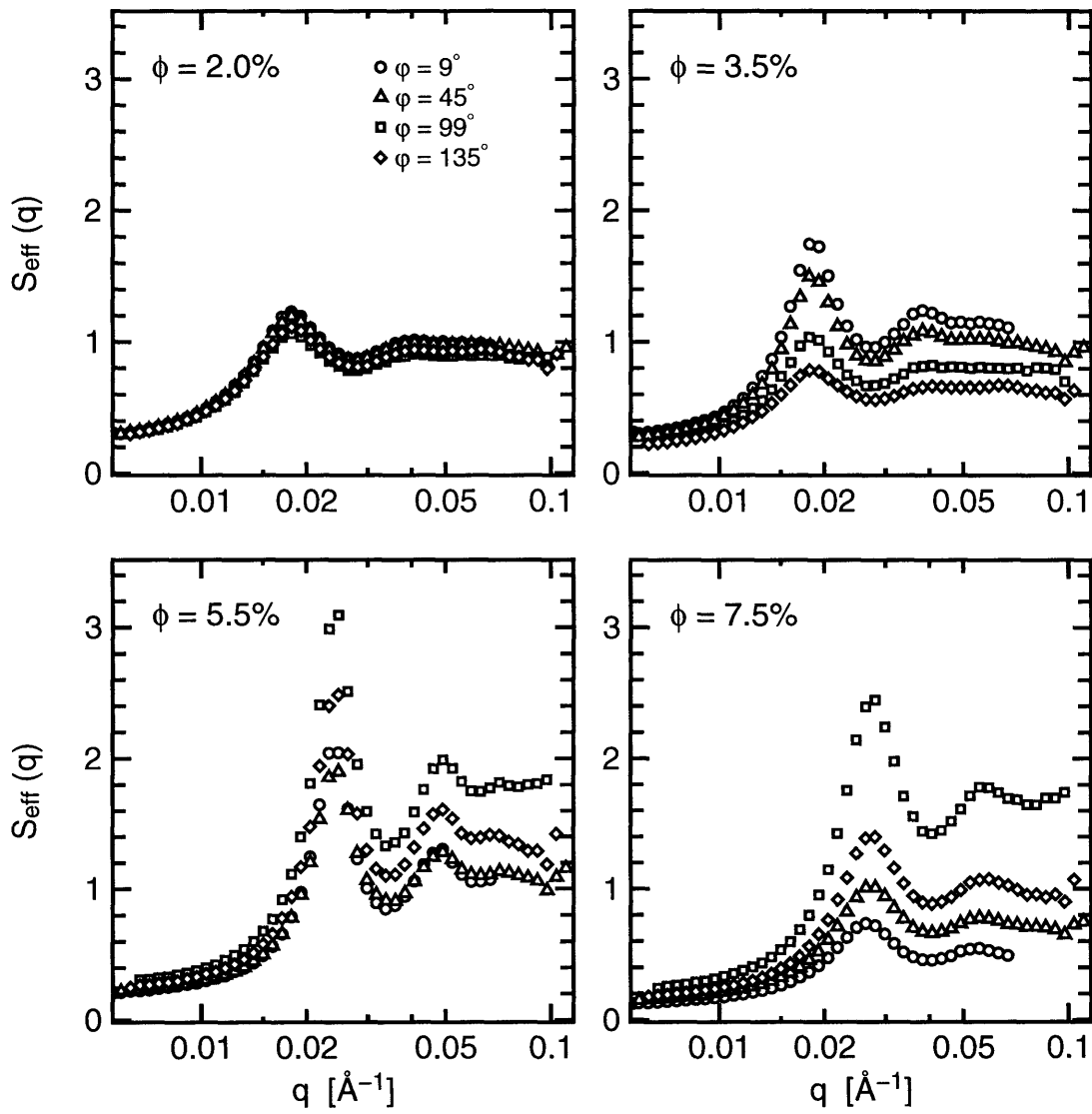


Figure 3-6: Measured effective interparticle structure factor as defined in Eqn. 3.41, plotted at several azimuthal angles for each of four böhmite-in-glycerol samples.

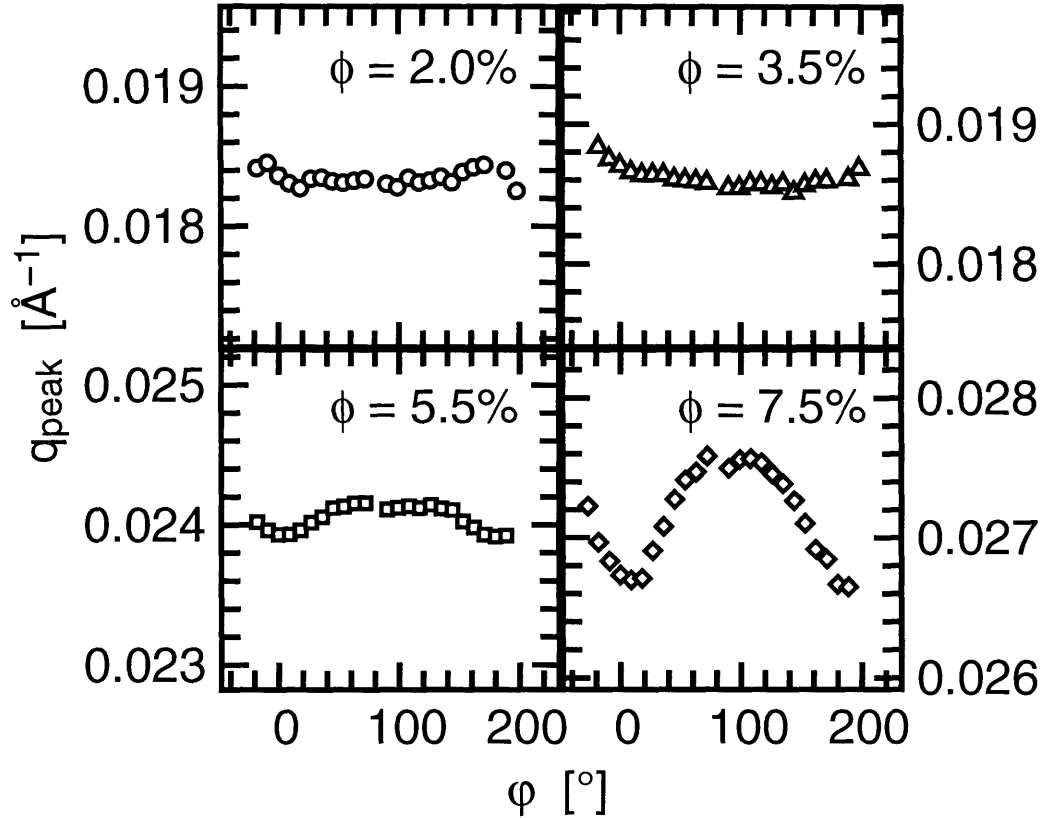


Figure 3-7: Azimuthal dependence of radial peak position for the effective structure factors plotted in Fig. 3-6.

in each sample: two nematic and one isotropic. Analogous to Eqn. 2.57, we could extend the second term of Eqn. 3.43 to be the incoherent superposition of three distinct interparticle interference functions, one for each phase. Unlike the azimuthal profile, however, in the radial case we have no ready functional form for the effective structure factor of any of the three domains. We therefore use indirect measures to infer characteristics of each domain. Specifically, in a lyotropic system, the nematic phase(s) would be expected to possess a higher local concentration of rods than the isotropic phase. Therefore, the structure factor peaks would appear at different q . Similarly, with three discrete densities present in the system, we would expect three discrete center-to-center correlation lengths, which would contribute to each structure factor peak's width.

3.3.2 Peak position and width versus azimuthal angle

None of the curves in Fig. 3-6 displayed easily resolvable sets of three primary peaks. With liquidlike positional ordering, correlation lengths on the order of the nearest neighbor separation are to be expected, resulting in relatively broad structure factor peaks that obscure one another. Nevertheless, each azimuthal angle should receive a unique combination of

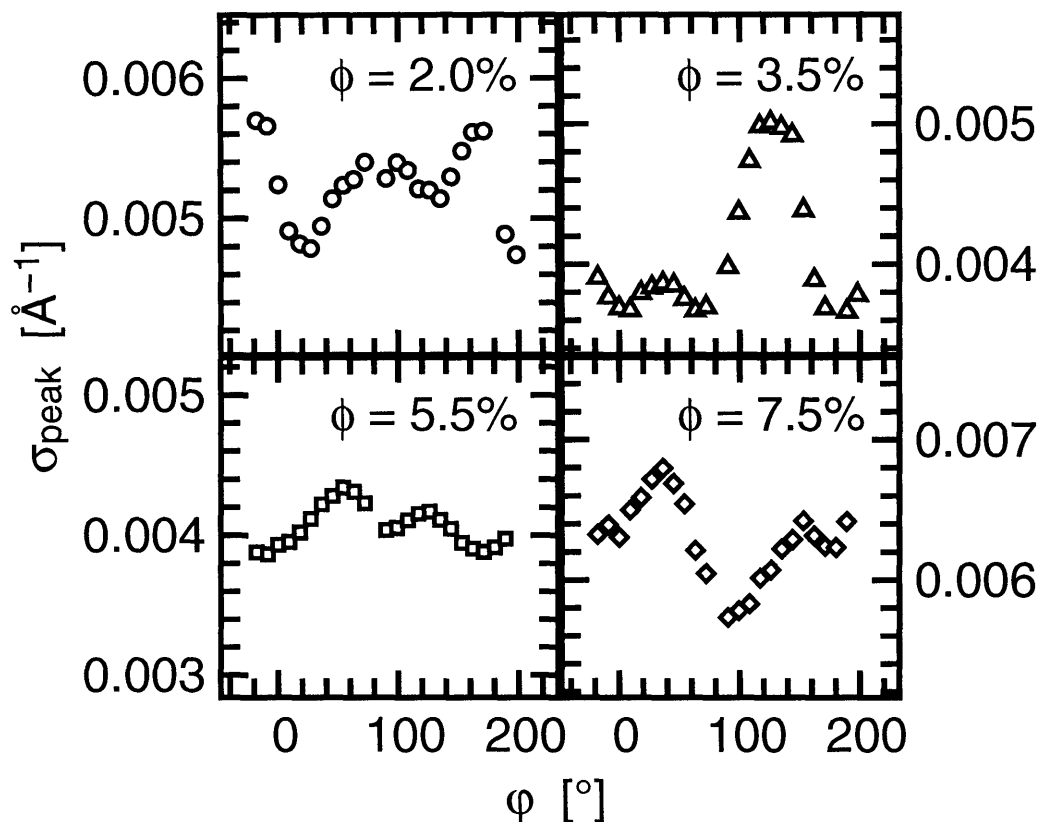


Figure 3-8: Azimuthal dependence of radial peak half-width for the effective structure factors plotted in Fig. 3-6.

scattering from the three domains, owing to the disparate orientations of the two nematic domains, as discussed in Sec. 2.3.2. This would give rise to an azimuthal dependence in the radial peak position. If one nematic domain has a higher density than the others, the effective structure factor peak should occur at greater q perpendicular to that domain's director.

We observed precisely this effect in our böhmite in glycerol samples, as shown in Fig. 3-7. Comparing the 7.5% data in Fig. 3-7 to Fig. 2-3, q_{peak} displayed a maximum at azimuthal angles corresponding to the azimuthal maximum in intensity. Despite significant orientational ordering, the location of the main peak in the effective structure factor indeed showed only weak dependence on azimuthal angle, φ , and only at higher volume fractions. Such small variation justifies the azimuthal-radial separability assumption mentioned in Sec. 2.1.3, which was a cornerstone of the method used in the previous chapter to determine the orientational order parameters, and also justifies the related assumption in Sec. 3.3.1. The near-complete lack of any variation at lower volume fractions was unsurprising, given that just above the ordering transition, isotropically distributed rods far outnumbered aligned rods (see Fig. 2-10).

It is tempting to consider using the azimuthal extrema of $2\pi/q_{\text{peak}}$ as estimates of the rod densities in the nematic and isotropic phases. With these samples, however, that proved impossible since the composite structure factor peak widths were at least a factor of five wider in q than the variation in q_{peak} , leading to near-complete overlap. This can be seen in Fig. 3-8. The peak width was estimated using

$$\sigma_{\text{peak}} = \sqrt{-\frac{S_{\text{eff}}}{\frac{\partial^2 S_{\text{eff}}}{\partial q^2}}}\bigg|_{q_{\text{peak}}}, \quad (3.44)$$

which gives approximately the half-width at half-height of gaussian, parabolic, *etc.* curves. Rather than derivatives based on the raw data, analytic derivatives were taken of the fitted polynomials from the q_{peak} determination outlined in Sec. 3.2.2.

While the positions of effective structure factor peaks followed the azimuthal dependence of intensity, the peak widths in Fig. 3-8 tended to track its inverse, and markedly so at all volume fractions for which orientational ordering was present. Isotropic samples (not shown) possessed no evident dependence of peak width on azimuthal angle. This behavior, too, may be understood in the context of scattering contributions from coexisting isotropic and nematic phases. At strong maxima in the azimuthal intensity profile, scattering came predominantly from one nematic domain; if that domain possessed the greatest correlation length, the relative peak width would display an azimuthal minimum in the same direction.

3.3.3 Peak position and width versus volume fraction

Since the location of the effective structure factor peak varied weakly, if at all, with azimuthal angle, trends in q_{peak} with volume fraction were clearly discernible. This is shown in Fig. 3-9, including the isotropic results previously plotted in Fig. 3-5. Although the predictions of $q_{\text{peak}} \propto \phi^{\frac{1}{2}}$ discussed in Sec. 3.2.2 do not strictly pertain to the nematic phase, it is reasonable to expect them to hold, so long as no significant positional ordering occurs at the isotropic-nematic boundary. Fig. 3-9 indicates a $\phi^{\frac{1}{2}}$ dependence in the nematic phase, but only at volume fractions well past the transition. The onset of nematic ordering at 2% volume fraction evidently led to a stagnation of the structure factor peak position up to approximately 3.5%.

A similar $\phi^{\frac{1}{2}}$ dependence has been predicted and observed [102,103] for the half-width, σ_{peak} , of the primary structure factor peak above the overlap concentration in isotropic systems of charged rods. As before, it would seem reasonable for this behavior to extend through and beyond the orientational ordering transition. Our results for the average peak width as a function of volume fraction are displayed in Fig. 3-10. Surprisingly, below the transition, σ_{peak} appeared constant, while above the transition it agreed well with a $\phi^{\frac{1}{2}}$ fit. The sudden decrease in σ_{peak} very near the transition concentration implied nearly a factor of three increase in the correlation length at the nematic transition.

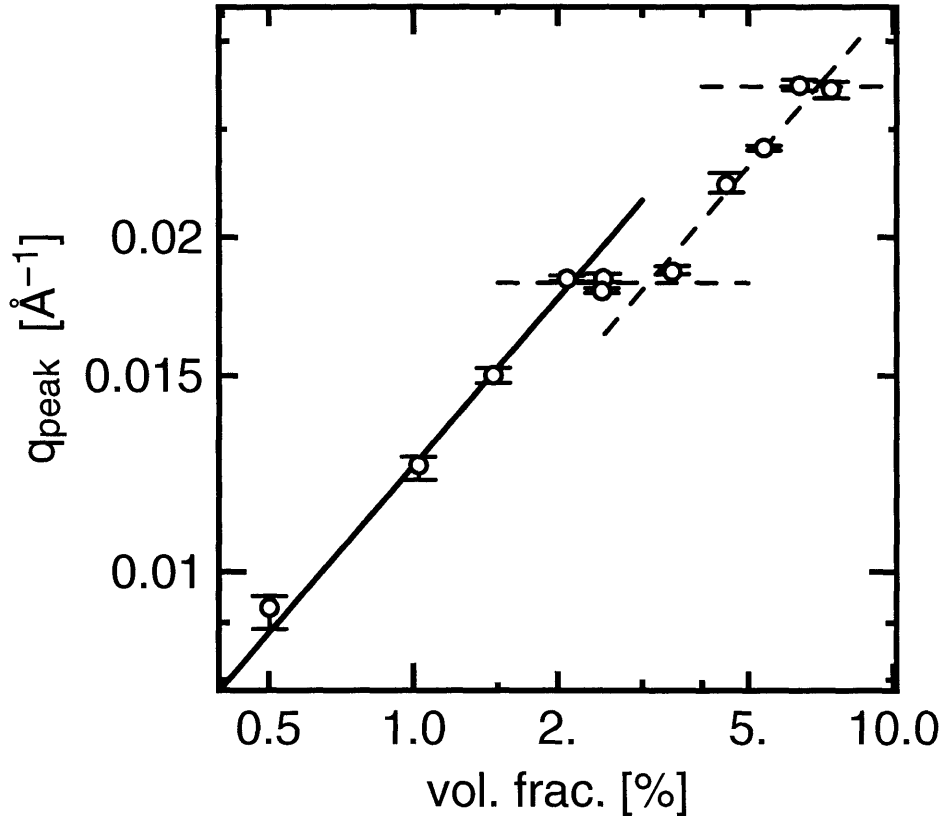


Figure 3-9: Azimuthal average of effective structure factor peak position vs. volume fraction for nematic samples. Isotropic data from Fig. 3-5 are included as well. Sloped lines represent $q_{\text{peak}} \propto \phi^{\frac{1}{2}}$. Dashed lines are guides to the eye. Error bars cover the full azimuthal variation of q_{peak} .

The concurrence of anomalous behavior in both q_{peak} and σ_{peak} seems to indicate that a positional restructuring did in fact occur while the orientational distribution function developed anisotropy.

3.3.4 Separating the structure factors of three domains

Perhaps the unexpected trends in the composite effective structure factor near the orientational transition were merely an artifact caused by the subtle interplay of the three constituent phases' structure factors as their relative proportions varied. If the three structure factors could be separated from one another, their individual q_{peak} and σ_{peak} dependences on volume fraction might appear better behaved than the total.

To test this hypothesis, we used as a crude approximation to the structure factor the results of fits to Eqn. 2.57, specifically the q -dependences of three of the seven parameters, $\nu_I I_I$, $\nu_{N_I} \langle I_{N_I} \rangle_\varphi$, and $\nu_{N_{II}} \langle I_{N_{II}} \rangle_\varphi$. We performed azimuthal fits to the quantity $S_{\text{eff}}(\mathbf{q})$ rather than the raw intensity. Separate fits were performed at each q value. Since the proportions

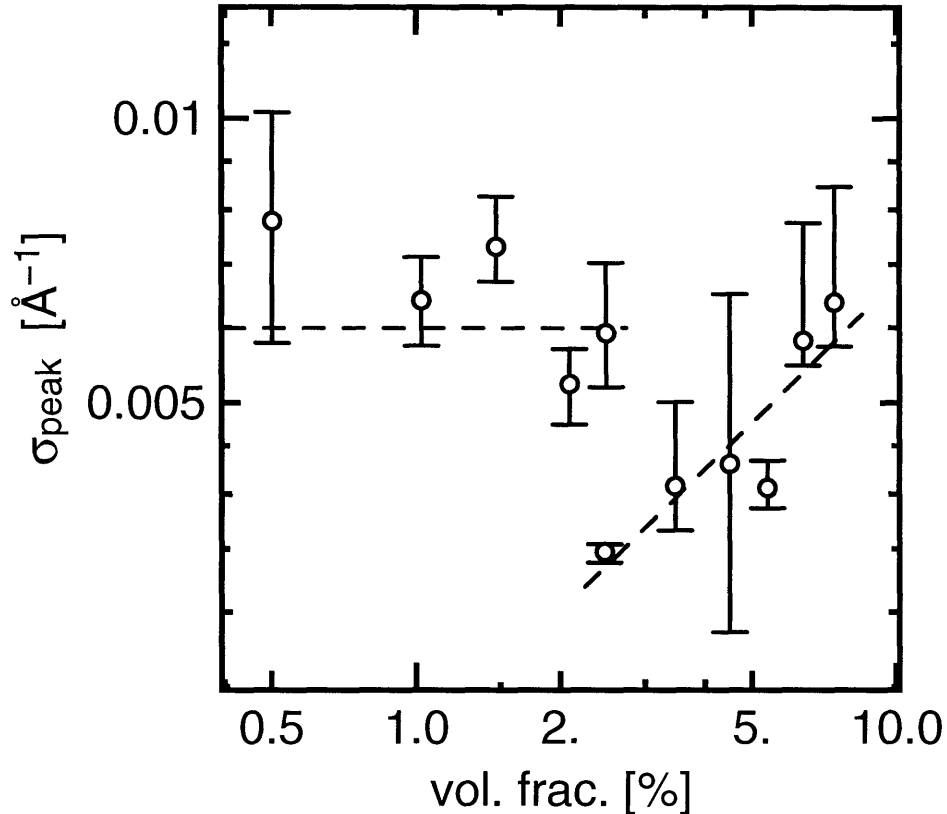


Figure 3-10: Azimuthal average of main peak width for structure factors in Figs. 3-4 and 3-6. Dashed lines are guides to the eye, one a constant value and the other displaying a $\phi^{\frac{1}{2}}$ dependence. Error bars cover the full azimuthal variation of σ_{peak} .

of the three phases, ν_I , ν_{N_I} , and $\nu_{N_{II}}$, do not depend on q , the fitted parameters reflect a quantity proportional to $S_{\text{eff}}(q)$. To improve fitting in cases where one nematic domain largely obscured the scattering from the other, we fixed the order parameter for the lesser domain to the average value for all samples. Specifically, we set $m^{(I)} = 1.82$ ($\langle P_2^{(I)} \rangle = 0.27$) for volume fractions $\leq 2.5\%$ and $m^{(II)} = 3.16$ ($\langle P_2^{(II)} \rangle = 0.46$) for volume fractions $\geq 5.5\%$. Typical results are plotted in Fig. 3-11.

Although the curves exhibited substantial noise, it was possible to use the methods discussed in Secs. 3.2.2 and 3.3.2 to extract an estimate of q_{peak} and σ_{peak} for each of the three phases in most samples. These are shown in Figs. 3-12 and 3-13. While the two figures generally reproduced the results in Figs. 3-9 and 3-10, several puzzling additional features emerged.

First, the N_I phase clearly displayed the largest of the three q_{peak} values, implying the highest density of the three phases. This agrees with the azimuthal dependence of q_{peak} seen in Fig. 3-7. However, the N_{II} phase displayed the greater nematic order parameter, as seen in Sec. 2.3.3. Typically, one expects larger order parameters to result from denser packing

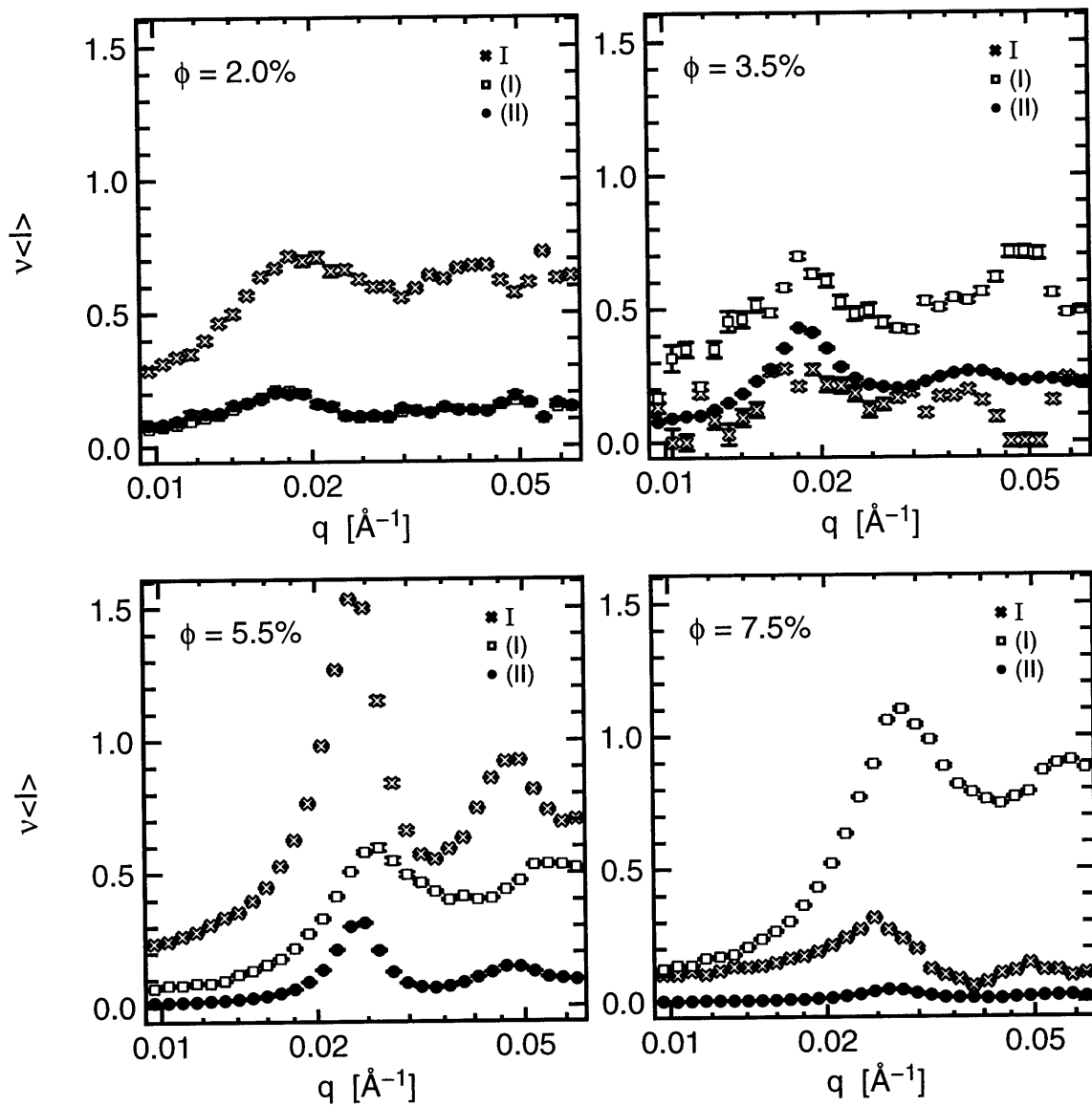


Figure 3-11: Best-fit values of nematic order parameter for each of three domains— I , N_{I_1} , and N_{II} —in four böhmite-in-glycerol samples.

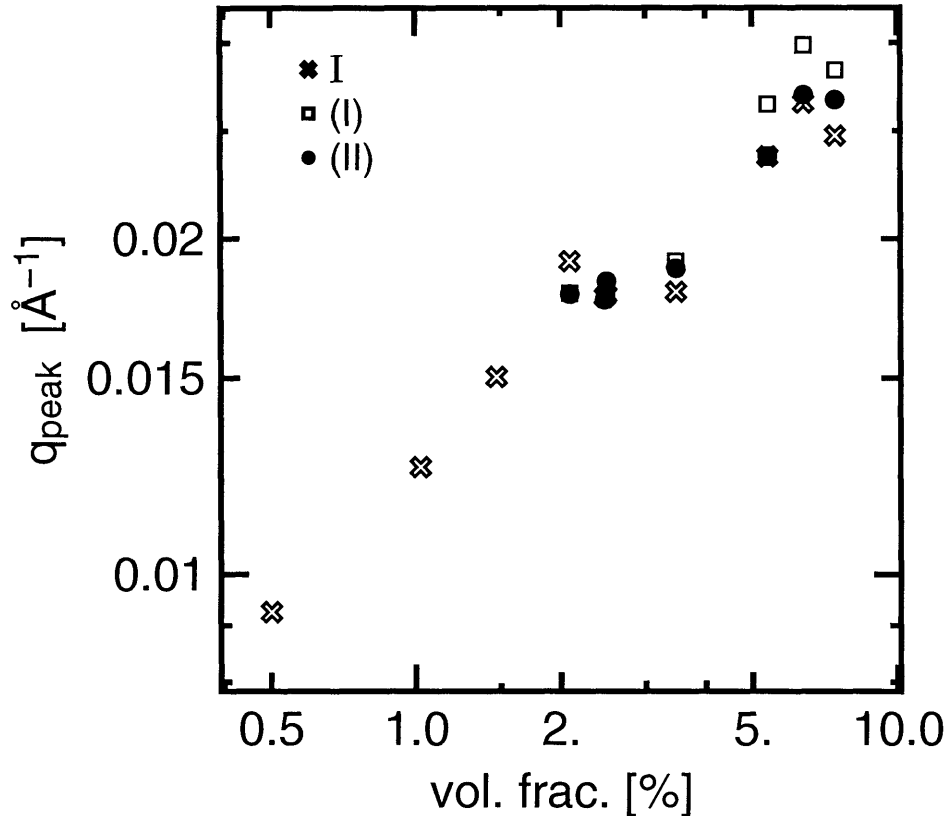


Figure 3-12: Effective structure factor radial peak positions for three phases as determined by fitting a three-phase model of the azimuthal scattering profile separately at each q .

of rods rather than the other way around.

Second, the peak position of the isotropic phase continued to increase well past the crossover into the three-phase coexistence regime, at densities where it would presumably have been unstable. Were it not unstable above 2% volume fraction, the sudden onset of nematic order would appear very unlikely, especially into two separate phases at a single, specific concentration.

Third, the N_{II} domain appeared to exhibit a structure factor peak width which was largely independent of volume fraction, while the I and N_I domains appeared roughly consistent with the expected $\phi^{\frac{1}{2}}$ dependence. Why the positional correlation behavior of the N_I phase would resemble that of the I phase, but not the N_{II} phase, is unclear.

Fourth, σ_{peak} of the isotropic phase displayed the same significant discontinuity at the transition as did the composite peak, and continued to change as volume fraction increased further. The properties of the isotropic phase are generally thought to remain unchanged except as to proportion once the volume fraction exceeds the critical value.

The tendency described in the two previous paragraphs, *i.e.* of the isotropic phase structure factor properties to track those of the composite peak suggest that perhaps this

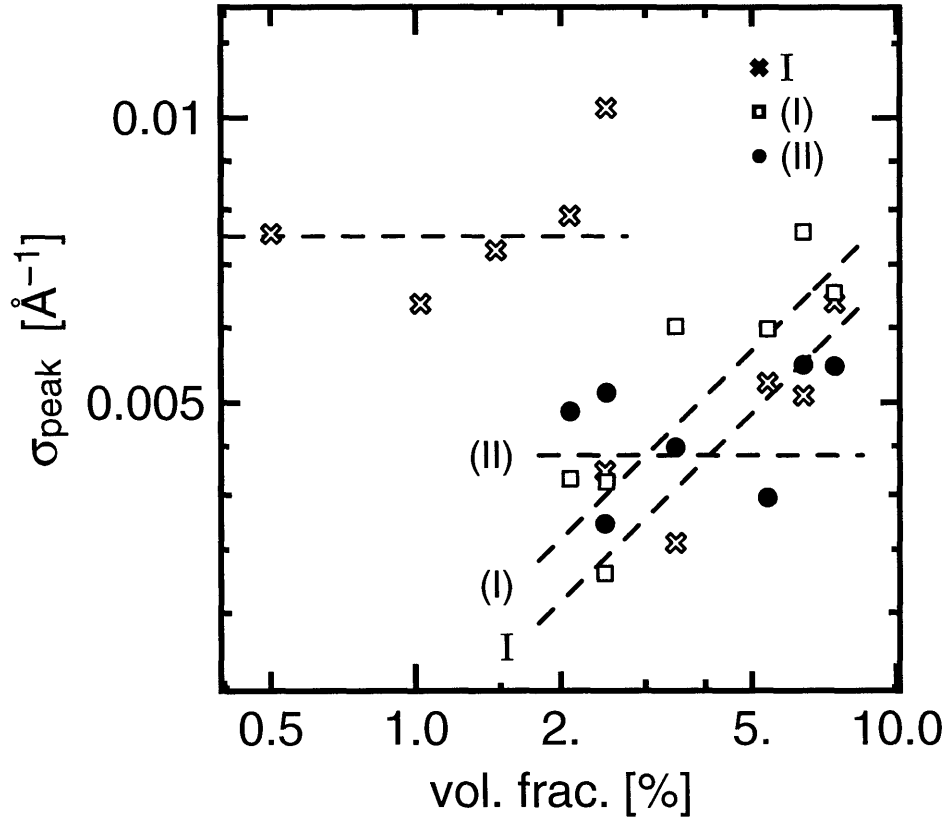


Figure 3-13: Effective structure factor radial peak half-widths for three phases as determined by fitting a three-phase model of the azimuthal scattering profile separately at each q . Dashed lines are guides to the eye, either constant in value or displaying a $\phi^{1/2}$ dependence.

method of extracting the proportion of scattering from the isotropic domain was prone to error. We discussed in Sec. 2.2.1.2 some reasons why this may occur when one or both nematic domains exhibit a low order parameter. The results for the two nematic domains, the scattering from which was more clearly distinguishable, are likely to be more accurate and further substantiate the claim that some positional reorganization was occurring at the nematic transition.

Chapter 4

X-ray photon correlation spectroscopy study of semidilute, isotropic suspensions of rigid rods

4.1 Theoretical formulation of the dynamic structure factor

4.1.1 The Smoluchowski equation

Equilibrium diffusion of noninteracting point particles in an isotropic medium is described by Fick's Law [30]. If a fraction $f(\mathbf{R}, t)$ of the particles are located at position \mathbf{R} at time t , Fick's Law states that the particle density flux, $\mathbf{J}(\mathbf{R}, t)$, is given by

$$\mathbf{J}(\mathbf{R}, t) = -D\nabla f(\mathbf{R}, t). \quad (4.1)$$

The constant, D , is known as the self-diffusion coefficient. Taking the divergence of both sides and substituting in the continuity equation,

$$\frac{\partial f(\mathbf{R}, t)}{\partial t} = -\nabla \cdot \mathbf{J}(\mathbf{R}, t), \quad (4.2)$$

yields the equation of simple diffusion,

$$\frac{\partial f(\mathbf{R}, t)}{\partial t} = D\nabla^2 f(\mathbf{R}, t). \quad (4.3)$$

When dealing with interacting, rigid, monodisperse, cylindrical particles in isotropic suspensions, several additional factors must be accounted for. First, each particle must be described by two vectors, the center of mass position, \mathbf{R} , and the primary axis direction unit vector, \mathbf{u} . Second, interparticle interactions and/or weak external fields that generate a potential, $U(\mathbf{R}, \mathbf{u}, t)$, give rise to an additional steady-state particle flux. Thus an extra term proportional to $-f(\mathbf{R}, \mathbf{u}, t)\nabla U(\mathbf{R}, \mathbf{u}, t)$ will appear on the right side of Eqn. 4.1.

Third, individual rodlike particles have three distinct modes of motion: translation parallel to the major axis, translation perpendicular to that axis, and rotation around a minor axis. We ignore the fourth motion, rotation around the major axis, on the grounds of cylindrical symmetry. Therefore, the diffusion coefficient splits into three pieces: D_{\parallel} , D_{\perp} , and D_r . Incorporating these three factors into the diffusion equation results in the Smoluchowski equation [30, 34]:

$$\begin{aligned} \frac{\partial}{\partial t} f(\mathbf{R}, \mathbf{u}, t) = & \nabla_{\mathbf{R}} \cdot [D_{\parallel} \mathbf{u} \mathbf{u} + D_{\perp} (\mathbf{I} - \mathbf{u} \mathbf{u})] \cdot \left(\nabla_{\mathbf{R}} f + f \nabla_{\mathbf{R}} \frac{U(\mathbf{R}, \mathbf{u}, t)}{k_B T} \right) \\ & + D_r \mathfrak{R} \cdot \left(\mathfrak{R} f + f \mathfrak{R} \frac{U(\mathbf{R}, \mathbf{u}, t)}{k_B T} \right), \end{aligned} \quad (4.4)$$

where $\nabla_{\mathbf{R}} f \equiv \partial f / \partial \mathbf{R}$, \mathbf{I} is the identity matrix, and \mathfrak{R} is the angular momentum operator,

$$\mathfrak{R} f \equiv \mathbf{u} \times \frac{\partial f}{\partial \mathbf{u}}. \quad (4.5)$$

4.1.2 Dynamic structure factor and the fluctuation dissipation theorem

The fluctuation dissipation theorem [30, 105] states that for a system under an applied field $\xi(t)$, the time correlation function $\langle A(\mathbf{R}, t) B(\mathbf{R}, 0) \rangle$ of two quantities of the system, $A(\mathbf{R}, t)$ and $B(\mathbf{R}, t)$, can be expressed as [30]

$$\langle A(\mathbf{R}, t) B(\mathbf{R}, 0) \rangle_{\xi} = \langle A(\mathbf{R}, t) \rangle_0 \langle B(\mathbf{R}, 0) \rangle_0 + k_B T \int_t^{\infty} dt' \chi(\mathbf{R}, t'), \quad (4.6)$$

provided that the potential arising from the field is of the form

$$U_{\text{applied}}(\mathbf{R}, t) = -\xi(t) B(\mathbf{R}, 0). \quad (4.7)$$

The notation $\langle \rangle_0$ refers to the ensemble average in the absence of the field, and $\chi(\mathbf{R}, t)$ is the response function as defined by

$$\langle A(\mathbf{R}, t) \rangle_{\xi} = \langle A(\mathbf{R}, t) \rangle_0 + \int_{-\infty}^t dt' \chi(\mathbf{R}, t - t') \xi(t'). \quad (4.8)$$

Omitting for simplicity the absolute normalization factors discussed in Sec. 3.1.2, the dynamic structure factor is given by [30, 34, 105]

$$S(\mathbf{q}, t) = \frac{1}{cL} \langle \delta\rho(\mathbf{q}, t) \delta\rho(-\mathbf{q}, 0) \rangle, \quad (4.9)$$

where $\delta\rho(\mathbf{q}, t)$ is the spatial Fourier transform of the excess (relative to the mean) electron density. Thus, given a hypothetical field $\xi(t)$ satisfying the condition

$$U_{\text{applied}}(\mathbf{q}, t) = -\xi(t) \delta\rho(-\mathbf{q}, 0), \quad (4.10)$$

it follows that [105]

$$\langle \delta\rho(\mathbf{q}, t) \rangle_\xi = \int_{-\infty}^t dt' \chi(\mathbf{q}, t - t') \xi(t') \quad (4.11)$$

and

$$S(\mathbf{q}, t) = \frac{k_B T}{cL} \int_t^\infty dt' \chi(\mathbf{q}, t'). \quad (4.12)$$

The three equations above indicate that if we can determine a system's mean density fluctuations in response to a particular applied field—and can extract from that the response function—we may immediately identify the system's dynamic structure factor (and *vice versa*).

For cylinders, the evaluation of $\langle \delta\rho \rangle$ is relatively straightforward [34, 94],

$$\langle \delta\rho(\mathbf{q}, t) \rangle = c \int d\mathbf{R} \int d\mathbf{u} \int_{-L/2}^{L/2} dr e^{i\mathbf{q}\cdot(\mathbf{R}+r\mathbf{u})} f(\mathbf{R}, \mathbf{u}, t) \quad (4.13)$$

$$= c \int d\mathbf{u} L j_0\left(\mathbf{q}\frac{L}{2}\cdot\mathbf{u}\right) f(\mathbf{q}, \mathbf{u}, t), \quad (4.14)$$

making the potential for one rod

$$U_{\text{applied}}(\mathbf{q}, \mathbf{u}, t) = -\xi(t) cL j_0\left(\mathbf{q}\frac{L}{2}\cdot\mathbf{u}\right). \quad (4.15)$$

The function $j_0(x) = \sin x/x$ is the spherical Bessel function of the first kind of order zero, and $j_0(-x) = j_0(x)$. Note that Eqn. 4.13—unlike Eqn. 2.2 and the subsequent treatments in the previous two chapters—is valid only for $qR \ll 1$, R being the rod radius.

4.1.3 The Smoluchowski equation in reciprocal space

Secs. 1.2.1 and 4.1.2 indicate that in order to determine the dynamic structure factor, we will need to incorporate the mean field and applied potentials into the Smoluchowski equation. Since U_{mean} depends on the distribution f , it is convenient to look only at small perturbations from the noninteracting case, meaning that we expand f as [106]

$$f(\mathbf{R}, \mathbf{u}, t) = \frac{1}{4\pi} + \delta f(\mathbf{R}, \mathbf{u}, t) \quad (4.16)$$

and keep terms in the Smoluchowski equation up to the lowest order in δf ,

$$\begin{aligned} \frac{\partial}{\partial t} \delta f &= \nabla_{\mathbf{R}} \cdot [D_{\parallel} \mathbf{u}\mathbf{u} + D_{\perp} (\mathbf{I} - \mathbf{u}\mathbf{u})] \cdot \nabla_{\mathbf{R}} \left[\delta f + \frac{1}{4\pi k_B T} (U_{\text{applied}} + U_{\text{mean}}) \right] \\ &+ D_r \mathfrak{R}^2 \left[\delta f + \frac{1}{4\pi k_B T} (U_{\text{applied}} + U_{\text{mean}}) \right]. \end{aligned} \quad (4.17)$$

The spatial Fourier transform of the mean field potential from Eqn. 1.5 is

$$U_{\text{mean}}(\mathbf{q}, \mathbf{u}, t) = ck_B T \int d\mathbf{u}' w(\mathbf{q}, \mathbf{u}, \mathbf{u}') f(\mathbf{q}, \mathbf{u}', t) \quad (4.18)$$

and the transform of the Smoluchowski equation, based on Eqns. 4.15, 4.17, and 4.18 is [105]

$$\begin{aligned} \frac{\partial}{\partial t} f(\mathbf{q}, \mathbf{u}, t) = & - \left[D_{\parallel}(\mathbf{q} \cdot \mathbf{u})^2 + D_{\perp} \left(q^2 - (\mathbf{q} \cdot \mathbf{u})^2 \right) - D_r \mathfrak{R}^2 \right] \\ & \times \left[f(\mathbf{q}, \mathbf{u}, t) - \frac{cL}{4\pi k_B T} \xi(t) j_0 \left(\mathbf{q} \frac{L}{2} \cdot \mathbf{u} \right) \right. \\ & \left. + \frac{c}{4\pi} \int d\mathbf{u}' w(\mathbf{q}, \mathbf{u}, \mathbf{u}') f(\mathbf{q}, \mathbf{u}', t) \right]. \end{aligned} \quad (4.19)$$

Note that

$$f(\mathbf{q}, \mathbf{u}, t) \equiv \int d\mathbf{R} f(\mathbf{R}, \mathbf{u}, t) e^{i\mathbf{q} \cdot \mathbf{R}} \quad (4.20)$$

$$= \int d\mathbf{R} \delta f(\mathbf{R}, \mathbf{u}, t) e^{i\mathbf{q} \cdot \mathbf{R}} \quad (4.21)$$

for $\mathbf{q} \neq 0$.

4.1.4 Solving for the rod distribution function and the dynamic structure factor

Doi, Shimada, and Okano [105] determined the dynamic structure factor from Eqn. 4.19 as follows. They used the more compact notation,

$$\frac{\partial}{\partial t} f(\mathbf{q}, \mathbf{u}, t) = -\theta(\mathbf{q}, \mathbf{u}) \Phi(\mathbf{q}, \mathbf{u}) f(\mathbf{q}, \mathbf{u}, t) + \frac{cL}{4\pi k_B T} \xi(t) \theta(\mathbf{q}, \mathbf{u}) j_0 \left(\mathbf{q} \frac{L}{2} \cdot \mathbf{u} \right), \quad (4.22)$$

where the operators

$$\theta(\mathbf{q}, \mathbf{u}) F(\mathbf{q}, \mathbf{u}) = \left[D_{\parallel}(\mathbf{q} \cdot \mathbf{u})^2 + D_{\perp} \left(q^2 - (\mathbf{q} \cdot \mathbf{u})^2 \right) - D_r \mathfrak{R}^2 \right] F(\mathbf{q}, \mathbf{u}) \quad (4.23)$$

and

$$\Phi(\mathbf{q}, \mathbf{u}) F(\mathbf{q}, \mathbf{u}) = F(\mathbf{q}, \mathbf{u}) + \frac{c}{4\pi} \int d\mathbf{u}' w(\mathbf{q}, \mathbf{u}, \mathbf{u}') F(\mathbf{q}, \mathbf{u}') \quad (4.24)$$

for any function $F(\mathbf{q}, \mathbf{u})$. The expressions for the excluded volumes of hard and charged rods, Eqns. 1.8 and 1.13, respectively, provide an intuitive understanding of the form of the Fourier-transformed Mayer function required in Eqn. 4.24. Recalling from Sec. 1.2.3.2 that charged rods in the isotropic phase can be described as hard rods of radius R_{eff} , we find

that [36, 105],

$$w(\mathbf{q}, \mathbf{u}, \mathbf{u}') = \int_{-L/2}^{L/2} d\xi \int_{-L/2}^{L/2} d\eta \int_{-2R_{\text{eff}}}^{2R_{\text{eff}}} d\zeta |\mathbf{u} \times \mathbf{u}'| e^{i\mathbf{q} \cdot \xi \mathbf{u} + \eta \mathbf{u}' + \zeta \frac{\mathbf{u} \times \mathbf{u}'}{|\mathbf{u} \times \mathbf{u}'|}} \quad (4.25)$$

$$\simeq 4R_{\text{eff}} L^2 |\mathbf{u} \times \mathbf{u}'| j_0\left(\frac{L}{2} \cdot \mathbf{u}\right) j_0\left(\frac{L}{2} \cdot \mathbf{u}'\right), \quad (4.26)$$

where once again we have assumed $qR_{\text{eff}} \ll 1$.

The solution to the differential equation, 4.22, is

$$f(\mathbf{q}, \mathbf{u}, t) = \frac{cL}{4\pi k_B T} \int_{-\infty}^t dt' \xi(t') e^{-(t-t')\theta(\mathbf{q}, \mathbf{u})\Phi(\mathbf{q}, \mathbf{u})} \theta(\mathbf{q}, \mathbf{u}) j_0\left(\frac{L}{2} \cdot \mathbf{u}\right). \quad (4.27)$$

Next, based on Eqn. 4.14,

$$\langle \delta\rho(\mathbf{q}, t) \rangle_{\xi} = \int_{-\infty}^t dt' \xi(t') \frac{cL^2}{4\pi k_B T} \int d\mathbf{u} j_0\left(\frac{L}{2} \cdot \mathbf{u}\right) e^{-(t-t')\theta\Phi} \theta j_0\left(\frac{L}{2} \cdot \mathbf{u}\right). \quad (4.28)$$

Then, comparison with Eqn. 4.11 indicates that

$$\chi(\mathbf{q}, t) = \frac{cL^2}{4\pi k_B T} \int d\mathbf{u} j_0\left(\frac{L}{2} \cdot \mathbf{u}\right) e^{-t\theta(\mathbf{q}, \mathbf{u})\Phi(\mathbf{q}, \mathbf{u})} \theta(\mathbf{q}, \mathbf{u}) j_0\left(\frac{L}{2} \cdot \mathbf{u}\right), \quad (4.29)$$

and from Eqn. 4.12 the dynamic structure factor is

$$S(\mathbf{q}, t) = \frac{L}{4\pi} \int_t^{\infty} dt' \int d\mathbf{u} j_0\left(\frac{L}{2} \cdot \mathbf{u}\right) e^{-t'\theta(\mathbf{q}, \mathbf{u})\Phi(\mathbf{q}, \mathbf{u})} \theta(\mathbf{q}, \mathbf{u}) j_0\left(\frac{L}{2} \cdot \mathbf{u}\right). \quad (4.30)$$

4.2 Dynamic structure factor in matrix form

Eqn. 4.30 is not of a form ready-made for comparing the theoretical dynamic structure factor with experimentally obtained correlation functions. Maeda and Fujime [107] and Maeda [98, 108] have developed a representation facilitating the efficient, direct, numerical evaluation of Eqn. 4.30 at all t and at all $q \ll 1/R$ for concentrated, isotropic suspensions of monodisperse, rigid rods. The solution takes the form of a sum over single exponentials,

$$S(\mathbf{q}, t) = L \sum_{l=0, \text{ even}}^{\infty} S_l(q) e^{-\Gamma_l(q)t}. \quad (4.31)$$

In this section we will outline their procedure for determining $\Gamma_l(q)$ and $S_l(q)$. While other, related, theoretical treatments provide simpler expressions for the dynamic structure factor, those either do not account for any interparticle interactions [109, 110], are applicable only at short times [96, 111, 112], or calculate only the $l = 0$ term [113]. Polydispersity is often accounted for by cumulant expansions to second or higher order [34, 114, 115], but these expansions too are only appropriate for short times.

4.2.1 Useful identities

Generally speaking, the Maeda formalism involves projecting the functions and operators in Eqn. 4.30 onto the generalized spherical harmonics, $D_{m,n}^l$ [74]. Due to the symmetries exhibited by each term—which arise from the cylindrical symmetries of the particles themselves—nonzero components are found only for $m = n = 0$ and l even. The functions $D_{0,0}^l$ are more commonly known as the Legendre polynomials, P_l . The Legendre polynomials [77, 116] themselves form an orthogonal,

$$\int_{-1}^1 dx P_l(x) P_{l'}(x) = \frac{2}{(2l+1)} \delta_{ll'}, \quad (4.32)$$

and complete,

$$\sum_l \frac{(2l+1)}{2} P_l(x) P_l(x') = \delta(x-x'), \quad (4.33)$$

basis. They are eigenfunctions of the angular momentum operator, with

$$\mathfrak{R}^2 P_l(x) = -l(l+1) P_l(x). \quad (4.34)$$

We evaluate below the projection coefficients of several elementary functions that will be relevant in subsequent sections. Henceforth, $l, l', l'' \dots$ should be understood to be even, nonnegative integers.

4.2.1.1 x^2

$$\int dx P_l(x) x^2 P_{l'}(x) = \int dx P_l(x) \frac{1}{3} (1 + 2P_2(x)) P_{l'}(x) \quad (4.35)$$

$$= \frac{2}{3(2l+1)} \delta_{ll'} + \frac{4}{3} \begin{pmatrix} l & 2 & l' \\ 0 & 0 & 0 \end{pmatrix}^2 \quad (4.36)$$

$$= \frac{2}{(2l+1)} \left[\frac{2l^2 + 2l - 1}{(2l+3)(2l-1)} \delta_{ll'} + \frac{l(l-1)}{(2l-1)(2l-3)} \delta_{l-2,l'} + \frac{(l+1)(l+2)}{(2l+5)(2l+3)} \delta_{l+2,l'} \right] \quad (4.37)$$

The notation $\begin{pmatrix} l & l' & l'' \\ m & m' & m'' \end{pmatrix}$ refers to the Wigner 3j symbol [117, 118].

4.2.1.2 $e^{i\mathbf{q}\cdot\mathbf{r}\mathbf{u}}$

$$\int d\mathbf{u} e^{i\mathbf{q}\cdot\mathbf{r}\mathbf{u}} P_l(\hat{\mathbf{q}} \cdot \mathbf{u}) = 4\pi i^l j_l(qr) \quad (4.38)$$

corresponds to the Rayleigh expansion of a plane wave [90, 98]. The function $j_l(x)$ is the spherical bessel function of the first kind.

4.2.1.3 $j_0(\mathbf{q}\frac{L}{2} \cdot \mathbf{u})$

$$j_0\left(\mathbf{q}\frac{L}{2} \cdot \mathbf{u}\right) = \frac{1}{L} \int_{-L/2}^{L/2} dr e^{i\mathbf{q}\cdot r\mathbf{u}}, \quad (4.39)$$

and thus

$$\int d\mathbf{u} j_0\left(\mathbf{q}\frac{L}{2} \cdot \mathbf{u}\right) P_l(\hat{\mathbf{q}} \cdot \mathbf{u}) = 4\pi i^l b_l\left(\frac{L}{2}\right), \quad (4.40)$$

where [90, 107]

$$b_l(x) \equiv \frac{1}{x} \int_0^x dz j_l(z). \quad (4.41)$$

It follows that

$$\int d\mathbf{u} P_l(\hat{\mathbf{q}} \cdot \mathbf{u}) j_0\left(\mathbf{q}\frac{L}{2} \cdot \mathbf{u}\right) P_{l'}(\hat{\mathbf{q}} \cdot \mathbf{u}) = 4\pi K_{ll'}(q), \quad (4.42)$$

with [98]

$$K_{ll'}(q) = K_{l'l}(q) \equiv \sum_{l''=0}^{\infty} (2l''+1) i^{l''} b_{l''}\left(\frac{L}{2}\right) \begin{pmatrix} l & l'' & l' \\ 0 & 0 & 0 \end{pmatrix}^2. \quad (4.43)$$

4.2.1.4 $|\mathbf{u} \times \mathbf{u}'|$

Since [36, 98]

$$|\mathbf{u} \times \mathbf{u}'| = \frac{\pi}{4} - 2\pi^2 \sum_{l=2}^{\infty} \frac{(l-1)}{l+2} \left(\frac{(l-3)!!}{l!!}\right)^2 \sum_{m=-l}^l Y_{lm}^*(\mathbf{u}) Y_{lm}(\mathbf{u}') \quad (4.44)$$

and $P_l(\hat{\mathbf{q}} \cdot \mathbf{u}) = \sqrt{4\pi/(2l+1)} Y_{l0}(\mathbf{u})$,

$$\begin{aligned} \int d\mathbf{u}' P_{l'}(\hat{\mathbf{q}} \cdot \mathbf{u}') |\mathbf{u} \times \mathbf{u}'| P_l(\hat{\mathbf{q}} \cdot \mathbf{u}') &= \frac{\pi^2}{2l'+1} \delta_{l'l} - 2\pi^2 \sum_{l=2}^{\infty} \frac{(2l+1)(l-1)}{l+2} \\ &\times \left(\frac{(l-3)!!}{l!!}\right)^2 \begin{pmatrix} l' & l'' & l \\ 0 & 0 & 0 \end{pmatrix}^2 P_l(\hat{\mathbf{q}} \cdot \mathbf{u}) \end{aligned} \quad (4.45)$$

Therefore, using Eqns. 4.42 and 4.43,

$$\begin{aligned} \int d\mathbf{u}' j_0\left(\mathbf{q}\frac{L}{2} \cdot \mathbf{u}'\right) |\mathbf{u} \times \mathbf{u}'| P_{l'}(\hat{\mathbf{q}} \cdot \mathbf{u}') &= \pi^2 i^{l'} b_{l'}\left(\frac{L}{2}\right) - 2\pi^2 \sum_{l=2}^{\infty} \frac{(2l+1)(l-1)}{l+2} \\ &\times \left(\frac{(l-3)!!}{l!!}\right)^2 K_{ll'}(q) P_l(\hat{\mathbf{q}} \cdot \mathbf{u}). \end{aligned} \quad (4.46)$$

Incidentally,

$$\frac{(l-3)!!}{l!!} = \frac{(l-2)!l}{2^l \left[\left(\frac{l}{2}\right)!\right]^2}. \quad (4.47)$$

4.2.2 Matrix representations of operators

We can use the identities in Sec. 4.2.1 to find the Legendre polynomial expansion coefficients of the terms j_0 , θ , and Φ seen in Eqn. 4.30 [98]. From Eqn. 4.40,

$$j_{0,l}(q) \equiv \frac{\sqrt{2l+1}}{4\pi} \int d\mathbf{u} j_0 \left(\mathbf{q} \frac{L}{2} \cdot \mathbf{u} \right) P_l(\hat{\mathbf{q}} \cdot \mathbf{u}) \quad (4.48)$$

$$= \sqrt{2l+1} i^l b_l \left(q \frac{L}{2} \right). \quad (4.49)$$

Eqns. 4.23 and 4.37 give

$$\theta_{l'l'}(q) \equiv \frac{\sqrt{(2l+1)(2l'+1)}}{4\pi} \int d\mathbf{u} P_l(\hat{\mathbf{q}} \cdot \mathbf{u}) \theta(\mathbf{q}, \mathbf{u}) P_{l'}(\hat{\mathbf{q}} \cdot \mathbf{u}) \quad (4.50)$$

$$= \frac{\sqrt{(2l+1)(2l'+1)}}{4\pi} \int d\mathbf{u} P_l(\hat{\mathbf{q}} \cdot \mathbf{u}) \times \left[D_{\parallel}(\mathbf{q} \cdot \mathbf{u})^2 + D_{\perp} \left(q^2 - (\mathbf{q} \cdot \mathbf{u})^2 \right) - D_r \mathfrak{R}^2 \right] P_{l'}(\hat{\mathbf{q}} \cdot \mathbf{u}) \quad (4.51)$$

$$= \left[q^2 D_{\perp} + l(l+1) D_r \right] \delta_{l'l'} + q^2 (D_{\parallel} - D_{\perp}) \frac{\sqrt{(2l+1)(2l'+1)}}{4\pi} \int d\mathbf{u} P_l(\hat{\mathbf{q}} \cdot \mathbf{u}) (\hat{\mathbf{q}} \cdot \mathbf{u})^2 P_{l'}(\hat{\mathbf{q}} \cdot \mathbf{u}) \quad (4.52)$$

$$= \left[l(l+1) D_r + q^2 D_{\perp} + q^2 (D_{\parallel} - D_{\perp}) \frac{2l^2 + 2l - 1}{(2l+3)(2l-1)} \right] \delta_{l'l'} + q^2 (D_{\parallel} - D_{\perp}) \frac{l(l-1)}{(2l-1) \sqrt{(2l+1)(2l-3)}} \delta_{l-2,l'} + q^2 (D_{\parallel} - D_{\perp}) \frac{(l+1)(l+2)}{(2l+3) \sqrt{(2l+5)(2l+1)}} \delta_{l+2,l'}. \quad (4.53)$$

Similarly, we use Eqns. 1.13, 1.20, 4.24, and 4.46 to find

$$\Phi_{l'l'}(q) \equiv \frac{\sqrt{(2l+1)(2l'+1)}}{4\pi} \int d\mathbf{u} P_l(\hat{\mathbf{q}} \cdot \mathbf{u}) \Phi(\mathbf{q}, \mathbf{u}) P_{l'}(\hat{\mathbf{q}} \cdot \mathbf{u}) \quad (4.54)$$

$$= \delta_{l'l'} + \frac{\sqrt{(2l+1)(2l'+1)}}{4\pi} \int d\mathbf{u} P_l(\hat{\mathbf{q}} \cdot \mathbf{u}) \frac{c}{4\pi} \int d\mathbf{u}' w(\mathbf{q}, \mathbf{u}, \mathbf{u}') P_{l'}(\hat{\mathbf{q}} \cdot \mathbf{u}') \quad (4.55)$$

$$= \delta_{l'l'} + \frac{cL^2 R_{\text{eff}}}{4\pi^2} \sqrt{(2l+1)(2l'+1)} \int d\mathbf{u} P_l(\hat{\mathbf{q}} \cdot \mathbf{u}) j_0 \left(\mathbf{q} \frac{L}{2} \cdot \mathbf{u} \right) \times \int d\mathbf{u}' j_0 \left(\mathbf{q} \frac{L}{2} \cdot \mathbf{u}' \right) |\mathbf{u} \times \mathbf{u}'| P_{l'}(\hat{\mathbf{q}} \cdot \mathbf{u}') \quad (4.56)$$

$$= \delta_{l'l'} + \frac{1}{4} cL^2 R_{\text{eff}} \sqrt{(2l+1)(2l'+1)} i^{l'} b_{l'} \left(q \frac{L}{2} \right) \int d\mathbf{u} P_l(\hat{\mathbf{q}} \cdot \mathbf{u}) j_0 \left(\mathbf{q} \frac{L}{2} \cdot \mathbf{u} \right)$$

$$\begin{aligned}
& -\frac{1}{2}cL^2R_{\text{eff}}\sqrt{(2l+1)(2l'+1)}\sum_{l''=2}^{\infty}\frac{(2l''+1)(l''-1)}{l''+2}\left(\frac{(l''-3)!!}{l''!!}\right)^2K_{l''l''}(q) \\
& \times\int d\mathbf{u}P_l(\hat{\mathbf{q}}\cdot\mathbf{u})j_0\left(\mathbf{q}\frac{L}{2}\cdot\mathbf{u}\right)P_{l''}(\hat{\mathbf{q}}\cdot\mathbf{u}) \tag{4.57}
\end{aligned}$$

$$\begin{aligned}
& =\delta_{ll'}+\pi cL^2R_{\text{eff}}\left[j_{0,l}(q)j_{0,l'}(q)-2\sqrt{(2l+1)(2l'+1)}\sum_{l''=2}^{\infty}\frac{(2l''+1)(l''-1)}{l''+2}\right. \\
& \left.\times\left(\frac{(l''-3)!!}{l''!!}\right)^2K_{ll''}(q)K_{l''l'}(q)\right]. \tag{4.58}
\end{aligned}$$

4.2.3 Matrix representation of $S(\mathbf{q}, t)$

4.2.3.1 Full solution

Using the definitions in Eqns. 4.48, 4.50, and 4.54, one can show that the Doi-Shimada-Okano dynamic structure factor, Eqn. 4.30, is equivalent to [98]

$$S(\mathbf{q}, t) = L \sum_{\nu} j_{0,\nu}(q) \sum_{\nu''} \int_t^{\infty} dt' e^{-t' \sum_l \theta_{\nu l}(q) \Phi_{l\nu''}(q)} \sum_{\nu'''} \theta_{\nu''\nu'''}(q) j_{0,\nu'''}(q). \tag{4.59}$$

This expression can be simplified by introducing the eigenvalues Γ_l and eigenvectors $U_{\nu l}$ of the operator $\Omega \equiv \theta\Phi$ [98, 105]. That is,

$$\sum_{\nu''\nu'''} \theta_{\nu''\nu'''} \Phi_{\nu''\nu'''} U_{\nu''\nu'''} = U_{\nu l} \Gamma_l. \tag{4.60}$$

It follows that

$$\int_t^{\infty} dt' e^{-t' \sum_l \theta_{\nu l} \Phi_{l\nu''}} = \int_t^{\infty} dt' e^{-t' \sum_l U_{\nu l} \Gamma_l U_{l\nu''}^{-1}} \tag{4.61}$$

$$= \sum_l U_{\nu l} \int_t^{\infty} dt' e^{-t' \Gamma_l} U_{l\nu''}^{-1} \tag{4.62}$$

$$= \sum_l U_{\nu l} \frac{1}{\Gamma_l} e^{-\Gamma_l t} U_{l\nu''}^{-1}. \tag{4.63}$$

Eqn. 4.59 then becomes

$$S(\mathbf{q}, t) = L \sum_{\nu} j_{0,\nu}(q) \sum_l U_{\nu l}(q) \frac{1}{\Gamma_l(q)} e^{-\Gamma_l(q)t} \sum_{\nu''} U_{l\nu''}^{-1}(q) \sum_{\nu'''} \theta_{\nu''\nu'''}(q) j_{0,\nu'''}(q), \tag{4.64}$$

which is precisely in the desired form, $S(\mathbf{q}, t) = L \sum_l S_l(q) \exp[-\Gamma_l(q)t]$, with

$$S_l(q) = \frac{1}{\Gamma_l(q)} \sum_{\nu} j_{0,\nu}(q) U_{\nu l}(q) \sum_{\nu''} U_{l\nu''}^{-1}(q) \sum_{\nu'''} \theta_{\nu''\nu'''}(q) j_{0,\nu'''}(q). \tag{4.65}$$

4.2.3.2 Special case of no interactions and isotropic diffusion

The simplest diffusion equation one can write for rigid, rodlike particles omits interactions between the particles ($w = 0$) and ignores the anisotropy in the diffusion coefficient ($D_{\parallel} = D_{\perp} = D$). In this special case,

$$\theta_{ll'}(q) = [l(l+1)D_r + q^2D] \delta_{ll'}, \quad (4.66)$$

$$\Phi_{ll'}(q) = \delta_{ll'}, \quad (4.67)$$

$$U_{ll'}(q) = U_{ll'}^{-1}(q) = \delta_{ll'}, \quad (4.68)$$

making

$$\Gamma_l(q) = l(l+1)D_r + q^2D \quad (4.69)$$

and

$$\begin{aligned} S_l(q) &= \frac{1}{l(l+1)D_r + q^2D} \sum_{l'} j_{0,l'}(q) \delta_{ll'} \sum_{l''} \delta_{ll''} \\ &\quad \times \sum_{l'''} [l''(l''+1)D_r + q^2D] \delta_{l''l'''} j_{0,l'''}(q) \end{aligned} \quad (4.70)$$

$$= [j_{0,l}(q)]^2. \quad (4.71)$$

This result was first obtained by Pecora [119,120].

4.2.4 Summary

Maeda's procedure for numerical evaluation of the dynamic structure factor of rigid rods in isotropic suspension involves the following steps. Starting with input parameters L , cL^2R_{eff} , D_{\parallel} , D_{\perp} , and D_r , calculate the following up to some maximum $l, l' = l_{\text{max}}$:

1. The matrix forms $j_{0,l}$, $\theta_{ll'}$, $\Phi_{ll'}$ from Eqns. 4.49, 4.53, and 4.58, respectively.
2. Γ_l and $U_{ll'}$, the eigenvalues and eigenvectors of $\Omega_{ll'} = \sum_{l''} \theta_{ll''} \Phi_{l''l'}$. These can be found numerically [88,121].
3. $S_l(q)$ from Eqn. 4.65.
4. $S(\mathbf{q}, t)$ from Eqn. 4.31.

Only elements for which both l and l' are even need be evaluated, since odd elements will be zero. All four steps must be repeated for each q value of interest.

4.3 Measured dynamics of isotropic suspensions of böhmite in glycerol

Representative examples of X-ray photon correlation spectroscopy measurements on böhmite in glycerol are displayed in Fig. 4-1. In order that the timescales of diffusion would be accessible to our apparatus, we cooled the samples to -12.0°C .

We used two functional forms in a nonlinear, least-squares routine to fit the measured correlation functions for two isotropic samples. We will compare the two fitting functions below. The first form involved an empirical, double-exponential function for the dynamic structure factor [34, 90],

$$S(\mathbf{q}, t) = L \left[S_{\text{slow}}(q) \exp\left(-\frac{t}{\tau_{\text{slow}}(q)}\right) + S_{\text{fast}}(q) \exp\left(-\frac{t}{\tau_{\text{fast}}(q)}\right) \right], \quad (4.72)$$

which resembles Eqn. 4.31 except limited to two terms. A separate fit was performed for each q value. The solid lines in Fig. 4-1 display this form. The fitted values of $\tau_{\text{fast,slow}}(q)$ are shown in Fig. 4-2 and appeared consistent with a q^{-2} dependence. When this is the case, the proportionality constants are typically interpreted as effective diffusion coefficients, $D_{\text{fast,slow}}$. For our samples those coefficients are listed in Table 4.1.

The second form used to fit $g_2(q, t)$ was the matrix representation developed by Maeda [98], as detailed in Sec. 4.2. One advantage of this form is that the q -dependence of the dynamic structure factor is built-in, so for a given sample we were able to perform a single fit at all q and t values simultaneously. For the q values of interest, we found that elements of Eqn. 4.64 above $l_{\text{max}} = 20$ had negligible effect on the calculated dynamic structure factors. With these relatively small 11×11 matrices, the fitting procedure converged rapidly, never requiring more than a few seconds to execute.

The best-fit results for the Maeda form can be seen as the dashed lines in Fig. 4-1 and the parameters in Table 4.1. As expected [30, 122–125], the perpendicular and rotational diffusions were strongly hindered in these semidilute suspensions, the parallel diffusion coefficient less so. When the rod length parameter, L , was allowed to vary, the fits for both samples converged to $1900 \leq L \leq 2000 \text{ \AA}$, regardless of the initial parameters given to the fitting function. The strong q -dependence of $j_{0,l}(q)$ in Eqn. 4.64 means that L can be determined with some precision by photon correlation spectroscopy even at $q \gg L/2$, where the static scattering cross-section is generally insensitive to L . Our XPCS measurements corroborate TEM measurements indicating $\langle L \rangle \simeq 1935 \text{ \AA}$, removing our earlier uncertainty in Sec. 3.1.6. We subsequently fixed L to more tightly constrain the other four parameters.

On comparing the two types of fits to the data, we found that the double-exponential form more closely agreed with the measured correlation functions. There are two reasons for this: first, with separate fits at each q , the double-exponential method effectively possessed many more adjustable parameters than the Maeda form; second, the Maeda form does not

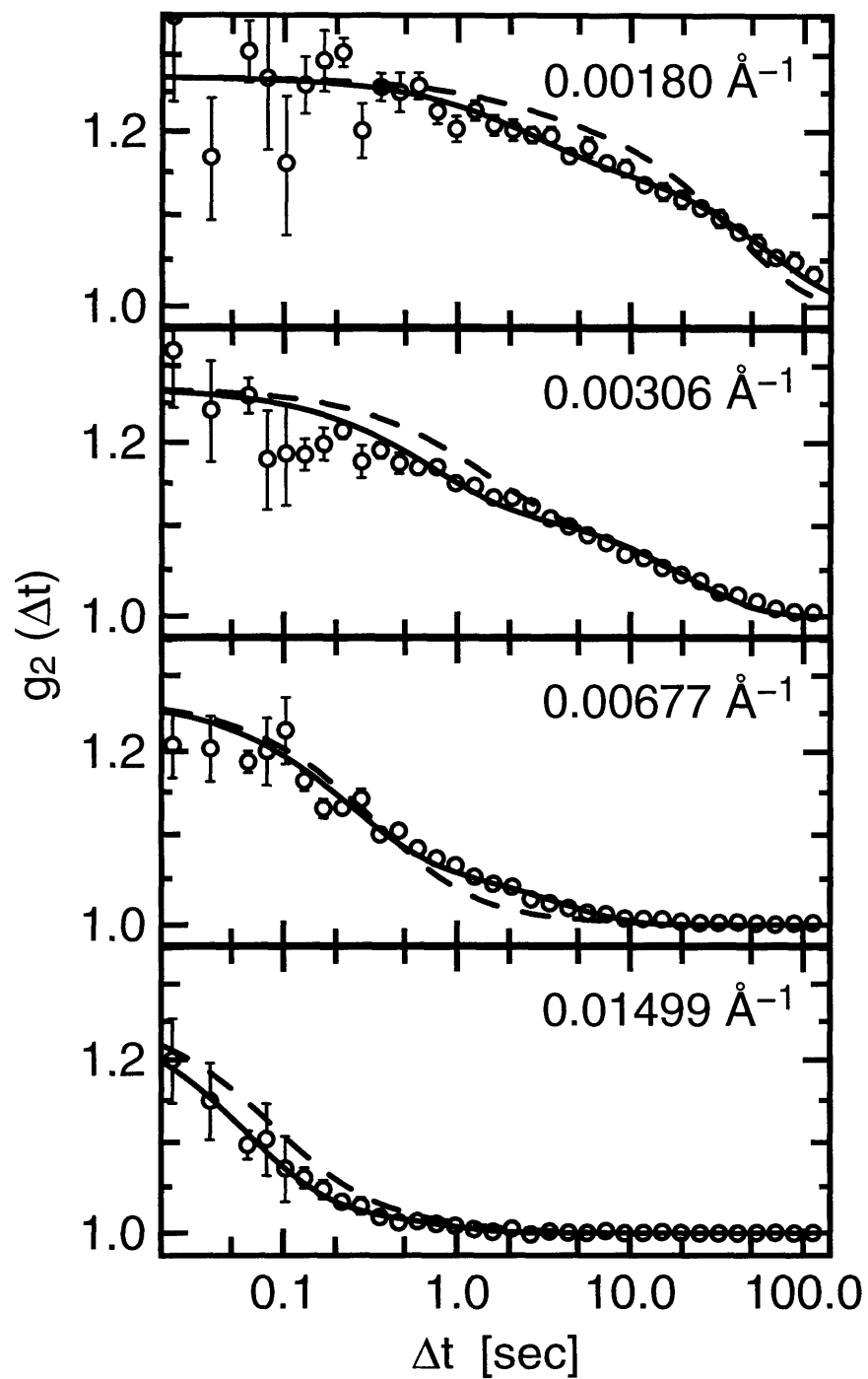


Figure 4-1: Intensity-intensity autocorrelation functions for 1.5% volume fraction sample of böhmite in glycerol at -12.0°C as measured by XPCS. Lines are fits to double-exponential decay (*solid*) and Maeda's matrix expression (*dashed*).

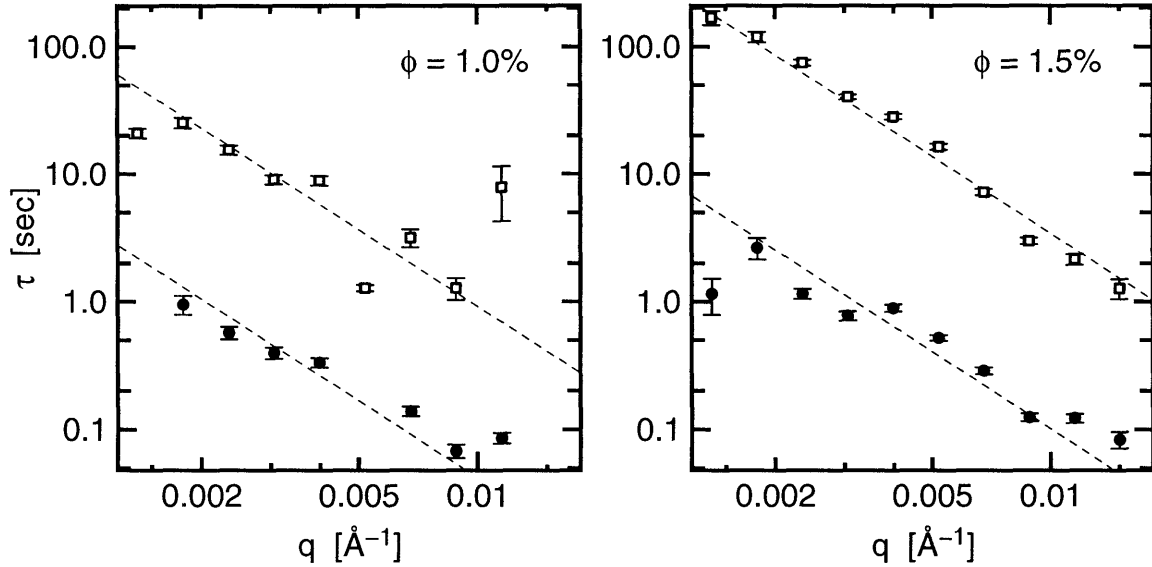


Figure 4-2: Fitted characteristic times of double-exponential decays as in Eqn. 4.72 for 1.0% and 1.5% böhmite volume fractions. Lines indicate $\tau \propto q^{-2}$.

account in any way for polydispersity. Consequently, the measured correlation functions appear “wider” and more “smeared” than their fitted counterparts.

It is unclear how one might go about incorporating polydispersity into Eqn. 4.64. To simply take a weighted average over the correlation functions expected for various L [34, 90, 126–129], analogous to our treatment of the static form factor in Sec. 3.1.1, requires adopting *a priori* a function that dictates how the diffusion coefficients depend on the rod dimensions. Although many authors [30, 34, 90, 122–125, 130–136] have addressed the connection between rod size and diffusion coefficients, it is still not well understood for semidilute and concentrated suspensions.

The two sets of diffusion coefficients in Table 4.1 are not easily identifiable with one another. The slow coefficient resembled the parallel coefficient, but only to within a factor of two. The fast coefficient had no clear analogue on the Maeda side of the table. To investigate this further, we have plotted in Fig. 4-3 the fitted $1/\tau$ values along with the first few $\Gamma_l(q)$ functions obtained from the fits to the Maeda form. The Γ_l were nearly

ϕ	double exponential		Maeda			
	D_{slow}	D_{fast}	D_{\parallel}	D_{\perp}	D_r	cL^2R_{eff}
1.0%	1.1×10^4	2.4×10^5	6.3×10^3	0.0091	0.10	1.3
1.5%	2.9×10^3	9.8×10^4	4.5×10^3	0.32	0.091	1.6

Table 4.1: Fitted diffusion coefficients from two fitting methods. Units of D_{slow} , D_{fast} , D_{\parallel} , and D_{\perp} are $\text{\AA}^2/\text{s}$. Units of D_r are $1/\text{s}$.

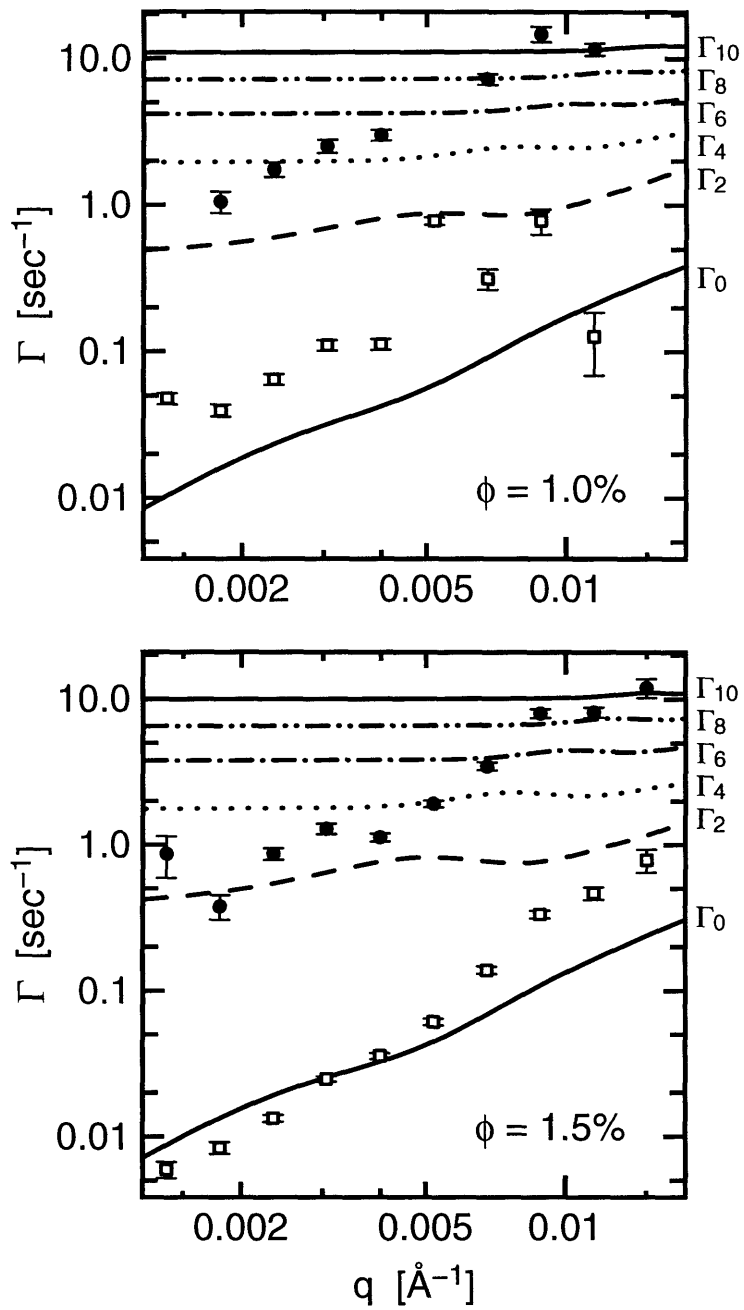


Figure 4-3: Decay coefficients $1/\tau_{\text{fast,slow}}(q)$ for the double-exponential fits (*points*) and $\Gamma_l(q)$ for fits to Maeda's form (*curves*). Curves are labeled at right.

independent of q , except for $l = 0$. This can be understood by looking at Pecora's simpler model in Sec. 4.2.3.2, specifically Eqn. 4.69. In that approximation, higher- l modes are mostly rotational, while the $l = 0$ mode is entirely translational, giving Γ_0 a q^2 dependence not shared by other modes.

At first glance, the two methods appear to produce incompatible estimates for the first two decay modes of the correlation function. However, the relative amplitude of each decay mode must be considered as well. These are shown for our data in Fig. 4-4. There is again no obvious similarity between the two types of results. Nevertheless, the two methods are consistent with one another. The $S_l(q)$ curves in Fig. 4-4 indicate that different modes dominate the dynamic structure factor at different q . The double-exponential time constants, $\tau_{\text{fast,slow}}$, can then be understood to arise from a composite of all of the decays, primarily representing whichever two modes have the highest relative amplitude.

At low q , then, the slow mode will dominate and be nearly identical to the $l = 0$ mode. The fast mode will be weaker and resemble the $l = 2$ mode. As q increases, the $l = 0, 2$ modes will be supplanted by higher modes, but not completely so, since S_0 plateaus near 0.2 and S_2 near 0.1. Thus, the slow mode will gradually weaken and its time constant will shift toward the $l = 2$ mode with increasing q , while the more dominant fast mode will mirror the time constant of whichever S_l happens to peak at a given q . This is precisely the behavior exhibited by the points in Fig. 4-3, and may help to explain some of the deviations from q^{-2} dependence seen in a number of recent studies [113, 137–142] of semidilute suspensions of rodlike particles.

It should be stressed that the particular behaviors of $\tau_{\text{fast,slow}}$ from double-exponential fits are not unambiguously indicative of specific diffusion processes in the sample, but, like first cumulants, may possess features associated with several different modes. Similar effects may occur in numerical inverse Laplace transformations of data in computer programs such as the commonly used CONTIN package [143, 144], which looks for the “simplest” set of decay coefficients consistent with a measured correlation function. Rather than extracting only D_r by restricting measurements to extremely low q [139, 145], and rather than attempt to calculate a first cumulant or approximate “effective” diffusion coefficients to compare with the result of a fit [107, 111, 113, 139, 146–148], the fast modern computer makes it possible to directly fit Maeda's full form for monodisperse, rigid, hard rods to correlation functions at all q and t with only five adjustable parameters.

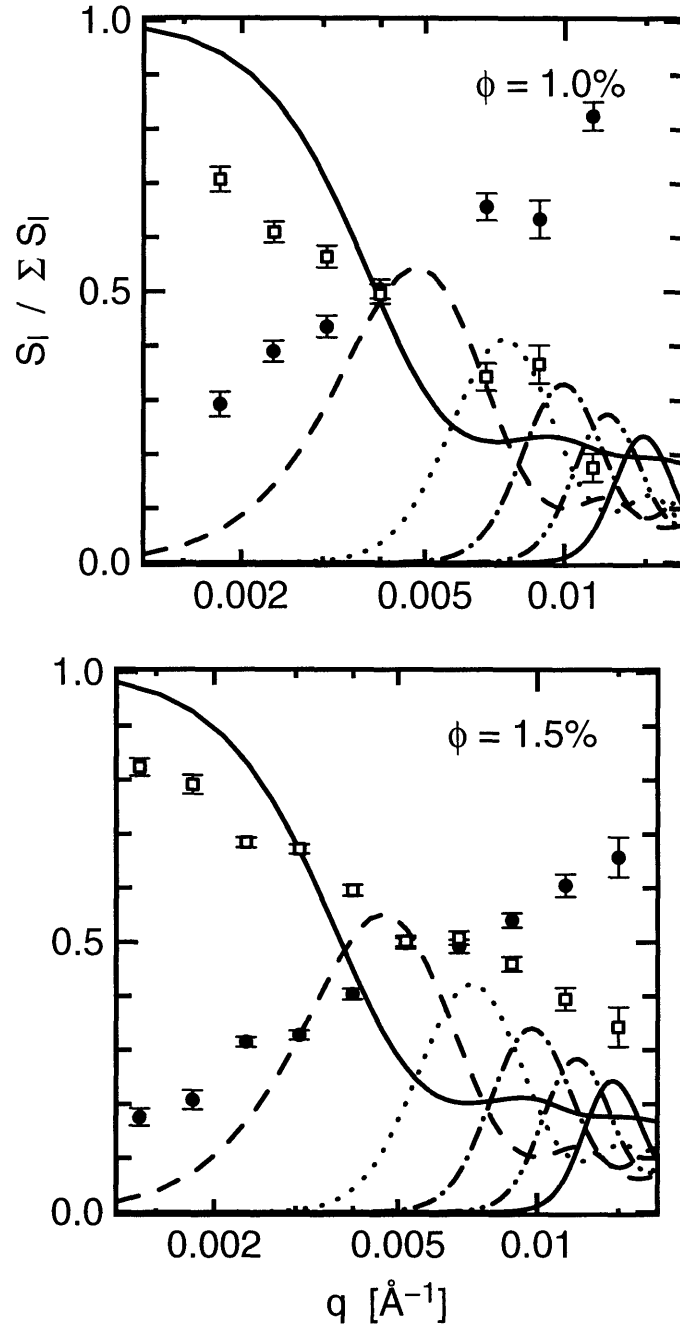


Figure 4-4: Relative mode amplitudes $S_{\text{fast,slow}}/(S_{\text{fast}} + S_{\text{slow}})$ and $S_l(q)/\sum_l S_l(q)$ for correlation functions fitted to the double-exponential form (*points*) and the Maeda form (*curves*), respectively. Curve labels are shown in Fig. 4-3. Generally speaking, $S_l(q)$ peaks at higher q as l is increased.

Chapter 5

X-ray photon correlation spectroscopy study of concentrated, nematic suspensions of rigid rods

5.1 Models of dynamics in nematic liquid crystals

5.1.1 Director fluctuations

The most common picture of equilibrium density fluctuations in oriented liquid crystals involves collective dynamics, specifically those that arise from long-wavelength fluctuations in the nematic director orientation [1, 149]. There are three modes—bend, splay, and twist—that characterize distortions in the “director field” characterized at equilibrium by the unit vector \mathbf{n} . When one part of the field slightly reorients by an amount $\delta\mathbf{n}(\mathbf{R})$ perpendicular to \mathbf{n} , the associated free energy density is

$$d\mathcal{F}(\mathbf{R}) = \frac{1}{2}K_1(\nabla \cdot \delta\mathbf{n})^2 + \frac{1}{2}K_2(\mathbf{n} \cdot \nabla \times \delta\mathbf{n})^2 + \frac{1}{2}K_3[\mathbf{n} \times (\nabla \times \delta\mathbf{n})]^2. \quad (5.1)$$

$K_{1,2,3}$ are the splay, twist, and bend elastic constants, respectively. Writing this in terms of the Fourier transform, $\delta\mathbf{n}(\mathbf{q})$, of the fluctuations gives [1, 150]

$$d\mathcal{F}(\mathbf{q}) = \frac{1}{2}K_1[\mathbf{q} \cdot \delta\mathbf{n}(\mathbf{q})]^2 + \frac{1}{2}K_2[\mathbf{n} \cdot \mathbf{q} \times \delta\mathbf{n}(\mathbf{q})]^2 + \frac{1}{2}K_3[\mathbf{n} \times (\mathbf{q} \times \delta\mathbf{n}(\mathbf{q}))]^2 \quad (5.2)$$

$$= \frac{1}{2}K_1[\delta\mathbf{n}(\mathbf{q}) \cdot \mathbf{q}]^2 + \frac{1}{2}K_2[\delta\mathbf{n}(\mathbf{q}) \cdot \mathbf{q} \times \mathbf{n}]^2 + \frac{1}{2}K_3[\delta\mathbf{n}(\mathbf{q})]^2(\mathbf{q} \cdot \mathbf{n})^2. \quad (5.3)$$

It follows from the equipartition theorem that there will be two modes of fluctuation that are “mixtures” of the three “pure” modes.

$$\langle (\delta\mathbf{n}(\mathbf{q}) \cdot \hat{\mathbf{q}})^2 \rangle = \frac{k_B T}{V} \cdot \frac{1}{K_1 q_{\perp}^2 + K_3 q_{\parallel}^2} \quad (5.4)$$

is the “splay-bend” mode, and

$$\langle (\delta \mathbf{n}(\mathbf{q}) \cdot \hat{\mathbf{q}} \times \mathbf{n})^2 \rangle = \frac{k_B T}{V} \cdot \frac{1}{K_2 q_{\perp}^2 + K_3 q_{\parallel}^2}, \quad (5.5)$$

is the “twist-bend” mode, where $q_{\parallel}^2 \equiv (\mathbf{q} \cdot \mathbf{n})^2$ and $q_{\perp}^2 \equiv q^2 - (\mathbf{q} \cdot \mathbf{n})^2$. It can be shown (see [1, 151] and references therein) that photon correlation spectroscopy measurements would be expected to display two corresponding decay modes with time constants

$$\tau_{1,2}(\mathbf{q}) = \frac{\eta_{1,2}(\hat{\mathbf{q}})}{K_{1,2} q_{\perp}^2 + K_3 q_{\parallel}^2}. \quad (5.6)$$

The effective viscosities $\eta_{1,2}(\hat{\mathbf{q}})$, along with the elastic constants, can be calculated from first principles [1, 30, 37, 97, 152–156] for comparison with experimental results. Such measurements have historically been possible by rotating the sample in the apparatus [149, 157] or by using depolarized scattering [150] in order to acquire data at several $\mathbf{q} \cdot \mathbf{n}$ values. However, multispeckle experiments such as ours offer the advantage of probing the full range of $\mathbf{q} \cdot \mathbf{n}$ simultaneously.

5.1.2 Self-diffusion

Another approach to predicting the equilibrium dynamics in nematics is to expand the Doi-Shimada-Okano formalism discussed in Sec. 4.1 to correctly treat the distribution functions, $f(\mathbf{R}, \mathbf{u}, t)$, in the orientationally ordered phase. This method, developed by van der Schoot and Odijk [158], involves rewriting Eqn. 4.16 so that the equilibrium distribution function is no longer isotropic:

$$f(\mathbf{R}, \mathbf{u}, t) = f_{\text{eq}}(\mathbf{u}) + \delta f(\mathbf{R}, \mathbf{u}, t). \quad (5.7)$$

This adds a term to the definition of the operator θ in Eqn. 4.23,

$$\begin{aligned} \theta(\mathbf{q}, \mathbf{u}) F(\mathbf{q}, \mathbf{u}) &= \left[D_{\parallel} (\mathbf{q} \cdot \mathbf{u})^2 + D_{\perp} (q^2 - (\mathbf{q} \cdot \mathbf{u})^2) - D_r \Re^2 \right] F(\mathbf{q}, \mathbf{u}) \\ &\quad - D_r \Re F(\mathbf{q}, \mathbf{u}) \Re \int d\mathbf{R} \int d\mathbf{u}' w(\mathbf{q}, \mathbf{u}, \mathbf{u}') f_{\text{eq}}(\mathbf{u}'), \end{aligned} \quad (5.8)$$

and also alters the operator Φ in Eqn. 4.24,

$$\Phi(\mathbf{q}, \mathbf{u}) F(\mathbf{q}, \mathbf{u}) = F(\mathbf{q}, \mathbf{u}) + c f_{\text{eq}}(\mathbf{u}) \int d\mathbf{u}' w(\mathbf{q}, \mathbf{u}, \mathbf{u}') F(\mathbf{q}, \mathbf{u}'). \quad (5.9)$$

Despite its relative complexity, the single-particle picture might be more appropriate than the collective fluctuation model to characterize scattering at large qL values reached by X-ray wavelengths, where the system no longer completely resembles a continuum of “point rods”. It also has the advantage of providing clear continuity across the orientational ordering transition with expressions for diffusion in the isotropic phase. However, Eqns.

5.8 and 5.9 appear to require foreknowledge of the equilibrium orientational distribution function. Also, we know of no commonly used forms of the ODF—such as the Maier-Saupe form described in Sec. 2.1.2.1—to have been incorporated into Maeda’s matrix framework (Sec. 4.2) for straightforward computation of correlation functions.

5.2 Measured dynamics of orientationally ordered suspensions of böhmite in glycerol

We have measured correlation functions of two different concentrations of böhmite in glycerol, one (2.0% volume fraction) just above the orientational transition, the other (7.5%) well into the aligned phase. As with the isotropic samples in Sec. 4.3, we selected sample temperatures that produced dynamics on experimentally accessible timescales.

To briefly recount our findings in Sec. 2.3, both the 7.5% and 2.0% samples displayed azimuthal anisotropy in their static scattering patterns. For the 2.0% sample, two azimuthal peaks were visible: one that would indicate rods parallel to the capillary, and the other originating from rods perpendicular to the capillary. We interpreted this as evidence for the coexistence of two nematic domains with distinct directors. In the 7.5% sample, the peak from the parallel domain had all but vanished, while the perpendicular domain generated the bulk of the scattering. In addition, fits to the azimuthal profiles indicated that significant portions of both samples were isotropic.

In these studies, unlike the isotropic data of the previous chapter, we observed both radial and azimuthal dependences to the dynamics. Instead of using area plots displaying the entire (q, φ) -space spanned by our measurements, we will show here representative “slices” through that space: first, curves depicting the variation of some quantity along q for several φ , then *vice versa*. Our intention is to convey the overall radial and azimuthal trends while still presenting quantitative results. When the data displayed some relatively simple q -dependence, we fit to a trial function at each φ and then plotted the fit parameters versus φ .

5.2.1 Near the orientational transition point

Several measured correlation functions for the 2.0% sample are shown in Figs. 5-1 and 5-2. The overall shapes of the correlation functions closely resembled those of the isotropic 1.0% and 1.5% samples. We once again used a double-exponential function (Eqn. 4.72) to fit the correlation functions. Time constants of the fitted decays are plotted in Fig. 5-3. While the fast mode appeared consistent with $\tau_{\text{fast}} \propto q^{-2}$, the slow mode seemed more or less independent of q . Dashed lines in Fig. 5-3 indicate fits to find the effective diffusion coefficient, $D_{\text{fast}}(\varphi) = q^2\tau_{\text{fast}}(q, \varphi)$. The slow mode displayed little variation with q .

It may have been the case, however, that $\tau_{\text{slow}}(q, \varphi)$ was not always accurately measured in this data set, in part because of noise on the correlation functions, but mostly because

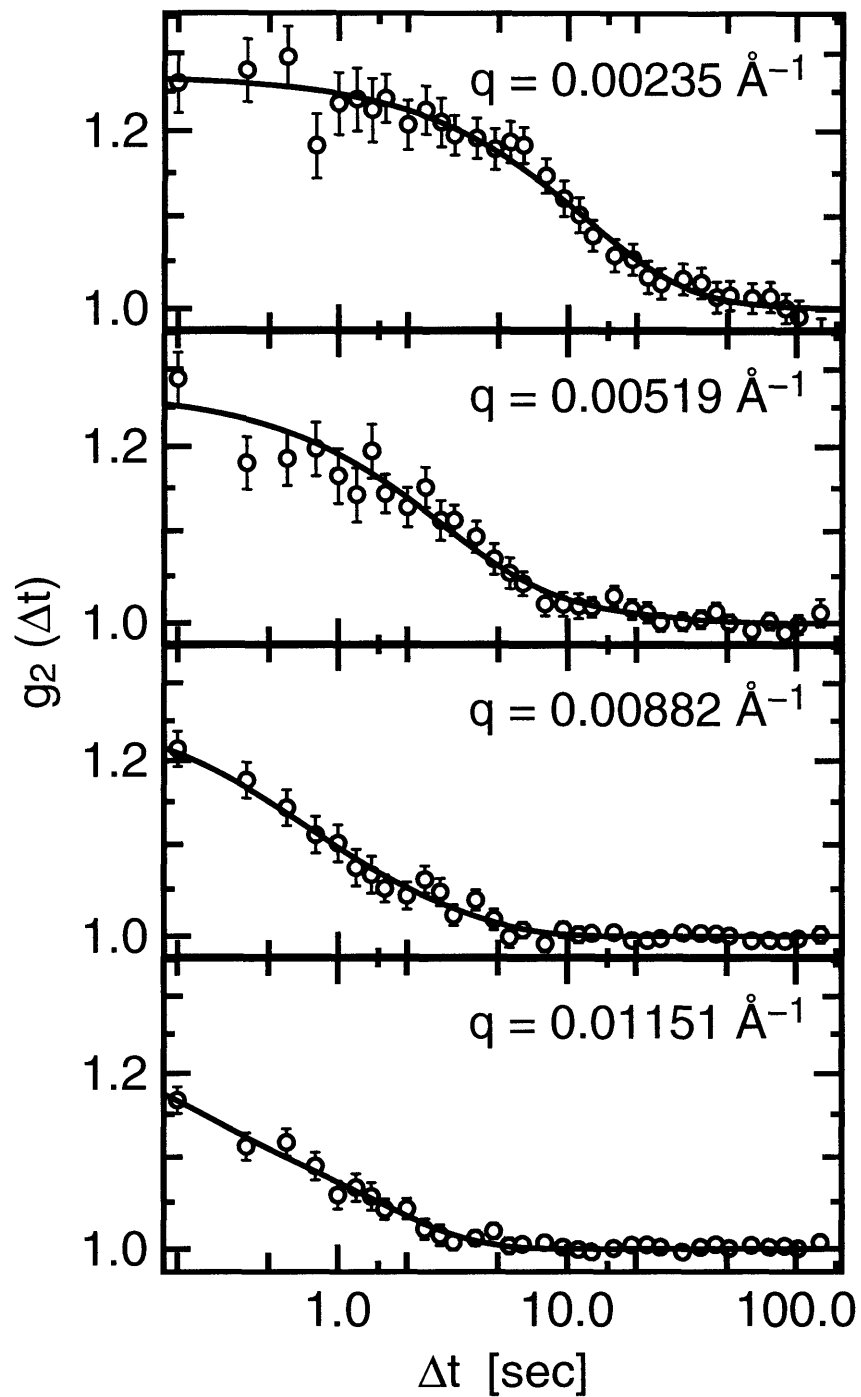


Figure 5-1: Intensity-intensity autocorrelation functions at azimuthal angle $\varphi = 144^\circ$ for 2.0% volume fraction sample of böhmite in glycerol at -12.3°C as measured by XPCS. Lines are fits to double-exponential decay.

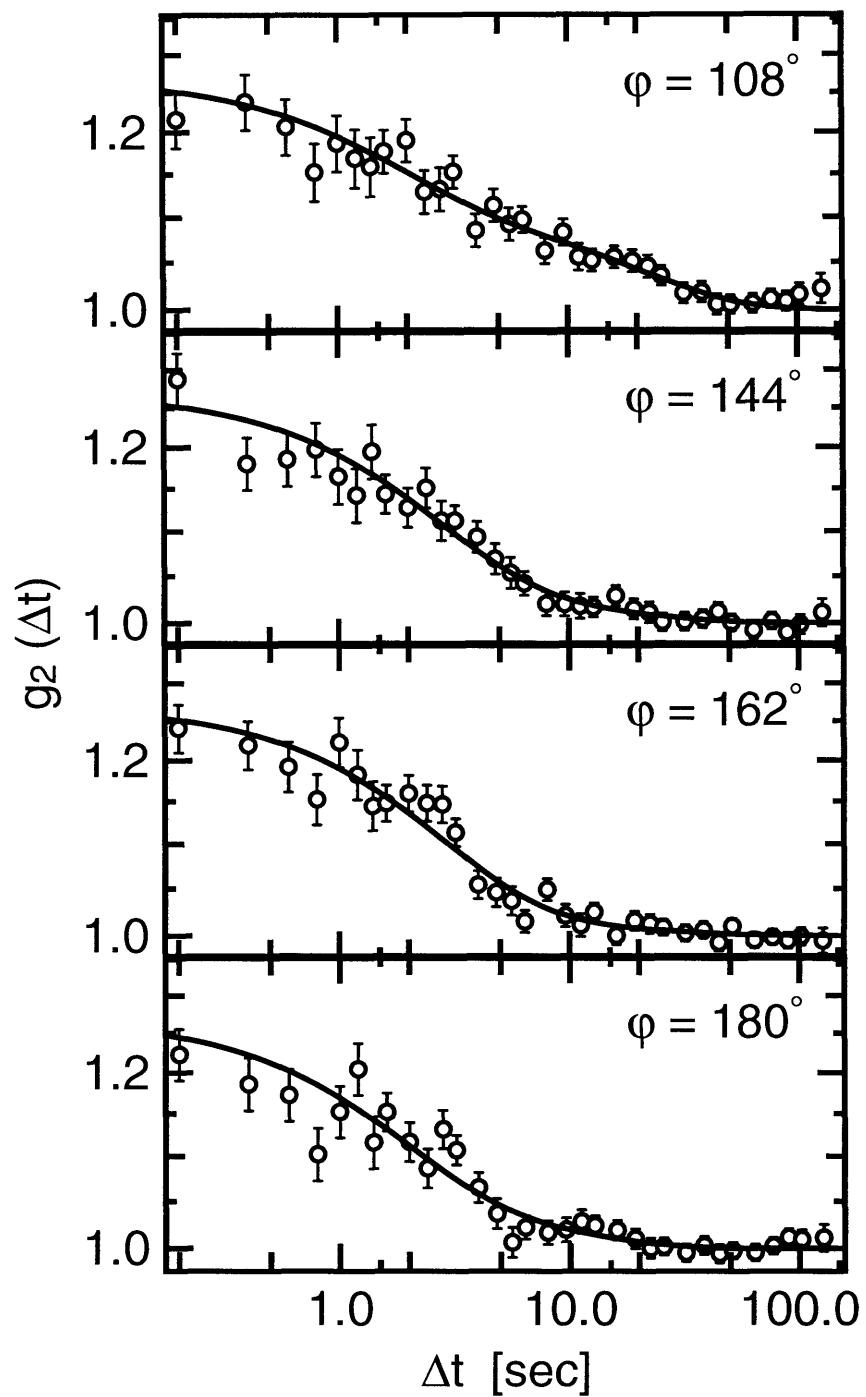


Figure 5-2: Intensity-intensity autocorrelation functions at $q = 0.00519 \text{ \AA}^{-1}$ for 2.0% volume fraction sample of böhmite in glycerol at -12.3°C as measured by XPCS. Lines are fits to double-exponential decay.

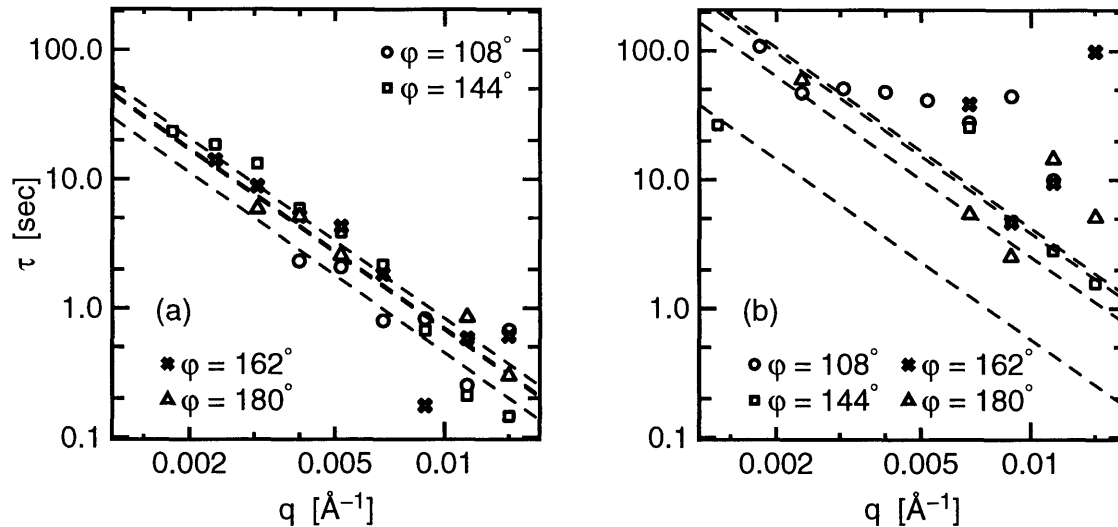


Figure 5-3: Fitted characteristic times of double-exponential decays as in Eqn. 4.72 for 2.0% volume fraction sample of böhmite in glycerol at -12.3°C . Several φ values are shown for both $\tau_{\text{fast}}(q, \varphi)$ (a) and $\tau_{\text{slow}}(q, \varphi)$ (b). Lines indicate $\tau \propto q^{-2}$.

of the relatively large amplitude of the fast mode, as seen in Fig. 5-4. One striking feature of the measured $S_{\text{fast}}(q, \varphi)$ was that it varied little with q except near $\varphi = 90^\circ$, where it gradually increased with q in a manner reminiscent of the isotropic fast mode in Fig. 4-4. And indeed, Figs. 2-6 and 2-10 indicated that near $\varphi = 90^\circ$ a large portion of the scattering arose from the isotropic part of the sample.

In Fig. 5-5 we show the fitted fast-mode diffusion coefficient and the azimuthal behavior of S_{fast} , along with a representative azimuthal slice of the static scattering cross-section. The fast mode amplitude seemed more or less independent of φ , although at low q the fast mode was weaker near the structure factor peak, *i.e.* in the nematic domain. Similarly, the diffusion coefficient displayed a shallow minimum in the nematic region. As we saw in Fig. 4-3, the higher-amplitude modes are largely rotational. It would seem reasonable to expect rotational diffusion to be hindered in the nematic phase even more strongly than in a semidilute isotropic phase.

5.2.2 High concentration

In general, sample viscosities increased markedly with concentration, and the 7.5% sample was substantially more viscous than other samples discussed thusfar. Our measurements on this sample, consequently, were made at room temperature instead of -12°C . The scattered intensity was also significantly higher, as would be expected.

Correlation functions can be found in Figs. 5-6 and 5-7. Surprisingly, a double-exponential decay did not satisfactorily fit all the measured correlation functions. The marked “compression” of the decay seen in Fig. 5-7 as φ approaches 180° provides one clear example.

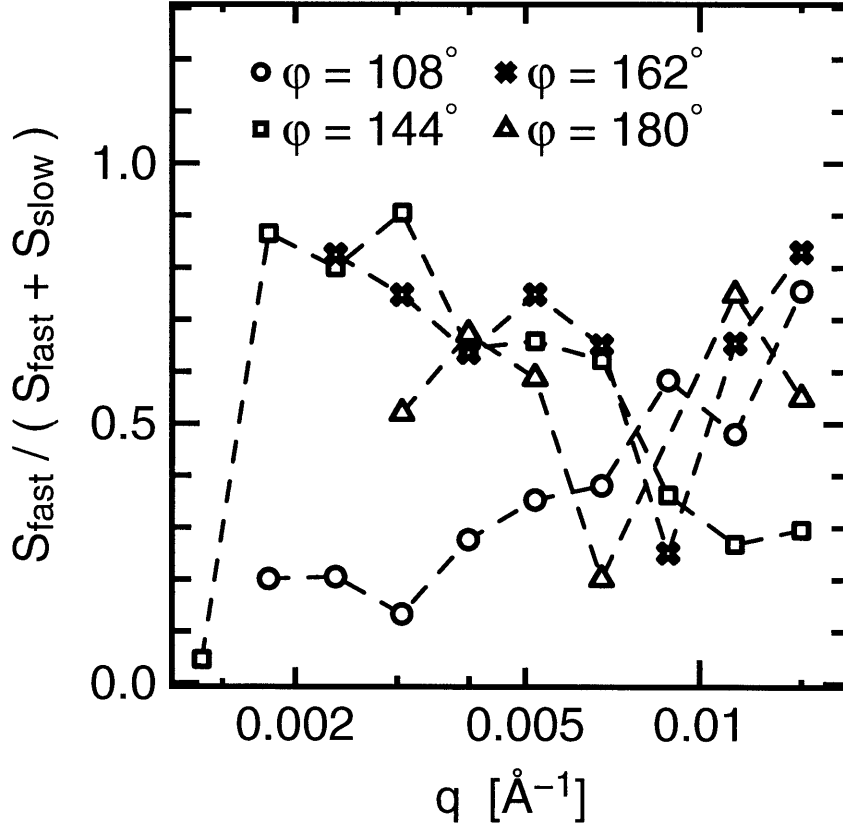


Figure 5-4: Relative amplitude of fast decay mode for the 2.0% sample at several azimuthal angles. Lines are guides to the eye.

Excellent fitting was obtained, however, with a stretched exponential [115]:

$$S(\mathbf{q}, t) \propto \exp \left[- \left(\frac{t}{\tau(q, \varphi)} \right)^{\nu(q, \varphi)} \right]. \quad (5.10)$$

In this form the exponent $\nu(q, \varphi)$, rather than separate, additional decay modes, serves to distort the dynamic structure factor from a simple exponential decay.

Both parameters exhibited unexpected behavior. The time constants, seen in Fig. 5-8, were best fit by a function $\gamma(\varphi) = q\tau(q, \varphi)$ instead of the $D(\varphi) = q^2\tau(q, \varphi)$ function that characterized more dilute samples. Also, while there was little apparent q -dependence to the exponent ν (Fig. 5-9), it displayed striking variations with φ (Fig. 5-10), at some points even dropping below 1.0.

Each of these three features, $\tau \propto q^{-1}$, ν universal for q , and $\nu > 1$, have been recently

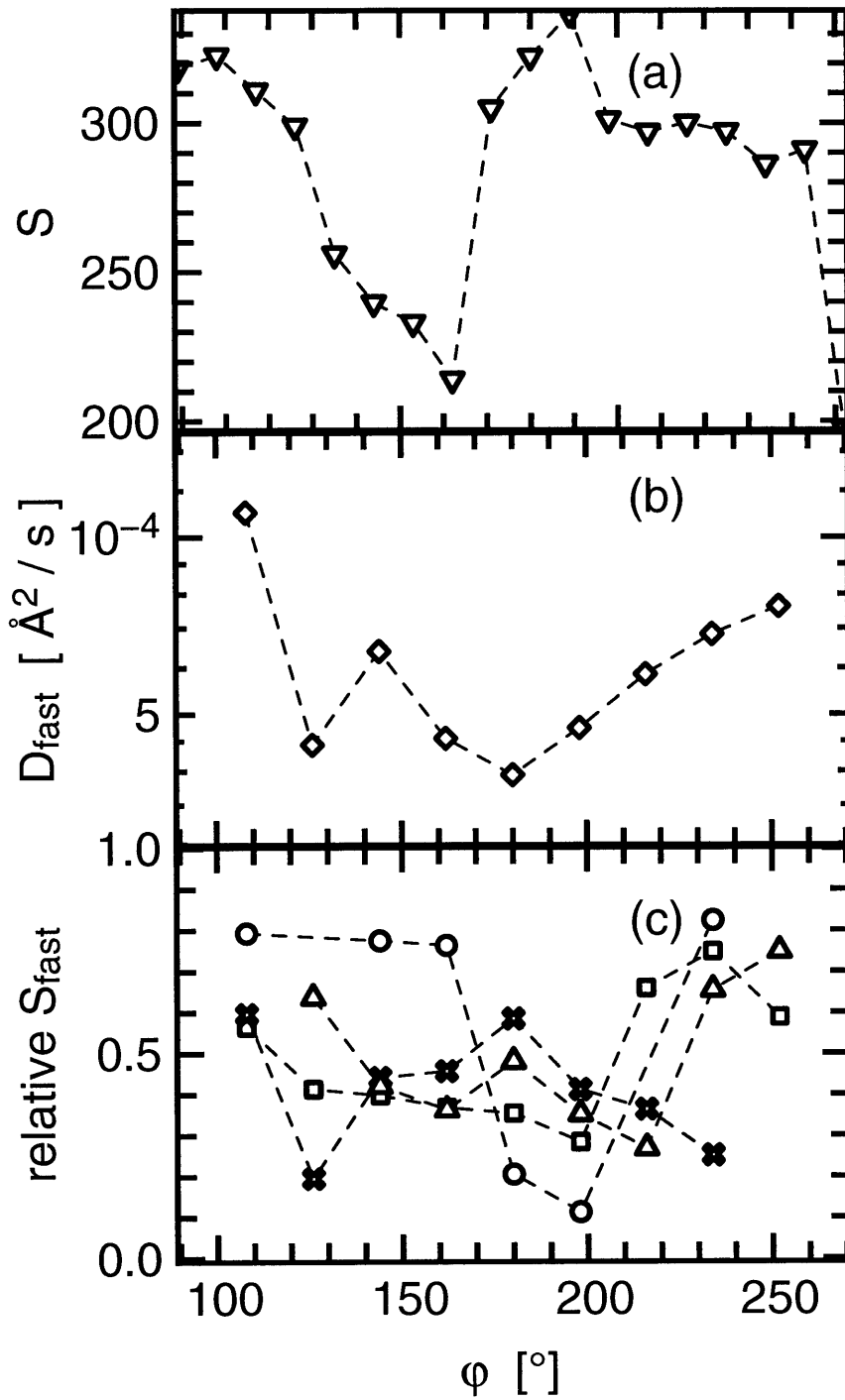


Figure 5-5: Azimuthal dependences of (a) the static scattering as in Sec. 2.3.1, (b) the apparent fast-mode diffusion coefficient, and (c) the fast-mode amplitude for the 2.0% sample. The four sets of points in (c) correspond to $q = 0.00235 \text{ \AA}^{-1}$ (circles), 0.00519 \AA^{-1} (squares), 0.00882 \AA^{-1} (X's), and 0.01151 \AA^{-1} (triangles). Lines are guides to the eye.

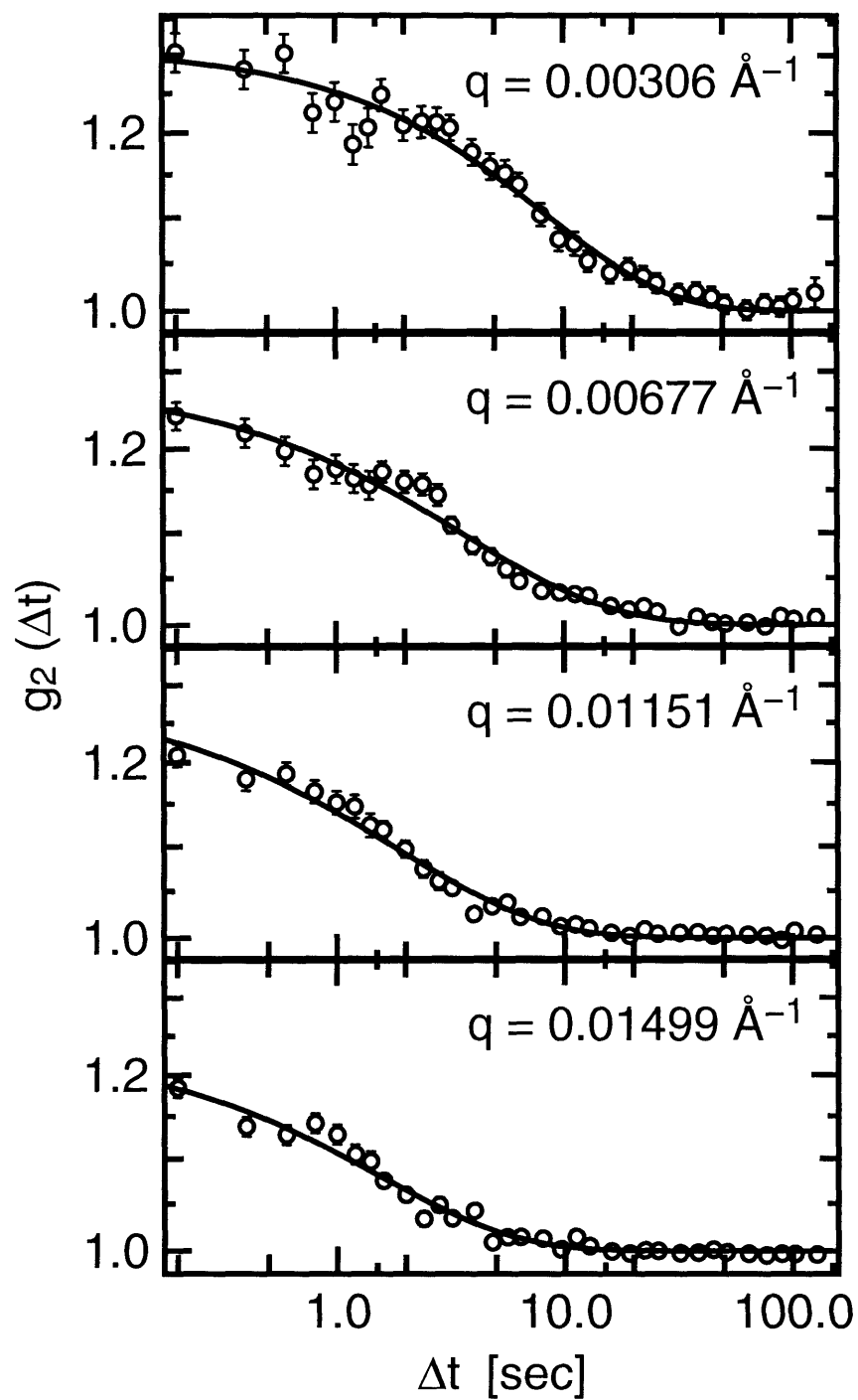


Figure 5-6: Intensity-intensity autocorrelation functions at azimuthal angle $\varphi = 144^\circ$ for 7.5% volume fraction sample of böhmite in glycerol at 25.5°C as measured by XPCS. Lines are fits to stretched- (or compressed-) exponential decay.

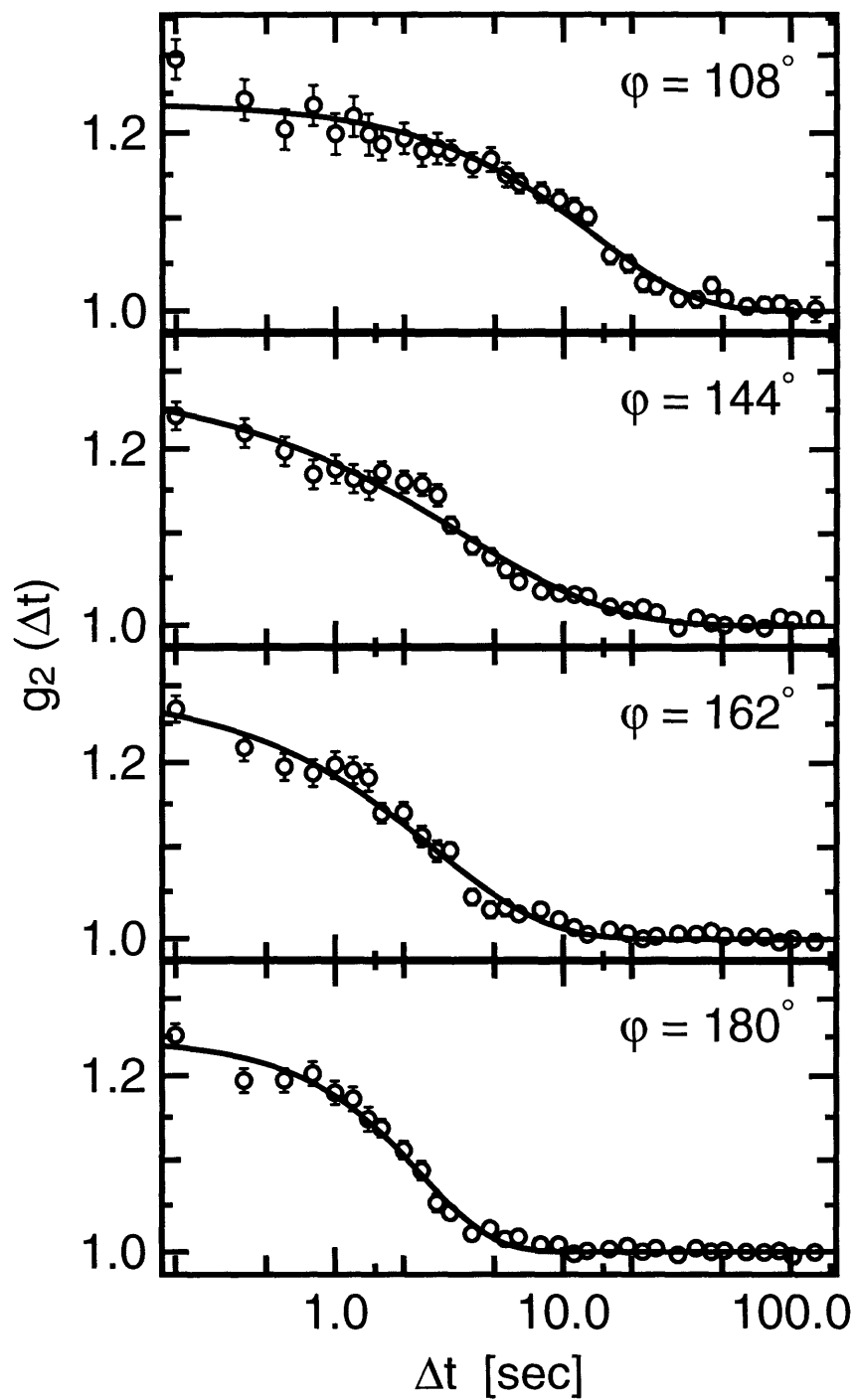


Figure 5-7: Intensity-intensity autocorrelation functions at $q = 0.00519 \text{ \AA}^{-1}$ for 7.5% volume fraction sample of böhmite in glycerol at 25.5 °C as measured by XPCS. Lines are fits to stretched- (or compressed-) exponential decay.

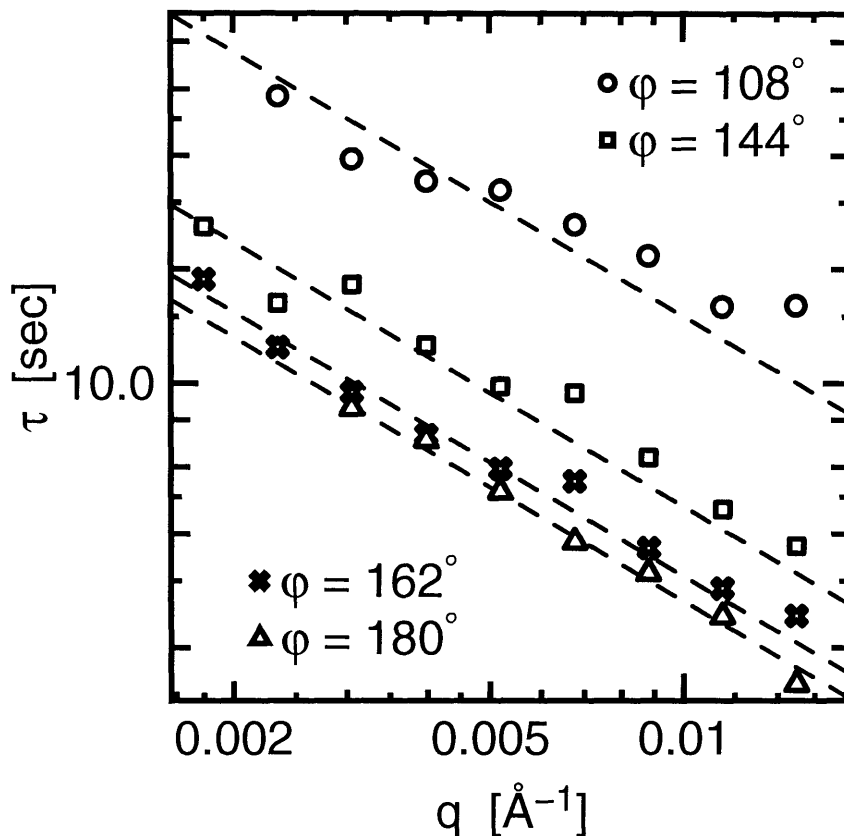


Figure 5-8: Fitted characteristic times of stretched-exponential decays as in Eqn. 5.10 for 7.5% volume fraction sample of böhmite in glycerol at 25.5 °C. Several φ values are shown. Lines indicate $\tau \propto q^{-1}$.

reported in “jammed” materials [159–161]; that is, systems such as glasses and gels which are fixed in a nonequilibrium configuration due to strong interparticle interactions. The $\tau \propto q^{-1}$ dependence is characteristic of ballistic motion of a free particle [34], which in this case corresponds to the behavior of large-scale inhomogeneities in the sample as they relax elastically toward equilibrium over extremely long (essentially infinite) timescales [159]. Stresses are initially “frozen” into the sample through some quenching event, such as the centrifugation process we used to load our samples into the capillaries. The resulting displacement field leads to $\nu \sim 1.5$ [160]. It seems highly likely that the aligned domain in this 7.5% sample was not in an equilibrium phase, but rather existed in a jammed state due to the very high density of rods it contained.

Intriguingly, in our samples the three notable traits of jamming seemed absent in a narrow azimuthal region around $\varphi = 180^\circ$. Fig. 5-10 displays this clearly. In that range the dynamics were nearly eight times as fast, the correlation functions were not compressed, but rather stretched (and hence potentially in agreement with a double-exponential or even the van der Schoot-Odijk dynamic structure factor). As well, the static scattering was less

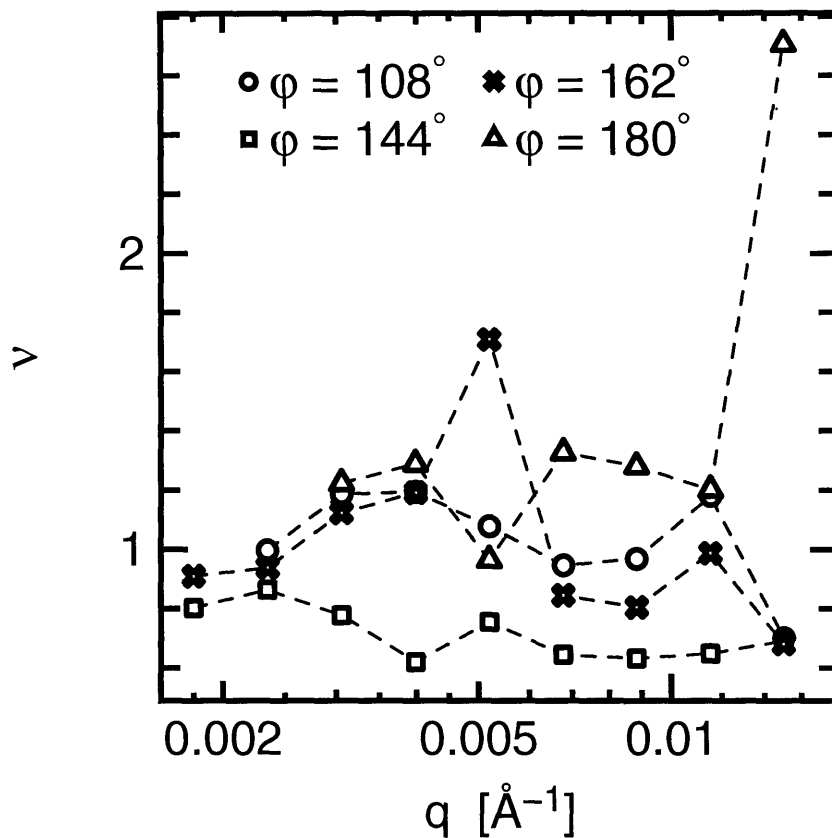


Figure 5-9: Fitted characteristic exponents of stretched-exponential decays as in Eqn. 5.10 for 7.5% volume fraction sample of böhmite in glycerol at 25.5 °C. Several φ values are shown. Lines are a guide to the eye.

intense. In this 7.5% sample, our analysis in Sec. 2.3, combined with the separation of each domain's scattering shown in Fig. 3-11, indicated that even when the vast majority of the sample is aligned, the small amount of lingering isotropic material still provided the majority of the scattering at low q and at φ values away from the main nematic peak.

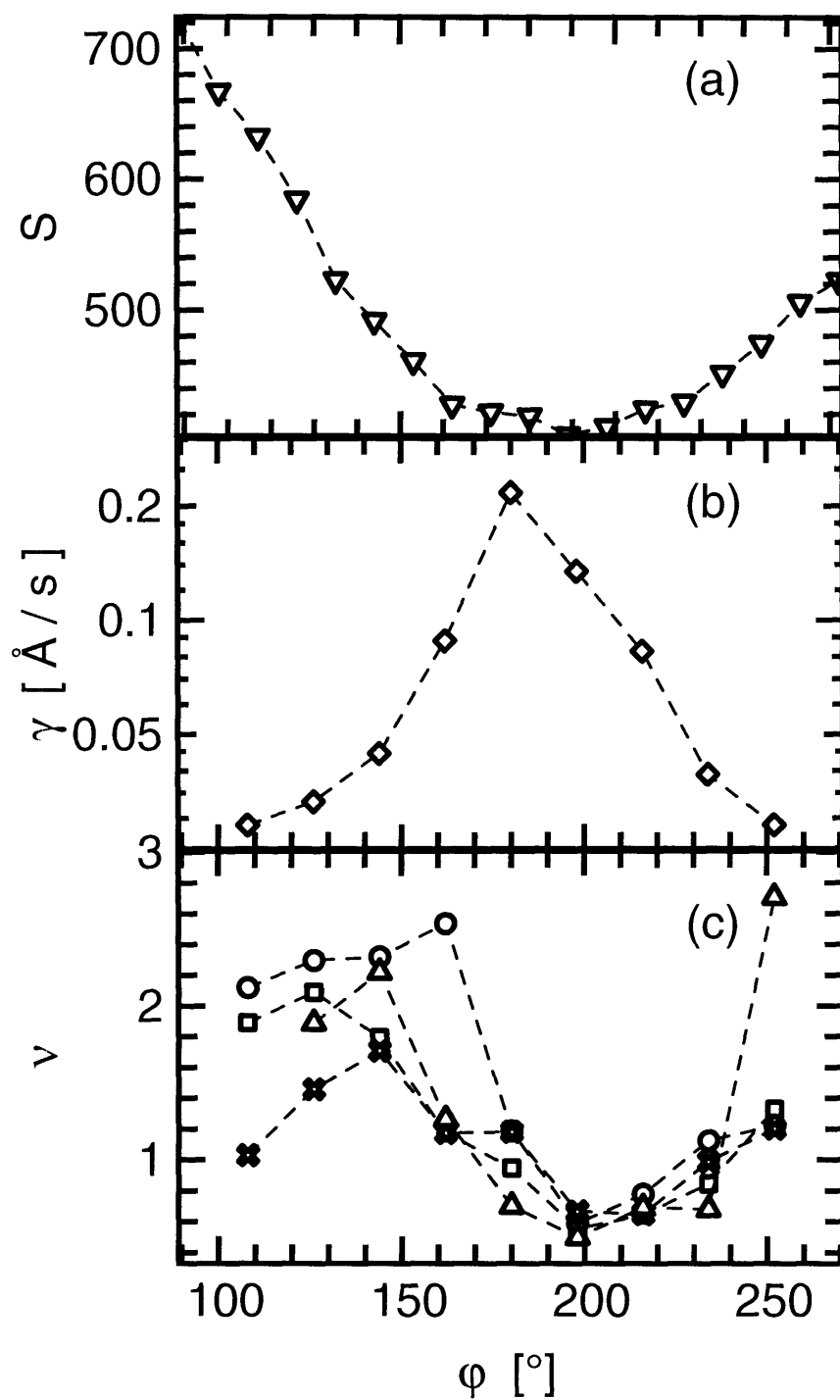


Figure 5-10: Azimuthal dependences of (a) the static scattering, (b) the time constant proportionality coefficient, and (c) the stretching (compressing) exponent. The four sets of points in (c) correspond to $q = 0.00235 \text{ \AA}^{-1}$ (circles), 0.00519 \AA^{-1} (squares), 0.00882 \AA^{-1} (X's), and 0.01151 \AA^{-1} (triangles). Lines are guides to the eye.

Chapter 6

Conclusion

In this thesis we have used X-ray scattering to explore the structure and dynamics of rigid, colloidal böhmite rods in solution. We found that nematic alignment occurred at volume fractions well below the classic Onsager prediction, which was to be expected, given that charge and polydispersity effects shift the nematic transition to lower concentrations. Two distinct aligned domains were detected in our samples, and we sought to characterize each separately.

We used the azimuthal dependence of the static scattering cross-section to identify the proportion, orientation, and nematic order parameter of each domain. One nematic domain grew in size with concentration. This domain was oriented perpendicular to the sample-holding capillary, and we presumed its orientation was determined by interactions with the capillary walls. The other domain, which was aligned parallel to the capillary—presumably by flow—disappeared at higher volume fractions. In attempting to ascertain the nematic order parameters, we concluded that Davidson’s general form for the orientational distribution function would inevitably lead to ambiguous results when applied to multidomain samples. Using the Maier-Saupe distribution function we found that the perpendicular domain had the lower order parameter of the two but displayed an intriguing peak at wavevectors corresponding to the interparticle spacing. This may indicate a subtle positional correlation among neighboring rods in the nematic phase. We also found that isotropic material persisted in the samples even far above the orientational transition.

To investigate the rod-rod interactions, we measured the effective radial interparticle structure factor over a range of rod concentrations up to the transition and into the aligned phase. Doing so required a numerical evaluation of the form factor for polydisperse, rigid rods, which we compared to the lowest-volume-fraction data. It seemed as though the rods were significantly thinner than TEM studies had indicated, even when a crude accounting for an electrical double-layer was included. As expected for suspensions of charged rods, the wavevector of the radial peak in the effective structure factor varied as volume fraction to the one-half power, except for a small plateau observed around the nematic transition. In that same regime, a discontinuity in the radial peak width lent further credence to our supposition

of a positional reorganization in concert with the onset of alignment. We attempted to separate from one another the interparticle structure factors of the isotropic and nematic phases, but we found that the structure factor peaks were too broad to cleanly resolve the individual components.

We characterized the equilibrium dynamics of our suspensions just below and above the ordering transition. The two were qualitatively similar, with pairs of effective time constants that decayed roughly as the inverse square of the wavevector. In the isotropic samples, we implemented a well-known but complicated and hence little-used matrix formulation for the dynamic structure factor. We adapted the routines for use in nonlinear least-squares fits and used them directly extract our samples' self-diffusion coefficients from the measured correlation functions. We suggested that deviations from an inverse-square dependence of effective time constants on wavevector can be easily understood as the result of confluence of multiple dynamical modes. We observed that while the matrix formalism is especially suited for XPCS measurements at high wavevectors and long times, its applicability would substantially broaden with extensions to incorporate of polydispersity and non-isotropic orientational distribution functions.

In the nematic samples, we were able to study the dynamics of both the primary nematic phase and the remnant isotropic phase simultaneously. This was possible because different azimuthal angles received scattering from different components of the sample. The fast decay mode was especially prominent in the nematic phase, although it tended toward slower time constants overall than in the isotropic phase. The largest-volume-fraction sample behaved remarkably unlike the isotropic and less concentrated nematic samples. It displayed the stretched-exponential, high-exponent correlations and strongly hindered diffusion indicative of the elastic relaxation of a nonequilibrium, "jammed" system.

This thesis highlights the fact that even seemingly simple orientationally anisotropic particles in suspension can exhibit a rich and complex variety of structural and dynamical behaviors. Not surprisingly, those behaviors are profoundly interrelated, and a full understanding requires further advances in the theoretical, instrumental, and analytical tools available for studying orientationally ordered materials. We believe we have demonstrated here that the combination of SAXS and XPCS facilitates the simultaneous characterization of many aspects of a sample—its nematic domain structure, degree(s) of orientational ordering, interparticle separation, positional correlation length, and self-diffusion coefficients—all on length scales comparable to the particle sizes. Such measurements offer great potential for new insights into these fascinating materials.

Appendix A

Data analysis for anisotropic correlation functions

The use of charge-coupled device (CCD) arrays for correlation spectroscopy began roughly a decade ago [162,163], and the field of CCD-based X-ray Photon Correlation Spectroscopy (XPCS) is nearly as old [164–166]. Since then, a number of important data collection and processing techniques specific to multi-speckle analysis have been developed [52, 54, 167]. Several advancements beyond these are underway [55,168], and more are undoubtedly ahead. The field is beginning to attract a broad user base and as such merits distilling the aforementioned collective expertise into a small number of standard software packages. Ideally, an XPCS data reduction program would be easily accessible to novice users while simultaneously allowing developers sufficient flexibility to implement and test new algorithms within a unified framework. It would generate on-the-fly results during beam time as well as allow for careful analysis offsite.

A first attempt at such an “all-in-one” software package, called ‘coherent’, has been developed at MIT and tested at the Advanced Photon Source beamline 8-ID. This public-domain software is written in the Yorick interpreted language [169,170]. Yorick is not only freely available for several operating systems but is also optimized for performing intensive mathematical operations on large, multidimensional arrays of the sort generated by CCD detectors.

Since correlation function normalization entails the use of the static scattering cross-section, ‘coherent’ also doubles as a SAXS analysis tool. (This can be seen in Eqn. 1.28.) By keeping track of intensities on a frame-by-frame basis, ‘coherent’ can also be used in experiments that study transient responses to nonequilibrium conditions such as quenches and applied fields.

This appendix will highlight several new concepts in correlation function spectroscopy data analysis that have been developed specifically for ‘coherent’. Many arise out of one of the major design goals for ‘coherent’: comprehensive treatments of dynamics measurements

in orientationally anisotropic materials.

A.1 Data structure

The primary working assumption of the routines described here is that raw data has been collected in a filled, rectangular array of three dimensions: position (x), position (z), and time (t), with a constant interval between all neighboring indices along a particular dimension. The time dimension requirement renders this approach unsuitable for so-called “realtime” analyses, where processing is performed separately for each 2-D image while the next is being acquired. On the other hand, the structure used here makes it algorithmically simple and computationally efficient to perform operations and transformations—especially time averages—on the entire data set simultaneously.

With, in principle, no limit on the number of exposures in a sequence, data sets may become so large as to outstrip a computer’s memory limits. Recognizing that each pixel in the array can be treated as a unique detector independent of all others, we can circumvent memory limits by ensuring that all routines can be applied sequentially on several x - z “segments” (subsets) of the full data array, and by then adding a final step organizing the results from all segments. Segments must themselves be filled, rectangular arrays but may be as small as a single pixel times the number of exposures.

We also strive to make all routines compatible with “kinetics mode” acquisition, wherein only a “slice” (a subset) of the detector array is illuminated, with the rest of the array serving as high-speed memory for the storage of a rapid sequence of separate exposures accumulated into a single detector “frame” (image) [52]. In this case, raw data comes in an x - z - t format, but most pixel coordinates have been shifted from their original location by the kinetics mode. Since a delay is typically incurred when transferring a frame to the computer, there will also be a time gap between the last slice on one frame and the first slice on the next, which exceeds that between neighboring slices on a single frame. We can both correct for the pixel shift and recognize the two disparate timescales by reshaping the raw data into a four-dimensional, x - z - t_{frame} - t_{slice} configuration. It then remains to design all analyses to handle either one or two time dimensions.

A.2 Image partitioning and masking

The x - z grid based on the detector dimensions, which is used for data input, is generally an undesirable format into which to cast analysis results. For comparisons with theory, simulations, and other experiments, the scattering vector \mathbf{q} is the natural and conventional choice for an independent variable. Different experimental geometries or sample symmetries, however, may favor the breaking down of \mathbf{q} into different sets of components.

Analysis software should therefore allow the user to select which component set to use,

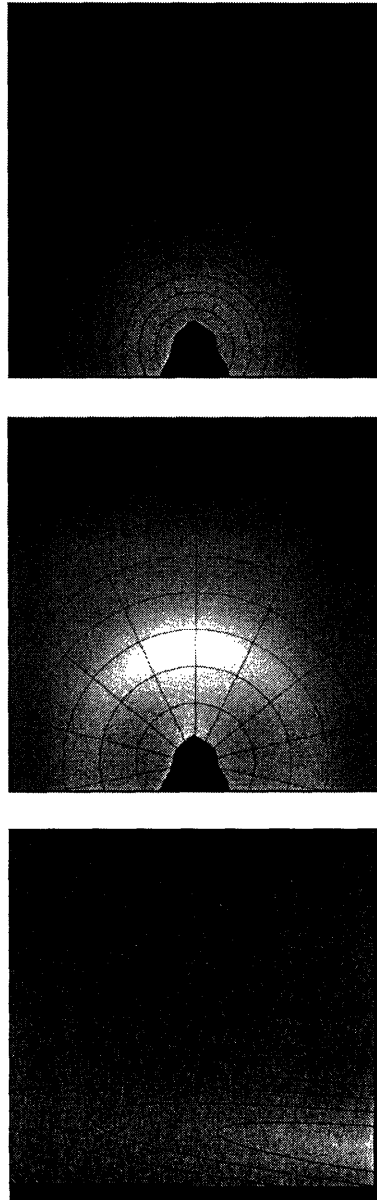


Figure A-1: Three examples of image partitioning: radial only in transmission geometry (*top*), radial and azimuthal in transmission (*middle*), and radial and axial in reflection geometry (*bottom*). Colors represent measured scattering intensity, white being greatest. Lines represent partition boundaries. Black regions at the lower ends of each image represent areas blocked by a beamstop, and have been masked out. The top and middle data sets correspond, respectively, to 1.5% and 7.5% volume fraction suspensions of böhmite in glycerol.

evaluate the coordinates of each pixel along those components, and then group pixels with similar coordinates into partitions for the averaging together of results. Corrections for distortions introduced by fiber-optic tapers in phosphor-coupled CCD arrays [171] can be made as an intermediate step during the calculation of \mathbf{q} for each pixel.

The ‘coherent’ software package allows the user to specify the number of partitions spanning the image along each component of \mathbf{q} and whether to space the partitions evenly or cluster them more closely in regions of high intensity. Several partitioning schemes are depicted in Fig. A-1. Each pixel is assigned a single partition number based on its coordinates in both dimensions. Two sets of partitions are chosen: one for averaging the static cross-section and one for averaging correlation functions. Statics partitions can usually be significantly smaller than those for correlation functions (“dynamics” partitions), because static cross-sections typically require fewer total photons for accurate measurement.

The user can also interactively select pixels to exclude from analysis in ‘coherent’. This is useful when regions of the detector are damaged, obstructed by other parts of the experimental apparatus (*e.g.* beamstop), or dominated by scattering from apparatus elements other than the sample (*e.g.* slit scattering). Pixels outside the user-defined “mask” are reassigned to partition number 0, which is discarded at the end of analysis.

A.3 Averaging analysis results over partitions

Averaging quantities of interest over all pixels within a partition—for example, averaging across pixels the time-averaged, corrected intensities to obtain the static scattering cross-section—becomes nontrivial when that partition spans several segments. (Image segments were described in Sec. A.1.) One cannot simply force the segments to correspond to partitions since partitions are generally not rectangular, nor can one rely on the user to always choose partitions small enough to fit entirely into memory.

The solution is to calculate sums of relevant quantities rather than averages, and to divide by the number of pixels in a partition only after all segments have been processed. Estimates of error can be obtained by measuring the RMS variation of a quantity across pixels in a partition, which requires storing the sum of the square of a quantity in addition to the sum itself.

Some partitions may contain no pixels at all, especially when 2-D partitioning is used. One example can be seen when using a polar (q, φ) grid such as the one in the center image of Fig. A-1. Several (q, φ) pairs fall off the image, despite being within the limits of q and the limits of φ spanned by the image. This will generally occur any time a nonrectangular partitioning scheme is used. If the result output is formatted in a rectangular array, as it is in ‘coherent’, the number of pixels per partition must be included alongside so that display routines and any subsequent analyses can identify which partitions contain meaningful information.

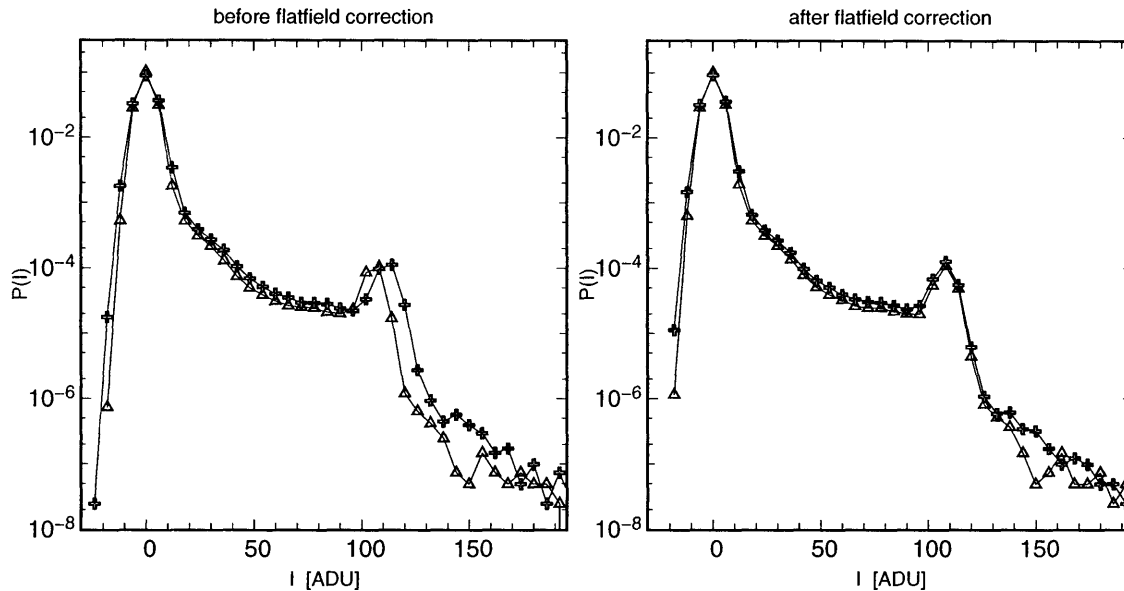


Figure A-2: Flatfield correction. Points represent intensity histograms from two separate 8000-pixel regions of a CCD array, each over a sequence of 850 exposures. Lines are a guide to the eye.

A.4 Image correction

A.4.1 Before time-averaging

Prior to any analysis, raw data should undergo a series of corrective adjustments on a pixel-by-pixel basis to isolate signal counts. Steps used in ‘coherent’ proceed in the following order:

1. Pixels reaching the analog-to-digital converter’s saturation value at any point during the exposure sequence are placed outside the mask and are not factored into final results.
2. Dark counts, as measured by time-averaging an unilluminated series of exposures taken just prior to and/or after data collection, are subtracted.
 - Although it is more computationally efficient to remove dark effects from fully processed correlation functions and/or scattering cross-sections [167], the subsequent steps in the image correction and normalization processes require initial dark subtraction.
 - Currently under development are algorithms to allow dark levels to be scaled on a frame-by-frame basis according to readings in an unilluminated detector region during data collection.

3. Flatfield normalization is applied, bringing the pixels' per-photon response to uniform levels. This amounts to applying a pixel-specific multiplicative constant to all readings.
 - Uniform illumination, which is difficult to achieve, is not strictly necessary to determine the relative responsiveness of a pixel in comparison to others in a detector array. The scattering from any sample of known scattering cross-section can be used as a source of illumination. The known cross-section vs. scattering vector can be evaluated (interpolated, if from a calibrated measurement) at the scattering vector of each pixel and compared to the measured cross-section.
 - If all pixels have nearly equivalent quantum efficiencies, variations in response will arise from spurious variations in the single-photon intensity distribution function, $P(I)$, among pixels. These variations can be eliminated by the flatfield correction, as demonstrated in Fig. A-2.
4. For direct-detection CCD arrays, lower-level discrimination [52] is applied to each data point.
 - To increase signal-to-noise levels at low intensities, readings below a predetermined threshold, deemed a “no-photon” level, are reset to zero.
 - In ‘coherent’, the discriminator threshold may be set to a specific analog-to-digital unit level or to some multiple of each pixel’s dark RMS.
 - Further details on the effects of lower-level discrimination can be found in Appendix B.

A.4.2 After time-averaging

There are some corrections that require better statistics than can be obtained from most single frames, especially in high-speed (low-intensity) exposure sequences. These include masking out “zingers” [171] and undoing distortions introduced by lower-level discrimination (Appendix B). Such corrections are best evaluated after the main analysis, specifically after all averages over frames and/or pixels have been taken.

A.5 Multiple tau correlation

We recall Eqn. 1.28, which states that correlation functions for any given pixel in an array can be obtained from the corrected intensity, $I(\mathbf{q}, t)$, by calculating

$$g_2(\mathbf{q}, \Delta t) = \frac{\langle I(\mathbf{q}, t) I(\mathbf{q}, t + \Delta t) \rangle_t}{\langle I(\mathbf{q}, t) \rangle_t^2}. \quad (\text{A.1})$$

In the most basic, “brute force” correlation method, a data set comprising N frames will yield $N - 1$ possible time delays, Δt , and thus $N - 1$ independent values of g_2 at each pixel.

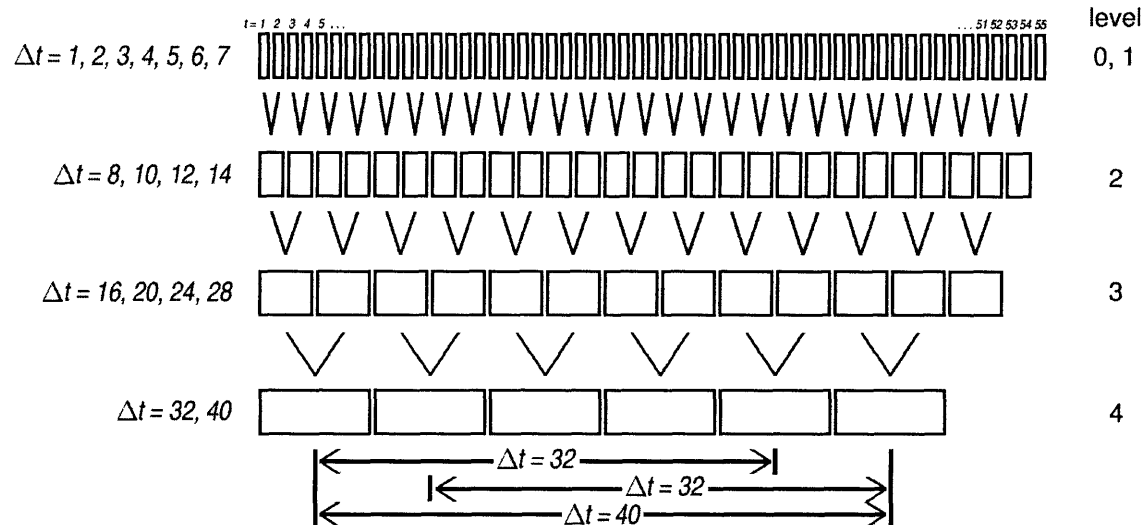


Figure A-3: Schematic of multiple tau averaging scheme. Rectangles represent frames (or kinetics mode slices), and all times are given as multiples of the time per frame (slice). Correlations for delays listed at left are calculated at the corresponding multiple tau level; this example utilizes four delays per level and averages pairs of frames between each level.

Full details on multiple tau correlation, including its comparative advantages over “brute force” correlation, can be found elsewhere [167,172–174], and a graphical depiction is shown in Fig. A-3. In short, several consecutive frames are averaged together before long-delay correlations are evaluated; this improves signal-to-noise levels and reduces logarithmically the number of delays involved.

When “kinetics mode” acquisition is used and data has been collected in the x - z - t_{frame} - t_{slice} format discussed in Sec. A.1, the multiple tau process becomes more complicated. For the shortest delay times, only correlations between slices on a single frame are relevant, making each frame essentially a separate entity. In the short-time limit, then, correlations are made over only the final dimension of the data structure, similar to what would occur in the usual x - z - t case. Very long delay times involve only correlations among widely separated frames. For large delays, all slices on a single frame may be averaged together, and the structure reverts directly to the standard x - z - t . It is advantageous to store averages over slices prior to beginning the multiple tau process, since some slices may be dropped during multiple tau averaging, as can be seen for the final slice in Fig. A-3.

The additional complexity introduced by kinetics mode occurs for intermediate time delays, especially when using a large number of delays per level. In this case, the delay between consecutive frames may not be long enough to justify averaging together all slices on a single frame before correlating among frames. In other words, the x - z - t_{frame} - t_{slice} structure persists, and correlations are evaluated over the third dimension rather than the final one. The correlations themselves will ultimately be time averaged, of course (see Eqn.

A.1), and here that averaging should be applied to *both* the third and fourth dimensions, instead of the final dimension alone as would be appropriate to the standard case.

As the correlator routine works through the sequence of time delays, therefore, it must determine at each delay which of the above situations—slices-only, slices-frames, or frames-only—applies.

A.6 Normalizing correlation functions

Array detectors, by measuring intensities at multiple \mathbf{q} simultaneously, offer the possibility of multi-speckle approaches to correlation function normalization [52, 167]. The advantages of multi-speckle normalization include:

- improved signal-to-noise
- lower systematic error through corrections for time variations in overall (*e.g.* incident) intensity
- the ability to obtain reliable correlation functions for slow dynamics and non-ergodic samples

Specifically, the denominator of Eqn. A.1, $\langle I(\mathbf{q}, t) \rangle_t^2$, serves as the standard normalization for point-correlator experiments [172]. It is an estimate of the intensity that would be measured were all speckles to be averaged out, as they might with an incoherent source. Under partially coherent illumination, the intensity across a detector partition typically displays small-scale features due to speckle and large-scale features due to the \mathbf{q} -dependence of the static scattering cross-section. The speckles are nominally short-lived compared to any time-dependence in the overall intensity. Ideally, then, correlation functions from one partition of an area detector should be normalized by the square of a quantity that approximates the average intensity but also reflects its long-term, long-range variations. The simple expression $\langle I(\mathbf{q}, t) \rangle_t^2$ does not satisfy the latter criterion. Multi-speckle experiments permit the use of averages across pixels to improve such estimates.

In this appendix we shall denote an average over pixels within a single detector partition as $\langle \rangle_{\mathbf{q}}$, which is *not* intended to signify the inclusion of every pixel in the array. Section A.2 details the partitioning process. In ‘coherent’, for example, statics partitions are used when calculating $\langle I(\mathbf{q}, t) \rangle_{\mathbf{q}}$, since that quantity corresponds to the static scattering cross-section; on the other hand, *dynamics* partitions are used when evaluating $\langle g_2(\mathbf{q}, \Delta t) \rangle_{\mathbf{q}}$.

A.6.1 Accounting for long-term intensity variations

It is instructive to rewrite Eqn. A.1 in the equivalent form,

$$g_2(\mathbf{q}, \Delta t) = \left\langle \frac{I(\mathbf{q}, t)}{\langle I(\mathbf{q}, t) \rangle_t} \cdot \frac{I(\mathbf{q}, t + \Delta t)}{\langle I(\mathbf{q}, t) \rangle_t} \right\rangle_t. \quad (\text{A.2})$$

This calls attention to treating the normalization as an operation on the intensities rather than the correlation products.

A.6.1.1 Standard normalization

Ideally, either a time-average or a pixel-average of the intensity array will remove speckle-related features. To isolate the long-term and long-range variations, then, we may approximate

$$I(\mathbf{q}, t) \approx \frac{\langle I(\mathbf{q}, t) \rangle_t \langle I(\mathbf{q}, t) \rangle_{\mathbf{q}}}{\langle I(\mathbf{q}, t) \rangle_{\mathbf{q}, t}} \quad (\text{A.3})$$

for the purposes of normalization. Replacing the normalization in Eqn. A.2 with the right side of Eqn. A.3 yields the multi-speckle version of the standard normalization [52, 54],

$$g_2(\mathbf{q}, \Delta t) = \left\langle \frac{I(\mathbf{q}, t)}{\frac{\langle I(\mathbf{q}, t) \rangle_t \langle I(\mathbf{q}, t) \rangle_{\mathbf{q}}}{\langle I(\mathbf{q}, t) \rangle_{\mathbf{q}, t}}} \cdot \frac{I(\mathbf{q}, t + \Delta t)}{\frac{\langle I(\mathbf{q}, t) \rangle_t \langle I(\mathbf{q}, t + \Delta t) \rangle_{\mathbf{q}}}{\langle I(\mathbf{q}, t) \rangle_{\mathbf{q}, t}}} \right\rangle_t \quad (\text{A.4})$$

$$= \left\langle \frac{I(\mathbf{q}, t)}{\langle I(\mathbf{q}, t) \rangle_{\mathbf{q}}} \cdot \frac{I(\mathbf{q}, t + \Delta t)}{\langle I(\mathbf{q}, t + \Delta t) \rangle_{\mathbf{q}}} \right\rangle_t \cdot \frac{\langle I(\mathbf{q}, t) \rangle_{\mathbf{q}, t}^2}{\langle I(\mathbf{q}, t) \rangle_t^2}. \quad (\text{A.5})$$

We have selected for Eqn. A.5 notation that emphasizes the utility of dividing the array of *intensities* by partition averages before correlating instead of normalizing the correlation products. The latter method would require computing a separate normalization for each $(t, \Delta t)$ pair.

A.6.1.2 Symmetric normalization

While the standard normalization can be computed relatively quickly, the accuracy of the normalization can be further improved by taking time-averages of $\langle I(\mathbf{q}, t) \rangle_{\mathbf{q}}$ in Eqn. A.5. In order to preserve the long-term intensity variations, though, the time-averages should not be evaluated over all frames but rather some subset. The number of frames that can be averaged without distorting the long-term behavior will depend on the Δt of interest. This is the strategy behind the multi-speckle version [52, 54, 167] of the “symmetric” normalization scheme [172, 175].

From a practical standpoint, given a data set containing N frames, the time-averaging involved in calculating $\langle I(\mathbf{q}, t) \rangle_t^2$ spans at most $1 \leq t \leq N$, while the correlation products in $\langle I(\mathbf{q}, t) I(\mathbf{q}, t + \Delta t) \rangle_t$ can only cover $1 \leq t \leq N - \Delta t$. This means that the first term in $\langle I(\mathbf{q}, t) I(\mathbf{q}, t + \Delta t) \rangle_t$ is evaluated over the “left” subset of frames $1 \leq t_{\text{left}} \leq N - \Delta t$, and the second term is evaluated over the “right” subset, $\Delta t + 1 \leq t_{\text{right}} \leq N$. It is natural, then, to use in normalization one time-average of $\langle I(\mathbf{q}, t) \rangle_{\mathbf{q}}$ over the left subset and another over

the right,

$$g_2(\mathbf{q}, \Delta t) = \frac{\langle I(\mathbf{q}, t) I(\mathbf{q}, t + \Delta t) \rangle_t}{\langle I(\mathbf{q}, t) \rangle_{\mathbf{q}, t_{\text{left}}} \langle I(\mathbf{q}, t) \rangle_{\mathbf{q}, t_{\text{right}}}} \cdot \frac{\langle I(\mathbf{q}, t) \rangle_{\mathbf{q}, t}^2}{\langle I(\mathbf{q}, t) \rangle_t^2}. \quad (\text{A.6})$$

Note that $\langle I(\mathbf{q}, t) \rangle_{\mathbf{q}, t_{\text{left}, \text{right}}}$ depend on Δt but not \mathbf{q} or t . This means that, unlike in the standard scheme, normalizations must inevitably be recalculated for each Δt , and there is therefore no advantage conveyed by applying the normalization to the intensities instead of the correlation products.

Eqn. A.6 is distinct from the two forms used in Refs. [52] and [167], respectively. Like Cipelletti *et al.* [167], we average over pixels prior to the symmetric normalization. However, we include the additional term $\langle I(\mathbf{q}, t) \rangle_{\mathbf{q}, t}^2 / \langle I(\mathbf{q}, t) \rangle_t^2$ to preserve any long-range trends in intensity with \mathbf{q} , along the lines of what was done in the standard normalization scheme above.

It should also be noted that the symmetric normalization factor, $\langle I(\mathbf{q}, t) I(\mathbf{q}, t + \Delta t) \rangle_t$, can easily be generated by inputting $\langle I(\mathbf{q}, t) \rangle_{\mathbf{q}}$ to the same routine that, when given $I(\mathbf{q}, t)$, calculates correlation products. It is essential, though, to pass with $\langle I(\mathbf{q}, t) \rangle_{\mathbf{q}}$ a flag to indicate that time-averages should be calculated *before* taking products instead of after.

A.6.2 Precisely accounting for long-range intensity variations

A main premise of Sec. A.6.1.2 is that averaging over a combination of pixels and time—as opposed to averaging over pixels alone—can improve the precision of the normalization. In this section, we similarly seek some combination of pixel- and time-averages to replace the time averages, $\langle I(\mathbf{q}, t) \rangle_t$, in the denominators of Eqns. A.5 and A.6. This is especially important for studies of non-ergodic samples or measurements wherein the total time spanned by the exposure sequence is of the same order of magnitude (or less) than the longest time constants of the sample dynamics in the range of \mathbf{q} probed. In such cases the experimentally accessible $\langle I(\mathbf{q}, t) \rangle_t$ will still contain speckle features.

If a partition contains only a few pixels, or if the intensity does not vary much across the partition (as would be the case for a thin ring of pixels at a particular scattering vector magnitude, provided the sample is isotropic), then a simple average over pixels will suffice. There is, of course, the usual tradeoff between partition size and signal-to-noise, especially at low intensities.

One technique that can reliably wash out small-scale features in intensity across a large partition involves applying a two-dimensional smoothing operation to the time-averaged intensities within the partition. We have found, not unexpectedly, that smoothing is optimized when the smoothing function is given the pixels' scattering vector coordinates instead of their x - z locations in the array. In transmission geometries, the azimuthal (φ) and *inverse* radial ($1/q$) coordinates tend to be the most suitable choice, since scattering almost always has an inverse relationship with the magnitude of the wavevector.

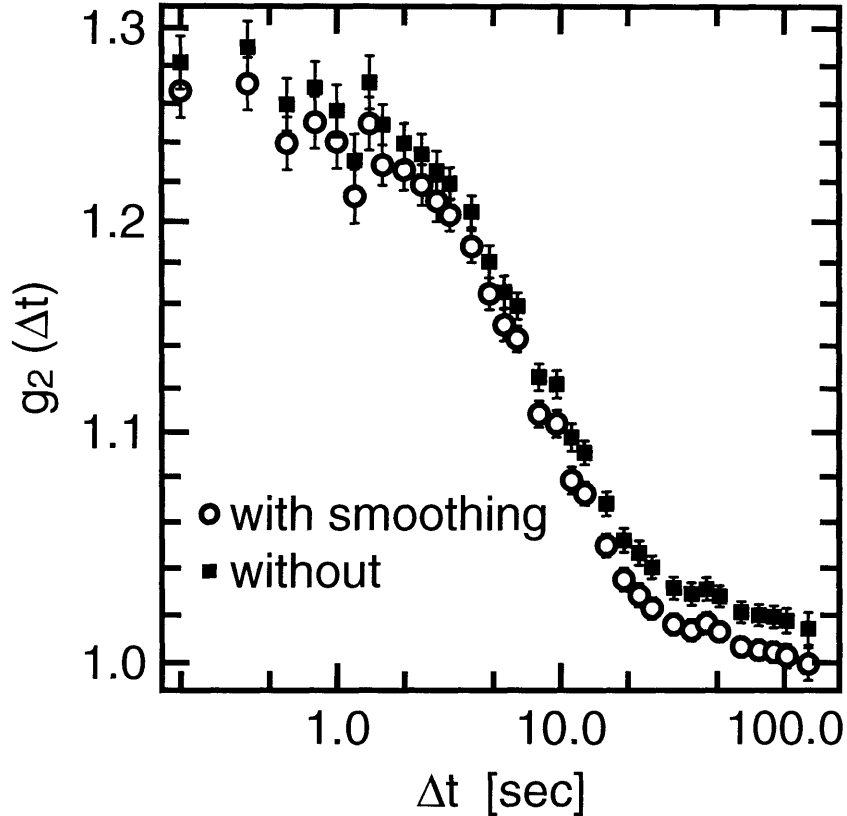


Figure A-4: Comparison between smoothing and simple averaging normalization methods in correlation function calculation.

Specifically, for each partition, ‘coherent’ finds the coefficients a_{ij} of the function

$$s(\mathbf{q}) = \sum_{i,j=0}^4 a_{ij} \frac{\varphi^j}{q^i} \quad (\text{A.7})$$

that most closely equate $s(\mathbf{q})$ to $\langle I(\mathbf{q}, t) \rangle_t$. It then calculates either Eqn. A.5 or Eqn. A.6 (whichever the user specifies) with $s(\mathbf{q})$ in place of $\langle I(\mathbf{q}, t) \rangle_t$. We have found empirically that fourth-order polynomials provide sufficient curvature to accurately reproduce most large-scale intensity variations without being oversensitive to small-scale fluctuations. Of course, a partition must contain a sufficient number of data points for the fits to reliably converge; ‘coherent’ allows users to specify the minimum number of pixels for a partition to qualify for normalization smoothing (the default is 100). Otherwise the partition is considered small and a simple average is used.

Fig. A-4 provides an example of the improvement that smoothing can provide. In it we plot the results of a single data set, analyzed once with a smoothing correction and once with simple averages only. The data plotted is the average correlation function for an isotropic sample over a dynamics partition comprising 35,741 pixels. Because the intensity varied

substantially within the dynamics partition, much smaller statics partitions—ten of them, with between 3,000 and 4,500 pixels each—were used for normalization. The partitions extended through the full azimuthal range accessible to the camera and were relatively narrow in the radial direction ($0.002 \leq \Delta q/q \leq 0.004$). A perfectly normalized correlation function will approach unity at large Δt . The smoothing correction clearly shifted the calculated correlation function toward the ideal case without significantly modifying the overall shape of the decay.

In principle, one could instead adjust the coefficients $a'_{ij}(t)$ of

$$s'(\mathbf{q}, t) = \sum_{i,j=0}^4 a'_{ij}(t) \frac{\varphi^j}{q^i} \quad (\text{A.8})$$

to match $I(\mathbf{q}, t)$ and then evaluate g_2 with the standard,

$$g_2(\mathbf{q}, \Delta t) = \left\langle \frac{I(\mathbf{q}, t)}{s'(\mathbf{q}, t)} \cdot \frac{I(\mathbf{q}, t + \Delta t)}{s'(\mathbf{q}, t + \Delta t)} \right\rangle_t, \quad (\text{A.9})$$

or symmetric,

$$g_2(\mathbf{q}, \Delta t) = \frac{\langle I(\mathbf{q}, t) I(\mathbf{q}, t + \Delta t) \rangle_t}{\langle s'(\mathbf{q}, t) \rangle_{t_{\text{left}}} \langle s'(\mathbf{q}, t) \rangle_{t_{\text{right}}}}, \quad (\text{A.10})$$

normalization schemes. This would provide a second-order correction for incident intensity variations, but at the cost of a loss of computational speed along with an increased likelihood of failures to converge.

A.6.3 Image segments and normalization

It is also essential that, as mentioned in Secs. A.1 and A.3, our correlation normalization process be compatible with the use of individual image segments in lieu of full images. Within a given segment, some partitions may contain only a few pixels, perhaps only a single pixel, even if the partition as a whole spans thousands. If only a partition's pixels in a single segment are used, multi-speckle averages will not have as high a signal-to-noise ratio and may not even cover multiple speckles. One remedy for this problem is to perform the entire static cross-section analysis—and hence obtain the full $\langle I(\mathbf{q}, t) \rangle_{\mathbf{q}}$ for every partition—before beginning correlation function calculations. The drawback of this course of action is that each segment of raw data must be read from disk a second time, which can significantly slow the analysis process. In ‘coherent’, the user is expressly given this choice between speed and quality in the analysis.

Appendix B

Lower-level discrimination: Noise reduction for CCD measurements at low intensities

Three regimes of CCD data acquisition tend to incur low photon rates per pixel per image,

1. High-speed dynamics/kinetics (small Δt)
2. Low scattering cross-section samples
3. Azimuthally anisotropic scattering

The third category arises because anisotropic scattering does not involve a broad swath of pixels across the CCD that all receive ostensibly identical intensities. In most experiments on isotropic materials, one can enhance signal to noise by averaging together all pixels at the same radial wavevector. One may further reduce noise at low intensities by throwing away all counts that do not rise above some threshold indicating detection of a photon [52]. For realistic CCDs, this “lower-level discrimination” introduces a bias in the data. We present here a method for correcting that bias.

B.1 CCD response

B.1.1 Photon detection

The number of photons registered at one pixel in a detector is typically treated as being distributed according to Poisson’s formula,

$$P(n) = e^{-b} \frac{b^n}{n!}. \quad (\text{B.1})$$

The average number of detected photons per pixel per measurement is $\langle n \rangle = \sum_{n=0}^{\infty} nP(n) = b$, which defines b . The standard deviation is $\sigma_n = \sqrt{\langle n^2 \rangle - \langle n \rangle^2} = \sqrt{b^2 + b - b^2} = \sqrt{b}$. The true photon rate is b divided by the detector efficiency.

Detected photons give rise to an electric charge, which is typically measured, digitized, and converted to dimensionless Analog-to-Digital Units (ADU). Raw data, which we will denote by I , is most often kept as ADU. An ideal detector would have the obvious connection between ADU and detected photon rate of

$$I = bA_0. \quad (\text{B.2})$$

A_0 is a constant conversion factor. Most experiments seek to determine b —or some function of b —from measurements of I .

Real CCD pixels commonly display a variety of nonidealities in response, including: (1) “dark” ADU arising from sources other than photons; (2) variable ADU per photon; and (3) spreading of accumulated charge among neighboring pixels. At high intensities such behavior tends to negligibly affect results, but quantitative analysis of CCD data at low intensities may require significant corrections for any or all of the above effects.

B.1.2 Dark background

We group into the collective term “dark background” the various ADU accumulated even when no photons are incident on the detector, including dark current and readout noise [171]. These can be approximated by a normal distribution with standard deviation σ_d about some mean D_0 , $P(D) = \exp\left[-(D - D_0)^2 / 2\sigma_d^2\right] / \sqrt{2\pi}\sigma_d$. It is common practice to subtract from raw data the average of several dark (unilluminated) measurements [52,168,176,177]. Ideally only the fluctuations in the dark remain, and we will model them with the distribution,

$$P(d) = g(d, \sigma_d) \equiv \frac{1}{\sqrt{2\pi}\sigma_d} e^{-\frac{d^2}{2\sigma_d^2}}. \quad (\text{B.3})$$

This dark noise is added to the photon count (Eqn. B.1) to yield

$$P(I) = e^{-b} \sum_{n=0}^{\infty} \frac{b^n}{n!} g(I - nA_0, \sigma_d) \quad (\text{B.4})$$

$$\langle I \rangle = bA_0 \quad (\text{B.5})$$

$$\sigma_I = \sqrt{bA_0^2 + \sigma_d^2}. \quad (\text{B.6})$$

Eqn. B.6 indicates that dark fluctuations will dominate over Poisson noise at low intensities, specifically when $b \lesssim \sigma_d^2 / A_0^2$.

Any actual estimate of D_0 comes from some finite number N_d , of dark measurements.

Calling the estimate \hat{D}_0 , the expected difference is

$$|\Delta D_0| \equiv \left\langle \left| \hat{D}_0 - D_0 \right| \right\rangle \sim \frac{\sigma_d}{\sqrt{N_d}}. \quad (\text{B.7})$$

Other phenomena, such as variations in detector temperature, can further alter D_0 , either during a sequence of measurements or between sequences. To keep the treatment general, we will carry the “known” quantity ΔD_0 through calculations, without specifying it further. We will approximate it as remaining constant from measurement to measurement, as it would for a single pixel corrected by the same dark average over a measurement sequence. This will demonstrate salient features of dark drift while avoiding excessive complexity. With these assumptions in place, the standard deviation remains unchanged from Eqn. B.6, and the mean intensity becomes

$$\langle I \rangle = bA_0 + \Delta D_0. \quad (\text{B.8})$$

The “dark drift,” ΔD_0 , dominates the measured intensity for $b \lesssim |\Delta D_0| / A_0$.

B.1.3 Variable response

In practice, a single CCD pixel is unlikely to respond in an identical fashion to every detected photon, despite the photons themselves being for all intents and purposes indistinguishable. The ADU per photon then exhibits some probabilistic distribution. For example, although most photon events correspond to absorption within a pixel’s depletion region, some small fraction are absorbed outside the depletion region, producing fewer detectable photoelectrons. This leads to a strongly peaked ADU distribution with a weak, continuous tail extending down to very low levels [168, 177]. Similarly, spreading of accumulated charge, which will be discussed in the next section, is typically also a random process.

It becomes necessary, then, to identify the detector’s response to a single photon with the more general function, $P_1(A)$. The simpler treatment in previous sections applies to the special case where $P_1(A) = \delta(A - A_0)$. Instances of two detected photons have an ADU distribution which is the convolution of $P_1(A)$ with itself,

$$P_2(A) = \int_{-\infty}^{\infty} dA' P_1(A') P_1(A - A') \quad (\text{B.9})$$

Similarly, three-photon-detection and higher events give rise to the distributions

$$\begin{aligned} P_3(A) &= \int_{-\infty}^{\infty} dA' P_2(A') P_1(A - A') \\ P_4(A) &= \int_{-\infty}^{\infty} dA' P_3(A') P_1(A - A') \\ P_n(A) &= \int_{-\infty}^{\infty} dA' P_{n-1}(A') P_1(A - A'). \end{aligned} \quad (\text{B.10})$$

Taking into account the likelihoods of each number of detections from Eqn. B.1, the total ADU contribution from photons is given by

$$F(A, b) \equiv \sum_{n=1}^{\infty} \frac{b^n}{n!} P_n(A), \quad (\text{B.11})$$

making the total response

$$P(I) = e^{-b} [\delta(I) + F(I, b)]. \quad (\text{B.12})$$

In other words, once the single-photon response function is known, it becomes possible to predict the detector response at any intensity level.

When the dark background (Eqn. B.3) is included, Eqn. B.12 becomes

$$P(I) = e^{-b} \left[g(I - \Delta D_0, \sigma_d) + \int_{-\infty}^{\infty} dA F(A, b) g(I - \Delta D_0 - A, \sigma_d) \right] \quad (\text{B.13})$$

$$\langle I \rangle = b \langle A \rangle + \Delta D_0 \quad (\text{B.14})$$

$$\sigma_I = \sqrt{b \left(\langle A \rangle^2 + \sigma_A^2 \right) + \sigma_d^2}, \quad (\text{B.15})$$

where $\langle A \rangle$ and σ_A refer to the single-photon values,

$$\langle A \rangle \equiv \int_{-\infty}^{\infty} dA A P_1(A) \quad (\text{B.16})$$

$$\sigma_A \equiv \sqrt{\int_{-\infty}^{\infty} dA (A - \langle A \rangle)^2 P_1(A)}. \quad (\text{B.17})$$

Note that $\int_{-\infty}^{\infty} dA A P_n(A) = n \langle A \rangle$.

It should also be noted that Eqn. B.13 can also be written as

$$P(I) = e^{-b} \left[g(I - \Delta D_0, \sigma_d) + \sum_{n=1}^{\infty} \frac{b^n}{n!} Z_n(I - \Delta D_0, \sigma_d) \right], \quad (\text{B.18})$$

with

$$Z_n(I, \sigma_d) \equiv \int_{-\infty}^{\infty} dA P_n(A) g(I - A, \sigma_d) \quad (\text{B.19})$$

$$= \int_{-\infty}^{\infty} dA Z_{n-1}(A) P_1(I - A), \quad (\text{B.20})$$

the last line being applicable for $n > 1$ and arising from Eqn. B.10.

B.1.4 Charge spreading

The charge generated by a photon may in part be distributed among several of the pixel's neighbors; this charge "leakage", also referred to as "spreading", can occur as part of the readout process or when a photon is stopped on the boundary between pixels. Spreading has two main consequences: it influences the form of the response function, $P_1(A)$, and it makes a pixel responsive to photons that strike elsewhere. As a simplistic example, imagine that spreading involves only a single neighbor, with each photon event generating 40%-40% accumulation (and 20% loss) of 10 ADU. In this case, it is necessary to set $P_1(A) = \delta(A - 4)$, rather than $\delta(A - 8)$ or $\delta(A - 10)$. It is also important to reduce b by a factor of two in order to avoid double-counting photons.

More generally, multiple-counting can be eliminated by replacing b in all calculations with βb , where β is the number of pixels involved in a single-photon event. Then, for example, Eqns. B.13–B.15 become

$$P(I) = e^{-\beta b} \left[g(I - \Delta D_0, \sigma_d) + \int_{-\infty}^{\infty} dA F(A, \beta b) g(I - \Delta D_0 - A, \sigma_d) \right] \quad (\text{B.21})$$

$$\langle I \rangle = \beta b \langle A \rangle + \Delta D_0 \quad (\text{B.22})$$

$$\sigma_I = \sqrt{\beta b (\langle A \rangle^2 + \sigma_A^2) + \sigma_d^2}. \quad (\text{B.23})$$

If β varies from event to event, it can be set to the maximum number of pixels involved in any single-photon event. Then an appropriate value of $P_1(A = 0)$ must be used to account for the portion of events spreading to fewer than β pixels. For instance, suppose the 40%-40% spreading from the previous paragraph occurs in two-thirds of photon detections, with no spreading in the remaining one-third. It is then useful to set $\beta = 2$ and $P_1(A) = \frac{1}{6}\delta(A) + \frac{2}{3}\delta(A - 4) + \frac{1}{6}\delta(A - 10)$.

B.1.5 Experimentally characterizing the single-photon response

Eqns. B.18 and B.20 allow a determination of the detector response at any intensity level given only the single-photon response, $P_1(A)$, and knowledge of the dark noise. The latter is straightforward to obtain with an unilluminated data set. It is therefore of interest to find $P_1(A)$; this can be accomplished directly by first identifying the single-photon detection events in a dark-subtracted and flatfield-corrected data set and then histogramming the analog-to-digital units from the pixels that record one (or part of one) photon. In practice, this is most reliably done when the ADU per photon heavily outweigh the dark noise, which is typically the case in direct-detection CCDs and not always so for phosphor-coupled CCDs [171]. By including only confirmed photon events in the histogram, the dark drift can be assumed to be an insignificant part of the recorded ADU and hence ignored.

Determining which pixels in a set of exposures are involved in photon events is a task for

which the so-called “droplet” algorithm [177] was tailor made. For the purpose of determining $P_1(A)$, however, a more rudimentary approach suffices. If data of extremely low intensity are used, the vast majority of detections will be single-photon events, and the few multi-photon events that do occur may be easily identified and discarded. Subpixel precision in locating the “center of mass” of each event is also not required.

We have developed an efficient “photon isolation” algorithm suitable for finding the single-photon ADU distribution. It requires choosing *a priori* a “photon area,” the local group of pixels around the center of a photon event in which the routine should look for ADU. We have found that a reasonable size for the photon area, which we called β in Sec. B.1.4, can range anywhere from three to ten pixels, depending on the detector and the desired level of precision, *i.e.* one to four pixels at the center of the photon event receive most of the ADU, and spreading may shift two to fifteen percent of the ADU to surrounding pixels. The photon isolation routine tests all pixels in parallel to determine which are the centers of single-photon events. It first calculates the sum of the ADU at a pixel in question together with the surrounding photon area. (Pixels on the edges of the detector, having an incomplete set of neighbors, are ignored.) It also calculates the sum of ADU in a ring surrounding the photon area. To be considered the site of a single-photon event, these sums must satisfy four criteria:

1. The photon area sum must exceed some multiple of the dark RMS (scaled with $\sqrt{\beta}$). This ensures that the ADU are not the result of random noise.
2. The photon area sum must *not* exceed a preset value corresponding to a double-photon hit.
3. The ring sum must fall below another threshold (again, a multiple of σ_d , scaled to the square root of the number of pixels summed). This prevents inclusion of situations such as when ADU from one photon event spread atop a second event nearby, leading to an overestimate of the ADU count for the second event.
4. The ADU center of mass for the photon area must lie somewhere within the pixel in question. This avoids double-counting photons when wide spreading occurs.

From the list of single-photon event coordinates, a list of pixels in the relevant photon areas is compiled. The ADU at those pixels is histogrammed to produce an estimate of the single-photon ADU distribution, $P(I)$.

Having obtained $P(I)$ for single-photon events, the dark noise must subsequently be removed to generate an estimate of $P_1(A)$ that (a) is suitable for use with any level of dark noise—which can vary significantly across a CCD array; and (b) will not cause the dark noise to incorrectly proliferate when multiple convolutions involving $P_1(A)$ are performed during the numerical reconstruction of multi-photon distributions. The deconvolution of the dark noise from $P(I)$ is an inherently imprecise process, so it is advisable to concentrate

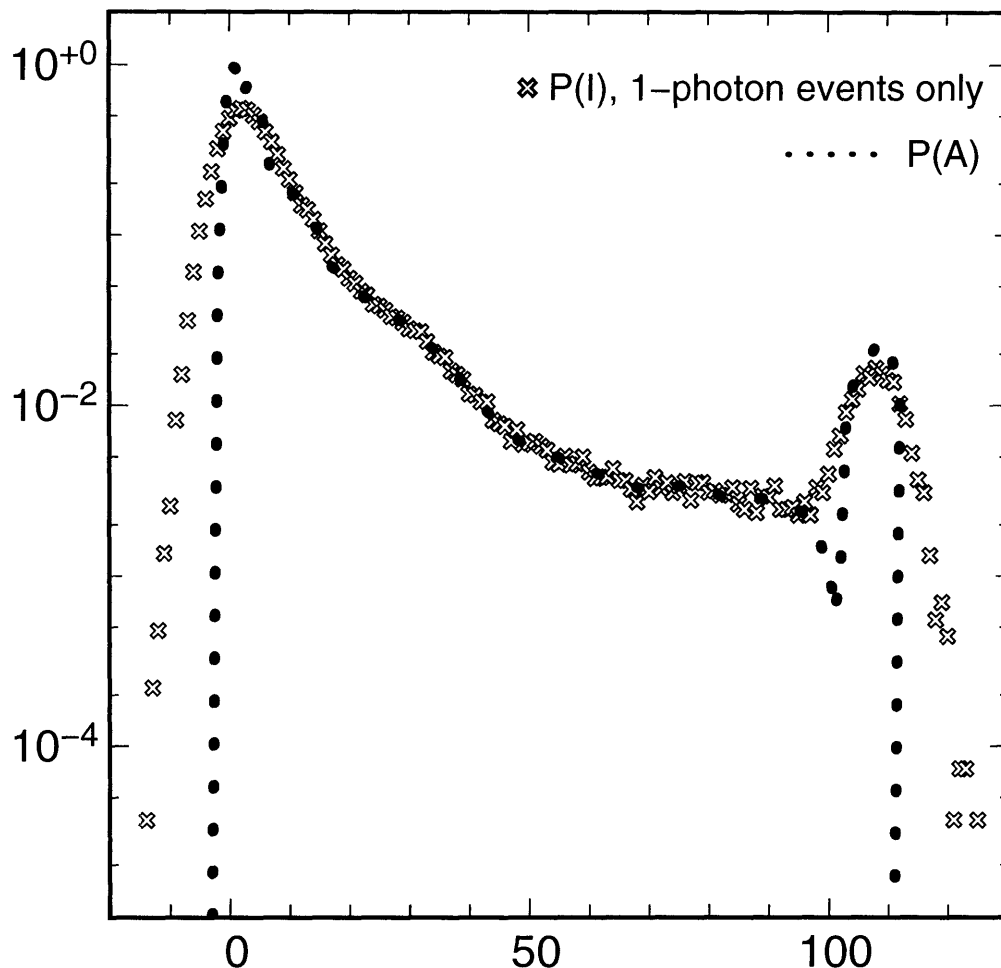


Figure B-1: Extracting the single-photon response, $P_1(A)$, from a measured single-photon intensity distribution, $P(I)$, for 200 msec exposures with the SMD1M60 CCD described in Refs. [55,168]. The eight pixels closest each photon event were used to generate $P(I)$. Details of the deconvolution process are given in the text.

on single-photon events from a region of the CCD array that exhibits the lowest dark RMS. Fortunately, determinations of b are usually consistent among a wide range of approximations to $P(A)$.

A specific example of deconvolution is shown in Figure B-1. The crude method used here took advantage of the fact that $P_1(A)$ influences $P(I)$ over a narrow range of I , only within a few times σ_d . A trial function was set up at A values separated by approximately $2\sigma_d$, except near the easily discernible peaks at the high- and low- I ends of $P(I)$ where a slightly closer spacing was used. Every point in the trial function was treated as an adjustable parameter and allowed to vary (though constrained to be > 0 everywhere) in a nonlinear least-squares fit to the measured $P(I)$. The function used in the fit was the convolution of this trial $P_1(A)$ with a Gaussian of variance equal to that measured in this CCD region

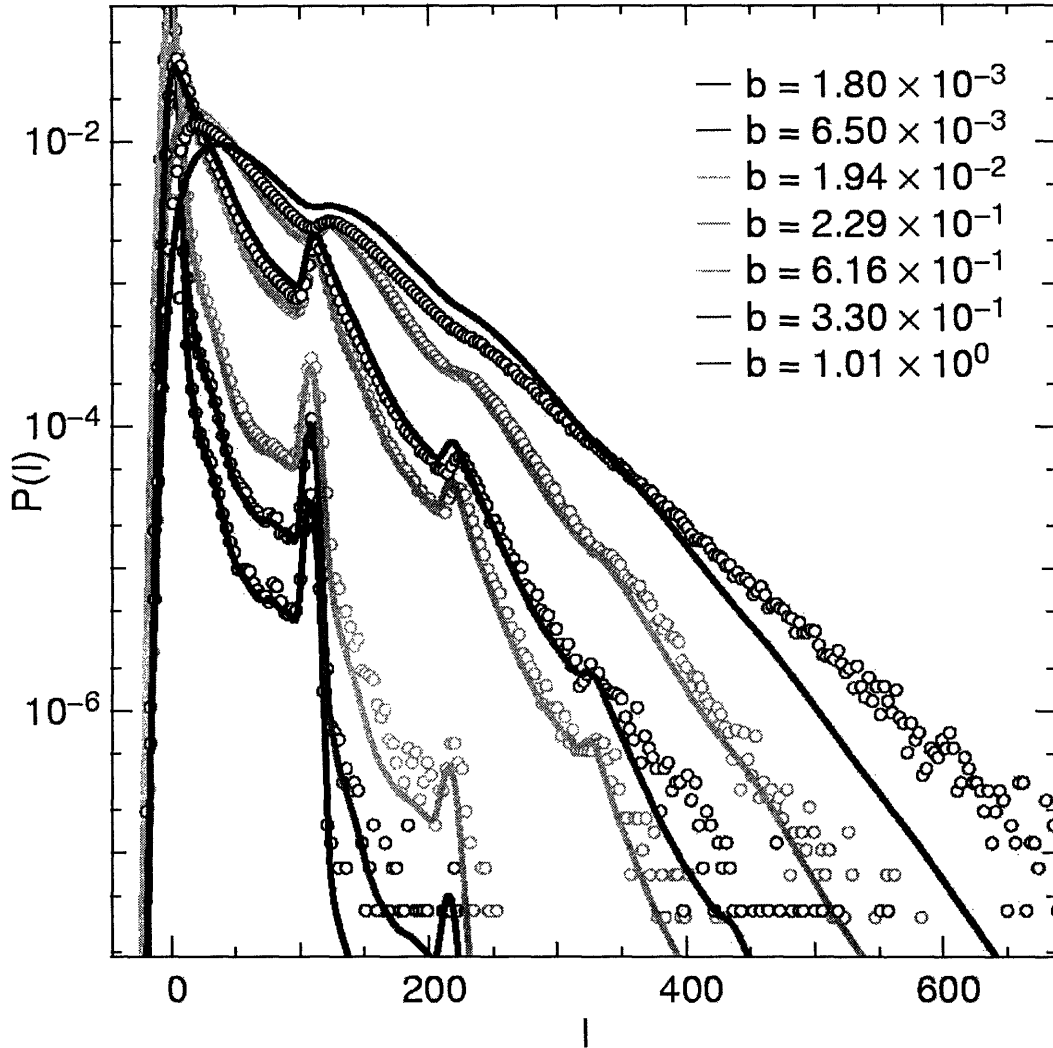


Figure B-2: Expected and measured values of the intensity distribution function, Eqn. B.18, at various photon rates.

during a series of zero-illumination (dark) frames. The result was by no means a unique solution for $P_1(A)$ but did reproduce well the intensity histograms of data that included a significant contribution from multi-photon events, as shown in Figure B-2.

In Fig. B-2 we test Eqn. B.18 against real data. A section of CCD was illuminated by a series of samples of increasing volume fraction and hence increasing scattering intensity. For $P_1(A)$ we histogrammed the photon events in the lowest-intensity image. Deviations from predictions at high photon number may be the result of artifacts introduced by many convolution iterations in Eqn. B.19.

It should be noted that while $P_1(A)$ seemingly applies across all pixels after flatfield correction (Sec. A.4.1), one may need to evaluate it separately for each exposure time. For example, the SMD1M60 detector utilized here [55,168] showed a peak at $A = 109$ ADU for

200 msec exposures. That peak appeared instead at 99 ADU when an exposure time of 20 msec was used. In addition, $P_1(A)$ obviously needs to be recalculated whenever the incident X-ray energy is changed.

We show in the rest of this appendix that the time-consuming process of determining $P_1(A)$ need not be carried out anew during every analysis—even when lower-level discrimination is used. Comparison of histograms as in Figs. B-1 and B-2 is necessary only for vetting a candidate $P_1(A)$ for a particular detector, exposure time, and X-ray energy. Once a suitable approximation to $P_1(A)$ has been found, it can be stored for repeated use in routine data analysis.

B.1.6 Determining photon rate from measured intensities

Given $\langle A \rangle$, β , and ΔD_0 , it is straightforward to invert Eqn. B.22 to find \hat{b} , the estimate of the photon rate (more correctly, the photon rate times the efficiency):

$$\hat{b} = \frac{I - \Delta D_0}{\beta \langle A \rangle}. \quad (\text{B.24})$$

Similarly, the error on \hat{b} is obtained from Eqn. B.23,

$$\sigma_{\hat{b}} = \frac{1}{\beta} \sqrt{\left(\frac{I - \Delta D_0}{\langle A \rangle} \right)^2 \left[1 + \left(\frac{\sigma_A}{\langle A \rangle} \right)^2 \right] + \left(\frac{\sigma_d}{\langle A \rangle} \right)^2}. \quad (\text{B.25})$$

B.2 Lower-level discrimination

Lower-level discrimination can dramatically lessen the significance of dark noise and dark drift, by eliminating both whenever no photons are detected. The discriminator algorithm reassigns readings below a threshold, $I < L$, to $I_L = 0$, while preserving readings of $I > L$ as $I_L = I$. This is reminiscent of so-called “clipping” of the photon distribution [178–180], except clipping typically entails the reduction of I to a one-bit value.

The distribution of I_L has the general form

$$P(I_L) = P(I = I_L) \theta(I_L - L) + \delta(I_L) \int_{-\infty}^L dI P(I) \quad (\text{B.26})$$

$$\langle I_L \rangle = \int_L^{\infty} dI I P(I) \quad (\text{B.27})$$

$$= \langle I \rangle - \int_{-\infty}^L dI I P(I) \quad (\text{B.28})$$

$$\sigma_{I_L} = \sqrt{\int_L^\infty dI I^2 P(I) - \langle I_L \rangle^2} \quad (\text{B.29})$$

$$= \sqrt{\sigma_I^2 - \int_{-\infty}^L dI I^2 P(I) + \langle I \rangle^2 - \langle I_L \rangle^2} \quad (\text{B.30})$$

where $\theta(I_L)$ is the Heaviside Step Function and $\delta(I_L)$ is the Dirac Delta Function. Eqn. B.28 indicates that the mean number of ADU measured while using discrimination may differ from the mean without discrimination, so the simple conversion from ADU to photon rate found in Eqn. B.24 will not hold. We will focus primarily on the relationship between $\langle I_L \rangle$ and b , accounting for the various nonidealities in detector response already outlined.

B.2.1 Ideal lower-level discrimination

In the ideal situation, a discriminator threshold, L , could be chosen such that

$$\Delta D_0 + \sigma_d \ll L \ll A_0 - \sigma_d. \quad (\text{B.31})$$

For clarity, we again start with a perfectly uniform response, $P_n(A) = \delta(A - nA_0)$, and no charge spreading, $\beta = 1$. Using Eqns. B.26-B.30, the discriminated versions of Eqns. B.4-B.8 are

$$P(I_L) = e^{-b} \left[\delta(I_L) + \sum_{n=1}^{\infty} \frac{b^n}{n!} g(I_L - \Delta D_0 - nA_0, \sigma_d) \right] \quad (\text{B.32})$$

$$\langle I_L \rangle = bA_0 + (1 - e^{-b}) \Delta D_0, \quad (\text{B.33})$$

$$\sigma_{I_L} = \sqrt{bA_0^2 + (1 - e^{-b}) \sigma_d^2 + e^{-b} \Delta D_0 [2bA_0 + (1 - e^{-b}) \Delta D_0]}. \quad (\text{B.34})$$

Photon signal now heavily outweighs dark drift and dark noise at all intensities. In the low-intensity ($b \rightarrow 0$) limit, $\langle I_L \rangle = bA_0 + b\Delta D_0 \approx bA_0$ and $\sigma_{I_L} = \sqrt{b(A_0 + \Delta D_0)^2 + b\sigma_d^2} \approx \sqrt{b}A_0$. Note that in this limit both unwanted effects are now multiplied by a factor of b , meaning that their size *relative to the signal* ceases to depend on b . The high-intensity ($b \gg 1$) regime displays the same limiting values, $\langle I_L \rangle \approx bA_0$ and $\sigma_{I_L} \approx \sqrt{b}A_0$.

B.2.2 Real lower-level discrimination, ignoring dark background

When accounting for variable response with the distribution $P_1(A)$, and also for charge spreading, Eqn. B.31 may not be satisfied. The possibility arises for some fraction of the photon signal to fall below the discriminator threshold and be removed from subsequent analysis. To keep the treatment relatively simple, we will leave the general case for the next

section and deal here with the case of $\Delta D_0 = 0$ and $\sigma_d = 0$. Then,

$$\langle I_L \rangle = \int_L^\infty dI I P(I) \quad (\text{B.35})$$

$$= \langle I \rangle - \int_{-\infty}^L dI I P(I) \quad (\text{B.36})$$

$$= \beta b \langle A \rangle - e^{-\beta b} \sum_{n=1}^{\infty} \frac{(\beta b)^n}{n!} \int_{-\infty}^L dI I P_n(I) \quad (\text{B.37})$$

$$= \beta b \langle A \rangle \left(1 - e^{-\beta b} \sum_{n=0}^{\infty} \frac{(\beta b)^n}{n!} W_{n+1}(L) \right). \quad (\text{B.38})$$

$W_n(L)$ is the expected fraction of ADU eliminated by the discriminator in measurements where n photons are detected,

$$W_n(L) \equiv \frac{1}{n \langle A \rangle} \int_{-\infty}^L dA A P_n(A). \quad (\text{B.39})$$

Based on the recurrence relation for $P_n(A)$, Eqn. B.10, it can be shown that a similar convolution-based recurrence relation holds for W_n when $n > 1$:

$$W_n(L) = \int_{-\infty}^{\infty} dA W_{n-1}(A) P_1(L - A). \quad (\text{B.40})$$

Eqn. B.40 enables calculation of $W_n(L)$ directly from $P_1(A)$ without requiring prior, explicit evaluations of the higher-order $P_n(A)$.

Interestingly, in the special case where $P_1\left(\frac{L}{n} \leq A \leq L\right) = 0$ (if $P_1(A < 0) \neq 0$ then the condition becomes $P_1\left(\frac{L}{n} \leq A \leq L - A_{\min}\right) = 0$, where A_{\min} is defined by $P_1(A < A_{\min}) = 0$, Eqn. B.40 simplifies considerably to

$$\begin{aligned} W_n(L) &= W_{n-1} \left(L - \frac{L}{n} \right) \int_{-\infty}^{L/n} dA P_1(A) \\ &= W_{n-1}(L) \int_{-\infty}^L dA P_1(A) \\ &= W_{n-1}(L) X_1(L) \\ &= W_1(L) [X_1(L)]^{n-1}, \end{aligned} \quad (\text{B.41})$$

defining $X_1(L)$ as $\int_{-\infty}^L dA P_1(A)$. Provided this special case holds for arbitrarily large n , substitution back into Eqn. B.38 yields

$$\langle I_L \rangle = \beta b \langle A \rangle \left(1 - e^{-\beta b} \sum_{n=0}^{\infty} \frac{(\beta b)^n}{n!} W_1(L) [X_1(L)]^n \right) \quad (\text{B.42})$$

$$= \beta b \langle A \rangle \left(1 - W_1(L) e^{-\beta b [1 - X_1(L)]} \right). \quad (\text{B.43})$$

This expression may serve as a simple approximation for more realistic forms of $P_1(A)$, provided $\int_{L/2}^L dA P_1(A) \ll 1$ [168]. It tends to overestimate the difference between $\langle I \rangle$ and $\langle I_L \rangle$ at higher intensities (because Eqn. B.41 overestimates W_n at higher n values). However, that difference is inversely related to intensity, so the relative error in determining $\langle I_L \rangle$ remains small.

B.2.3 Real lower-level discrimination, including dark background

Accounting for dark background adds some notational complexity, but does not modify the overall strategy of the preceding section. Nonetheless, two noteworthy additional terms will appear. A useful identity to mention at the outset is

$$\int_{-\infty}^L dI I g(I - A, \sigma_d) = -\sigma_d^2 g(L - A, \sigma_d) + A h(L - A, \sigma_d), \quad (\text{B.44})$$

with

$$h(L, \sigma_d) \equiv \int_{-\infty}^L dI g(I, \sigma_d) \quad (\text{B.45})$$

$$= \frac{1}{2} \operatorname{erfc}\left(-\frac{L}{\sqrt{2}\sigma_d}\right). \quad (\text{B.46})$$

We begin by substituting the full ADU distribution, Eqn. B.21, into Eqn. B.28.

$$\begin{aligned} \langle I_L \rangle &= \langle I \rangle - \int_{-\infty}^L dI I e^{-\beta b} [g(I - \Delta D_0, \sigma_d) \\ &\quad + \int_{-\infty}^{\infty} dA F(A, \beta b) g(I - \Delta D_0 - A, \sigma_d)] \end{aligned} \quad (\text{B.47})$$

$$\begin{aligned} &= \langle I \rangle - e^{-\beta b} \left[\int_{-\infty}^L dI I g(I - \Delta D_0, \sigma_d) \right. \\ &\quad \left. + \sum_{n=1}^{\infty} \frac{(\beta b)^n}{n!} \int_{-\infty}^{\infty} dA P_n(A) \int_{-\infty}^L dI I g(I - \Delta D_0 - A, \sigma_d) \right]. \end{aligned} \quad (\text{B.48})$$

Utilizing Eqns. B.22 and B.44,

$$\begin{aligned} \langle I_L \rangle &= \beta b \langle A \rangle + \Delta D_0 + e^{-\beta b} [\sigma_d^2 g(L - \Delta D_0, \sigma_d) - \Delta D_0 h(L - \Delta D_0, \sigma_d)] \\ &\quad + e^{-\beta b} \sum_{n=1}^{\infty} \frac{(\beta b)^n}{n!} \int_{-\infty}^{\infty} dA P_n(A) [\sigma_d^2 g(L - \Delta D_0 - A, \sigma_d) \\ &\quad - (A + \Delta D_0) h(L - \Delta D_0 - A, \sigma_d)] \quad (\text{B.49}) \\ &= \beta b \langle A \rangle - e^{-\beta b} \sum_{n=1}^{\infty} \frac{(\beta b)^n}{n!} \int_{-\infty}^{\infty} dA A P_n(A) h(L - \Delta D_0 - A, \sigma_d) \\ &\quad + \sigma_d^2 e^{-\beta b} \left[g(L - \Delta D_0, \sigma_d) + \sum_{n=1}^{\infty} \frac{(\beta b)^n}{n!} \int_{-\infty}^{\infty} dA P_n(A) g(L - \Delta D_0 - A, \sigma_d) \right] \end{aligned}$$

$$\begin{aligned}
& +\Delta D_0 \left[1 - e^{-\beta b} h(L - \Delta D_0, \sigma_d) \right] \\
& -\Delta D_0 e^{-\beta b} \sum_{n=1}^{\infty} \frac{(\beta b)^n}{n!} \int_{-\infty}^{\infty} dA P_n(A) h(L - \Delta D_0 - A, \sigma_d). \tag{B.50}
\end{aligned}$$

The most important new term in the full treatment above is $\sigma_d^2 e^{-\beta b} g(L - \Delta D_0, \sigma_d)$ since it may not vanish in the low-intensity limit. It is the result of allowing the highest dark-only ADU to pass the discriminator while their negative counterparts are set (increased) to zero. This term is maximized at $L = \Delta D_0$, where it will be the major contributor to $\langle I_L \rangle$ for intensities $b \lesssim \sigma_d^2 / (\beta \langle A \rangle)$. Fortunately, this spurious signal can be removed completely by choosing a threshold above the dark noise, $L \gtrsim 4\sigma_d$, and well above the dark drift, $L \gg |\Delta D_0|$. Then $g(L - \Delta D_0, \sigma_d) \approx 0$ and $h(L - \Delta D_0, \sigma_d) \approx 1$, making

$$\begin{aligned}
\langle I_L \rangle \approx & \beta b \langle A \rangle - e^{-\beta b} \sum_{n=1}^{\infty} \frac{(\beta b)^n}{n!} \int_{-\infty}^{\infty} dA A P_n(A) h(L - A, \sigma_d) + \tag{B.51} \\
& +\sigma_d^2 e^{-\beta b} \sum_{n=1}^{\infty} \frac{(\beta b)^n}{n!} \int_{-\infty}^{\infty} dA P_n(A) g(L - A, \sigma_d) + \\
& +\Delta D_0 \left[1 - e^{-\beta b} \left(1 + \sum_{n=1}^{\infty} \frac{(\beta b)^n}{n!} \int_{-\infty}^{\infty} dA P_n(A) h(L - A, \sigma_d) \right) \right].
\end{aligned}$$

When $\langle A \rangle \gg |\Delta D_0|$, the final term above is negligible compared to the first, leaving

$$\langle I_L \rangle \approx \beta b \langle A \rangle \left[1 - e^{-\beta b} \sum_{n=0}^{\infty} \frac{(\beta b)^n}{n!} \left(V_{n+1}(L) + \frac{\sigma_d^2}{n+1} U_{n+1}(L) \right) \right], \tag{B.52}$$

where

$$V_n(L) \equiv \frac{1}{n \langle A \rangle} \int_{-\infty}^{\infty} dA A P_n(A) h(L - A, \sigma_d) \tag{B.53}$$

$$= \int_{-\infty}^{\infty} dA V_{n-1}(A) P_1(L - A) \tag{B.54}$$

and

$$U_n(L) \equiv \frac{1}{\langle A \rangle} \int_{-\infty}^{\infty} dA P_n(A) g(L - A, \sigma_d) \tag{B.55}$$

$$= \int_{-\infty}^{\infty} dA U_{n-1}(A) P_1(L - A). \tag{B.56}$$

The great advantage of Eqn. B.52 is that the dark drift, ΔD_0 , appears nowhere within. This makes it unnecessary to determine any information about ΔD_0 except to ensure it is small compared to $\langle A \rangle$ and L .

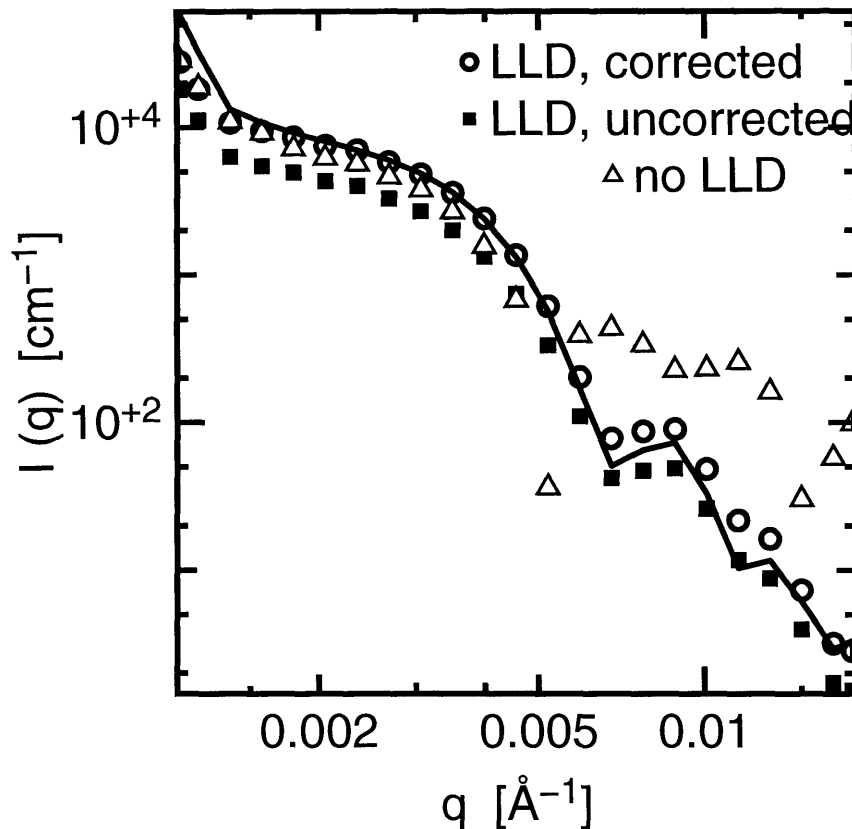


Figure B-3: Effect of LLD and LLD distortion correction on measured, high-speed data. Points represent the same data set of 850 frames of 20 msec exposures analyzed three different ways. Line represents 200 msec exposures on the same sample. “No LLD” points (*triangles*) at $q > 0.006 \text{ \AA}^{-1}$ were negative and $|I(q)|$ is plotted instead.

B.2.4 Determining Photon Rate from Discriminated Intensities

Unfortunately, none of the equations we have derived above—specifically, Eqns. B.50 and B.52, and not even the approximation of Eqn. B.43—can be inverted in a straightforward manner to find b from a measured I_L . There are, however, several less-direct means of extracting b .

One strategy is to find and use the precise value of L for which the last three terms in Eqn. B.50 sum to zero, leaving $\langle I_L \rangle \approx \beta b \langle A \rangle$. This amounts to balancing lost ADU from photons with an equal amount of passed ADU from the dark background. This method is best suited for single-pixel detectors, since the process of determining the correct L is a computationally demanding one that strongly depends on the value of the dark noise, σ_d , and σ_d typically varies from pixel to pixel in a CCD array.

A second strategy is to assume that two or fewer photons are detected in any single

measurement. Expanding Eqn. B.52 to order b^2 results in the quadratic equation

$$0 = \langle I_L \rangle - \beta b \langle A \rangle (1 - V_1(L) - \sigma_d^2 U_1(L)) - \beta^2 b^2 \langle A \rangle \left[V_1(L) - V_2(L) + \sigma_d^2 \left(U_1(L) - \frac{1}{2} U_2(L) \right) \right]. \quad (\text{B.57})$$

Although this can be solved exactly for b , it pertains only to very low intensities. Unlike Eqn. B.43, at $b \gg 1$ Eqn. B.57 *diverges* from the correct formula, $\langle I_L \rangle = \beta b \langle A \rangle$.

A third strategy involves solving for $\langle I_L \rangle$ in Eqn. B.52 over a set of preselected b and σ_d values. Interpolation within such a “lookup table” can yield with good precision the b value corresponding to a measured I_L and a given (*i.e.* previously ascertained) value of σ_d . Because Eqn. B.52 depends weakly on σ_d , evaluations at only a few values of σ_d may suffice. In addition, full calculations need be carried out only for $b \sim 1$. For $I_L \gg \beta \langle A \rangle$, $\hat{b} \approx I_L / \beta \langle A \rangle$ may be used, and for very small I_L , $\hat{b} \approx I_L / \beta \langle A \rangle (1 - V_1(L) - \sigma_d^2 U_1(L))$ (see Eqn. B.57).

We have taken the third approach. In addition, the recursive forms of Eqns. B.54 and B.56 are readily implemented using FFT-based convolution algorithms [88]. These make for relatively swift correction calculations even for large data sets. Fig. B-3 shows an example of discrimination’s benefits for a sample of polystyrene latex spheres in glycerol. Without using an LLD, the data at higher q is dominated by dark drift, dropping rapidly below zero. Using the LLD clearly retrieves signal from all q , as evidenced by the longer-exposure data shown for comparison in Fig B-3. Though analysis with no LLD correction is superior to not using an LLD at all, the uncorrected results are underestimated by as much as a factor of 2. This is especially visible at lower q , where the corrected results agree very well with the (long-exposure) reference curve.

A straightforward, if notationally cumbersome, expansion of this method should in principle enable corrections for bias introduced into correlation functions by lower-level discrimination as well.

Bibliography

- [1] P. G. de Gennes and J. Prost. *The Physics of Liquid Crystals*. Oxford University Press, New York, 1993.
- [2] T. E. Strzelecka, M. W. Davidson, and R. L. Rill. Multiple liquid crystal phases of DNA at high concentrations. *Nature*, 331(6155):457–460, 1988.
- [3] S. Fraden. Phase transitions in colloidal suspensions of virus particles. In M. Baus, L. F. Rull, and J. P. Ryckaert, editors, *Observation, prediction, and simulation of phase transitions in complex fluids*. Kluwer Academic, Dordrecht, 1995.
- [4] M. E. Cates and S. J. Candau. Statics and dynamics of wormlike surfactant micelles. *J. Phys. Cond. Matt.*, 2(33):6869–6892, 1990.
- [5] P. van der Schoot and M. E. Cates. Growth, static light scattering, and spontaneous ordering of rodlike micelles. *Langmuir*, 10(3):670–679, 1994.
- [6] P. Davidson, P. Batail, J.-C. P. Gabriel, J. Livage, C. Sanchez, and C. Bourgaux. Mineral liquid crystalline polymers. *Prog. Polym. Sci.*, pages 913–936, 1997.
- [7] J.-C. P. Gabriel and P. Davidson. New trends in colloidal liquid crystals based on mineral moieties. *Adv. Mat.*, 12(1):9–20, 2000.
- [8] B. J. Lemaire, P. Davidson, J. Ferré, P. Panine, I. Dozov, and J. P. Jolivet. Outstanding magnetic properties of nematic suspensions of goethite (α -FeOOH) nanorods. *Phys. Rev. Lett.*, 88(12):125507, 2002.
- [9] B. M. I. van der Zande, M. R. Böhmer, L. G. J. Fokkink, and C. Schönenberger. Aqueous gold sols of rod-shaped particles. *J. Chem. Phys.*, 101(6):852–854, 1997.
- [10] B. M. I. van der Zande, M. R. Böhmer, L. G. J. Fokkink, and C. Schönenberger. Colloidal dispersions of gold rods: synthesis and optical properties. *Langmuir*, 16(2):451–458, 2000.
- [11] P. A. Buining, C. Pathmamanoharan, M. Bosboom, J. B. H. Jansen, and H. N. W. Lekkerkerker. Effect of hydrothermal conditions on the morphology of colloidal boehmite particles—implications for fibril formation and monodispersity. *J. Am. Cer. Soc.*, 73(8):2385–2390, 1990.
- [12] P. A. Buining, C. Pathmamanoharan, J. B. H. Jansen, and H. N. W. Lekkerkerker. Preparation of colloidal boehmite needles by hydrothermal treatment of aluminum oxide precursors. *J. Am. Cer. Soc.*, 74(6):1303–1307, 1991.

- [13] P. A. Buining. *Preparation and properties of dispersions of colloidal boehmite rods: a systems-oriented study*. PhD thesis, Utrecht University, 1992.
- [14] P. A. Buining, A. P. Philipse, and H. N. W. Lekkerkerker. Phase behavior of aqueous dispersions of colloidal boehmite rods. *Langmuir*, 10(7):2106–2114, 1994.
- [15] A. Wierenga, A. P. Philipse, and H. N. W. Lekkerkerker. Aqueous dispersions of colloidal boehmite: structure, dynamics, and yield stress of rod gels. *Langmuir*, 14(1):55–65, 1998.
- [16] P. A. Buining, Y. S. J. Veldhuizen, C. Pathmamanoharan, and H. N. W. Lekkerkerker. Preparation of a non-aqueous dispersion of sterically stabilized boehmite rods. *Colloids and Surfaces*, 64:47–55, 1992.
- [17] P. A. Buining and H. N. W. Lekkerkerker. Isotropic-nematic phase separation of a dispersion of organophilic boehmite rods. *J. Phys. Chem.*, 97(44):11510–11516, 1993.
- [18] J. Buitenhuis. *Colloidal dispersions of sterically stabilized boehmite rods: Particle clustering, light scattering, phase separations and sedimentation*. PhD thesis, Utrecht University, 1994.
- [19] J. Buitenhuis, J. K. G. Dhont, and H. N. W. Lekkerkerker. Static and dynamic light scattering by concentrated colloidal suspensions of polydisperse sterically stabilized boehmite rods. *Macromolecules*, 27(25):7267–7277, 1994.
- [20] J. Buitenhuis and A. P. Philipse. Orientational order in sediments of colloidal rods. *J. Colloid Interface Sci.*, 176(1):272–276, 1995.
- [21] M. P. B. van Bruggen, F. M. van der Kooij, and H. N. W. Lekkerkerker. Liquid crystal phase transitions in dispersions of rod-like colloidal particles. *J. Phys. Cond. Matt.*, 8:9451–9456, 1996.
- [22] M. P. B. van Bruggen, J. K. G. Dhont, and H. N. W. Lekkerkerker. Morphology and kinetics of the isotropic-nematic phase transition in dispersions of hard rods. *Macromolecules*, 32(7):2256–2264, 1999.
- [23] M. P. B. van Bruggen and H. N. W. Lekkerkerker. Metastability and multistability: Gelation and liquid crystal formation in suspensions of colloidal rods. *Langmuir*, 18(19):7141–7145, 2002.
- [24] M. van Bruggen. *Liquid crystal formation and diffusion in dispersions of colloidal rods*. PhD thesis, Utrecht University, 1996.
- [25] M. P. B. van Bruggen. Preparation and properties of colloidal core-shell rods with adjustable aspect ratios. *Langmuir*, 14(9):2245–2255, 1998.
- [26] C. M. van Kats. Private communication. 1999.
- [27] R. Holyst and P. Oswald. Liquid-crystalline order in polymer systems: Basic models. *Macromol. Theory Simul.*, 10(1):1–16, 2001.
- [28] T. Odijk. Theory of lyotropic polymer liquid crystals. *Macromolecules*, 19(9):2313–2329, 1986.

- [29] T. Odijk. Elastic constants of nematic solutions of rod-like and semi-flexible polymers. *Liq. Cryst.*, 1(6):553–559, 1986.
- [30] M. Doi and S. Edwards. *The Theory of Polymer Dynamics*. Oxford University Press, Oxford, 1986.
- [31] J. P. Hansen and I. R. McDonald. *Theory of simple liquids*. Academic Press, London, 1986.
- [32] P. van der Schoot. Structure factor of a semidilute solution of polydisperse rodlike macromolecules. *Macromolecules*, 25(11):2923–2927, 1992.
- [33] G. J. Vroege and H. N. W. Lekkerkerker. Phase transitions in lyotropic colloidal and polymer liquid crystals. *Rep. Prog. Phys.*, 55:1241–1309, 1992.
- [34] B. J. Berne and R. Pecora. *Dynamic Light Scattering, with Applications to Chemistry, Biology, and Physics*. Wiley, New York, 1976.
- [35] A. Stroobants, H. N. W. Lekkerkerker, and T. Odijk. Effect of electrostatic interaction on the liquid crystal phase transition in solutions of rodlike polyelectrolytes. *Macromolecules*, 19(8):2232–2238, 1986.
- [36] T. Maeda. Structure factor of a solution of charged rodlike macromolecules in the isotropic phase. *Macromolecules*, 24(10):2740–2747, 1991.
- [37] S.-D. Lee and R. B. Meyer. Computations of the phase equilibrium, elastic constants, and viscosities of a hard-rod nematic liquid crystal. *J. Chem. Phys.*, 84(6):3443–3448, 1986.
- [38] L. Onsager. The effects of shape on the interaction of colloidal particles. *Ann. NY Acad. Sci.*, 51(4):627–659, 1949.
- [39] H. N. W. Lekkerkerker, P. Coulon, and R. van der Haegen. On the isotropic-liquid crystal phase separation in a solution of rodlike particles of different lengths. *J. Chem. Phys.*, 80(7):3427–3433, 1984.
- [40] T. Odijk and H. N. W. Lekkerkerker. Theory of the isotropic-liquid crystal phase separation for a solution of bidisperse rodlike macromolecules. *J. Phys. Chem.*, 89(10):2090–2096, 1985.
- [41] G. J. Vroege and H. N. W. Lekkerkerker. Theory of the isotropic-nematic-nematic phase separation for a solution of bidisperse rodlike particles. *J. Phys. Chem.*, 97:3601–3605, 1993.
- [42] R. van Roij and B. Mulder. Absence of high-density consolute point in nematic hard rod mixtures. *J. Chem. Phys.*, 105(24):11237–11245, 1996.
- [43] G. J. Vroege and H. N. W. Lekkerkerker. Theory of phase separation for a solution of tridisperse rodlike particles. *Coll. Surf. A*, 129–130:405–413, 1997.
- [44] A. Speranza and P. Sollich. Isotropic-nematic phase equilibria of polydisperse hard rods: the effect of fat tails in the length distribution. *J. Chem. Phys.*, 118(11):5213–5223, 2003.

- [45] A. Speranza and P. Sollich. Isotropic-nematic phase equilibria in the onsager theory of hard rods with length polydispersity. *Phys. Rev. E*, 67:061702, 2003.
- [46] H. H. Wensink and G. J. Vroege. Isotropic-nematic phase behavior of length-polydisperse hard rods. *J. Chem. Phys.*, 119(13):6868–6882, 2003.
- [47] T. Itou and A. Teramoto. Triphase equilibrium in aqueous solutions of the rodlike polysaccharide schizophyllan. *Macromolecules*, 17(7):1419–1420, 1984.
- [48] A. Guinier and G. Fournet. *Small-angle scattering of X-rays*. Wiley, New York, 1955.
- [49] O. Glatter. Data treatment. In O. Glatter and O. Kratky, editors, *Small-angle X-ray scattering*. Academic Press, London, 1982.
- [50] G. Porod. General theory. In O. Glatter and O. Kratky, editors, *Small-angle X-ray scattering*. Academic Press, London, 1982.
- [51] M. Sutton, S. G. J. Mochrie, T. Greytak, S. E. Nagler, L. E. Berman, G. A. Held, and G. B. Stephenson. Observation of speckle by diffraction with coherent X-rays. *Nature*, 352:608–610, 1991.
- [52] D. Lumma, L. B. Lurio, and S. G. J. Mochrie. Area detector based photon correlation in the regime of short data batches: data reduction for dynamic x-ray scattering. *Rev. Sci. Inst.*, 71(9):3274–3289, 2000.
- [53] L. B. Lurio, D. Lumma, M. A. Borthwick, P. Falus, S. G. J. Mochrie, and M. Sutton. Creating coherent X-rays and putting them to use: x-ray photon correlation spectroscopy at beamline 8-ID at the Advanced Photon Source. *Synch. Rad. News*, 13(2):28–37, 2000.
- [54] D. Lumma. *Probing the microscopic dynamics of complex fluids with X-ray photon correlation spectroscopy*. PhD thesis, Massachusetts Institute of Technology, 2000.
- [55] P. Falus. *X-ray photon correlation spectroscopy studies of the dynamics of self-assembling block copolymer structures*. PhD thesis, Massachusetts Institute of Technology, 2004.
- [56] A. C. Price, L. B. Sorensen, S. D. Kevan, J. Toner, A. Poniewierski, and R. Holyst. Coherent soft-X-ray dynamic light scattering from smectic-A films. *Phys. Rev. Lett.*, 82(4):755–758, 1999.
- [57] A. Fera, I. P. Dolbnya, G. Grübel, H. G. Muller, B. I. Ostrovskii, A. N. Shalaginov, and W. H. de Jeu. Complex dynamic behavior of fluctuating smectic-A films as studied by scattering with coherent X-rays. *Phys. Rev. Lett.*, 85(11):2316–2319, 2000.
- [58] I. Sikharulidze, I. P. Dolbnya, A. Fera, A. Madsen, B. I. Ostrovskii, and W. H. de Jeu. Smectic membranes in motion: approaching the fast limits of X-ray photon correlation spectroscopy. *Phys. Rev. Lett.*, 88:115503, 2002.
- [59] I. Sikharulidze, B. Farago, I. P. Dolbnya, A. Fera, A. Madsen, and W. H. de Jeu. Surface and bulk elasticity determined fluctuation regimes in smectic membranes. *Phys. Rev. Lett.*, 91:165504, 2003.

- [60] A. Madsen, J. Als-Nielsen, and G. Grübel. Viscosity of a liquid crystal near the nematic-smectic A phase transition. *Phys. Rev. Lett.*, 90(8):085701, 2003.
- [61] D. Liang, M. A. Borthwick, and R. L. Leheny. Smectic liquid crystals in anisotropic colloidal silica gels. *J. Phys. Cond. Matt.*, 16(19):S1989–S2002, 2004.
- [62] B. E. Warren. *X-ray Diffraction*. Addison-Wesley, Reading, Mass., 1969.
- [63] A. J. Leadbetter and E. K. Norris. Distribution functions in three liquid crystals from X-ray diffraction measurements. *Mol. Phys.*, 38(3):669–686, 1979.
- [64] I. W. Hamley. Scattering from uniform, cylindrically symmetric particles in liquid crystal phases. *J. Chem. Phys.*, 95(12):9376–9383, 1991.
- [65] M. Deutsch. Orientational order determination in liquid crystals by x-ray diffraction. *Phys. Rev. A*, 44(12):8264–8270, 1991.
- [66] P. Davidson, D. Petermann, and A. M. Levelut. The measurement of the nematic order parameter by X-ray scattering reconsidered. *J. Phys. II (France)*, 5:113–131, 1995.
- [67] M. A. Bates and G. R. Luckhurst. X-ray scattering patterns of model liquid crystals from computer simulation: Calculation and analysis. *J. Chem. Phys.*, 118(14):6605–6614, 2003.
- [68] A. J. Leadbetter and P. G. Wrighton. Order parameters in SA, SC, and N phases by X-ray diffraction. *J. Phys. (France)*, 40:C3–234–C3–242, 1979.
- [69] R. M. Richardson and J. M. Allman. Neutron scattering from mixtures of isotopically labelled molecules: a new method for determining the orientational distribution function in liquid crystals. *Liq. Cryst.*, 7(5):701–719, 1990.
- [70] R. Oldenbourg, X. Wen, R. B. Meyer, and D. L. D. Caspar. Orientational distribution function in nematic tobacco-mosaic-virus liquid crystals measured by X-ray diffraction. *Phys. Rev. Lett.*, 61(16):1851–1854, 1988.
- [71] P. Davidson, C. Bourgaux, P. Sergot, and J. Livage. A small-angle X-ray scattering study of the lyotropic nematic phase of vanadium pentoxide gels. *J. Appl. Cryst.*, 30:727–732, 1996.
- [72] K. R. Purdy, Z. Dogic, S. Fraden, A. Rühm, L. B. Lurio, and S. G. J. Mochrie. Measuring the nematic order of suspensions of colloidal fd virus by x-ray diffraction and optical birefringence. *Phys. Rev. E*, 67:031708, 2003.
- [73] W. Maier and A. Saupe. *Z. Naturforsch.*, 13a:564, 1958.
- [74] G. R. Luckhurst. Molecular field theories of nematics. In G. R. Luckhurst and G. W. Gray, editors, *The molecular physics of liquid crystals*. Academic Press, London, 1979.
- [75] V. K. Kelkar and A. S. Paranjpe. Orientational order parameter of liquid crystals by X-ray diffraction: a simple approach. *Mol. Cryst. Liq. Cryst. Letters*, 4(5):139–144, 1987.

- [76] A. S. Paranjpe and V. K. Kelkar. Chain ordering in the nematic phase of 4OBA. *Mol. Cryst. Liq. Cryst.*, 102:(Letters) 289–294, 1984.
- [77] M. Abramowitz and I. A. Stegun, editors. *Handbook of mathematical functions with formulas, graphs, and mathematical tables*. U.S. Govt. Print. Off., Washington, 1972.
- [78] G. Friedel. *Comptes Rendus Hebd. Acad. Sci. (Paris)*, 157:1533–1536, 1913.
- [79] B. Jerome. Surface effects and anchoring in liquid crystals. *Rep. Prog. Phys.*, 54(3):391–451, 1991.
- [80] G. A. Carri and M. Muthukumar. Attractive interactions and phase transitions in solutions of similarly charged rod-like polyelectrolytes. *J. Chem. Phys.*, 111(4):1765–1777, 1999.
- [81] S. B. Chen and D. L. Koch. Isotropic-nematic phase transitions in aqueous solutions of weakly charged, rodlike polyelectrolytes. *J. Chem. Phys.*, 104(1):359–374, 1996.
- [82] I. I. Potemkin, R. E. Limberger, A. N. Kudlay, and A. R. Khoklov. Rodlike polyelectrolyte solutions: Effect of the many-body Coulomb attraction of similarly charged molecules favoring weak nematic ordering at very small polymer concentration. *Phys. Rev. E*, 66:011802, 2002.
- [83] R. Pecora and Y. Tagami. Light scattering from polydisperse rods and gaussian coils: ii. spectral distribution of the pure translational term. *J. Chem. Phys.*, 51(8):3298–3305, 1969.
- [84] E. W. Weisstein. Log normal distribution. *MathWorld—A Wolfram Web Resource*, <http://mathworld.wolfram.com/LogNormalDistribution.html>, 2004.
- [85] D. E. Yates, S. Levine, and T. W. Healy. *J. Chem. Soc. Faraday Trans.*, 70(1):1807, 1974.
- [86] J. A. Davis, R. O. James, and J. O. Leckie. Surface ionization and complexation at the oxide/water interface: I. Computation of electrical double layer properties in simple electrolytes. *J. Colloid Interface Sci.*, 63(3):480–499, 1978.
- [87] C. F. Wu, S. H. Chen, L. B. Shih, and J. S. Lin. Direct measurement of counterion distribution around cylindrical micelles by small-angle X-ray scattering. *Phys. Rev. Lett.*, 61(5):645–648, 1988.
- [88] W. H. Press, B. P. Flannery, S. A. Teukolsky, and W. T. Vetterling. *Numerical Recipes in C: The Art of Scientific Computing*. Cambridge University Press, Cambridge, 1989.
- [89] D. R. Lide, editor. *CRC Handbook of Chemistry and Physics*. CRC Press, Cleveland, 84 edition, 2003.
- [90] K. S. Schmitz. *Dynamic light scattering by macromolecules*. Academic Press, Boston, 1991.
- [91] A. J. Leadbetter. Structural studies of nematic, smectic A and smectic C phases. In G. R. Luckhurst and G. W. Gray, editors, *The molecular physics of liquid crystals*. Academic Press, London, 1979.

- [92] J. Schneider, W. Hess, and R. Klein. The static structure factor of a dilute system of charged rods in solution. *J. Phys. A: Math. Gen.*, 18:1221–1228, 1985.
- [93] J. Schneider, D. Karrer, J. K. G. Dhont, and R. Klein. The pair-distribution function and light-scattered intensities for charged rod-like macromolecules in solution. *J. Chem. Phys.*, 87(5):3008–3015, 1987.
- [94] T. Shimada, M. Doi, and K. Okano. Concentration fluctuation of stiff polymers. I. Static structure factor. *J. Chem. Phys.*, 88(4):2815–2821, 1988.
- [95] P. van der Schoot and T. Odijk. Structure factor of semidilute solutions of rodlike macromolecules. *Macromolecules*, 23(18):4181–4182, 1990.
- [96] B. Weyerich, B. D’Aguanno, E. Canessa, and R. Klein. Structure and dynamics of suspensions of charged rod-like particles. *Faraday Discuss. Chem. Soc.*, 90:245–259, 1990.
- [97] T. Odijk. The theory of light scattering from rod-like polyelectrolytes. In W. Brown, editor, *Light scattering : Principles and development*. Oxford University Press, Oxford, 1996.
- [98] T. Maeda. Matrix representation of the dynamical structure factor of a solution of rodlike polymers in the isotropic phase. *Macromolecules*, 22(4):1881–1890, 1989.
- [99] J. Schneider, W. Hess, and R. Klein. A dumbbell model for the structure of charged, rodlike macromolecules in dilute solution. *Macromolecules*, 19(6):1729–1732, 1986.
- [100] M. Hagenbüchle, B. Weyerich, M. Deggleman, C. Graf, R. Krause, E. E. Maier, S. F. Schulz, R. Klein, and R. Weber. Static light scattering by aqueous solutions of rodlike fd-virus particles. *Physica A*, 169:29–41, 1990.
- [101] E. E. Maier, R. Krause, M. Deggelmann, M. Hagenbüchle, R. Weber, and S. Fraden. Liquidlike order of charged rodlike particle solutions. *Macromolecules*, 25(3):1125–1133, 1992.
- [102] V. Castelletto, R. Itri, L. Q. Amaral, and G. P. Spada. Small-angle X-ray scattering of DNA fragments: Form and interference factors. *Macromolecules*, 28(24):8395–8400, 1995.
- [103] V. Castelletto and L. Q. Amaral. Short range order of rodlike polyelectrolytes in the isotropic phase. *Macromolecules*, 32(10):3469–3473, 1999.
- [104] M. Miriam de Souza Lima and R. Borsali. Static and dynamic light scattering from polyelectrolyte microcrystal cellulose. *Langmuir*, 18(4):992–996, 2002.
- [105] M. Doi, T. Shimada, and K. Okano. Concentration fluctuation off stiff polymers. II. Dynamical structure factor of rod-like polymers in the isotropic phase. *J. Chem. Phys.*, 88(6):4070–4075, 1988.
- [106] J. W. Winters, T. Odijk, and P. van der Schoot. Spinodal decomposition in a semidilute suspension of rodlike micelles. *Phys. Rev. E*, 63:011501, 2000.

- [107] T. Maeda and S. Fujime. Spectrum of light quasielastically scattered from solutions of very long rods at dilute and semidilute regimes. *Macromolecules*, 17(6):1157–1167, 1984.
- [108] T. Maeda. Matrix representation of the dynamical structure factor of a solution of rodlike polymers in the isotropic phase. 2. VH-depolarized scattering. *Macromolecules*, 23(5):1464–1474, 1990.
- [109] J. M. Rallison and L. G. Leal. Dynamic light scattering from macromolecules: the separation of translation from rotational and deformational modes. *J. Chem. Phys.*, 74(9):4819–4825, 1981.
- [110] F. R. Hallett, B. Nickel, and T. Craig. Quasielastic light scattering from long rigid rods. *Biopolymers*, 24:947–960, 1985.
- [111] J. Wilcoxon and J. M. Schurr. Dynamic light scattering from thin rigid rods: anisotropy of translational diffusion of tobacco mosaic virus. *Biopolymers*, 22:849–867, 1983.
- [112] T. Kirchhoff, H. Löwen, and R. Klein. Dynamical correlations in suspensions of charged rodlike macromolecules. *Phys. Rev. E*, 53(5):5011–5022, 1996.
- [113] J. K. Phalakornkul, A. P. Gast, and R. Pecora. Rotational and translational dynamics of rodlike polymers: a combined transient electric birefringence and dynamic light scattering study. *Macromolecules*, 32(9):3122–3135, 1999.
- [114] D. E. Koppel. Analysis of macromolecular polydispersity in intensity correlation spectroscopy: the method of cumulants. *J. Chem. Phys.*, 57(11):4814–4820, 1972.
- [115] P. Štěpánek. Data analysis in dynamic light scattering. In W. Brown, editor, *Dynamic light scattering: The method and some applications*. Clarendon Press, Oxford, 1993.
- [116] J. D. Jackson. *Classical Electrodynamics*. Wiley, New York, 1999.
- [117] M. E. Rose. *Elementary theory of angular momentum*. Dover, New York, 1995.
- [118] E. W. Weisstein. Wigner 3j-symbol. *MathWorld—A Wolfram Web Resource*, <http://mathworld.wolfram.com/Wigner3j-Symbol.html>, 2004.
- [119] R. Pecora. Doppler shifts in light scattering from pure liquids and polymer solutions. *J. Chem. Phys.*, 40(6):1604–1614, 1964.
- [120] R. Pecora. Spectral distribution of light scattered by monodisperse rigid rods. *J. Chem. Phys.*, 48(9):4126–4128, 1968.
- [121] J. H. Wilkinson and C. Reich. *Handbook for automatic computation, volume II: Linear algebra*. Springer-Verlag, Berlin, 1971.
- [122] M. Fixman. Entanglements of semidilute polymer rods. *Phys. Rev. Lett.*, 54(4):337–339, 1985.
- [123] M. Fixman. Dynamics of semidilute polymer rods: an alternative to cages. *Phys. Rev. Lett.*, 55(22):2429–2432, 1985.

- [124] I. Teraoka and R. Hayakawa. Theory of dynamics of entangled rod-like polymers by use of a mean-field Green function formulation: i. transverse diffusion. *J. Chem. Phys.*, 89(11):6989–6995, 1988.
- [125] I. Teraoka and R. Hayakawa. Theory of dynamics of entangled rod-like polymers by use of a mean-field Green function formulation: ii. rotational diffusion. *J. Chem. Phys.*, 91(4):2643–2648, 1988.
- [126] Y. Tagami and R. Pecora. Light scattering from polydisperse rods and gaussian coils: i. integrated intensities. *J. Chem. Phys.*, 51(8):3298–3305, 1969.
- [127] C. E. Montague and J. Newman. Comparison of approximations for the analysis of static and dynamic light scattering data from distributions of rodlike polymers: applications to model systems for fibrin and actin. *Macromolecules*, 17(7):1391–1396, 1984.
- [128] J. Drögmeier, H. Hinssen, and W. Elmer. Flexibility of F-actin in aqueous solution: a study on filaments on different average lengths. *Macromolecules*, 27(1):87–95, 1994.
- [129] J. Drögmeier, H. Hinssen, and W. Elmer. Polarized and depolarized dynamic light scattering study on F-actin in solution: comparison with model calculations. *Macromolecules*, 27(1):96–101, 1994.
- [130] S. Broersma. Rotational diffusion constant of a cylindrical particle. *J. Chem. Phys.*, 32(6):1626–1631, 1960.
- [131] S. Broersma. Viscous force constant for a closed cylinder. *J. Chem. Phys.*, 32(6):1631–1635, 1960.
- [132] S. Broersma. Viscous force and torque constants for a cylinder. *J. Chem. Phys.*, 74(12):6989–6990, 1981.
- [133] M. M. Tirado and José García de la Torre. Translational friction coefficients of rigid, symmetric top macromolecules: application to circular cylinders. *J. Chem. Phys.*, 71(6):2581–2587, 1979.
- [134] M. M. Tirado and José García de la Torre. Rotational dynamics of rigid, symmetric top macromolecules: application to circular cylinders. *J. Chem. Phys.*, 73(4):1986–1993, 1980.
- [135] I. Teraoka, N. Ookubo, and R. Hayakawa. Molecular theory on the entanglement effect of rodlike polymers. *Phys. Rev. Lett.*, 55(24):2712–2715, 1985.
- [136] G. Szamel. Reptation as a dynamic mean-field theory: study of a simple model of rodlike polymers. *Phys. Rev. Lett.*, 70(24):3744–3747, 1993.
- [137] P. S. Russo and F. E. Karasz. Dynamic light scattering study of semidilute solutions of a stiff-chain polymer. *J. Chem. Phys.*, 80(10):5312–5325, 1984.
- [138] T. Coviello, K. Kajiwara, W. Burchard, M. Dentini, and V. Crescenzi. Solution properties of xanthan: 1. dynamic and static light scattering from native and modified xanthans in dilute solutions. *Macromolecules*, 19(11):2826–2831, 1986.

- [139] L. M. DeLong and P. S. Russo. Thermodynamic and dynamic behavior of semiflexible polymers in the isotropic phase. *Macromolecules*, 24(23):6139–6155, 1991.
- [140] P. S. Russo. Dynamic light scattering from rigid and nearly rigid rods. In W. Brown, editor, *Dynamic light scattering: The method and some applications*. Clarendon Press, Oxford, 1993.
- [141] D. Lehner, H. Lindner, and O. Glatter. Determination of the translational and rotational diffusion coefficients of rodlike particles using depolarized dynamic light scattering. *Langmuir*, 16(4):1689–1695, 2000.
- [142] B. M. I. van der Zande, J. K. G. Dhont, M. R. Böhmer, and A. P. Philipse. Colloidal dispersions of gold rods characterized by dynamic light scattering and electrophoresis. *Langmuir*, 16(2):459–464, 2000.
- [143] S. W. Provencher. A constrained regularization method for inverting data represented by linear algebraic or integral equations. *Comput. Phys. Commun.*, 27(3):213–227, 1982.
- [144] S. W. Provencher. CONTIN: A general purpose constrained regularization program for inverting noisy linear algebraic and integral equations. *Comput. Phys. Commun.*, 27(3):229–242, 1982.
- [145] K. M. Zero and R. Pecora. Rotational and translational diffusion in semidilute solutions of rigid-rod macromolecules. *Macromolecules*, 15(1):87–93, 1982.
- [146] E. Loh. Quasielastic light scattering from solutions of filamentous viruses: ii. comparison between theories and experiments. *Biopolymers*, 18:2569–2588, 1979.
- [147] T. Maeda and S. Fujime. Dynamic light-scattering study of suspensions of fd virus: Application of a theory of the light-scattering spectrum of weakly bending filaments. *Macromolecules*, 18(12):2430–2437, 1985.
- [148] K. Kubota, H. Urabe, Y. Tominaga, and S. Fujime. Spectrum of light quasi-elastically scattered from suspensions of tobacco mosaic virus: Experimental study of anisotropy in translational diffusion. *Macromolecules*, 17(10):2096–2104, 1984.
- [149] Orsay Liquid Crystal Group. Quasielastic Rayleigh scattering in nematic liquid crystals. *Phys. Rev. Lett.*, 23(25):1361–1363, 1969.
- [150] R. Borsali, D. Y. Yoon, and R. Pecora. Determination of splay and twist relaxation modes in nematic liquid crystals from dynamic light scattering experiments. *J. Phys. Chem. B*, 102(33):6337–6341, 1998.
- [151] S.-D. Lee and R. B. Meyer. Light scattering measurements of anisotropic viscoelastic coefficients of a main-chain polymer nematic liquid crystal. *Liq. Cryst.*, 7(1):15–29, 1990.
- [152] J. P. Straley. Frank elastic constants of the hard-rod liquid crystal. *Phys. Rev. A*, 8:2181, 1973.
- [153] G. J. Vroege and T. Odijk. Elastic moduli of a nematic liquid-crystalline solution of polyelectrolytes. *J. Chem. Phys.*, 87(7):4223–4232, 1987.

- [154] K. Se and G. C. Berry. Frank elastic constants and Leslie-Ericksen viscosity coefficients of nematic solutions of a rodlike polymer. *Mol. Cryst. Liq. Cryst.*, 153:133–142, 1987.
- [155] T. Sato and A. Teramoto. On the Frank elastic constants of lyotropic polymer liquid crystals. *Macromolecules*, 29(11):4107–4114, 1996.
- [156] J. Fukuda and H. Yokoyama. Free energy of rigid rods: contribution of rotational entropy to Frank elasticity. *J. Phys. Soc. Japan*, 71(6):1463–1470, 2002.
- [157] D. Gu, A. M. Jamieson, C. Rosenblatt, D. Tomazos, M. Lee, and V. Percec. Dynamic light scattering from a nematic monodomain containing a side-chain liquid crystal polymer in a nematic solvent. *Macromolecules*, 24(9):2385–2390, 1991.
- [158] P. van der Schoot and T. Odijk. Static and dynamic light scattering from liquid crystalline solutions of rodlike macromolecules. *J. Chem. Phys.*, 93(5):3580–3592, 1990.
- [159] L. Cipelletti, S. Manley, R. C. Ball, and D. A. Weitz. Universal aging features in the restructuring of fractal colloidal gels. *Phys. Rev. Lett.*, 84(10):2275–2278, 2000.
- [160] L. Cipelletti, L. Ramos, S. Manley, E. Pitard, D. A. Weitz, E. E. Pashkovski, and M. Johansson. Universal non-diffusive slow dynamics in aging soft matter. *Faraday Discuss.*, 123:237–251, 2003.
- [161] R. Bandyopadhyay, D. Liang, H. Yardimci, D. A. Sessoms, M. A. Borthwick, S. G. J. Mochrie, J. L. Harden, and R. L. Leheny. Evolution of particle-scale dynamics in an aging clay suspension. *submitted for publication*, 2004.
- [162] A. P. Y. Wong and P. Wiltzius. Dynamic light scattering with a CCD camera. *Rev. Sci. Instr.*, 64(9):2547–2549, 1993.
- [163] S. Kirsch, V. Frenz, W. Schärtl, E. Bartsch, and H. Sillescu. Multispeckle autocorrelation spectroscopy and its application to the investigation of ultraslow dynamical processes. *J. Chem. Phys.*, 104(4):1758–1761, 1996.
- [164] S. B. Dierker, R. Pindak, R. M. Fleming, I. K. Robinson, and L. Berman. X-ray photon correlation spectroscopy study of Brownian motion of gold colloids in glycerol. *Phys. Rev. Lett.*, 75(3):449–452, 1995.
- [165] S. G. J. Mochrie, A. M. Mayes, A. R. Sandy, M. Sutton, S. Brauer, G. B. Stephenson, D. L. Abernathy, and G. Grübel. Dynamics of block copolymer micelles revealed by X-ray intensity fluctuation spectroscopy. *Phys. Rev. Lett.*, 78(7):1275–1278, 1997.
- [166] O. K. C. Tsui and S. G. J. Mochrie. Dynamics of concentrated colloidal suspensions probed by x-ray correlation spectroscopy. *Phys. Rev. E*, 57(2):2030–2034, 1998.
- [167] L. Cipelletti and D. A. Weitz. Ultralow-angle dynamic light scattering with a charge coupled device camera based multispeckle, multitaup correlator. *Rev. Sci. Instr.*, 70(8):3214–3221, 1999.
- [168] P. Falus, M. A. Borthwick, and S. G. J. Mochrie. A fast CCD camera for x-ray photon correlation spectroscopy and time-resolved x-ray scattering and imaging. *submitted for publication*, 2004.

- [169] D. H. Munro. Using the Yorick interpreted language. *Computers in Physics*, 9:609–615, 1995.
- [170] D. H. Munro. Yorick: an interpreted scientific programming language. <ftp://ftp-icf.llnl.gov/pub/Yorick/doc/index.html>, 2004.
- [171] S. M. Gruner, M. W. Tate, and E. F. Eikenberry. Charge-coupled device area x-ray detectors. *Rev. Sci. Inst.*, 73(8):2815–2842, 2002.
- [172] K. Schätzel. Single-photon correlation techniques. In W. Brown, editor, *Dynamic light scattering: The method and some applications*. Clarendon Press, Oxford, 1993.
- [173] K. Schätzel. Noise on photon correlation data: i. autocorrelation functions. *Quantum Opt.*, 2:287–305, 1990.
- [174] D. Magatti and F. Ferri. Fast multi-tau real-time software correlator for dynamic light scattering. *Appl. Opt.*, 40(24):4011–4021, 2001.
- [175] K. Schätzel, M. Drewel, and S. Stimac. Photon correlation measurements at large lag times: improving statistical accuracy. *J. Modern Optics*, 35(4), 1988.
- [176] E. Dufresne, R. Brüning, M. Sutton, B. Rodricks, and G. B. Stephenson. A statistical technique for characterizing position sensitive detectors. *Nucl. Instr. and Meth. in Phys. Res. A*, 364:380–393, 1995.
- [177] F. Livet, F. Bley, J. Mainville, R. Caudron, S. G. J. Mochrie, E. Geissler, G. Dolino, D. Abernathy, G. Grübel, and M. Sutton. Using direct illumination CCDs as high-resolution area detectors for X-ray scattering. *Nucl. Instr. and Meth. in Phys. Res. A*, 451:596–609, 2000.
- [178] J. H. van Vleck and D. Middleton. The spectrum of clipped noise. *Proc. IEEE*, 54(1):2–19, 1966.
- [179] E. Jakeman and E. R. Pike. Spectrum of clipped photon-counting fluctuations of Gaussian light. *J. Phys. A (Gen. Phys.)*, 2:411–412, 1969.
- [180] E. Jakeman. Theory of optical spectroscopy by digital autocorrelation of photon-counting fluctuations. *J. Phys. A (Gen. Phys.)*, 3:201–215, 1969.